AFRL-AFOSR-VA-TR-2023-0386

Ultra-high Strength Superelastic Transforming Metal Matrix-Graphene Composites

Reza Mirzaeifar
VIRGINIA POLYTECHNIC INST AND STATE UNIVERSITY
300 TURNER ST NW, SUITE 4200
BLACKSBURG, VA,
US

07/06/2023
Final Technical Report

DISTRIBUTION A: Distribution approved for public release.

Air Force Research Laboratory
Air Force Office of Scientific Research
Arlington, Virginia 22203
Air Force Materiel Command

REPORT DOCUMENTATION PAGE

PLEASE DO NOT RETURN YOUR FORM TO THE ABOVE ORGANIZATION.

1. REPORT DATE	2. REPORT TYPE	3. DATES COVERED	
20230706	Final	START DATE 20180401	END DATE 20220331

4. TITLE AND SUBTITLE
Ultra-high Strength Superelastic Transforming Metal Matrix-Graphene Composites

5a. CONTRACT NUMBER	5b. GRANT NUMBER	5c. PROGRAM ELEMENT NUMBER
	FA9550-18-1-0169	61102F
5d. PROJECT NUMBER	**5e. TASK NUMBER**	**5f. WORK UNIT NUMBER**

6. AUTHOR(S)
Reza Mirzaeifar

7. PERFORMING ORGANIZATION NAME(S) AND ADDRESS(ES)
VIRGINIA POLYTECHNIC INST AND STATE UNIVERSITY
300 TURNER ST NW, SUITE 4200
BLACKSBURG, VA
US

8. PERFORMING ORGANIZATION REPORT NUMBER

9. SPONSORING/MONITORING AGENCY NAME(S) AND ADDRESS(ES)	10. SPONSOR/MONITOR'S ACRONYM(S)	11. SPONSOR/MONITOR'S REPORT NUMBER(S)
Air Force Office of Scientific Research 875 N. Randolph St. Room 3112 Arlington, VA 22203	AFRL/AFOSR RTA1	AFRL-AFOSR-VA-TR-2023-0386

12. DISTRIBUTION/AVAILABILITY STATEMENT
A Distribution Unlimited: PB Public Release

13. SUPPLEMENTARY NOTES

14. ABSTRACT
A new generation of Metal Matrix Composites with an unprecedented strength and exceptional recoverable strain is developed in this research. Since the early dates of discovering superior intrinsic mechanical properties in nanoscale materials (i.e. graphene_, every attempt on adding these nanoscale materials to a metal matrix composite to achieve similar extraordinary properties at the bulk level has been disappointing. This failure is mainly die to the formation of dislocation in the metal matric, and very large local lattice strains around these dislocations which prevent as efficient load transfer from the nanoparticles to the metal matrix.

15. SUBJECT TERMS

16. SECURITY CLASSIFICATION OF:			17. LIMITATION OF ABSTRACT	18. NUMBER OF PAGES
a. REPORT	b. ABSTRACT	c. THIS PAGE		
U	U	U	UU	167

19a. NAME OF RESPONSIBLE PERSON	19b. PHONE NUMBER *(Include area code)*
MATTHEW KRISAK	

Standard Form 298 (Rev.5/2020)
Prescribed by ANSI Std. Z39.18

DISTRIBUTION A: Distribution approved for public release.

Ultra-high Strength Superelastic Transforming Metal Matrix-Graphene Composites

PI: Reza Mirzaeifar, Mechanical Engineering Department, Virginia Tech

Award Number *AFOSR 2018 YIP Award: FA9550-18-1-0169*

Report type

Final

Reporting Periods

Start: 04/01/2018- End: 03/31/2022

Distribution Statement

Distribution B - Not Approved For Public Release (There are multiple under review papers from this project, so if possible we request not distributing the report at the moment)

Program Officer Name

Dr. Martin Schmidt (Was Dr. Jaimie Tiley when he was in AFOSR)

Principal Investigator Name

Dr. Reza Mirzaeifar

Project Title

Ultra-high Strength Superelastic Transforming Metal Matrix-Graphene Composites

ABSTRACT

A new generation of Metal Matrix Composites with an unprecedented strength and exceptional recoverable strain is developed in this research. Since the early dates of discovering superior intrinsic mechanical properties in nanoscale materials (i.e. graphene), every attempt on adding these nanoscale materials to a metal matrix composite to achieve similar extraordinary properties at the bulk level has been disappointing. This failure is mainly due to the formation of dislocations in the metal matrix, and very large local lattice strains around these dislocations which prevent an efficient load transfer from the nanoparticles to the metal matrix. This research resulted in a novel Graphene-Metal composite in which the metal matrix undergoes a uniform large recoverable phase transformation when subjected to mechanical loading. It is shown that in this system, at the atomistic level, the uniform large recoverable lattice strain of the metal matrix due to the phase transformation deforms the embedded graphene elastically. Such a large elastic deformation in graphene, with the perfect interface between graphene and metal matrix transfers a huge strength from embedded graphene to the matrix, and leads to a material with ultra-high strength. As the deformation mechanisms in both the matrix and graphene are recoverable, the developed material also exhibits an exceptional large recoverable strain. Atomistic-scale computational investigations and experimental studies are designed to determine details of this hypothetical deformation mechanism, and fabricate samples of this material. The developed material, and the fundamental mechanistic insights of the deformation mechanisms in the proposed system, uniquely meet the requirements for aircraft and spacecraft applications as the material has exceptional strength and recoverable strains, and also the proposed concept is used to develop a material with same exceptional mechanical performance at high temperatures.

DISTRIBUTION A: Distribution approved for public release.

Ultra-high Strength Superelastic Transforming Metal Matrix-Graphene Composites

PI: Reza Mirzaeifar, Mechanical Engineering Department, Virginia Tech

Multiscale Structural Mechanics and Prognosis Portfolio

AFOSR 2018 YIP Award: FA9550-18-1-0169

DISTRIBUTION A: Distribution approved for public release.

I- Introduction

A new generation of Metal Matrix Composites with an unprecedented strength and exceptional recoverable strain is developed in this research. The proposed hypothetical atomistic-scale deformation mechanisms in this material overcome the long-standing challenge of transferring the extraordinary mechanical performance of nanoscale materials to the bulk level. Since the early dates of discovering superior intrinsic mechanical properties in nanoscale materials (i.e. graphene), every attempt on adding these nanoscale materials to a metal matrix composite to achieve similar extraordinary properties at the bulk level has been disappointing. This failure is mainly due to the formation of dislocations in the metal matrix, and very large local lattice strains around these dislocations which prevent an efficient load transfer from the nanoparticles to the metal matrix (Figure 1.1a). This research resulted in a novel Graphene-Metal composite in which the metal matrix undergoes a uniform large recoverable phase transformation when subjected to mechanical loading. It is shown that in this system, at the atomistic level, the uniform large recoverable lattice strain of the metal matrix due to the phase transformation deforms the embedded graphene elastically. Such a large elastic deformation in graphene, with the perfect interface between graphene and metal matrix transfers a huge strength from embedded graphene to the matrix, and leads to a material with ultra-high strength (Figure 1.1b-e). As the deformation mechanisms in both the matrix and graphene are recoverable, the developed material also exhibits an exceptional large recoverable strain. Atomistic-scale computational investigations and experimental studies are designed to determine details of this hypothetical deformation mechanism, and fabricate samples of this material. The developed material, and the fundamental mechanistic insights of the deformation mechanisms in the proposed system, uniquely meet the requirements for aircraft and spacecraft applications as the material has exceptional strength and recoverable strains, and also the proposed concept is used to develop a material with same exceptional mechanical performance at high temperatures.

The project is defined in two complementary tasks:

Task 1- Determining the Deformation Mechanisms, and Optimization: Density Functional Theory (DFT) calculations and Molecular Dynamics (MD) simulations are used to investigate the hypothetical deformation mechanisms and the interactions between graphene and NiTi alloy phase transforming metal matrix. DFT calculations are used to investigate the graphene-metal interface. MD modeling are used to investigate the hypothetical deformation mechanisms. The correlation between various geometrical properties and the mechanical performance are investigated and the optimum configuration is determined.

Task 2- Fabrication and Proof of Concept: Proof of concept samples are fabricated and characterized in this task. With the process explained in detail in the proposal, multi layer NiTi-Graphene composites are fabricated using E-beam evaporation/sputtering system and adding graphene layers (using spin-coating of aquatic dispersions of graphene flakes, and also single layer graphene sheets).

DISTRIBUTION A: Distribution approved for public release.

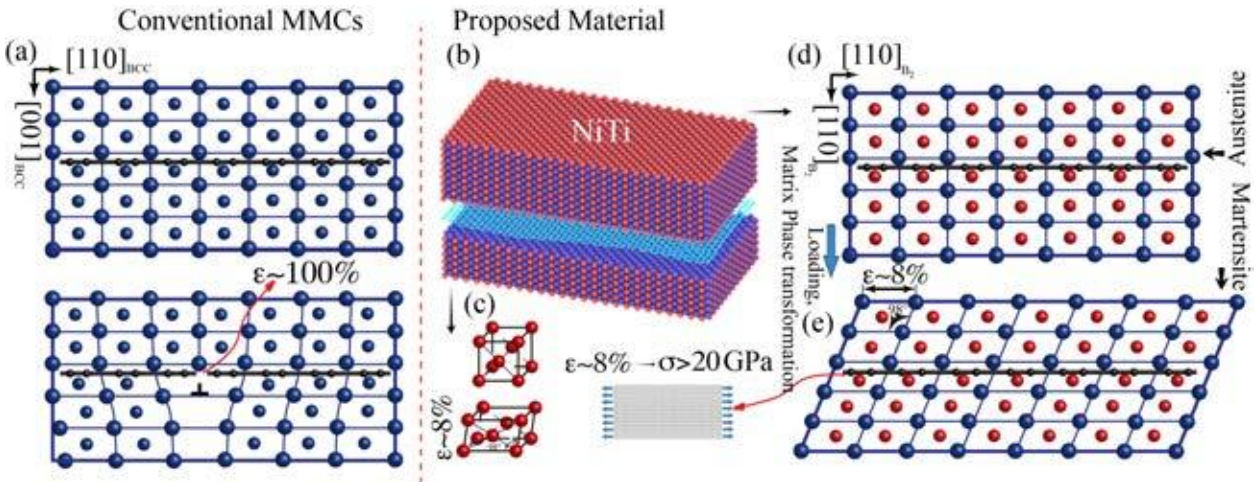

Figure 1.1: All the conventional metal matrix composites fail in achieving significantly high strengths as the interface between reinforcing nanoparticle and metal matrix loses its efficiency by forming dislocations in the matrix (a). In our novel NiTi-Graphene composite (b), the matrix lattice uniformly deforms up to 8% through phase transformation (c), and the nanoparticle reinforcement stretches with no defect (d, e), transferring a very high load to the matrix, and resulting an ultra-high strength composite.

Samples are heat treated and characterized by SEM, TEM, EBSD and Nanoindentation. Multiple free standing, and also thin films supported by compliant substrates are prepared, and tensile tests are performed to measure the strength and recoverable strain of the material.

So far, these tasks have been considered, and both are completed partially as reported in the following chapters. The results have been presented in multiple invited talks by the PI including:

- Joint Condensed Matter and Center for Soft Matter and Biological Physics Seminar, Department of Physics, July 2021, Virginia Tech.
- Brunel Research Festival. Institute of Manufacturing and Materials Showcase, May 27, 2021. Brunel University, London, UK (Virtual Meeting)
- Fall 2020 Mechanical Engineering Department Seminar Series, Virginia Tech
- Joint Condensed Matter and Center for Soft Matter and Biological Physics Seminar, Department of Physics, Virginia Tech.
- Invited talk in 18th U.S. National Congress for Theoretical and Applied Mechanics
- Invited talk by the Department of Materials Science and NanoEngineering at Rice University
- Invited talk in IUTAM Symposium on Phase transformation in shape memory materials: modeling and applications

The results have been also reported in the following journal papers:

1. A. Agrawal, R. Mirzaeifar. Copper-Graphene Composites; Developing the MEAM Potential and Investigating their Mechanical Properties. *Computational Materials Science*e. 2021. 188, 110204.

DISTRIBUTION A: Distribution approved for public release.

2. J. Charleston, A. Agrawal, R. Mirzaeifar. Effect of interface configuration on the mechanical properties and dislocation mechanisms in metal graphene composites. *Computational Materials Science*. 2020. 178, 109621.

3. A. Agrawal, R. Mirzaeifar. Graphene-Nickel Interaction in Layered Metal-matrix Composites. *Surface Science*. 2019. 688: 1-6.

4. S. Kurian, R. Mirzaeifar. Selective Laser Melting of Aluminum Nano-powder Particles, a Molecular Dynamics Study. *Additive Manufacturing*. 2020. **35**: 101272.

5. S. Kurian, R. Mirzaeifar. Deformation Mechanisms of the Subgranular Cellular Structures in Selective Laser Melted 316L Stainless Steel. *Mechanics of Materials*. 2020. **148**: 103478.

6. A. Agrawal, R. Mirzaeifar. Computational investigation of deformation mechanisms at the atomistic scale of metallic glass-graphene composites (MGGCs). *Journal of Applied Physics.* 2021. **130**: 155105.

7. A. Agrawal, J. Charleston, R. Mirzaeifar. Experimental Investigation of Deformation Mechanisms at the Microstructure of Copper-Graphene Thin Films. Under-Review in *Acta Materialia.*

8. J. Charleston, A. Agrawal, Y. Zhao, R. Mirzaeifar. Effect of processing parameters on the properties of sputtered NiTi thin films. Ready to be submitted.

Three more papers are also in preparation and will be submitted to highest ranked journals in the field in the following couple of months.

DISTRIBUTION A: Distribution approved for public release.

II- Experimental Investigation of Deformation Mechanisms at the Microstructure of Copper-Graphene Thin Films

2.1 Abstract

In the last decade, the mechanical properties of metals reinforced by graphene have been investigated in multiple works. However, multiple details of graphene's effect on the deformation mechanism of metals at the nano and micro-scale are still unknown. At these scales, metal matrices embedded with graphene are mainly assessed by nanoindentation or nanopillar compression that only introduces certain deformation and fracture mechanisms. In this work, for the first time, we perform uniaxial tensile tests to study the deformation mechanisms of nanolayered metallic thin films reinforced with dispersed graphene particles. The effects of graphene particles on crack propagation in nanolayered metal thin films are also investigated. Four samples of copper and copper-graphene composites (two ten-layered and two four-layered) with two different fracture mechanisms (channel cracking and microcrack) are fabricated. It is found that the changes in crack propagation cause an increase in the required stress for channel cracking of the ten-layer copper thin films by 50% and microcracks in four-layer copper thin films by 121%. Graphene particles also increase the crack onset strain in the four-layer samples from 1.3% to 2.4% by affecting the grain boundary sliding that causes microcracks. The observed crack deflections are explained by comparing the ratio energy release rate of crack deflection and penetration to the ratio fracture toughness of the copper-graphene interface and graphene particle. The molecular dynamics simulations are also used to study how graphene stops the growth of plastic zones and causes delamination at the interface, resulting in the deflection of cracks.

2.2 Introduction

Metal matrix composites reinforced with heterogeneous elements (or phases) have favorable properties, such as collaboratively improved strength and ductility. The properties of these composites depend on metal's microstructure, the load-bearing capacity of reinforcement, and the interaction between dislocations and reinforcement. Graphene is one of the strongest materials (Young's modulus $\simeq 1.0\,\mathrm{TPa}$, and breaking strength $\simeq 42\,\mathrm{N\,m^{-1}}$)[1] known to mankind since its discovery in

DISTRIBUTION A: Distribution approved for public release.

2004 [2]. The two-dimensional geometry and outstanding mechanical properties make graphene an ideal reinforcement for metal matrix composites. In the past decade, various innovative fabrication methods are developed for metal-graphene composites such as modified powder manufacturing [3–9], electrochemical deposition [10–12], and alternately depositing metal and transferring graphene to fabricate nanolayer composites [13]. The composites fabricated by these methods have shown higher strength than the metal samples without reinforcement. Graphene's influence on the strength and deformation mechanisms of the composites are complex, but often ascribed to the interactions between graphene and dislocations [14–16].

The two-dimensional geometry of graphene has encouraged fabrication of nanolayer composites with ultrahigh strength [9, 13, 17]. In nanolayer metal graphene composites, the load transfer between the metal matrix and graphene happens via the shear stress at the metal/graphene interface, and the strength of composites also depends on the orientation between the loading direction and graphene reinforcements [18, 19]. The nanolayer composites are fabricated either as thin films [13, 20] or as bulk composites [9, 18, 19]. The bulk nanolayer composites have been fabricated by compaction and hot pressing reduced graphene oxide-Al composite powders [18, 19, 21, 22]. The compressive stress relaxation tests show that the critical resolved shear stress required for dislocation cross-slip and nucleation in composites is higher than the metal samples without reinforcement [21]. The effect of RGO's (reduced graphene oxide) lateral dimension and orientation in bulk nanolayer composites are also studied using micro-compression and micro-tensile tests [18, 19, 22].

In comparison to bulk nanolayer composites, nanolayer thin film composites are investigated very little. Thin film nanolayer composites are fabricated by alternate deposition of metal films and transfer of graphene layers. Thin film metal graphene composites have been mechanically evaluated by compression test of nanopillars [13, 23], micro tensile test (amorphous metal-graphene composite) [24], and nanoindentation [20]. The external dimensions (for example, diameter of nanopillars) that have been used to investigate mechanical properties of the thin films are small and can couple with the effect of thin film's microstructure [21]. Graphene's complete coverage over the surface between metal layers (full graphene sheet) is present in most nanolayer thin film composites, studied in the literature. However, our group [20] has shown that not only the full graphene sheets but graphene particles covering a fraction of the interlayer area can also improve the thin film nanolayer metal-graphene composites.

The deformation and fracture mechanisms of metal thin (sub-micron) films depend on the grain diameter, grain orientation, and film thickness. For instance, The copper films with a thickness greater than 200 nm accommodate larger strains (experiencing extensive plastic deformation) than those with a thickness equal to or less than 100 nm [25]. Such variation in the deformation mechanism of the metal thin films can dramatically change the role of graphene particles in the composites. The experimental results show that the metal/graphene interface blocks dislocations and deflects cracks by changing the stress field near the crack tip, causing constraints in the crack propagation [13, 20, 23]. Depending on the microstructure (loading and defects in the composite) atomistic simulations also predict that the graphene may act as a source of dislocations and can weaken the metal matrix [15, 16, 26]. Understanding the mechanical behavior of nanolayer metal graphene thin film composites under tensile loading is essential to their design. However, tensile testing of free-standing sub-micron films with large external dimensions (order of 10^3 times higher than film thickness) is difficult, and several works have utilized polyimide films as a substrate to tensile test sub-micron metal films [27–30]. Copper-graphene nanolayer composites are also fabricated over polymer and shown to have high fatigue resistance due to deflection of fatigue

DISTRIBUTION A: Distribution approved for public release.

cracks by a full layer of graphene reinforcement [17]. The entire top surface of metal film covered by a single graphene layer (not embedded in the metal matrix) increases the yield strength by 47% and 83.3% for 100 nm and 230 nm, respectively, in copper films deposited over the polymer substrate [31, 32]. To the best of the authors' knowledge, no study reports the effect of reinforcing graphene particles in thin metal films over polymer substrates.

In this work, multiple copper-graphene nanolayer thin films are fabricated on Kapton substrate. Instead of having a graphene layer covering the entire surface of the sample, monolayer particles of graphene are embedded between the copper layers. Two sets (with and without graphene particles) of thin films are deposited at room temperature and at 100 °C to fabricate two different grain morphologies (columnar and equiaxed) and grain sizes. Here we show that the dispersion of graphene particles in sub-micron thin metal films improves the mechanical properties and increases fracture resistance. Depending on grain morphology, reinforcement of graphene particles can also change metal thin films' deformation and fracture mode.

2.3 Methods

A schematic of multiple steps that we used for fabricating the nanolayer copper-graphene composites is shown in Fig. 2.1. The Kapton foils (purchased from Dupont, USA) are laser cut into circles with a diameter of 120 mm to fit the substrate holder of the sputtering system. The AJA magnetron sputtering system deposits the copper layers over the circular Kapton substrate. Graphene particles are embedded by spin coating aqueous graphene solution over deposited copper layers. The desired concentration of aqueous graphene solution is achieved by adding deionized (DI) water to a 1.0-wt. % research-grade graphene water dispersion (purchased from US Research Nanomaterials Inc., USA). The spin coating is performed at 2000-rpm for the 40s. The aerial coverage of graphene particles increases with an increase in the concentration of graphene particles in the aqueous solution, as shown in Fig. S1 in the Supplementary document. The process of sputtering and spin-coating is repeated multiple times to fabricate the nanolayer copper-graphene composite over the Kapton substrate. The copper reference samples are prepared similarly by repeating the copper deposition and spin coating over the sample with DI water (0.0 wt. % Graphene). Four samples (consisting of two sets, each having one copper reference and one copper-graphene composite) are prepared using copper deposition and spin coating. The two sets are named as ten-layer and four-layer samples, representing the number of copper layers in each set. The parameters used for sputtering and spin coating are shown in Table 2.1. The samples' names are shortened, and ten-layer and four-layer samples are denoted as '10L' and '4L' for brevity in Table 2.1.

DISTRIBUTION A: Distribution approved for public release.

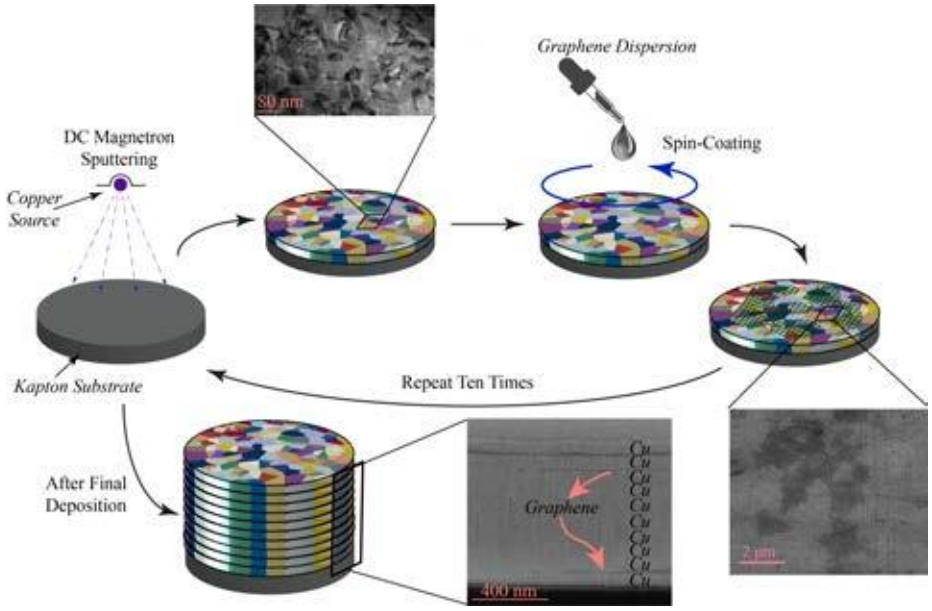

Figure 2.1: Process for fabricating nanolayer copper-graphene composites. The copper is deposited using the DC magnetron sputtering on Kapton. Spin coating is used to disperse the graphene particles on the surface of the deposited copper. The scanning electron microscopy is used to investigate the graphene dispersion over the copper layer and to investigate the cross-sections of the fabricated composites. Transmission electron microscopy is used to investigate copper layers' crystallinity and apparent grain morphology.

Table 2.1: Parameters used for sputtering and spin coating of the graphene dispersion. In all the samples the substrate is Kapton 100 HN, the target to substrate distance is 70 mm, each layer is deposited after 5 minutes of pre-sputtering the target, and soak time for the substrate temperature is 30 minutes ('10L' and '4L' denotes ten-layer and four-layer samples, respectively).

Name	Power (W)	Substrate Temperature (°C)	Coat Time (s)	Chamber Pressure (mT)	Layer Number	Graphene wt. %	Thickness (nm)
10L Cu	75	20	300	5	10	0	910
10L CuGr	75	20	300	5	10	0.2	965
4L Cu	200	110	600	5	4	0	511
4L CuGr	200	110	600	5	4	0.3	595

DISTRIBUTION A: Distribution approved for public release.

The sample surfaces are characterized (before and after failure) using FEI Quanta 600 FEG scanning electron microscope and LEO (Zeiss) 1550 scanning electron microscope. The cross-sections (before and after failure) are characterized using a focused ion beam (FIB) and high-resolution scanning electron microscope in FEI Helios 600 NanoLab. The metal films are sectioned after the deposition of the Platinum layer, and the SEM is used to measure the thickness and analyze the path of cracks in the thin metal films. Transmission electron microscope (TEM) and selected area electron diffraction (SAED) samples are prepared using Gatan PIPS II ion milling, and a Philips EM420 transmission electron microscope is used to study the crystalline structure of copper layers.

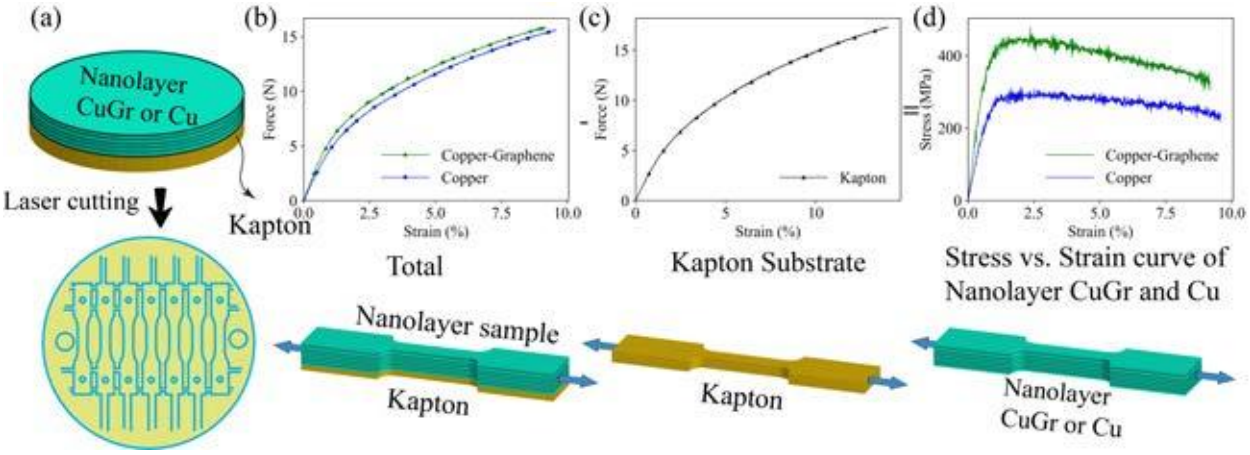

Figure 2.2: (a) Shows a sketch of the fabricated sample followed by laser cutting into dog bones for the tensile testing. (b) Shows the Force vs. Strain curves for two ten-layer samples (copper and copper-graphene) deposited over the Kapton substrate. Force vs. Strain for a Kapton layer without the metal deposition is shown in (c). (d) Shows the tensile stress-strain curve obtained for copper and copper-graphene thin film after subtraction of Kapton substrate's force. The maximum stress point represents where the channel cracking starts in the metal films. The presence of graphene particles covering around 30% of the area on the metal surface increases the required stress for fracture initiation from 293 MPa to 442 MPa ($\approx$ 50% increase).

The method to obtain the tensile stress-strain curves of nanolayer copper and copper-graphene composites is shown in Figure 2.2. The dog bone shaped uniaxial tensile specimens are laser cut from the deposited samples. Two tensile tests are performed to obtain the stress-strain curve of nanolayer metal thin films (see Fig. 2.2 b-d). In the first step tensile test is performed on nanolayer metal (or metal graphene composite) film with Kapton substrate, and a second test is performed on Kapton substrate that has experienced a similar environment but without any metal deposition. Both tensile tests are performed at same strain rate ($0.0001\ s^{-1}$). The tensile stress-strain curve of the composite is then obtained by subtracting the force of Kapton from the combined force of nanolayer thin metal (or metal graphene) film on Kapton substrate, as [28, 29, 32]:

$$F_{Composite} = F_{Composite+Kapton} - F_{Kapton} \tag{2.1}$$

where $F_{Composite+Kapton}$ is the force obtained from the tensile test in the experiments on the samples with nanolayer thin metal (or metal graphene) film on the Kapton, and F_{Kapton} represents the force obtained from the experiments on the Kapton substrate without any deposition. This equation

DISTRIBUTION A: Distribution approved for public release.

assumes that the force is identical in the Kapton film in a free-standing state and when coated with metal (or metal graphene) thin film for a given strain.

2.4 Results and Discussion

The cross-sections of both ten-layer copper, and copper-graphene thin films are shown in Fig. 2.3. Both samples have a layered structure as the nucleation point of crystal grains in each layer is different from the previously deposited layer. The copper-graphene sample shows that graphene particles are embedded between the copper layers. Magnified views in Fig. 2.3 reveal some defects and voids between the layers and grains in both copper and copper-graphene samples. A thinner sample with four layers and different morphology is also investigated in the present work, apart from the ten-layer sample. The cross-sections of both four-layer copper and copper-graphene samples are shown in Fig. S2 in the Supplementary document. The layered structure is not present in these samples as the four-layer samples are deposited at 100 °C. The elevated substrate temperature during the sputtering changes the growth mode and allows the copper layers to diffuse into each other [33]. The layered structure is present in the places where graphene particles are present, as shown in Fig. S2 (b1) in the Supplementary document. The ten-layer copper and copper-graphene samples have thicknesses of 910 and 965 nm, respectively. The aerial coverage of graphene in the ten-layer copper-graphene sample is 30% and for the four-layer copper-graphene sample is 55%, as shown in Fig. S3. The four-layer copper-graphene sample has more graphene coverage due to surface roughness and high weight percentage of graphene dispersion used during the spin coating. The ten-layer samples have a columnar grain structure with an average diameter of around 23 nm, as shown in Fig. 2.3 and Fig. S4. The four-layer samples consist of equiaxed grains with diameters ranging from 300 to 400 nm, as shown in Fig. S3 and Fig. S5. The TEM and SAED images of ten-layer samples, shown in Fig. 2.4, and of four-layer samples, shown in Fig. S6, confirm that all samples are crystalline and have nano twins.

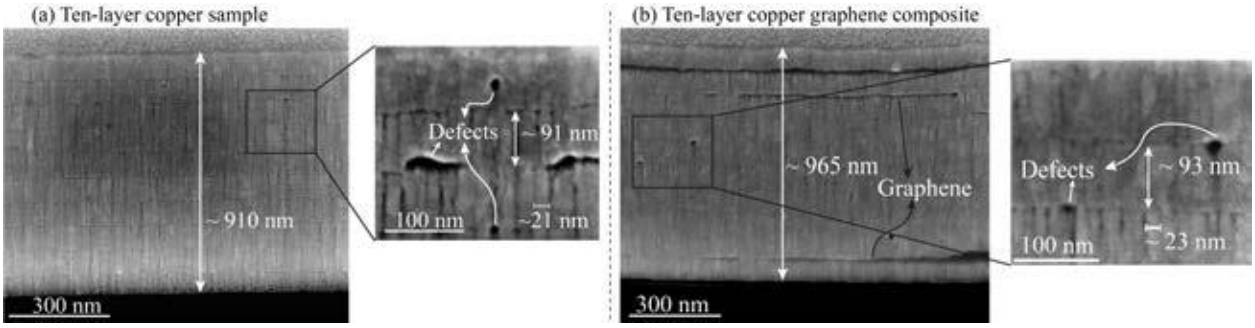

Figure 2.3: Cross-sections of ten-layer copper (a) and copper-graphene (b) samples show that both samples have similar thickness and grain structure. The cross-sections are prepared using Focused Ion Beam (FIB), and SEM images are taken at an inclination of 52 °. The thicknesses shown here are the corrected length.

DISTRIBUTION A: Distribution approved for public release.

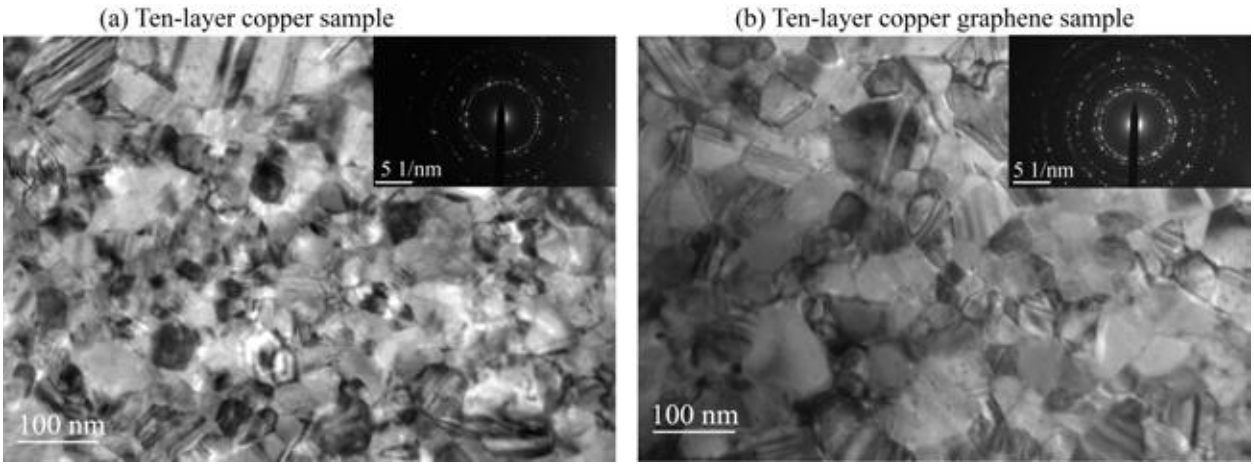

Figure 2.4: TEM images of ten-layer copper and copper-graphene samples confirm the crystallinity of both samples. They also show that both samples have similar grain size, structure, and twinning inside the nano-grains.

The stress-strain curve of the free-standing film is required to strictly characterize the copper and copper-graphene composites. However, the stress-strain curves generated by Eq. 2.1 are sufficient to study the effect of embedding graphene particles inside the copper matrix. A similar method is used to study the impact of chromium metal layers inside the CoZrNb film [27], and to study the role of copper and graphene interface in suppressing fatigue damage in copper-graphene composites [32]. The flaw in calculating forces in metal films using Eq. (2.1) stems from the differences in local strain caused by the formation of the free surface at the top of Kapton after the formation of a crack in the metal film. The free surface causes stress redistribution in Kapton, and this stress redistribution causes highly inhomogeneous longitudinal (loading direction) stress in the Kapton [34]. The stress redistribution at the crack tip, depending on the interfacial bonding, can also damage the substrate surface [35]. These differences cause the Kapton with metal film and free-standing Kapton to have different global forces at the same global strain. However, before the film cracking, the assumption of having the same forces in free-standing Kapton and Kapton in the metal-polymer composite is valid. The improvement caused by the embedding of graphene particles in the ten-layer sample and four-layer sample during uniaxial tensile loading is shown by stress-strain curves in Fig. 2.2 (d) and Fig. S7 in the Supplementary document. The 30% aerial coverage of the graphene in the ten-layer sample increases the stress required for channel cracking from 293 to 442 MPa, and 55% areal coverage of the graphene in the four-layer sample increases the required stress for microcracks from 103 to 228 MPa.

DISTRIBUTION A: Distribution approved for public release.

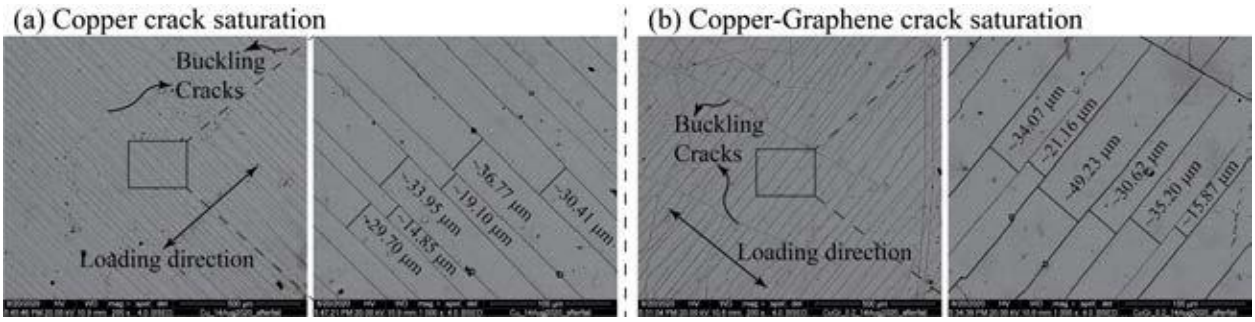

Figure 2.5: Buckling and channel cracks (from the top view) in the ten-layer copper and copper-graphene samples after failure show that both samples fracture by the intergranular cracks.

The metal films over polyimide substrate fail either by forming microcracks or macrocracks (channel cracks) based on the thickness, grain size, and morphology. The ten-layer samples fail by channel cracks, as shown in Fig. 2.5 and four-layer samples fail by the formation of microcracks, as shown in Fig. S8 and S9. The critical stress for crack propagation over the width of the film (channel crack) depends on the film thickness when the crack length exceeds a few times the film thickness [36]. The energy release rate G for the crack propagation for an elastic film on an elastic substrate [37]:

$$\mathrm{G} = \frac{\sigma^2 t g}{E} \tag{2.2}$$

where σ is stress, t is the thickness of the film, g is a non-dimensional function, and E is the Young modulus of the elastic film. The ten-layer samples rupture by channel cracking due to film thickness. In four-layer samples, the critical stress for channel cracking is not reached due to stress relaxation by grain-boundary sliding and the formation of microcracks (in the region with a high sliding rate) [38]. The failure mechanism of the copper film deposited at room temperature and annealed for one hour is shown to change from intergranular to transgranular fracture in uniaxial tensile testing when the thickness increases above 200 nm [25]. However, apart from the film thickness, grain sizes and morphology are also crucial in determining the failure mechanism of the metal film. Metal and metal graphene films fabricated in this work rupture by intergranular fracture. As small grain sizes constrain the dislocation activities inside the grain in the ten-layer samples, an increase in strain triggers grain boundary decohesion, causing the intergranular fracture (as shown in Figs. 2.6, and 2.7). The thicknesses of the four-layer copper samples are greater than 200 nm, but they also rupture by intergranular fracture, as shown in Figs. S8 and S9. The equiaxed grain morphology causes grain boundary sliding, and intergranular cracks form in the regions with high sliding rates [38].

DISTRIBUTION A: Distribution approved for public release.

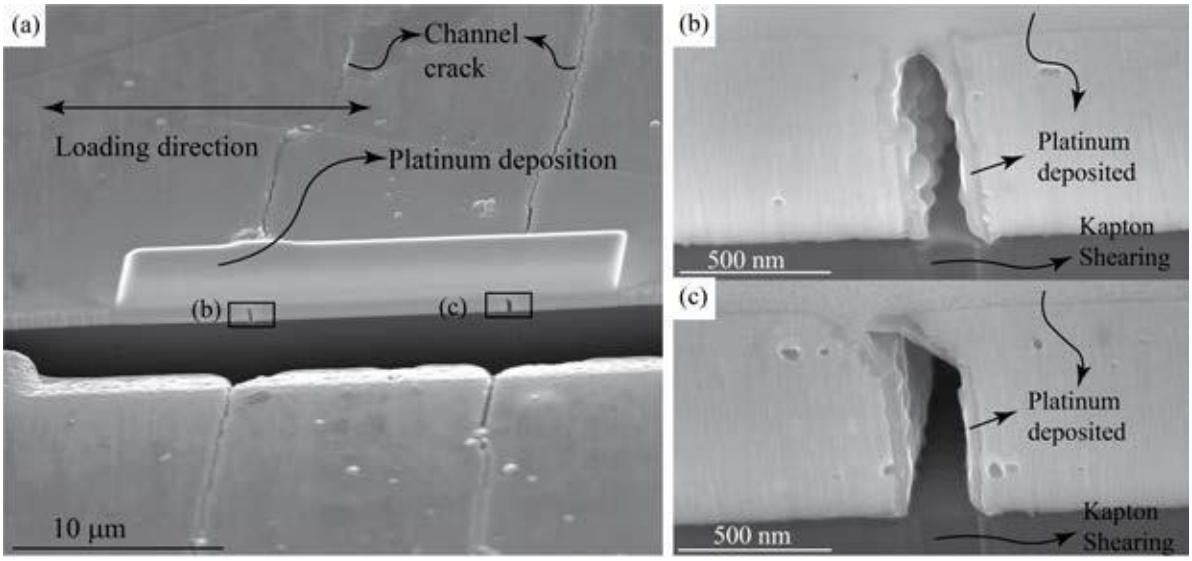

Figure 2.6: Channel crack profiles of the ten-layer copper sample prepared using Focused Ion Beam (FIB) show that the cracks are along grain boundaries with relatively straight paths. (a) Shows the region where the channel crack profile is prepared. (b) and (c) Show the depth profile of the channel cracks. The SEM images shown are taken at an inclination of 52°.

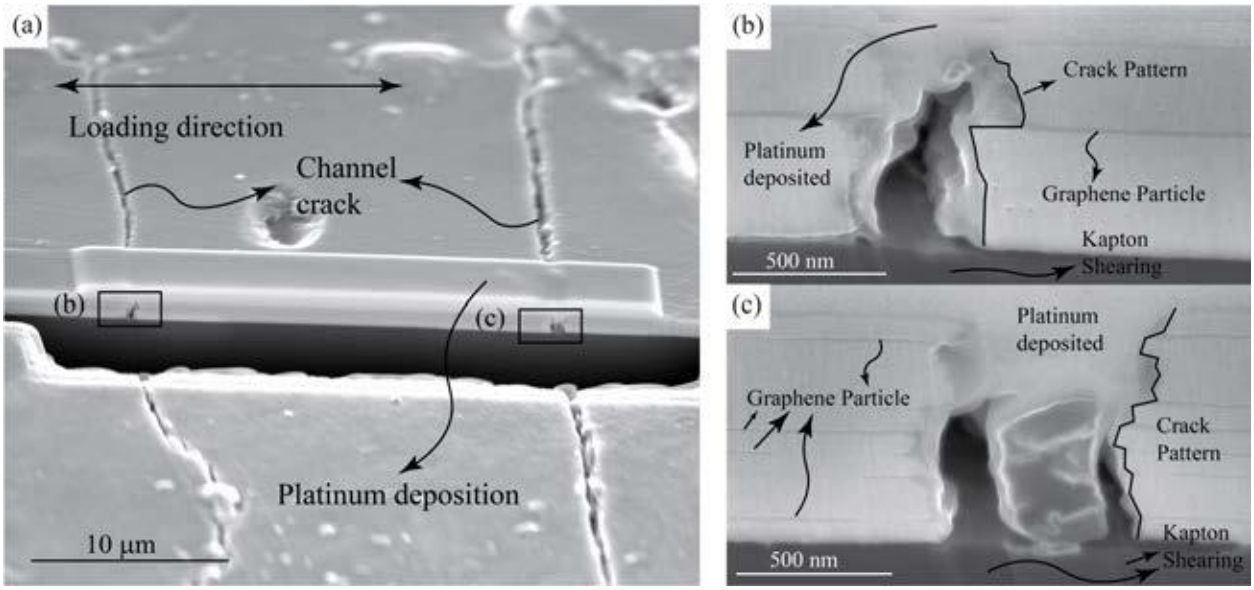

Figure 2.7: Channel crack profiles of the ten-layer copper-graphene sample prepared using Focussed Ion Beam (FIB) showing defection caused by graphene particles. (a) Shows the region where the FIB surface is prepared in the ten-layer copper-graphene sample. (b) and (c) show the depth profile of channel cracks. The cracks are deflected due to the presence of graphene particles (compare to ten-layer copper sample shown in Fig. 2.6). As shown the degree of deflection into the interface depends on the number graphene particles in the cracks path. The SEM images are taken at an inclination of 52°.

DISTRIBUTION A: Distribution approved for public release.

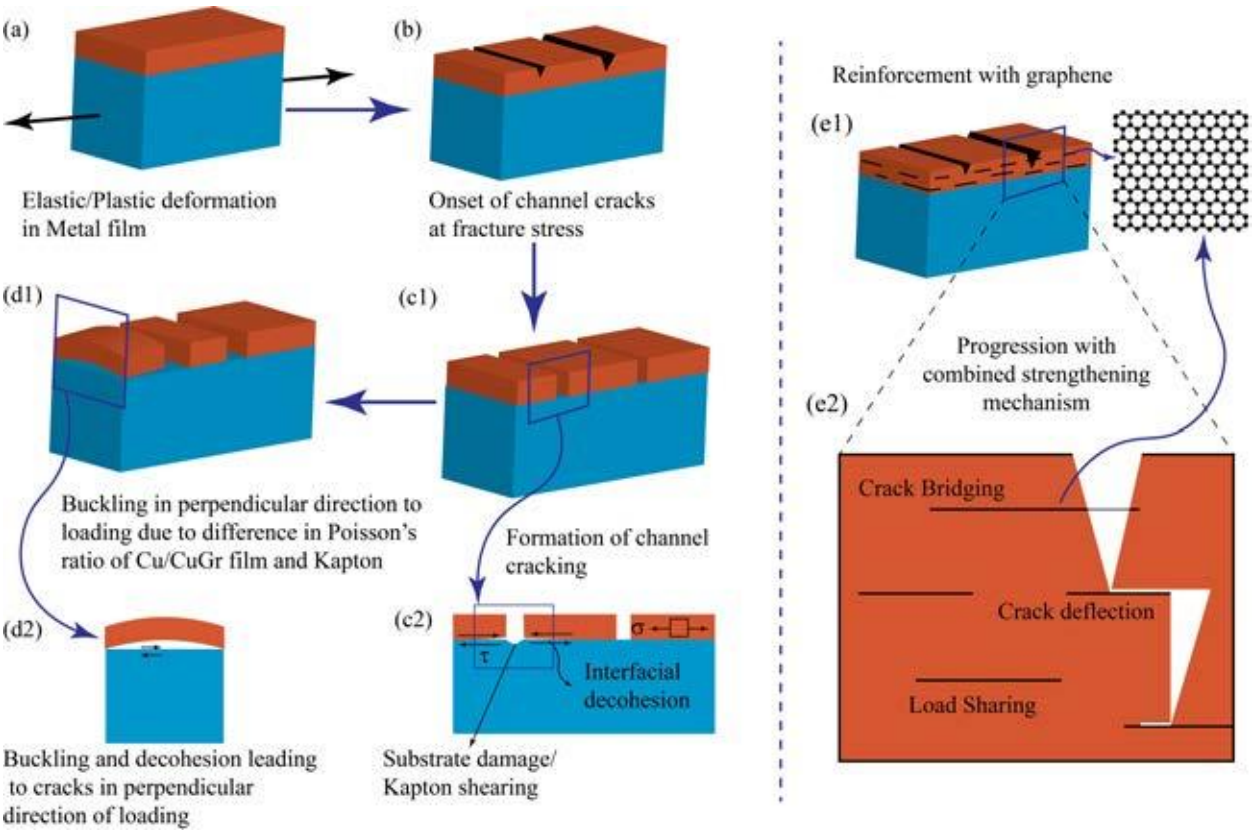

Figure 2.8: Schematic of the deformation of metal thin film over Kapton with and without graphene reinforcement. After the initial phase of elastic/plastic deformation without graphene, shown in (a), the film ruptures by the formation of channel cracks, shown in (b) and (c1). The channel cracks cause decohesion at the interface and substrate damage, as shown in (c2). Buckling cracks form in the metal film perpendicular to the loading direction due to the difference in Poisson's ratio of copper and Kapton, as shown in (d1) and (d2). When reinforced with graphene, deformation proceeds in the same manner; however, channel and buckling cracks paths are changed due to deflection at the metal graphene interface, as illustrated in (e1) and (e2). The presence of graphene increases the required stress for deformation by load transfer and provides resistance to crack propagation by crack deflection and bridging (e2), thus improving the overall mechanical properties of the thin metal film.

Graphene's involvement in the deformation mechanism of metal films over the Kapton substrate explains the improvement in copper-graphene thin films, as described in schematic Fig. 2.8. The metal film deforms elastically with the Kapton at the start of loading. The graphene particles increase the required stress for metal film deformation through load sharing and blocking dislocations at metal graphene interface [15, 16, 20, 26]. The metal film experiences extensive delocalized plastic deformation with the increase in strain [25, 39]. Regions with high local strain and preexisting defects form channel cracks under tensile loading [40] as shown in Fig. 2.5 for ten-layer samples. During the formation of channel cracks, graphene particles block the crack's path, thus increasing the required stress for the propagation of channel cracks through the thickness of copper-graphene thin film. The comparison of the channel cracks' through thickness profile in ten-layer copper and copper-graphene samples in Figs. 2.6 and 2.7 clearly show the deflection of cracks by graphene particles. Apart from longitudinal stress, the metal film also experiences transverse stress (stress perpendicular to loading direction) due to the difference in Poisson's ratio of the metal film and Kapton [41]. The transverse stress causes the metal film to buckle perpendicularly to the loading

DISTRIBUTION A: Distribution approved for public release.

direction. The buckling in the metal film causes film delamination, and fracture in the metal film perpendicular to the channel cracks [42]. The buckling cracks and delamination in ten-layer copper and copper-graphene samples are shown in Figs. 2.9 and 2.10, respectively. Graphene particles also deflect the buckling cracks, as shown in Fig. 2.10, and increase the stress required for complete fracture. The formation of channel and buckling cracks redistribute the stress at the interface and causes interfacial decohesion along with the substrate damage as shown in Figs. 2.6(b, c), and 2.7(b, c). In four-layer samples, the presence of graphene particles increases resistance to the grain boundary sliding, causing an increase in strain (from 1.3% to 2.4%) and stress (from 103 MPa to 239 MPa) for the formation of microcracks. The increase in stress value increases the microcracks' length in four-layer copper-graphene samples compared to copper samples, as shown in Fig. S9 in the supplementary documents.

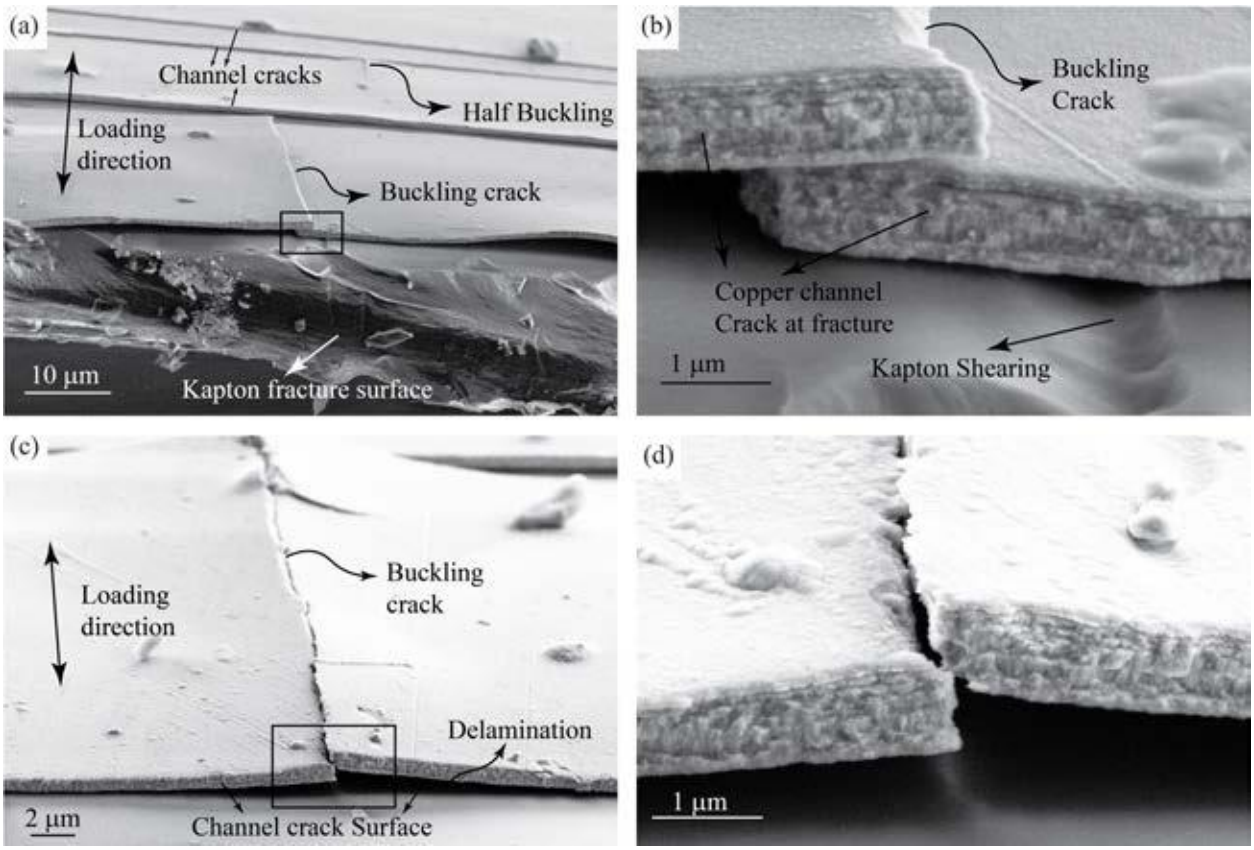

Figure 2.9: Post failure SEM images of the ten-layer copper sample. (a) Shows the fracture of the film near the area the substrate ruptured. (b) Shows the enlarged surface of the channel crack in (a) and the path of substrate damage to the Kapton's rupture point. (c) and (d) Show the surface of the channel crack that is not near the rupture point of the substrate. The buckling and channel cracks pass through the grain boundaries of the metal film. The images also show delamination due to the buckling cracks. The substrate's fracture surface indicates moderate necking before rupture.

The cracks can either penetrate or deflect at the interface between graphene and copper during uniaxial tensile loading. Considering a crack perpendicular to the interface and localized plane strain condition, the energy release rate ratio between penetration, $\mathcal{G}_p$, and deflection of crack, $\mathcal{G}_d$, is given by [43]:

$$\frac{\mathcal{G}_d}{\mathcal{G}_p} = \left[\frac{(1-\beta^2)}{1-\alpha}\right]\left[\frac{|d|^2+|e|^2+2R_e(de)}{c^2}\right] \tag{2.3}$$

DISTRIBUTION A: Distribution approved for public release.

where α and β are functions of shear modulus, μ, and Poisson's ratio, ν, of the materials on either side of the interface:

$$\alpha = \left[\frac{\mu_{Gr}(1-\nu_{Cu}) - \mu_{Cu}(1-\nu_{Gr})}{\mu_{Gr}(1-\nu_{Cu}) + \mu_{Cu}(1-\nu_{Gr})}\right] \tag{2.4}$$

$$\beta = \left[\frac{\mu_{Gr}(1-2\nu_{Cu}) - \mu_{Cu}(1-2\nu_{Gr})}{\mu_{Gr}(1-2\nu_{Cu}) + \mu_{Cu}(1-2\nu_{Gr})}\right] \tag{2.5}$$

Also, $d(\alpha, \beta)$ and $e(\alpha, \beta)$ are complex valued functions and $c(\alpha, \beta)$ is real valued function of α and β [43].

If $\mathcal{G}_{CuGr}$ and $\mathcal{G}_{Gr}$ are the fracture toughness of copper-graphene interface and toughness of graphene, respectively, the crack will be deflected if the following condition is satisfied:

$$\frac{\mathcal{G}_{CuGr}}{\mathcal{G}_{Gr}} < \frac{\mathcal{G}_d}{\mathcal{G}_p} \tag{2.6}$$

The above condition compares the ratio of fracture resistance to ratio of energy release rates and implies that crack propagation alongside the interface will be met at a lower load than penetration across the interface [43].

To calculate α and β values, we have $\mu_{Cu} \approx 45.4$ GPa, $\nu_{Cu} \approx 0.350$, $\mu_{Gr} \approx 280$ GPa, and $\nu_{Gr} \approx 0.19$ [44–46]. Substituting these values in Eqs. 2.4 and 2.5 we get $\alpha = 0.6638$ and $\beta = 0.2552$. The ratio of energy release rate of deflected crack to penetration ($\frac{\mathcal{G}_d}{\mathcal{G}_p}$) for different values of α and $\beta = 0.0$ is calculated by He et.al. [43]. The effect of β on the ratio is not large and correction for β^2 is sufficient to obtain the ratio [43]. For $\alpha = 0.6638$ and $\beta = 0.0$, reported value of ratio is 0.66 ($\frac{\mathcal{G}_d}{\mathcal{G}_p} \approx 0.66$) [43]. After correcting the ratio for $(1 - \beta^2)$ we get $\frac{\mathcal{G}_d}{\mathcal{G}_p} \approx 0.617$.

DISTRIBUTION A: Distribution approved for public release.

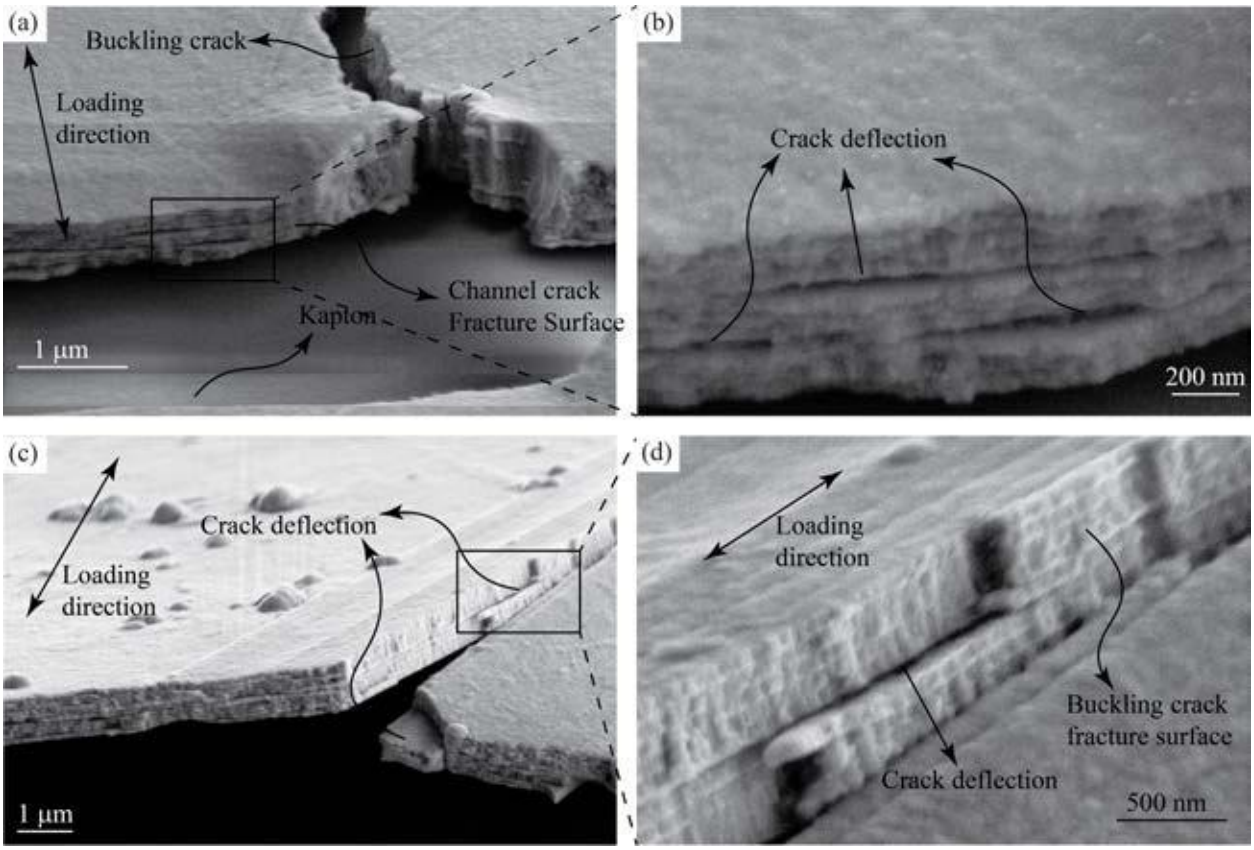

Figure 2.10: Surfaces of channel and buckling cracks in the ten-layer copper-graphene sample show the crack deflection caused by the graphene particles in comparison to the ten-layer copper sample (shown in Fig. 2.9).

The fracture toughness of graphene measured as the critical stress intensity factor is 4.0 ± 0.6 MPa$\sqrt{\text{m}}$ [47]. Interfacial fracture strength measured as a critical stress intensity factor ($\mathcal{G}_{CuGr} = \sqrt{4\gamma_d E}$) can be calculated using interfacial debonding energy, γ_d and Young's modulus, E of the materials [48, 49]. As both materials have different Young's modulus we have two values for critical stress intensity factor. The adhesive energy or interfacial debonding energy of copper and graphene is 0.72± 0.07 J m^{-2} [50]. The Young's modulus for copper and graphene is 0.1235 TPa and 1 TPa, respectively [1, 44]. The two values of critical stress intensity factor using Young's modulus of copper and graphene are 0.59638 and 1.70 MPa$\sqrt{\text{m}}$, respectively. The ratio between fracture toughness of interface (for both values) and graphene ($\frac{\mathcal{G}_{CuGr}}{\mathcal{G}_{Gr}}$) is 0.149 and 0.425. The calculated energy release rate ratio ($\frac{\mathcal{G}_d}{\mathcal{G}_p} \approx 0.617$) and fracture toughness ratio ($\frac{\mathcal{G}_{CuGr}}{\mathcal{G}_{Gr}} = 0.149$ or 0.425) satisfy the criterion for crack deflection as imposed by Eq. 2.6. The above simple condition determines whether or not the cracks deflect at the metal graphene interface for the given material. In the present work, the crack deflection is energetically favorable due to the high strength of graphene's Carbon-Carbon bonds compared to Carbon-Metal bonds of the metal graphene interface. The crack deflection increases the required area of new free surfaces, which need to be created for the propagation. The crack can only grow if the change in the potential energy (due to applied stress) is more than dissipation energy needed for crack growth. Thus, the increase in energy dissipation due to crack deflection increases the required applied stress for propagation in metal thin films.

Fracture surfaces from multiple areas of copper and copper-graphene samples after failure are

DISTRIBUTION A: Distribution approved for public release.

shown in Figs. 2.9 and 2.10. Different stages of deformation and damage accumulation depicted in schematic Fig. 2.8(a)-(d) are clearly exhibited by the sample in Fig 2.9. Fig 2.9 shows delamination of the metal film, substrate damage of the Kapton, channel cracks, and buckling/half-buckling cracks in the copper film. As predicted by the theory and illustrated in Fig. 2.8(e), the surfaces of the channel and buckling cracks in Fig. 2.10 show crack deflection in the copper-graphene sample. Crack deflections at metal-graphene interfaces have been reported as a mechanism behind increased toughness in RGO-aluminum composites and “brick and mortar" structured RGO-copper composites [9, 51, 52]. The increase in the total fracture surface area caused by crack deflection is ascribed to this toughening response in RGO-aluminum composites and “brick and mortar" structured RGO-copper composites [51, 52]. The crack deflection mechanism is also believed to cause a change in shear angle (from maximum resolved shear stress angle ~45 °) of the RGO-aluminium composite for different laminate orientations during uniaxial compression testing [18]. Although crack deflection is considered to be a strengthening mechanism in metal-graphene composites, direct observation of the crack deflection has been unattainable in most experimental works [13, 18, 51, 52]. Observations like increase in toughness [51, 52] or the variation in shear angles as a function of laminate orientation have been used to conclude the crack deflection occurred at metal-graphene interfaces [18]. The fracture surfaces of the copper samples reinforced with graphene particles in the present work offer direct evidence of crack deflection, as shown in Figs. 2.7(b)-(c) and 2.10.

Visualizing the mechanism behind the crack deflection caused by graphene particles is non-trivial in experiments but can be studied by atomistic simulations. Propagation of cracks follows the formation of a complex process zone (plastic zone) at the crack tip where the material is plastically deformed [53]. The changes in crack propagation in copper-graphene samples indicate that the graphene particles interact with the plastic zone near the crack tip. Thus, molecular dynamics simulations are used to understand the interaction and effect of graphene particles on the plastic zone. Section S1 in the Supplementary document describes the atomistic simulations’ method in detail. Plastic zones near the crack tip in copper and copper-graphene samples are visualized using the atomic von-Mises shear strain in Fig. 2.11. To better visualize the impact of graphene reinforcement in the copper system, the atoms with a shear strain value less than 0.15 are not shown in Fig. 2.11 (c)-(f). The results from simulations show that the graphene particle stops the growth of the plastic zone near the crack tip. The plastic zone is the precursor of crack growth, and by affecting its growth, graphene affects the growth of cracks. The presence of graphene changes the dimensions of the crack. At 12% strain, the crack’s length and width in the copper sample are 7.10 nm and 2.60 nm, while for the sample reinforced with two graphene particles, the crack’s length and width are 5.30 nm and 1.60 nm.

The evolution of cracks and local stress in copper-graphene samples with the increase in strain is shown in Fig. 2.12. The atoms are colored according to the von-Mises atomic stress. The atomic stress in the graphene particles is higher than in any other region, revealing the load transfer to the graphene sheet and particles through the metal graphene interface. The crack grows along the interface after delamination in the copper sample reinforced with a single graphene particle, as shown in Fig. 2.12(a1)-(a4). The copper-graphene interface experiences bending when the crack grows along the interface, as shown in Fig. 2.11(a4). When the graphene is constrained at the boundary, as in the case of the graphene sheet (Fig. 2.12(b1)-(b4)), the graphene sheet fractures after initial delamination due to the restriction on bending (shown in Fig. 2.12(b3)). Again after the fracture in the graphene sheet, the crack grows along the interface, as shown in Fig. 2.12(b4). The reinforcement of two graphene particles causes the plastic zone to shrink, as shown in Fig.

DISTRIBUTION A: Distribution approved for public release.

2.11(f), and further crack growth requires high strain. The atomistic simulation results explain the nanoscale deformation mechanisms behind the experimental observation for copper and copper-graphene nanolayer composites.

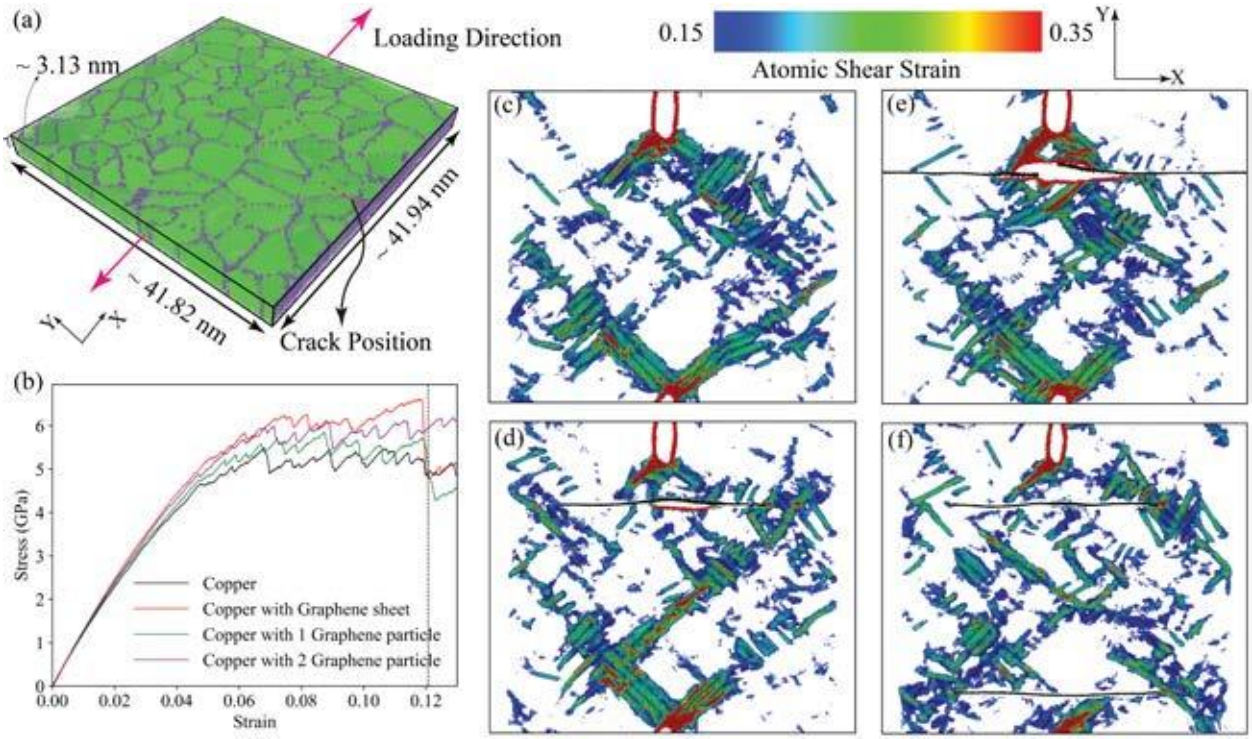

Figure 2.11: Strengthening mechanism behind improving mechanical properties and crack deflection by graphene particles. (a) Shows the dimension and geometry of the simulated system with loading direction (X-direction). (b) Shows stress-strain curve obtained in atomistic simulations. (c)-(f) Show the atomic shear strain in copper, copper with graphene particle, copper with graphene layer, and copper with two graphene particles at 12% strain. The atoms are visualized using von-Mises atomic shear strain, and atoms with shear strain below 0.15 are removed to visualize the high strain regions. The crack width (X-direction) and length (Y-direction) for the case (c) are 2.60 nm and 7.10 nm, for case (d) are 2.20 nm and 5.90 nm, for case (e) are 2.70 nm and 6.50 nm, and for case (f) are 1.60 nm and 5.30 nm. The crack width and length have decreased with the reinforcement of graphene and graphene particles. The plastic zone near the crack tip is altered and shrank due to the presence of graphene.

DISTRIBUTION A: Distribution approved for public release.

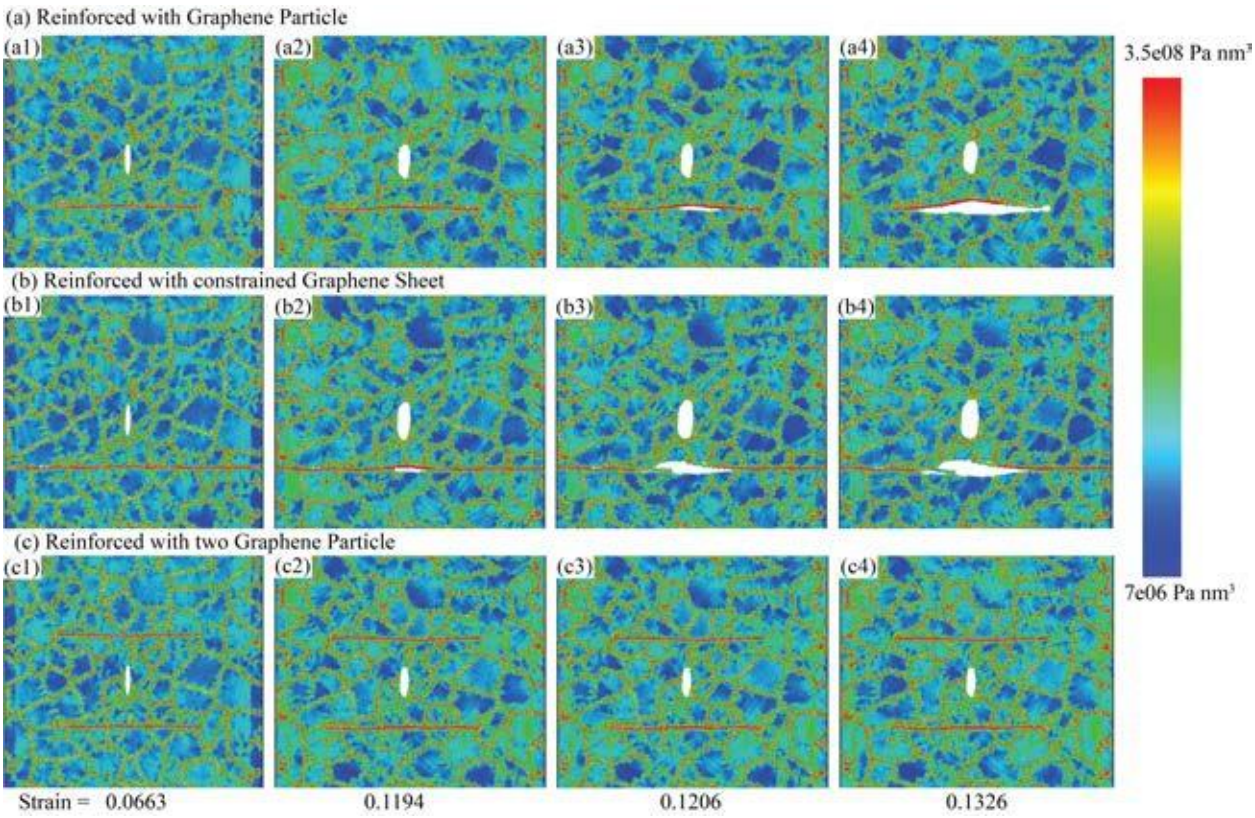

Figure 2.12: The evolution of crack and fracture for cases where graphene is reinforced. The atoms are visualized using von-Mises stress multiplied by the local atomic volume. The graphene atoms have high atomic stress, which shows the load transfer to graphene during the loading. (a1)-(a4) Show the delamination between graphene particle and copper with the increase in strain. The delamination starts around 12% of strain and grows as a fracture alongside the interface. (b1)-(b4) Show the fracture in the graphene sheet with the increase in strain. The graphene sheet cannot bend further after delamination (around 12% strain) due to constraints at the boundary that causes fracture in the graphene sheet. (c1)-(c4) Show the effect of two graphene particles. The plastic zone near the crack tip is affected, and 12% to 13% strain is insufficient to cause delamination or failure.

2.5 Conclusion

Metal graphene composites are emerging as an alternative to metals and alloys because embedded graphene in these composites increases the mechanical strength without compromising other properties like thermal and electrical conductivity. Several works have been reported on fabricating metal graphene composites and studying their strength improvement in the past few years. However, the effects of graphene on the deformation and fracture mechanisms are complex, and there are still many unknowns. To design reliable metal graphene composites, understanding the impact of graphene on the deformation mechanisms is critical. In the present work, a relatively simple and cost-effective process was used to fabricate two sets of sub-micron copper and copper-graphene thin films to understand how embedded graphene particles affect the deformation mechanisms and mechanical properties. One set of samples fails by channel cracking and the other by microcracks. The results indicate that the 30% and 55% coverage of graphene particles (in ten-layer and four-layer samples) increases the required stress by 50% for channel cracking and 112% for microcracks. The onset strain for microcracks increases from 1.3% in the four-layer copper sample to 2.4% in the four-

DISTRIBUTION A: Distribution approved for public release.

layer copper-graphene sample, which indicates that the graphene also affects the grain boundary sliding (pre-cursor of microcracks). The results show that the dispersed graphene particles improve the mechanical properties of metal thin films by a load transfer and crack deflection mechanism. Many experimental works have explained the increase in fracture toughness and change in shear angle by presuming crack deflection at the metal graphene interface. We investigated the crack paths and confirmed the crack deflection experimentally in metal graphene composites.

The experimental results agree with theory and atomistic simulations. A comparison of the energy release rate ratio of crack penetration and crack deflection with the fracture toughness ratio of the interface and graphene predicts crack deflection at the copper-graphene interface. This simple criterion can also be used to determine whether the graphene particles in the particular metal layer will deflect the crack into the interface or not. An increase in required stress for deformation and crack deflection in experiments indicates that graphene particle's presence affects the plastic zone near the crack tip. Molecular dynamics simulations confirm the effect of graphene particles on the plastic zone. The atomistic simulations successfully capture a decrease in the plastic zone and deflection of cracks. The results here indicate that graphene particles improve mechanical properties, but optimizing graphene distribution in metal layers is key to marked improvement of mechanical properties.

Acknowledgement

This material is based upon work supported by the Air Force Office of Scientific Research under award number FA9550-18-1-0169.

Data availability

Data are available from the authors upon reasonable request.

2.6 Appendix

1. Molecular Dynamics Method

A set of atomistic simulations is performed to understand the rationale behind the crack deflection and improvement caused by the graphene particles. A schematic of the graphene-metal composites used in this study is shown in Figure S10. The large-scale atomic/molecular massively parallel simulator (LAMMPS) [54] is used to perform the simulations, and OVITO [55] is used to visualize the results. The 2NN Modified Embedded Atom Method (MEAM) for the Cu-C system developed by the authors in previous work [16] is used to simulate the interaction between Cu-Cu, C-C, and Cu-C atoms. The initial geometry is created using Voronoi Polyhedra in Atomsk. We created geometry with dimensions 41.94 nm $\times$ 41.82 nm $\times$ 3.13 nm consisting of hundred 2d grains with [111] crystal direction perpendicular to the loading plane to understand the crack propagation. The created geometry shown in Figure S9 (a) was then relaxed at 20 K Temperature for 60 ps to remove residual stresses. The MD simulations are performed for four different systems (shown in Figure S9 (c)-(f)): (a) no graphene, (b) graphene sheet, (c) one graphene particle, and (d) two graphene

DISTRIBUTION A: Distribution approved for public release.

particles. The systems are periodic in Y and Z directions. In the loading direction (X-direction), the systems are non-periodic and shrink-wrapped. The following steps for relaxation (before loading) are performed for all four systems before loading:

- The system is equilibrated at 1 K using a canonical (NVT) ensemble for 40 ps.
- The system's temperature is increased from 1 K to 10 K using a canonical (nvt) ensemble in 20 ps.
- The system is equilibrated at 10 K using a canonical (NVT) ensemble for 20 ps.
- Finally, the system is equilibrated for zero pressure and 10 K temperature with the isothermal-isobaric (NPT) ensemble for 20 ps.

The two groups of atoms in the X-direction (non-periodic) are defined with the conditions: X < 2.0 nm and X > 39.7 nm (together called 'boundary group'). To simulate the loading, these two groups are assigned velocity values in x-direction 0.0 nm/ps and 0.001 nm/ps, respectively. For the atoms between these two groups (2.0 nm < X < 39.7 nm, called the 'non-boundary group'), the velocity is linearly ramped from 0.0 to 0.001 nm/ps. The non-boundary group atoms are simulated using an isothermal-isobaric ensemble (NPT) with stress components in directions other than the loading direction (X-direction) are allowed to relax, and with T = 10 K. The forces on boundary atoms are set as zero. The boundary atoms move at the constant assigned velocity (0.0 nm/ps and 0.001 nm/ps), and the plain time integration to update the position is done using a microcanonical ensemble (NVE). The crack is simulated by excluding the interaction between the following two groups of atoms: (a) X > 20 nm and Y > 36 nm, and (b) X < 20 nm and Y > 36 nm. This forms a planar crack in the YZ plane with a 6 nm length perpendicular to the loading direction. The high strain areas are visualized using atomic shear strain as implemented in OVITO.

DISTRIBUTION A: Distribution approved for public release.

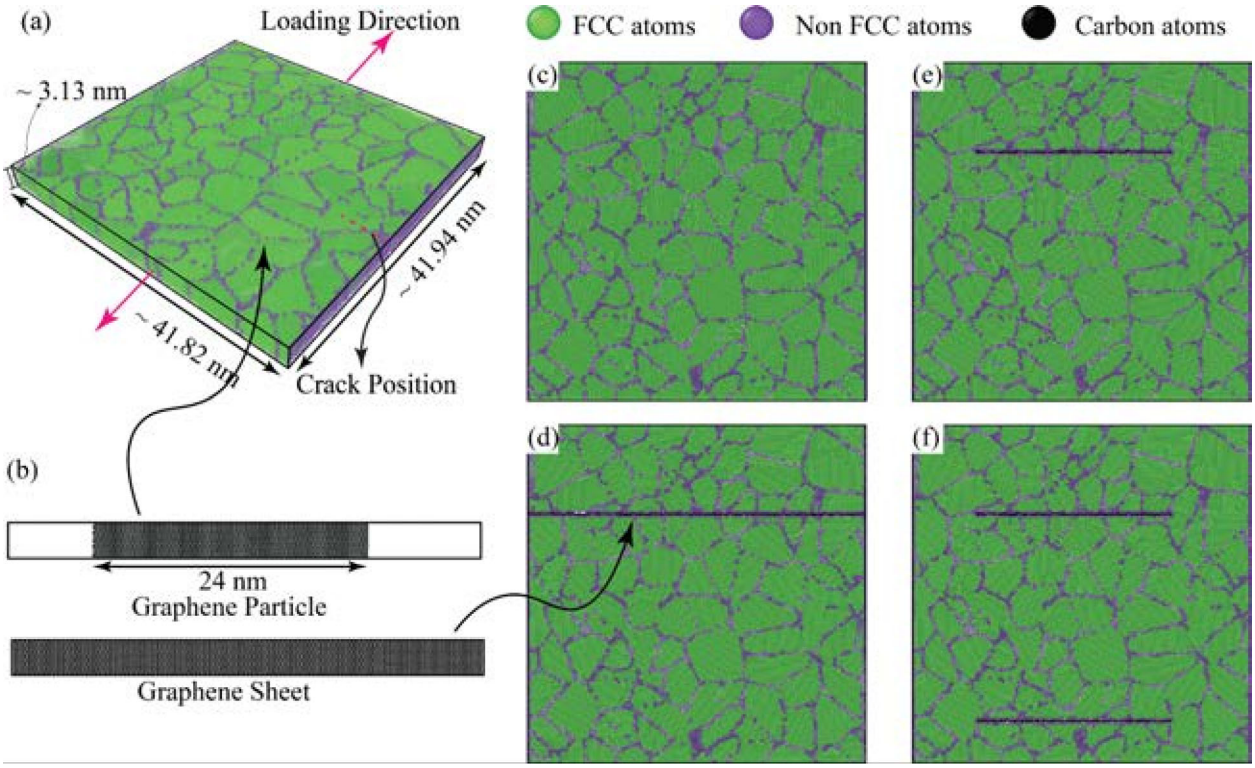

Figure 2.13: The dimensions and geometry of the MD systems are shown. (a) shows the loading direction and crack position in the system, which is the same for all four systems. (b) show the graphene particle and graphene sheet used for reinforcement. (c)-(f) show all four systems with and without reinforcement.

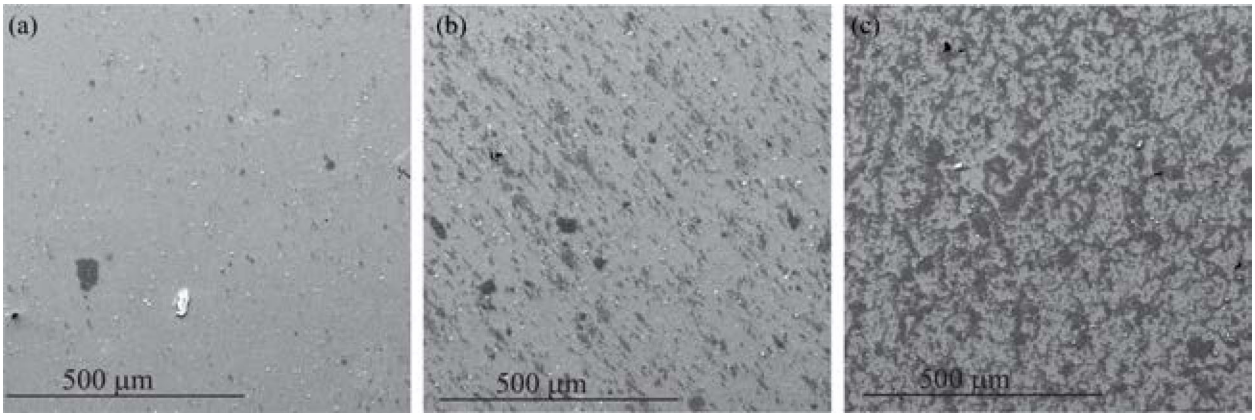

Figure 2.14: The difference in aerial dispersion of graphene is due to the difference in weight percentage of graphene dispersion during the spin coating. (a), (b) and (c) Show the aerial coverage of graphene spin-coated with 0.05, 0.10, and 0.50 wt. %. The spin coating is performed at 2000-rpm speed for 40 s.

DISTRIBUTION A: Distribution approved for public release.

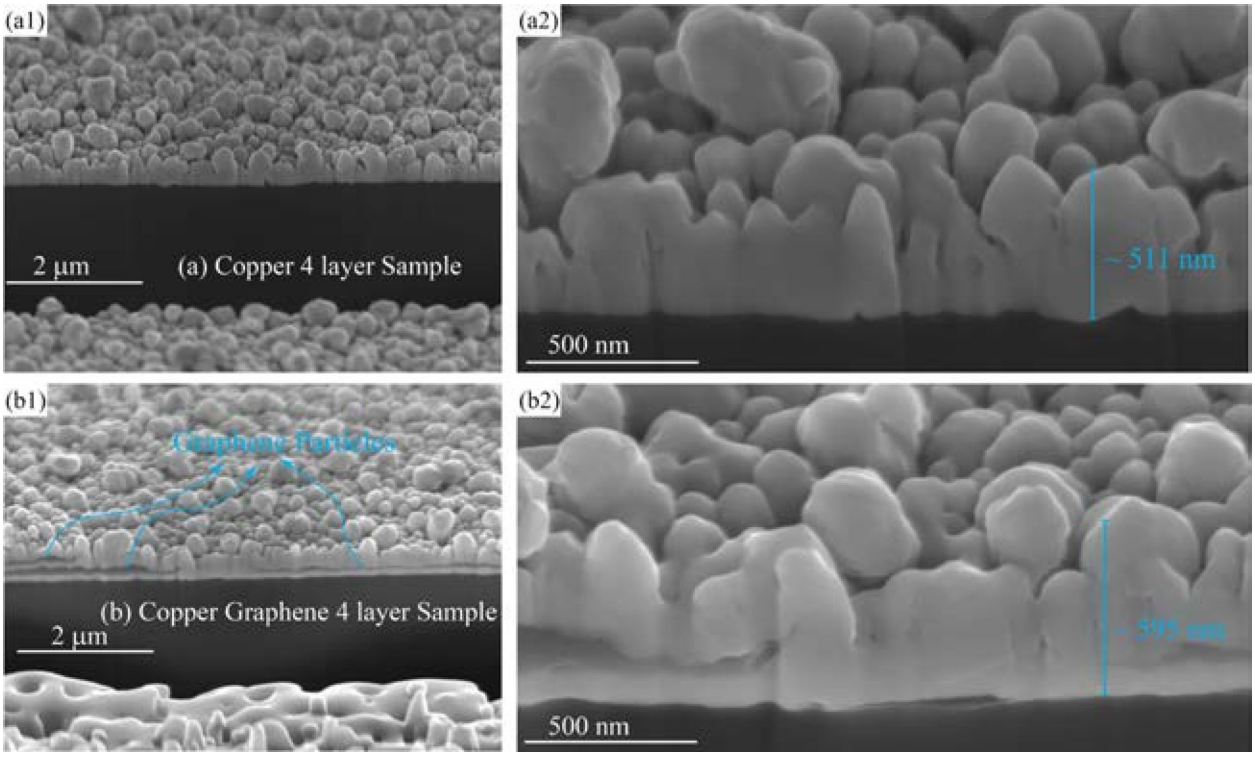

Figure 2.15: The cross-sections of the four-layer copper and copper graphene samples show that the metal film's growth has changed due to substrate temperature (100 degrees Celsius) compared to the ten-layer sample deposited at room temperature. The layered structure is present in the regions where graphene particles are embedded in the copper graphene sample.

DISTRIBUTION A: Distribution approved for public release.

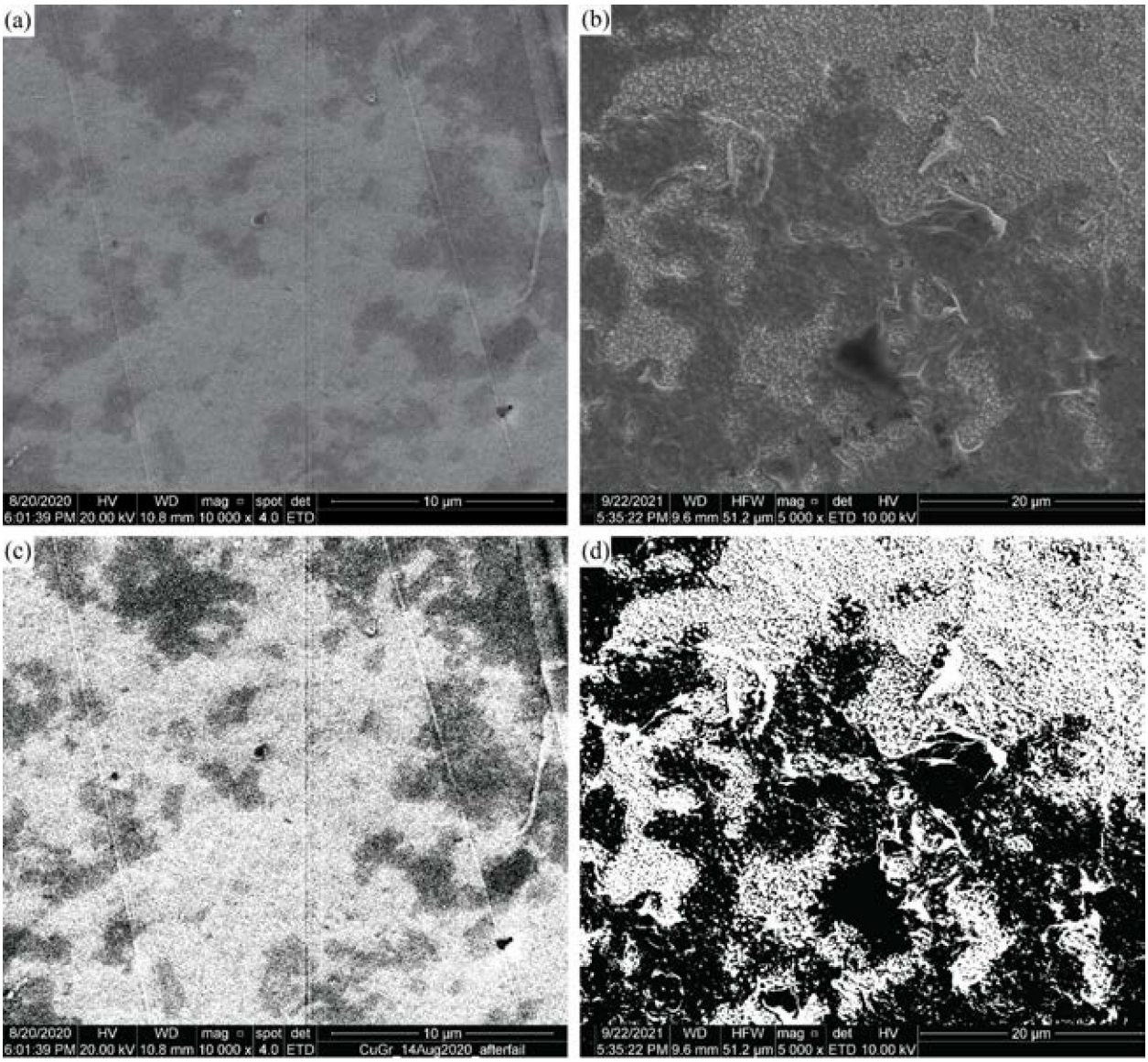

Figure 2.16: The graphene dispersion for ten-layer and four-layer samples are shown in (a) and (b), respectively. The four-layer sample has high graphene coverage and some places have multi-layer graphene due to increased roughness and increased graphene weight percentage during spin coating. (c) and (d) are binary converted images to quantify the aerial coverage of graphene in both sets of samples. The aerial coverage of graphene in the ten-layer sample is 30% and for the four-layer sample is 55%.

DISTRIBUTION A: Distribution approved for public release.

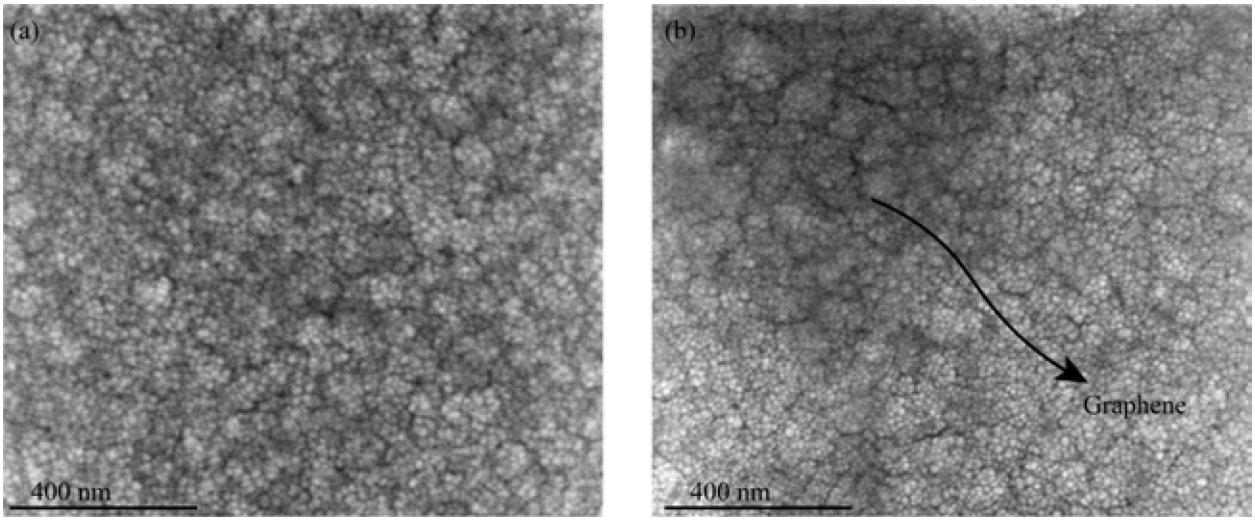

Figure 2.17: The top surface of the ten-layer Cu and CuGr sample in SEM is shown in (a) and (b), respectively. The grain morphology in both Copper and Copper-Graphene is columnar with the grain diameter around 23 nm.

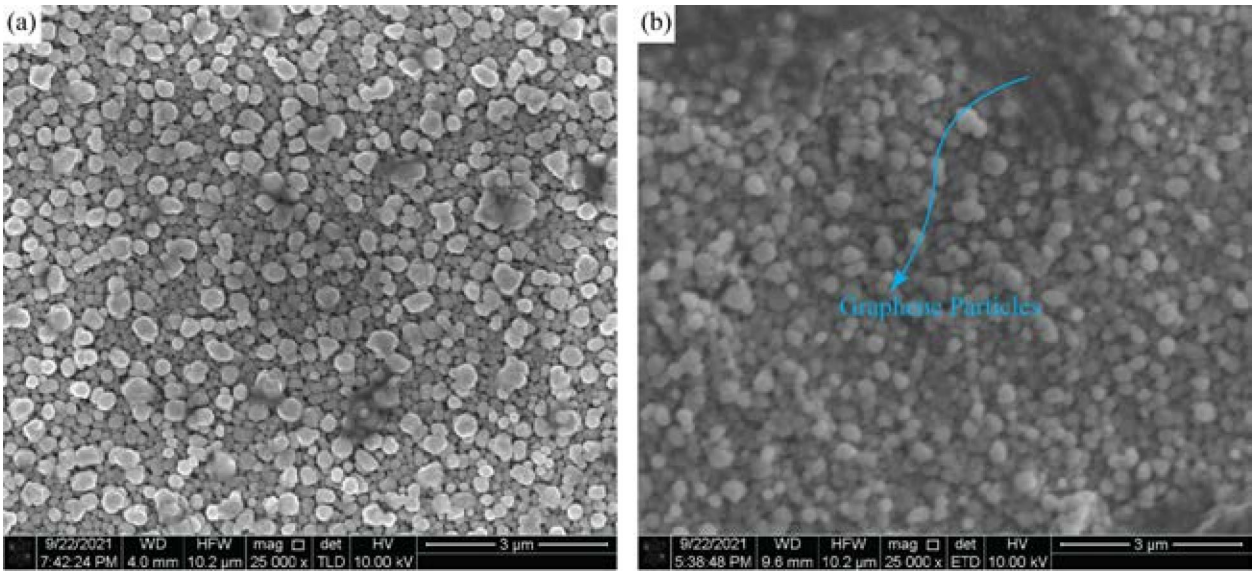

Figure 2.18: The top surface of the four-layer copper and copper graphene samples are shown in (a) and (b), respectively. The grains are equiaxed with diameters ranging from 200 nm to 300 nm.

DISTRIBUTION A: Distribution approved for public release.

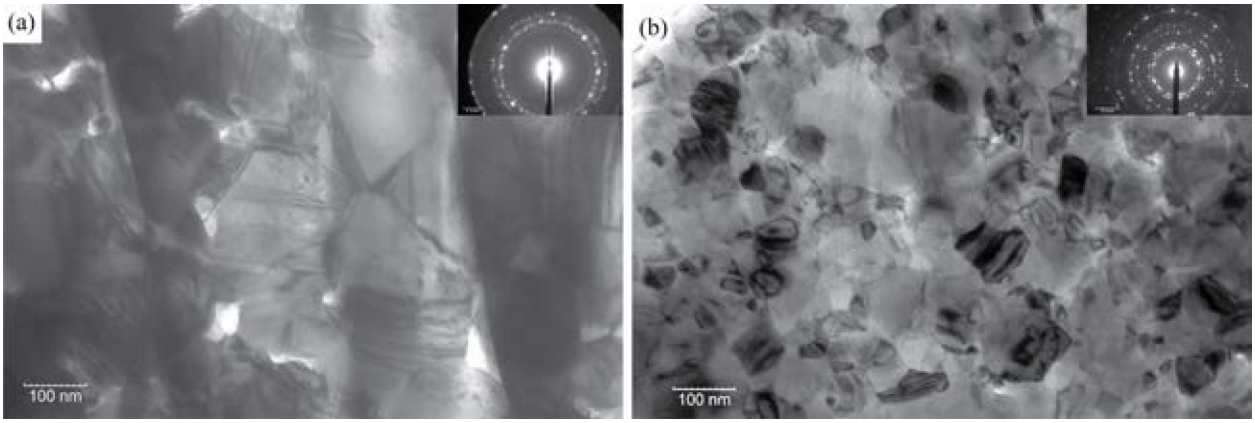

Figure 2.19: The TEM and SAED images of four-layer copper and copper graphene samples confirm the crystallinity in both samples with nanograins as expected. (a) Show copper sample and (b) show copper graphene sample.

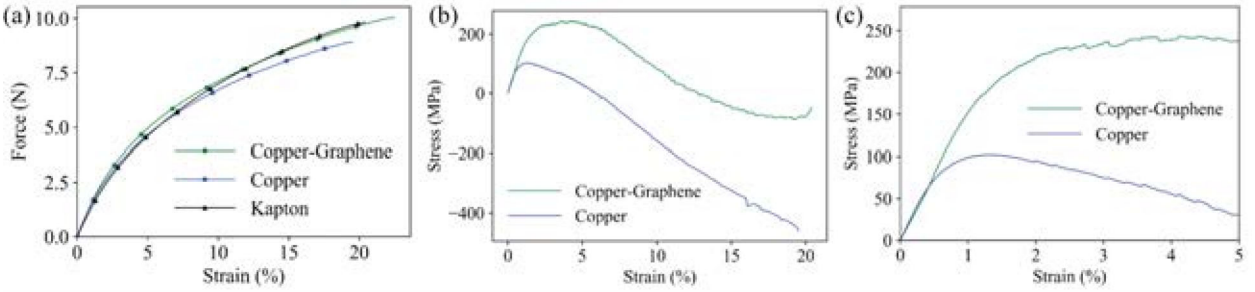

Figure 2.20: (a) Force-strain curves of the Kapton coated with four-layer copper and copper graphene samples. (b) and (c) Show the stress-strain curves after subtracting the force-strain curve of Kapton. The negative forces after subtraction are due to a flaw in the assumption that the Kapton in composite and Kapton without any metal layer carries the same forces. After the formation of cracks, there is a generation of the free surface at the top of Kapton, and stress redistribution happens. This stress redistribution causes highly inhomogeneous longitudinal stresses (stresses in the direction of loading). This difference in local strain causes the Kapton with metal film and free-standing Kapton to have different global forces at the same global strain. The microcracks form in the four-layer copper graphene sample at 228 MPa and 2.4% compared to 103 MPa and 1.3% in the copper sample. The presence of graphene particles covering around 55% of the area on the metal surface increases the required stress for cracking initiation by 121%.

DISTRIBUTION A: Distribution approved for public release.

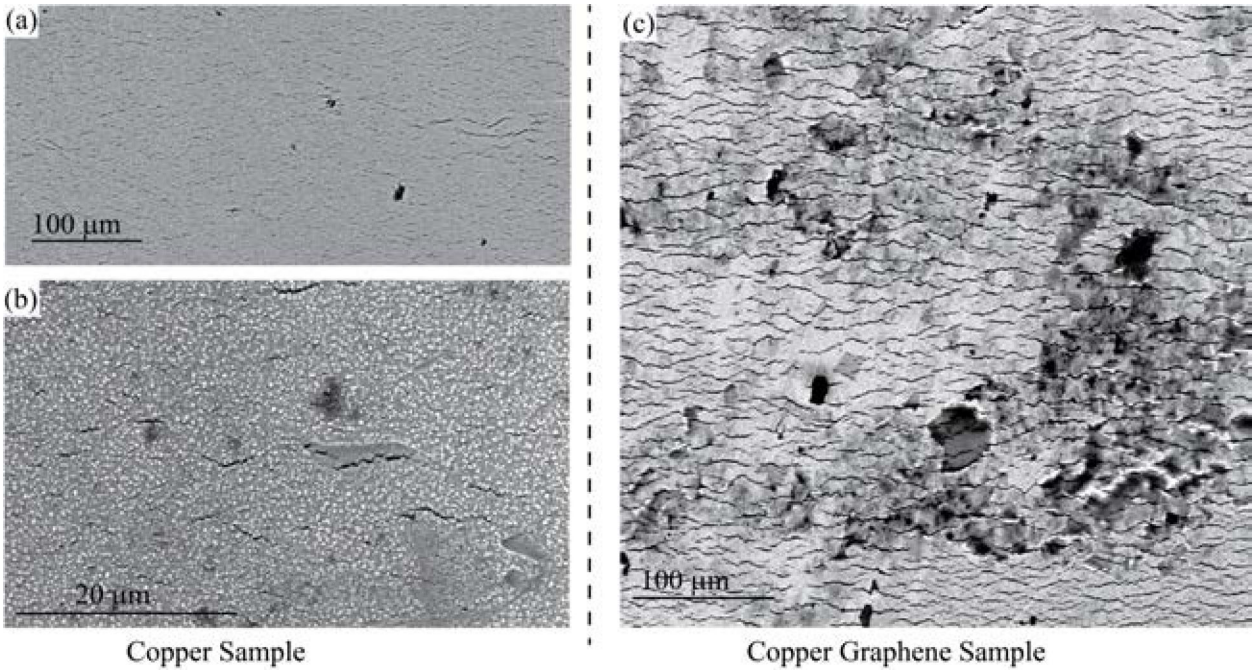

Figure 2.21: The cracking patterns in the four-layer copper and copper graphene samples are shown. (a) and (b) Show cracks in the four-layer copper sample. The dimensions of microcracks are smaller than the microcracks in the four-layer copper graphene samples as shown in (c). The microcracks in four-layer copper graphene samples are formed at high stress and thus have large lengths.

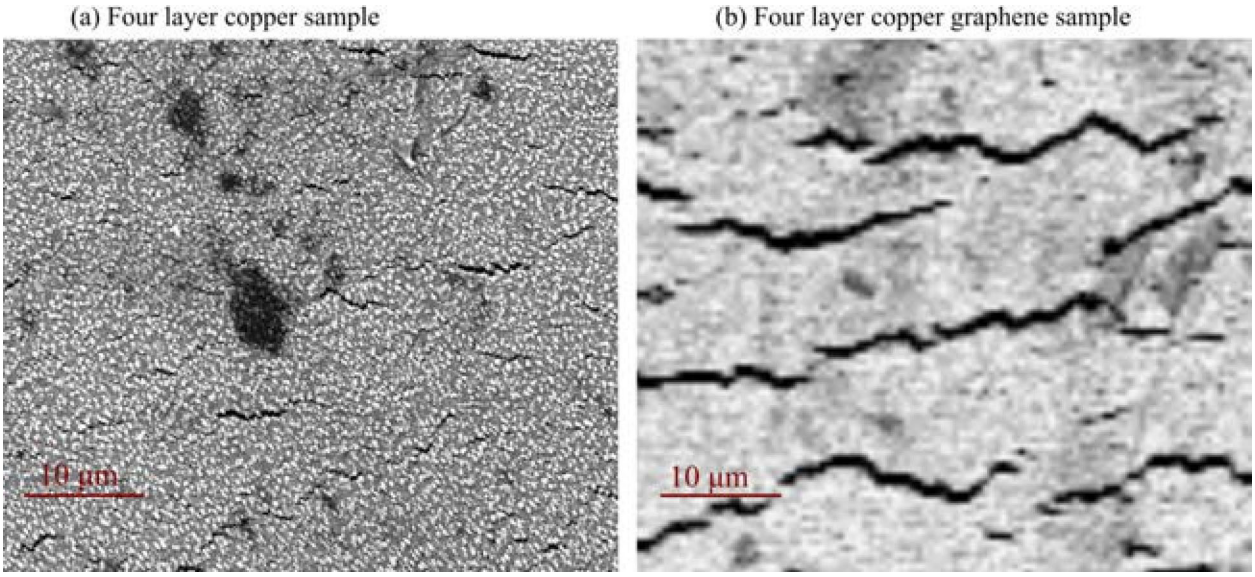

Figure 2.22: The comparison of microcracks between four-layer copper and copper graphene samples. The crack dimensions are large in copper graphene in comparison to the copper as the microcracks form at high stress. The microcracks are formed in the regions where the grain boundary sliding rate is high.

DISTRIBUTION A: Distribution approved for public release.

III- Mechanical properties of NiTi-Graphene composites using atomistic simulations

3.1 Introduction

Metal graphene composite is a class of material in which the dislocation impeding by the graphene leads to better mechanical properties. These dislocations create localized strain in the graphene. This mechanism does not allow the use of the full potential of graphene. NiTi is a shape memory alloy that can go up to high recoverable strains. The tensile properties of graphene can be utilized by reinforcing it in the metallic alloys that can go up to high strains. The pseudo-elasticity of shape memory alloys and the strength of graphene can give us a unique composite.

Atomic-scale simulations can provide useful information regarding the interaction of graphene with NiTi crystal structure. Interface energy between graphene and NiTi can affect the crystal structure of NiTi. The effect of interface energy on the crystal structure will affect the mechanical properties. These effects are difficult to measure experimentally but can be estimated using atomic-scale experiments. First principle calculations can provide the most reliable information but they are limited to a few hundred atoms. Atomistic simulations using semi-empirical potentials can also be used to study NiTi graphene composites. The accuracy of these simulations depends on the accuracy of the potential field. For NiTi and graphene composite we need a potential which has been formulated in a way to describe all the constituent element. Modified embedded atom method (MEAM) developed by Baskes *et. al.* is one such potential [56]. In this work, we have used NiTi MEAM potential developed by Ko et. al. [57] to develop NiTiC MEAM potential. We have developed a Carbon potential that can describe the mechanical properties of graphene, correctly and the interaction parameters required for the interaction between Ni (or Ti) and C atoms.

3.2 2NN MEAM potential

MEAM is the modified form of Embedded atom method (EAM) which is based on Stott-Zaremba corollary to DFT. Stott-Zaremba corollary states that energy of an impurity depends on the host material electron density without impurity [58, 59]. That is,

$$E = \mathcal{F}_{Z,\mathbf{R}}[\rho_H(\mathbf{r})] \tag{3.7}$$

DISTRIBUTION A: Distribution approved for public release.

where ρ_H is the unperturbed host electron density, and Z and **R** are the type and position of impurity. EAM uses this corollary by assuming each atom in a system as an impurity in the host consisting of all other atoms.

In the MEAM approach, the total energy of a system is approximated as

$$E = \sum_i \left[F_i(\overline{\rho}_i) + \frac{1}{2} \sum_{j(\neq i)} S_{ij}\phi_{ij}(R_{ij}) \right] \tag{3.8}$$

where F_i is the embedding energy as a function of background electron density $\overline{\rho}_i$. Further, S_{ij} and $\phi_{ij}(R_{ij})$ are the screening function and the pair interaction between atoms i and j separated by a distance (R_{ij}).

In essence, this potential has three sets of parameter- a) parameters involved in describing the function F_i, b) Short range electrostatic potential, ϕ described by the energy and elastic constants of reference structure, c) The set of parameters which define screening function between the atoms. The more details of the EAM and evolution to MEAM potential can be found in the series of papers by Baskes et. al. [56, 58–61].

Table 3.1: Set of MEAM potential parameters for pure Ni,Ti and C. The reference structure of Ni, Ti and C are fcc, bcc and diamond, respectively. The units of cohesive Energy E_c, equilibrium nearest-neighbor distance r_e and Bulk modulus are eV, Å and GPa

	E_c	r_e	B	A	$\beta^{(0)}$	$\beta^{(1)}$	$\beta^{(2)}$	$\beta^{(3)}$	$t^{(1)}$	$t^{(2)}$	$t^{(3)}$	C_{max}	C_{min}	d
Ni	4.45	2.490	185.86	0.79	2.48	1.94	3.46	2.56	2.84	-1.20	2.49	0.95	1.75	0.05
Ti	4.75	2.850	107.35	0.24	2.20	3.00	4.00	3.00	-18.0	-32.0	-44.0	0.25	1.58	0.00
C	7.37	1.545	444.20	1.00	3.00	3.20	3.00	2.80	1.60	0.40	-5.4	2.8	0.8	-0.16

DISTRIBUTION A: Distribution approved for public release.

The parameters for Ni, Ti and binary Ni-Ti has been taken from the work by Ko et.al. [57]. We developed the Carbon potential using differential evolution and the parameters used in this work are shown in table 3.1 and 3.2. For these parameters comparison of elastic constants with either experimental values or first principle calculations are shown in table 3.3.

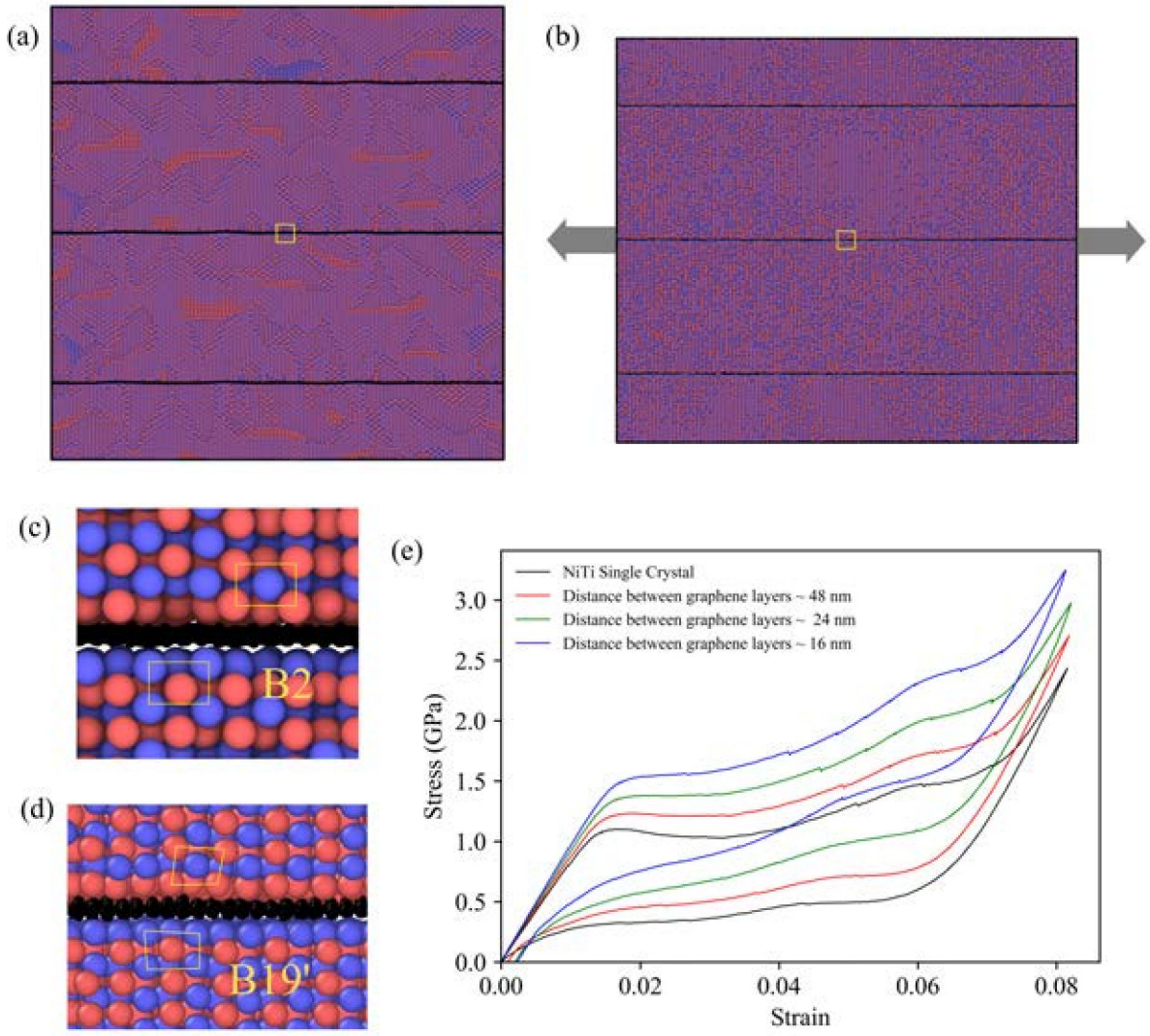

Figure 3.1: (a) and (b) Show the NiTi single crystal reinforced with graphene at the start of loading and unloading. (c) and (d) Shows the crystal structure inside the composite at (a) and (b), respectively. (e) Shows the stress-strain curve comparison between the NiTi single crystal and the NiTi single crystal reinforced with graphene. Decrease in the distance between graphene layers increases the mechanical properties of the composite and the residual strain increases with increase in graphene layers.

3.3 Method

We reinforced single crystal and poly-crystal of NiTi with different number of graphene layers. For poly-crystal two grain sizes (14.9 and 29.8 nm) has been considered. The dimension of simulation

DISTRIBUTION A: Distribution approved for public release.

Table 3.2: 2NN MEAM potential parameter sets for binary A-B systems (A = Ni, Ti and B = Ti, C). The reference structure of Ni-Ti, Ni-C and Ti-C are CsCl-type (B2) NiTi, NaCl-type (B1) NiC and $L1_2$ Ti_3C, respectively. The units of cohesive Energy E_c, equilibrium nearest-neighbor distance r_e and Bulk modulus are eV, Å and GPa

	Ni-Ti	Ni-C	Ti-C
E_c	4.96	6.987	5.166
r_e	2.612	2.04	2.715
B	128.18	256.00	148.1
d	0.025	0.0	0.0
$C_{min}(A,B,A)$	0.25	0.58	0.30
$C_{min}(B,A,B)$	0.09	0.95	1.00
$C_{min}(A,A,B)$	0.49	0.90	1.00
$C_{min}(B,B,A)$	1.60	1.10	1.00
$C_{max}(A,B,A)$	1.70	1.76	1.50
$C_{max}(B,A,B)$	1.70	2.33	2.80
$C_{max}(A,A,B)$	1.40	2.33	2.80
$C_{max}(B,B,A)$	1.70	2.45	2.80
ρ_0^B/ρ_0^A	1.0	6.0	6.0

box for single crystal is around $48\times48\times48$ nm^3. The lattice directions for single crystal are aligned with axis as folows X-axis[110], Y-axis[$\bar{1}$10] and Z-axis[001]. The simulation box before loading and unloading for single crystal is shown in Fig. 3.1 (a) and (b), respectively. The dimensions of poly-crystal simulation boxes for grain size 14.9 nm and 29.8 nm is $25\times25\times25$ nm^3 and $50\times50\times50$ nm^3, respectively.

Molecular Dynamics (MD) simulations are carried out using time integration on Noose-Hoover style non-Hamiltonian equations of motion. These equations update the position and velocity of each atom during discrete time steps using canonical (NVT) and isothermal-isobaric (NPT) ensembles[66, 67]. Periodic boundary conditions in x, y, and z were given to the cubes to simulate an infinitely large bulk crystal. The Large-scale Atomic/Molecular Massively Parallel Simulator (LAMMPS) is used to carry out all MD simulations in this work[54].

Energy minimization is done at the start of simulations to find the initial configuration of the composite or crystal. Minimization of total energy is done as a function of the Nth atom's coordinate. The position of atoms are iteratively adjusted until the energy change becomes less than 1e-10. Next, the system is equilibrated at a temperature of 500 K for 20 ps with zero stress in all directions using the NPT ensemble. The temperature 500 K make sure that the structure of NiTi before laoding is B2. In this work, the tensile stress is applied in X-direction of simulation box and stresses in other two direction is zero. The simulations are stress controlled with the stress rate 4.5 $\times$ $10^1$0 GPa per second. The value of stress, along with the change in cell dimensions for strain, has been extracted to plot stress-strain graphs. The Open Visualization Tool (OVITO)[55] is used for visualization.

DISTRIBUTION A: Distribution approved for public release.

Table 3.3: Elastic constant values comparison for the Carbon, TiC and NiC reference structure. The comparison for Ni, Ti and NiTi is presented in teh work by Ko et. al. [57]. The unit of all elastic constant (C_{11}, C_{12}, C_{44} and B) is GPa. The units of lattice length and energy of formation (E_c and ΔE_f) are Å and eV/atom, respectively.

Parameter	Experimental or DFT values	This work
Carbon (Diamond structure)		
Lattice length	3.567 [62]	3.567
C_{11}	1080.4 [63]	1091.9
C_{12}	127.0 [63]	120.4
C_{44}	576.6 [63]	653.0
B	444.8 [63]	444.2
E_c	7.37	7.37
Carbon (Graphene)		
Bond length	1.42	1.426
ΔE_c	0.02^a	0.26
NiC (B1 structure)		
Lattice length	4.073 [64],4.077[65]	4.08
ΔE_f	1.077 [64],1.053[65]	1.077
C_{11}	296.0 [64]	526.2
C_{12}	231.0 [64]	120.8
C_{44}	50.0 [64]	125.9
B	256.0 [64]	256.0
TiC ($L1_2$ structure)		
Lattice length	3.692^b	3.841
ΔE_f	-0.276^b	-0.239
C_{11}	177.2^b	207.3
C_{12}	133.8^b	118.50
C_{44}	88.4^b	87.20
B	148.2^b	148.1

^{a} Graphite force field,^{b} Our DFT calculations

DISTRIBUTION A: Distribution approved for public release.

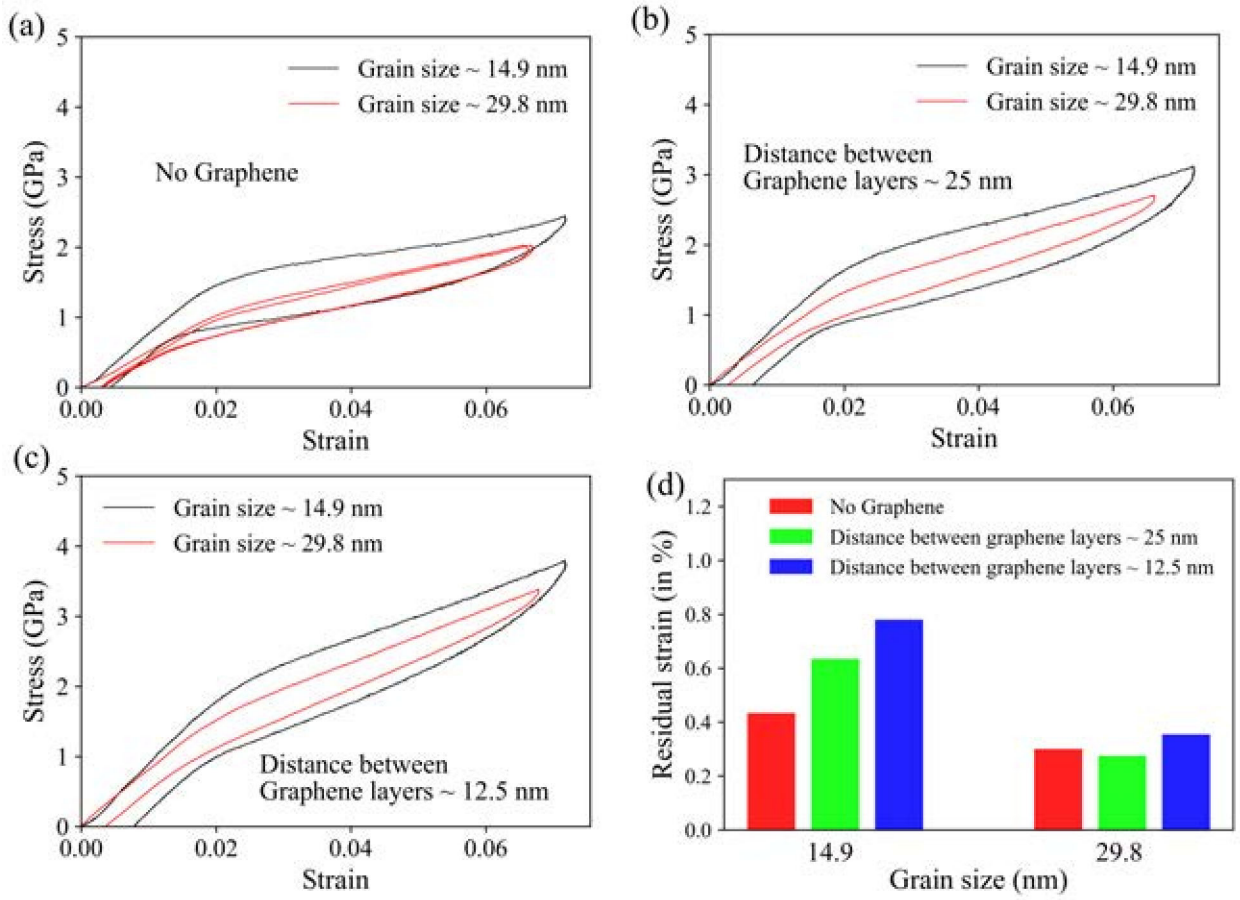

Figure 3.2: (a),(b) and (c) Show the stress-strain curve for the NiTi polycrystal with two different grain size reinforced with and without graphene. (d) Show the comparison of residual strain after a cycle of loading and unloading. The grain size 14.9 nm has better properties than 29.8 nm and graphene improves the property of poly-crystal in both the cases.

3.4 Result

NiTi binary alloy has the shape-memory effect and superelasticity due to change in crystal structure from austenite (B2) to martensite(B19') during loading. These effects combined with the strength of graphene can create a composite which shape-memory effect and superelasticity combined with higher strength. As shown in the figures 3.1, 3.2 and 3.3, atomistic simulations confirm that NiTi (single crystal or poly-crystal) reinforced with graphene layers have improved mechanical strength.

Figure 3.1 (c) and (d) shows the crystal structure in NiTi graphene composite before and after loading. The phase transformation from B2 to B19' is visible in the composite. Figure 3.1 (e) shows the stress-strain curve for the composite compared with NiTi single crystal. The stress required for the transformation has increased in the composite due to the addition of the load-bearing capacity of the graphene compare to the perfect crystal. The irrecoverable strain after a cycle of loading and unloading has increased with the decrease in distance between the graphene layers. There are microcracks in the graphene after the cycle of loading and unloading. The possible explanation for the irrecoverable strain is that the plastic deformation occurred near the graphene layer due to the interaction of Ni, Ti and C atoms.

DISTRIBUTION A: Distribution approved for public release.

The grain size plays an important role in atomic-scale processes, such as nucleation, growth and twinning [68]. These processes affect the mechanical properties of NiTi such as the disappearance of the plateau in the stress-strain response [68, 69]. Understanding the effect of grain size in NiTi graphene composite is important. As shown in figures 3.2 (a)-(c), the grain size diameter of 14.9 nm has a better mechanical response than grain size diameter of 29.8 nm. In both cases, reinforcement of graphene has increased the required stress for transformation and has improved mechanical properties. As shown in figure 3.2 (d), the residual (or irrecoverable) strain after a cycle of loading and unloading increases in the case of grain size 14.9 nm.

3.5 Conclusion

In this chapter, we have developed an interatomic potential for the ternary system based on the 2NN MEAM formalism. The potential has been developed by using the previously developed unary and binary NiTi potential. The unary C potential has been developed and resulting C potential successfully reproduces the mechanical properties of graphene. Using the developed NiTiC potential, NiTi Graphene composites have been investigated. The atomistic simulations show that the graphene improves the mechanical properties of NiTi while retaining the super-elasticity.

Acknowledgement

This material is based upon work supported by the Air Force Office of Scientific Research under award number FA9550-18-1-0169.

DISTRIBUTION A: Distribution approved for public release.

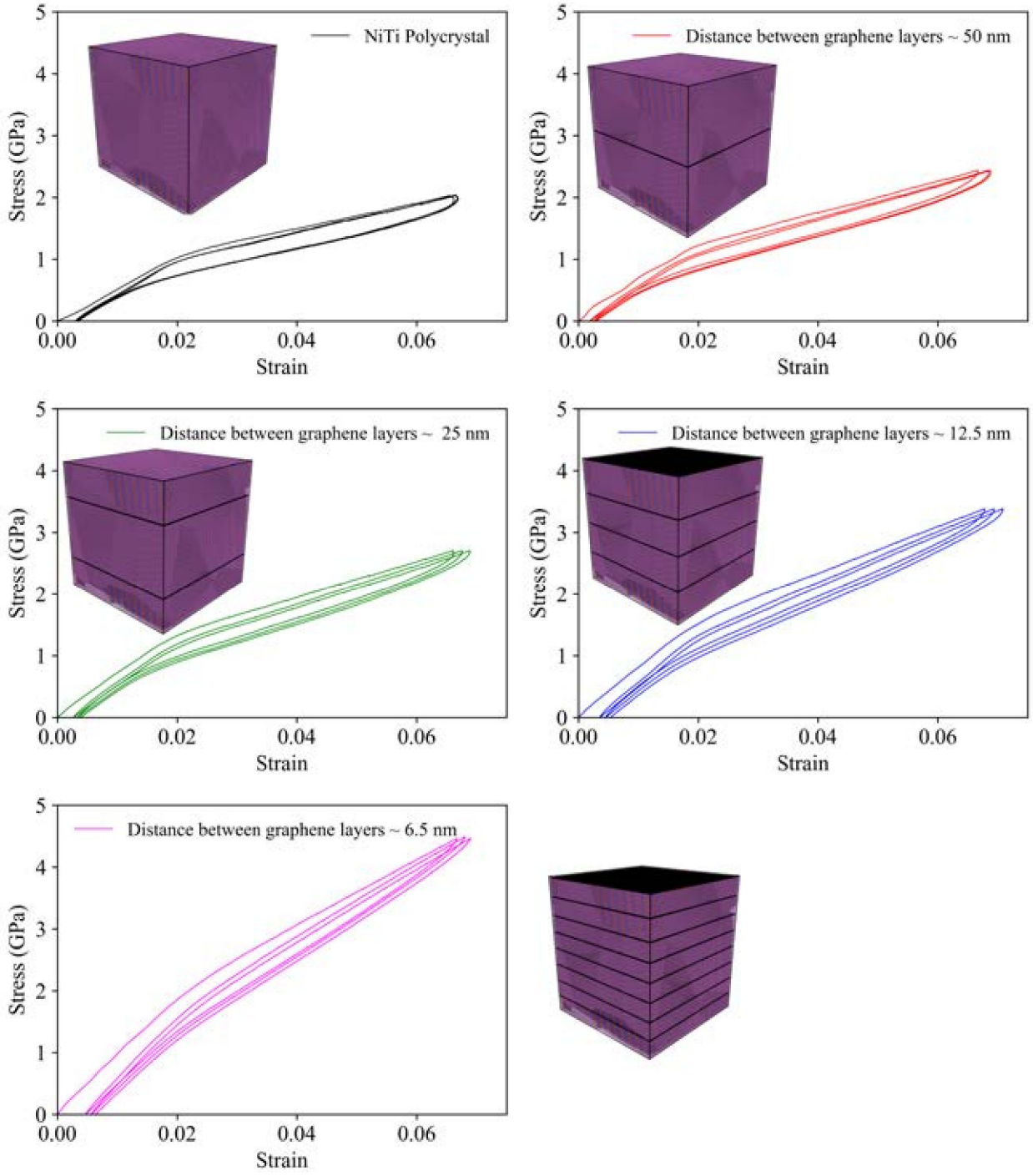

Figure 3.3: Stress-strain curve with decreasing distance between the graphene layers for 3 cycles of loading and unloading.

DISTRIBUTION A: Distribution approved for public release.

IV- Graphene-Nickel Interaction in Layered Metal-matrix Composites

4.1 Abstract

Graphene can be utilized as reinforcing interlayers in metal-matrix composites to improve their mechanical properties. This improvement is due to the ability of the graphene layers to transfer their exceptional strength to the metallic matrix, and their ability to hinder the propagation of dislocations inside the metallic systems. In these composites, the structure of the graphene layer (or nanoparticles) in the matrix and the interaction between graphene and metallic atoms play a vital role in the improvement of metal-graphene composites' mechanical properties. While the interaction between metal and graphene interface, when the graphene is on the top of a metallic layer, has been extensively studied, details of the interaction when the graphene is embedded inside a metal matrix are still highly unexplored. In this paper, we considered the structure of graphene and the interaction between graphene nanoparticle edges and nickel atoms when the graphene is embedded in the nickel matrix. Using *ab-initio* calculations, we found that when the graphene is embedded inside a nickel matrix, the most stable graphene structure is topfcc (with graphene nano-sheets being parallel to Ni(111) surface), which is a different configuration compared to the case of having graphene on the surface of a nickel slab. Also, we found that armchair edge energy is 0.8022(eV/Å) and zigzag edge energy is 2.5048(eV/Å) which implies armchair edge is more stable and creates less distortion inside the nickel matrix. Less distortion by armchair edge implies that nucleation of dislocation in composites will start later at armchair edges in comparison to zigzag edges during mechanical loading.

4.2 Introduction

Graphene, since its discovery, has generated extensive interest to be used as a reinforcement material to strengthen and enhance the properties of metals. The excellent mechanical properties (Young's modulus $\simeq$ 1.0 terapascals, breaking strength $\simeq 42Nm^{-1}$) [1] and the 2D structure of graphene makes it an ideal candidate for strengthening metals. The graphene can be either dispersed as nanoparticles or used as layered reinforcement in the metal matrix. The strengthening effect of graphene increases significantly if used as layered reinforcement compared to dispersing the graphene flakes inside the metal matrix [13]. The reason is that the layered graphene stops the propagation of dislocations inside the metal matrix more efficiently [13, 20, 70]. Besides the geometry and configuration of graphene in the metal matrix, there are also other factors, like the

DISTRIBUTION A: Distribution approved for public release.

formation of metal carbide [71, 72] and delamination at the metal-graphene interface, that can change the prominent failure mode [73]. While the change in prominent failure mode can decrease the strength of composite compared to pure metal, a carefully engineered reinforcement of graphene can significantly improve the mechanical strength of metal composites. Graphene composites with nickel, copper and aluminum have been successfully fabricated [7, 9, 13, 74–76] and found to have enhanced mechanical properties.

There have been various experimental and molecular dynamics studies which have shown that graphene can enhance the properties of nickel when used as layered reinforcement [13, 20, 77, 78]. In recent work, we have also shown that embedded graphene flakes, with a specific concentration, significantly improve the mechanical properties of polycrystalline nickel [20]. In experiments, It is found that the preferred plane of nickel crystal in composites with graphene is (111) [79, 80]. The reason is the high interaction of nickel and graphene in Ni(111) plane because of both physisorbed and chemisorbed bonding configurations [79, 81]. For graphene Ni(111) interface (with graphene layer being on the top of a Ni slab) there have been first-principle studies which conclude that the bridgetop structure of graphene over nickel is the most stable structure [82] followed by the topfcc and tophcp structure. The topfcc and tophcp structures of graphene over Ni(111) plane has been observed using low energy electron diffraction (LEED) I–V measurements and scanning tunnel microscopy (STM) [83, 84]. The bridgetop and topfcc structures have also been found co-existing over Ni(111) [85]. The observation from experiments has been found in a good agreement with density functional theory (DFT) analysis of Ni(111) graphene interface [83, 85] .

Interaction between graphene and Ni(111) interface changes depending on the interface structure [86], and the small interfacial adjustment in graphene composites can make big changes in electronic structure [87]. The change in the interaction of nickel and graphene by the graphene structure [1] can affect the mechanical properties of nickel graphene composites. First-principle studies provide the most reliable information at atomic scale material properties but they limit the size of the studying system to a few hundred atoms. This limitation had been overcome by employing molecular dynamics using Lennard-Jones (LJ) potential or modified embedded-atom method (MEAM) potential to mimic the interaction between C and Ni [13, 20, 73, 77, 88]. These potentials have not been fitted for the nickel-graphene composite. We need *ab-initio* data of nickel-graphene composite to check the applicability of these potentials in simulating the composite. Unlike nickel-graphene interface, to the best knowledge of the authors, there has been no experimental or theoretical study to determine the graphene structure in nickel composites.

In practice, graphene sheets employed in the composites are of finite length, and graphene edges can play a significant role in determining the properties of composites. The edge energies will determine the shape of stable graphene flakes inside the nickel [89, 90]. It has been reported that for graphene edge stress for all edge orientation is compressive [89]. Depending on the distortion of the nickel matrix and compressive stress of graphene edge, dislocations can nucleate near the edge during mechanical loading and can weaken the composites.

In this work, we have determined the stable graphene structure in the nickel-graphene composite and has compared it with the interface interaction of nickel and graphene. Also, we have calculated deformation energy per unit edge length for armchair and zigzag edge inside the nickel matrix. The analytical form of graphene edge energy [91] has been used to predict the shape of the graphene flake which causes minimum distortion in the nickel matrix.

[1] In this work, graphene structure refers to the position of graphene relative to the nickel layers.

DISTRIBUTION A: Distribution approved for public release.

4.3 Methods

The *ab-initio* calculations used in this work are based on density functional theory (DFT) with the use of pseudopotentials and a plane-wave expansion. Energy cutoff of 450 eV and 3300 eV has been used for plane wave basis and charge density grid, respectively. It is known that local (spin) density approximation (LDA) and generalized gradient approximation (GGA) functional tends to overbind and underbind the systems, respectively [86, 90]. GGA gives a better prediction for both metal and graphene, but in the case of the hybrid system like the interaction between metal and graphene interface, contrary to experiments, GGA predicts no binding between metal and graphene [90]. For nickel-graphene interface, the interfacial distance between topmost Ni layer and graphene predicted by LDA is 2.1 Å [82] which is close to the value found in experiments, that is, 2.11 ± 0.07 Å [84]. Hence, LDA has been used to approximate exchange-correlation functional [92].

All the calculations were spin polarized and were done using Vienna *ab initio* simulation package (VASP) (Version 5.4.1) [93] with the use of projected augmented-wave pseudopotential parameters [94] .

1. Graphene structure inside the nickel

We defined initial structure using Ni(111) as z-direction of supercell and normal to graphene structure. As shown in Fig. 4.4 (a) and (b) in the Appendix, DFT LDA predicts correct bond length for graphene, that is, 1.42 Å but overbinds the nickel lattice by predicting 3.41 Å as lattice constant. We used experimentally measured lattice constant of the nickel that is 3.52 Å for the supercell construction. The experimentally measured lattice constant of nickel has been used in the past studies of the hybrid system and has correctly predicted the inter-atomic distances between the layers and the stable structures of the graphene [82, 86]. As graphene is in the nickel bulk hybrid system, it will have the planar lattice constant close to the nickel. To match the periodic lattice of Ni(111) plane, graphene bond length has been stretched about 1.02%. In supercell, 48 layers of nickel in z-direction were considered, and graphene was inserted in between the nickel layers. These number of layers are found to be sufficient to simulate the hybrid system. As shown in Fig. S1 (c), the difference between inter-atomic layer distances for a system consisting of 48 layers and 72 layers is less 1.5 %. The Brillouin zone was sampled with a $15 \times 15 \times 1$ grid within the Monkhorst-Pack scheme [95] with the shift of (-0.5,-0.5,-0.5) (to make it gamma centered).

We moved the graphene in the δ-direction of supercell as shown in figure 4.1(a) and allowed geometric relaxation to get the total energy convergence of less than 0.1 meV. During geometry optimization, 12 layers of nickel on each side of graphene (in total 24) were allowed to relax in the z-direction. Since the force on the nickel atoms perpendicular to the δ-direction and in the plane parallel to graphene is zero, not allowing relaxation in that direction will not affect the optimized geometry and solution. The naming convention used here is based on interface naming shown in figure 4.1(c) which has been used in the past work studying Ni(111) plane and graphene interaction [82, 86, 96]. When graphene is inside the nickel, we have two interfacial interaction which can be the same or different according to the position of graphene as shown in figure 4.2(a)-(d). Here we have used + sign to specify both; for example, "bridgefcc + bridgetop" structure means that when one interface is bridgefcc the other will be bridgetop (or vice-versa). For topfcc + topfcc and bridgehcp + bridgehcp, both the interfaces are same, so we have used topfcc and bridgehcp as the names for them in the text.

DISTRIBUTION A: Distribution approved for public release.

2. Interface interaction

Graphene on Ni(111) is a strongly interacting system having a separation of approximately 2 Å [82, 86, 97]. To understand the difference of graphene on Ni(111) surface compared to graphene inside the nickel, we have fixed the Ni(111) graphene distance and have moved graphene over the nickel as shown in 4.1(b). For interface calculations (having graphene on the top of a Ni slab), a Ni(111) slab of nine layers was made, and graphene was placed at a distance of 2 Å from the slab. Vacuum space of 15 Å was used in the supercell. The Brillouin zone was sampled with a $15 \times 15 \times 1$ grid within the Monkhorst-Pack scheme [95] with shift of (-0.5,-0.5,-0.5) (to make it gamma centered). Without allowing geometric optimization, we moved graphene in δ-direction to get energy at different values of δ.

3. Graphene edge inside the nickel

Two supercells corresponding to the armchair and zigzag edge with the topfcc structure having nine nickel layers in the z-direction (111) were considered. The graphene particle which was periodic in one direction (as shown in figure 4.3 (a)-(b)) was inserted inside the nickel to calculate the edge energy in both cases. Size of armchair edge supercell was 19.9121 Å $\times$ 4.311 Å $\times$ 18.2905 Å and size of graphene in supercell was 9.956 Å $\times$ 4.311 Å. Size of zigzag edge supercell was 2.48902 Å $\times$ 34.4888 Å $\times$ 18.2905 Å and size of graphene in supercell was 2.48902 Å $\times$ 20.1185 Å. The size of supercell and graphene particles do not allow graphene edges to interact inside the supercell or with the graphene edges in periodic images. For both the edges Brillouin zone has been sampled using 25 k-points in the edge direction within the Monkhorst-Pack scheme [95]. As graphene mainly interacts with only three nearest layers of graphene (discussed in results), for geometric optimization we allowed three layers on each side of graphene to relax in all three directions.

4.4 Results and Discussion

1. Structure of Graphene

For interface between graphene and nickel, as shown in figure 4.1(e) the bridgetop configuration is the most stable interface structure followed by topfcc and tophcp. When graphene is inside the nickel, there are two layers of nickel which interact with graphene compared to the interface. For the case of topfcc and bridgehcp, there exists a mirror symmetry, both top and bottom layers interact in the same manner. When graphene structure is hcpfcc (or bridgefcc) relative to one side of the nickel layers, the structure is tophcp (or bridgetop) relative to other side of nickel layers. This geometry consideration is manifested in the interaction of nickel and graphene atoms. When graphene is inside nickel, we found that topfcc (in which half of the graphene atoms are inline with the below layer, and the other half is inline with the top layer) is the most stable configuration as shown in figure 4.1(d).

The energy shown in graph 4.1(d) has been calculated as $E_d = E_{comp} - E_{Ni_{bulk}} - E_{Gr}$ where E_{comp}, $E_{Ni_{bulk}}$ and E_{Gr} are the energy of composite, bulk nickel metal and isolated graphene monolayer. E_d is positive because this energy is the measure of how graphene has changed the

DISTRIBUTION A: Distribution approved for public release.

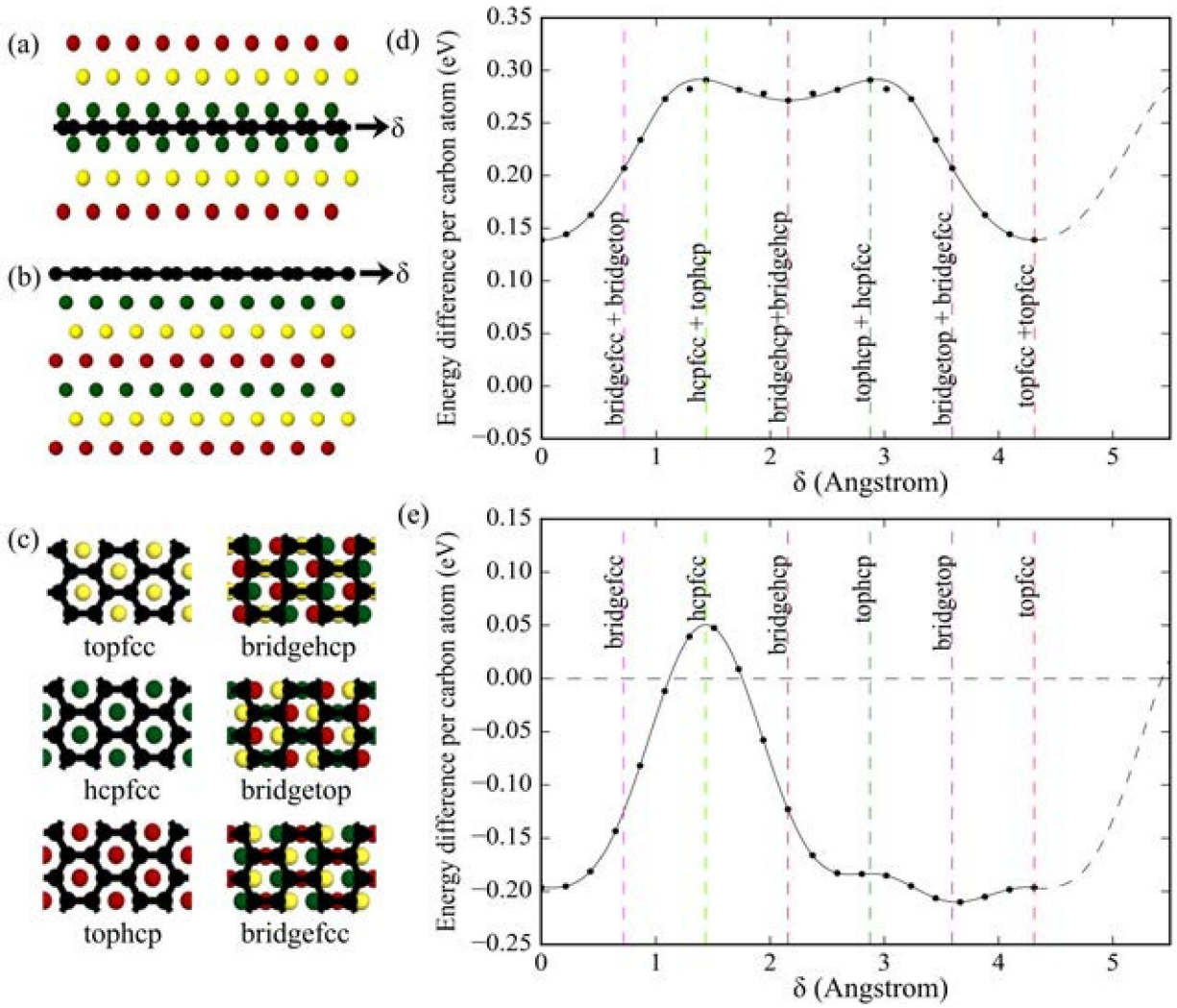

Figure 4.1: (a) shows the starting structure of graphene inside the nickel before relaxation (only 6 layers of nickel out of 48 are shown), (b) shows the Ni(111) graphene interface moving at fixed interfacial distance (2 Å), (c) shows the name of different graphene structures depending on the placement of graphene over nickel atoms, (d) is the case when graphene moves inside the nickel and nickel atoms are allowed to relax which shows that topfcc structure is the most stable structure (Names used in the graph is the graphene structure relative to 3 layers of nickel beneath the graphene), and (e) shows the energy curve for interface interaction. Color code: Ni atoms are green, yellow and red; C atoms are black; first, second and third nearest Ni layer to graphene is green yellow and red, respectively.

DISTRIBUTION A: Distribution approved for public release.

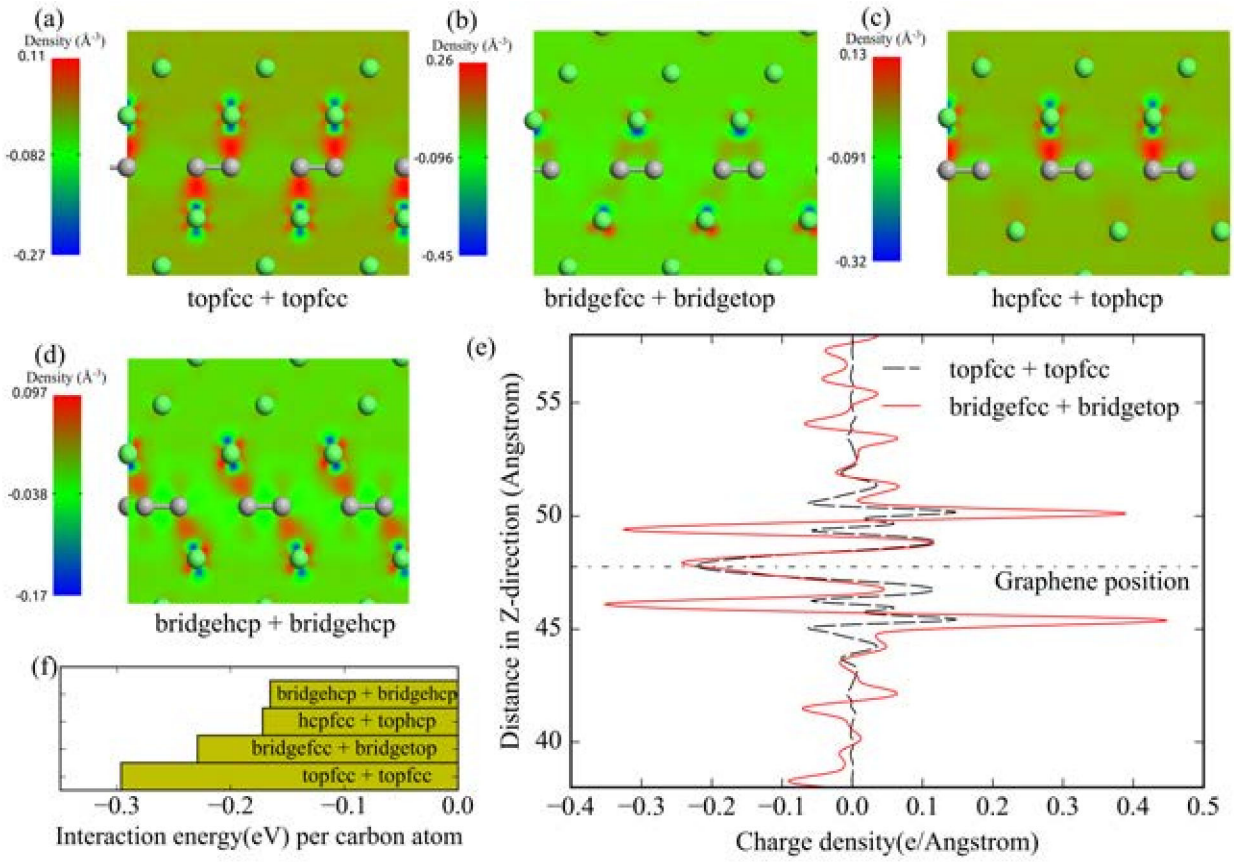

Figure 4.2: a)-d) shows the charge density difference or electron density interaction of graphene for different cases, e) charge density difference integrated over the x-y plane for topfcc stacking. A positive value means gain of the electron density and a negative value means the vice-versa, f) shows the interaction energy of topfcc case is the highest. For topfcc and bridgehcp structures, the top and bottom layers are symmetric. Color code: Ni atoms are green C atoms are grey

interatomic distances between the layers of nickel in the composite compared to the nickel crystalline structure.

The interaction energy shown in figure 4.2(f) has been calculated as $E_i = E_{comp} - E_{Ni_{deform}} - E_{Gr}$ where E_{comp}, $E_{Ni_{deform}}$ and E_{Gr} are the energy of composite, deformed nickel metal without graphene and isolated graphene monolayer. E_i is the measure of the interaction between graphene and nickel. The interaction energy is the quantification of the adherence of Ni layers with graphene. In the case of topfcc, the deformation of the nickel crystal structure is lowest, and the interaction between nickel and graphene is highest compared to other cases, which makes topfcc the most stable structure inside the Ni(111) crystal. High adherence in the topfcc case implies that high stress is needed to initiate interfacial debonding or sliding between nickel and graphene layer [98]. This explains why the delamination of the nickel-graphene interface is not the mode of failure for these composites. In the case of bridgehcp, there is less distortion compared to bridgefcc + bridgetop and hcpfcc + tophcp cases, but the interaction energy of nickel and graphene is more in these two cases.

DISTRIBUTION A: Distribution approved for public release.

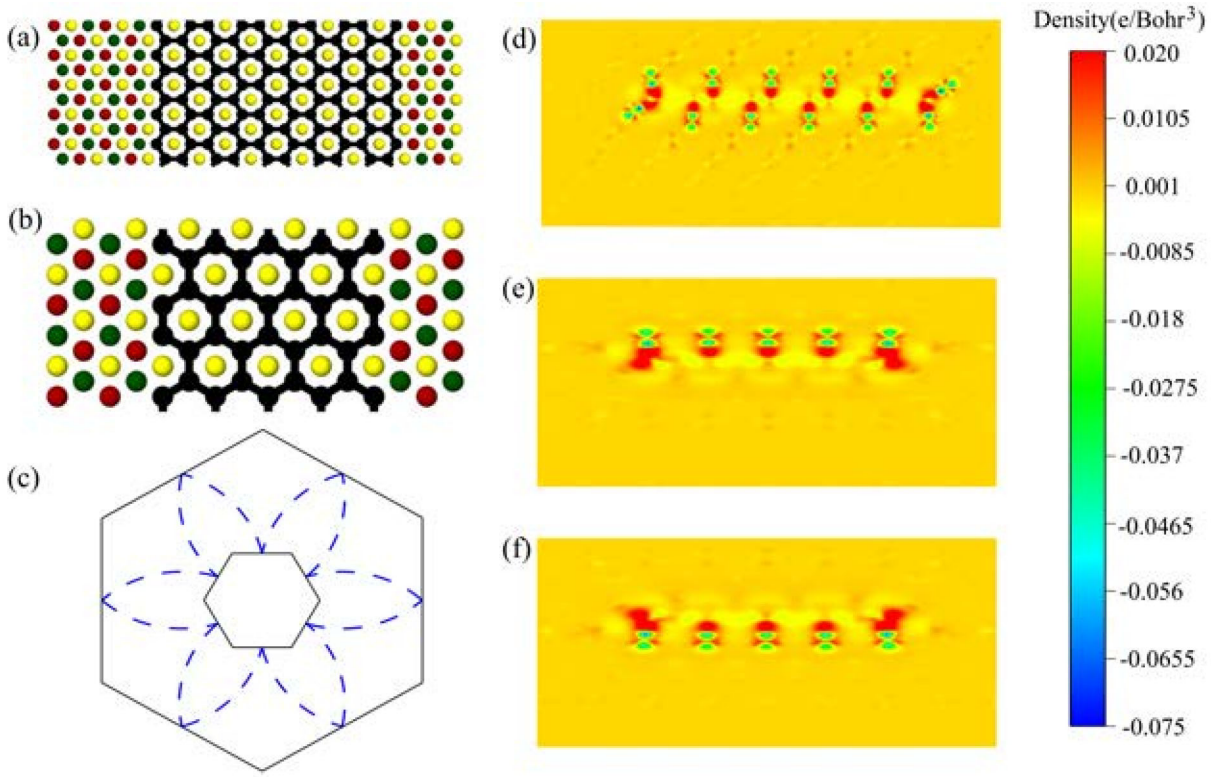

Figure 4.3: a) and b) respectively shows the zigzag and armchair edge graphene particle which are periodic in edge direction. c) shows the Wulff constructions of graphene topfcc structure inside the nickel, the small hexagon has armchair edges and large hexagon has zigzag edges, d)charge density difference on the plane passing through the carbon atom at the zigzag edge. e)-f) Charge density difference on the planes passing through the carbon atoms at the armchair edge. Color code: Ni atoms are green, yellow and red; C atoms are black; first, second and third nearest Ni layer to graphene is green yellow and red, respectively.

DISTRIBUTION A: Distribution approved for public release.

2. Charge density distribution

Apart from energies, DFT calculations provide valence electron-density distributions. The electron density distribution can help in understanding the bonding between the different atoms. These interactions can be better understood by looking at the charge transfer between them. Charge density is redistributed at the interface because of the difference in the chemical potential in the two materials. In nickel-graphene composite, the charge has been transferred from graphene to nickel to fill the d-orbitals of nickel. This charge transfer creates partial charges which generate attractive Coulomb force. The difference between the charge densities of the composite compared to the distorted nickel without graphene and the graphene monolayer helps in understanding the effect of charge transfer and how the interaction changes for different graphene structures. We calculated charge density difference as $\rho_i = \rho_{comp} - \rho_{Ni_{deform}} - \rho_{Gr}$ where ρ_{comp}, $\rho_{Ni_{deform}}$ and ρ_{Gr} are the charge densities of composite, deformed nickel metal without graphene and isolated graphene monolayer.

Figures 4.2 (a)-(d), shows the contour plots of charge density difference for different cases. In the topfcc case, as expected, both (top and bottom) layers interact with graphene. In unsymmetrical cases in figures 4.2(b) and (c), only one of the layers interacts and the other layer does not interact. For example, in the case of tophcp + hcpfcc, tophcp has positive binding energy at this level of separation compared to hcpfcc (as shown in figure 4.1(e)). Negative binding energy has moved the bottom nickel layers far from graphene compared to the top layer.

The charge transfer and distance between top nickel layer and graphene depends on the position of graphene inside the nickel. Depending on this, there are two kinds of interaction between nickel top layer and graphene, which are, chemisorption and physisorption [99]. Chemisorption happens between nickel layers and graphene when inter-atomic distance is around 2.1 Å [99]. As shown in figure 4.5 (e) in the Appendix, for topfcc, bridgehcp, tophcp and bridgetop interfaces in composite, interatomic distance is around 2.1 Å which implies that graphene is chemisorbed. Graphene chemisorbs implies that it forms donation/back-donation bonding with nickel. To correctly simulate the composite empirical potential should be able to simulate both chemisorption and physisorption of graphene over nickel depending on the position and distance of graphene over the nickel layer. In many studies, Lennard-Jones potential has been used to simulate the interaction between nickel and carbon atoms. The ϵ and σ parameters for the Lennard-Jones potential used in the simulations have been either found by using Lorentz-Berthelot mixing rules [73, 77] or by optimizing these parameters for nickel graphene interface (equilibrium distance and energy) in the case of composites [13, 88]. As shown in figure 4.5 (b) in the Appendix, both the set of parameters does not give topfcc as the stable structure of graphene inside the nickel. One of the reasons that L-J potential is not able to simulate the behavior of the composite is the charge transfer. The charge transfer affects the attractive long-range dispersion term (r^{-6}) of the potential. To resolve this drawback, a damping function needs to be multiplied in r^{-6} term of L-J potential [100]. This concludes that it is erroneous to assume that Lennard-Jones potential can correctly simulate the interaction between graphene and nickel in their composites.

3. Topfcc structure and graphene edge effect

Figure 4.2(e) shows the charge density difference integrated over the x-y plane. The dashed dotted line is the position of graphene, and it clearly shows that charge has been transferred from graphene

DISTRIBUTION A: Distribution approved for public release.

Table 4.1: Quantification of distortion caused by graphene edge in nickel.

	Armchair	Zigzag
Free energy of super cell, E_{comp} (eV)[a]	-1100.5874	-1119.6133
Free energy of nickel layers, $E_{Ni_{bulk}}$ (eV)[b]	-940.44675	-940.44675
Free energy of graphene particle, E_{Gr} (eV)	-169.5589	-194.4150
Number of carbon atom, n_{Catom}	18	20
Total deformation energy, E_d (eV)[c]	9.41823	15.24844
Deformation energy by edge of graphene particle, $E_{d_{edge}}$ (eV) [d]	6.91677	12.46904
Deformation energy per unit edge length (eV/Å)	0.8022	2.5048

[a] Nickel Graphene composite after relaxation

[b] Without any distortion by graphene

[c] $E_d = E_{comp} - E_{Ni_{bulk}} - E_{Gr}$

[d] $E_{d_{edge}} = E_d - (n_{Catom}) \times (E_{d_{topfcc}})$ where n_{Catom} is number of carbon atom in supercell, $E_{d_{topfcc}}$(= 0.13897 eV) is deformation energy per carbon atom in topfcc case when graphene is inserted as monolayer.

to nickel. In addition, it can be seen that the effect of graphene in topfcc drops sharply after the three layers of nickel(around 7 Å) compared to bridgefcc + bridgetop structure. This implies that the effect of graphene on nickel is short-ranged in topfcc.

During tensile or compression loading, dislocations are impeded by the graphene in the nickel [77, 78]. An increase in pile-up dislocations on graphene increases localized stress concentration on the graphene nickel interface. The high interaction energy of stable topfcc structure (as shown in figure 4.2(f)) increases the capacity of accommodating dislocation without sliding. This indicates that the single crystal nickel graphene composite will show strong strain hardening [101, 102] which implies the graphene monolayer can simultaneously increase the strength and the ductility of metal matrix [103].

Graphene particles are easy to manufacture, and we have recently shown that reinforcing graphene flakes into the nickel matrix can significantly improve the mechanical properties of nickel [20]. For graphene particles, edges can play a significant role in determining the mechanical properties. Graphene edges can also act as a source for nucleation of dislocations. Therefore, understanding the interaction between the graphene edge and nickel atoms is a necessary step to understand better the deformation mechanisms behind improving the mechanical properties in metal-graphene composites.

Overall symmetry for graphene is triangular rather than hexagonal for the graphene-nickel interface [104]. But for graphene inside the nickel (in topfcc structure) due to mirror symmetry of nickel atoms along the surface of the graphene sheet, overall symmetry is hexagonal. Deformation energy per unit edge length is calculated in Table 4.1 which shows that armchair edges cause less distortion comparing to zigzag edges inside the nickel. The distortion causes residual shear strain near the edge of the graphene when compared to the case having a graphene layer without edges. Atomic shear strain (of nickel atoms near graphene edge) based on the displacement of nickel atoms for all 12 slip systems in fcc crystal is shown in Table 4.2 and Table 4.3 in the Appendix. The maximum residual atomic shear strain (out of all 12 slip systems) is higher for the zigzag edge comparing to the armchair edge. While mechanical loading residual strains over slip planes in slip direction can initiate slipping and nucleation of dislocations in the planes.

DISTRIBUTION A: Distribution approved for public release.

Armchair edges having more carbon atom per unit edge length compare to the zigzag edge is expected to cause more distortion in nickel sideways atoms, but the formation of the triple bond at armchair edge [91] decreases the interaction between nickel and carbon atoms. The charge density difference plots in figure 4.3(d)-(f) shows that zigzag edge interacts more with the sideways atoms compare to the armchair edge. For arbitrary orientation, χ edge energy per unit length is given by following equation [91]:

$\gamma(\chi) = 2\gamma_A \sin(\chi) + 2\gamma_Z \sin(30° - \chi)$

where γ_A is armchair edge energy and γ_Z is zigzag edge energy. Using the above equation in polar coordinates we obtained Wulff diagram as shown in figure 4.3(c). Wulff diagram shows that hexagon having all edges as armchair is the most stable shape inside the nickel.

4.5 Conclusion

Layered metal-graphene composites are the new class of composites utilizing the excellent mechanical properties and 2D structure of graphene to improve the properties of regular metals. Nickel-graphene composite has been fabricated and had shown the improvement. In this work, we studied the graphene structure in the nickel-graphene composite by the means of the DFT calculations using local (spin) density approximation. The most stable structure of graphene on Ni(111) is bridgetop, but inside the nickel matrix, the most stable structure of graphene is topfcc. The topfcc position of graphene has maximum adhesion and minimum distortion compare to other positions of graphene inside the nickel matrix. Owing to the open d-orbital of nickel, electrons transfer from graphene to nickel matrix. The charge transfer depends on the position of graphene, and it cannot be captured by the Lennard-Jones potential. The distortion energy of the zigzag edge is higher than the armchair edge, which implies that for the composites the mechanical properties will depend on the type of graphene edge. It is found that a hexagonal graphene particle having all armchair edge will have the least distortion energy per unit length of the parameter.

Apart from thermodynamics, the graphene structure will also depend on the growth kinetics during the fabrication. The growth kinetics determines the shape of graphene particles on Ni(111) surfaces [104] and can affect the shape in the nickel-graphene composite, also. In the future, a model of graphene and nickel growth has to be used to investigate the growth kinetics. Effect on nickel atom deposition after graphene deposition (which is already over nickel atoms) during the fabrication process has to be investigated using growth kinetics. The effect of graphene defects and graphene grain boundaries on the composites are still unknown and will be reported in future work. Also, the results here indicate that there is a need for empirical force field which can capture the position dependent interaction of graphene with nickel.

Acknowledgement

This material is based upon work supported by the Air Force Office of Scientific Research under award number FA9550-18-1-0169.

DISTRIBUTION A: Distribution approved for public release.

4.6 Appendix

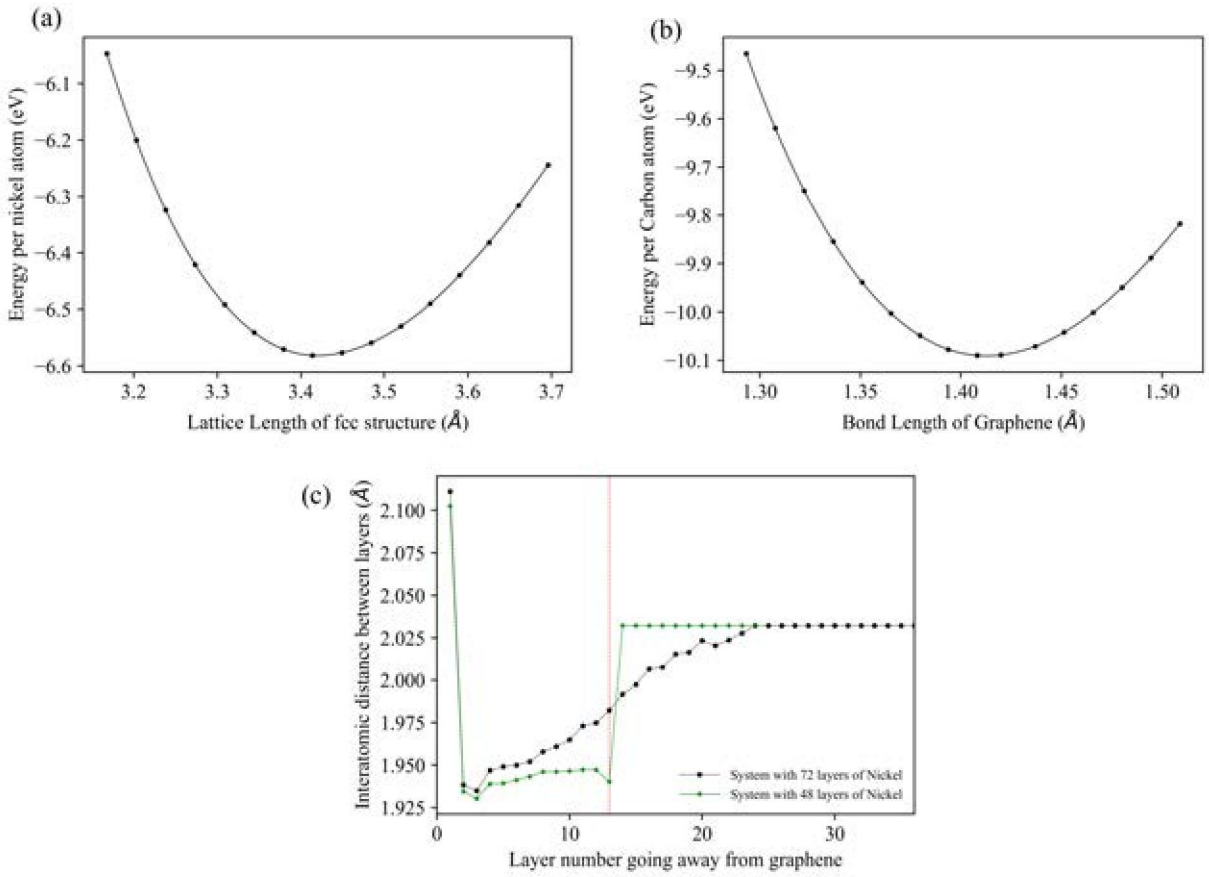

Figure 4.4: (a) shows the energy variation with nickel lattice length using DFT LDA. It gives 3.41 Å oppose to experimentally measured 3.52 Å as lattice constant for the nickel. (b) shows the energy variation with the bond length of graphene. It gives 1.42 Å as the bond length of graphene which has been also reported in experiments. (c) shows the inter-atomic distance of nickel layers for two systems having 48 and 72 layers of nickel. The maximum difference in the inter-atomic layer distances is less than 1.25 % of the inter-atomic layer distance.

DISTRIBUTION A: Distribution approved for public release.

Table 4.2: Components of Atomic Green-Lagrangian strain tensor on slip planes in the slip directions for the atoms near the armchair edge. The numbering of atoms is shown in fig. 4.6 (a)

Slip planes →	[1,1,-1]			[1,1,1]			[1,-1,1]			[1,-1,-1]		
Slip direction →												
———	[1,0,1]	[1,-1,0]	[0,1,1]	[1,-1,0]	[1,0,-1]	[0,-1,1]	[1,0,-1]	[1,1,0]	[0,1,1]	[1,1,0]	[1,0,1]	[0,-1,1]
Atom number ↓												
1	0.437	0.278	0.159	0.794	0.407	0.387	0.548	0.824	0.276	0.248	0.518	0.270
2	0.415	0.273	0.141	0.852	0.406	0.446	0.579	0.861	0.282	0.264	0.570	0.306
3	0.418	0.281	0.137	0.854	0.421	0.433	0.575	0.851	0.276	0.284	0.579	0.294
4	0.416	0.154	0.262	0.513	0.252	0.261	0.653	0.677	0.024	-0.010	0.489	0.499
5	0.397	0.201	0.197	0.782	0.393	0.389	0.551	0.787	0.236	0.196	0.547	0.351
6	0.423	0.252	0.171	0.759	0.382	0.377	0.640	0.800	0.160	0.211	0.599	0.388
7	0.410	0.255	0.155	0.759	0.390	0.369	0.554	0.779	0.225	0.235	0.533	0.298
8	0.401	0.252	0.148	0.771	0.383	0.388	0.500	0.789	0.289	0.235	0.483	0.248
9	0.413	0.258	0.155	0.774	0.384	0.390	0.474	0.803	0.329	0.230	0.445	0.216
10	0.434	0.282	0.152	0.899	0.440	0.459	0.517	0.894	0.377	0.288	0.523	0.235
11	0.426	0.271	0.155	0.801	0.388	0.413	0.535	0.839	0.304	0.233	0.497	0.264
12	0.416	0.241	0.175	0.689	0.338	0.351	0.437	0.767	0.330	0.163	0.358	0.195
13	0.360	0.230	0.130	0.674	0.329	0.345	0.458	0.705	0.247	0.199	0.427	0.228
14	0.396	0.246	0.149	0.727	0.355	0.372	0.473	0.768	0.295	0.205	0.432	0.227
15	0.404	0.253	0.151	0.760	0.376	0.384	0.465	0.788	0.323	0.225	0.437	0.212
16	0.411	0.256	0.155	0.815	0.396	0.419	0.500	0.830	0.330	0.241	0.485	0.244
17	0.413	0.254	0.159	0.754	0.376	0.378	0.477	0.791	0.314	0.217	0.440	0.223
18	0.432	0.265	0.167	0.834	0.413	0.421	0.455	0.853	0.398	0.247	0.436	0.190
Average	0.412	0.250	0.162	0.767	0.379	0.388	0.522	0.800	0.279	0.217	0.489	0.271

Table 4.3: Components of Atomic Green-Lagrangian strain tensor on slip planes along the slip directions for the atoms near the zigzag edge. The numbering of atoms is shown in fig. 4.6 (b)

Slip planes →	[1,1,-1]			[1,1,1]			[1,-1,1]			[1,-1,-1]		
Slip direction →												
———	[1,0,1]	[1,-1,0]	[0,1,1]	[1,-1,0]	[1,0,-1]	[0,-1,1]	[1,0,-1]	[1,1,0]	[0,1,1]	[1,1,0]	[1,0,1]	[0,-1,1]
Atom number ↓												
1	1.343	0.000	1.343	0.000	1.441	-1.441	0.117	-0.098	-0.215	0.098	0.215	0.117
2	0.644	0.000	0.644	0.000	0.827	-0.827	0.073	-0.184	-0.256	0.184	0.256	0.073
3	2.455	0.000	2.455	0.000	1.287	-1.287	0.439	1.168	0.729	-1.168	-0.729	0.439
4	1.208	0.000	1.208	0.000	0.872	-0.872	0.043	0.336	0.292	-0.336	-0.292	0.043
5	0.983	0.000	0.983	0.000	0.901	-0.901	0.194	0.081	-0.112	-0.081	0.112	0.194
6	0.803	0.000	0.803	0.000	0.504	-0.504	0.158	0.300	0.142	-0.300	-0.142	0.158
7	1.339	0.000	1.339	0.000	1.337	-1.337	0.140	0.002	-0.138	-0.002	0.138	0.140
8	1.052	0.000	1.052	0.000	0.729	-0.729	0.275	0.323	0.048	-0.323	-0.048	0.275
9	1.050	0.000	1.050	0.000	0.902	-0.902	0.238	0.148	-0.090	-0.148	0.090	0.238
10	1.398	0.000	1.398	0.000	0.984	-0.984	0.300	0.415	0.115	-0.415	-0.115	0.300
11	0.635	0.000	0.635	0.000	0.551	-0.551	0.202	0.084	-0.118	-0.084	0.118	0.202
12	3.014	0.000	3.014	0.000	2.119	-2.119	0.476	0.895	0.419	-0.895	-0.419	0.476
13	1.101	0.000	1.101	0.000	0.628	-0.628	0.298	0.473	0.175	-0.473	-0.175	0.298
14	1.621	0.000	1.621	0.000	1.065	-1.065	0.316	0.556	0.239	-0.556	-0.239	0.316
15	1.240	0.000	1.240	0.000	0.990	-0.990	0.255	0.250	-0.005	-0.250	0.005	0.255
16	1.297	0.000	1.297	0.000	0.629	-0.629	0.319	0.668	0.350	-0.668	-0.350	0.319
17	1.294	0.000	1.294	0.000	0.627	-0.627	0.321	0.667	0.346	-0.667	-0.346	0.321
18	1.262	0.000	1.262	0.000	1.000	-1.000	0.261	0.262	0.001	-0.262	-0.001	0.261
Average	1.319	0.000	1.319	0.000	0.966	-0.966	0.246	0.353	0.107	-0.353	-0.107	0.246

DISTRIBUTION A: Distribution approved for public release.

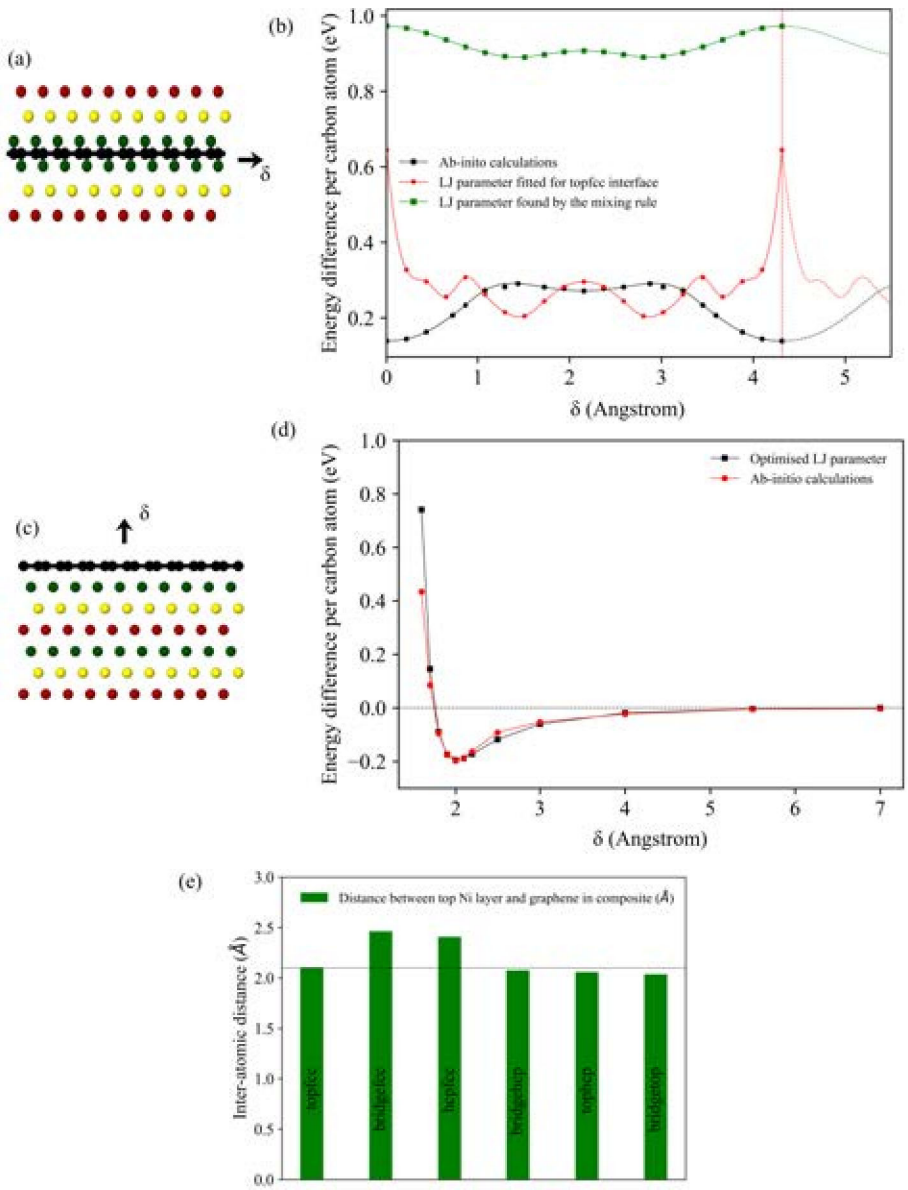

Figure 4.5: (a) shows the movement of graphene in the plane, (b) shows the corresponding distortion energy comparing the ab-initio energy with two sets of LJ parameter. (c) shows the movement of graphene perpendicular to nickel plane in topfcc structure. (d) plots the the optimized LJ parameter for the topfcc interface which has been used in (c). (e) shows the interatomic distance between the Ni layer and graphene for ab-initio calculation , the dashed line is at 2.1 Angstrom. Lennard Jone potential has been used for Ni-C interaction, for Ni-Ni interaction 2NN meam potential and for C-C interaction AIREBO has been used.

DISTRIBUTION A: Distribution approved for public release.

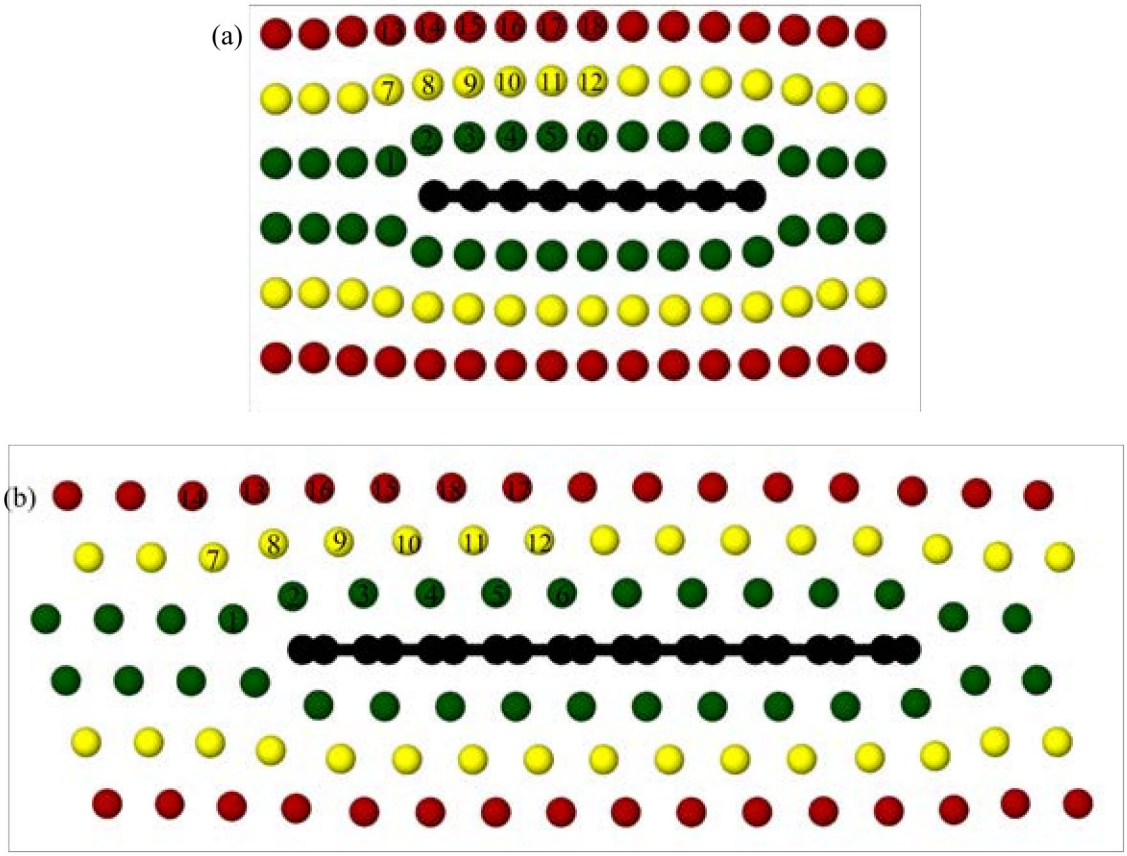

Figure 4.6: (a) shows the cross section view of armchair edge. (b) shows the cross section view of zigzag edge.

DISTRIBUTION A: Distribution approved for public release.

V- Effect of Interface Configuration on the Mechanical Properties and Dislocation Mechanisms in Metal Graphene Composites

5.1 Abstract

The effect of graphene-metal interface on dislocation gliding and generation is a key element in understanding the mechanical properties of graphene metal-matrix composites. Graphene-metal interfaces can impede the propagation of dislocations, which enhances the mechanical properties, particularly the strength. On the other hand, the presence of such interfaces can also act as the dislocation source in the metal matrix, which can significantly weaken the material properties. This implies that graphene will not always improve the mechanical properties of metals, but alternatively, it can even significantly weaken the properties. Whether graphene acts as a dislocation sink or source primarily depends on the metal-graphene interface and also other pre-existing defects in the matrix. In this paper, we investigate these two opposing effects at the atomistic scale, using Molecular Dynamics (MD) simulations. To study the effect of the interface and to isolate the effects of dislocations from defects, we have reinforced a perfect crystal of nickel with graphene. We found that in the perfect crystal, the graphene in any interface structure acts as a defect and weakens the metal matrix. Each interface structure in the composite has a different effect on the system, and the topfcc structure of the graphene-nickel interface results in the least strength reduction. For graphene particles, apart from the interface, edges can also act as a dislocation nucleation site. We investigated the two edges -Zigzag and Armchair edge of graphene- and found that both the edges cause decrease in mechanical strength. Experimental results (always reported an increase in mechanical strength) are in contradiction to what we found in this work. The reason for this contradiction is that in the real metallic system, defects are already present, and those acts as a dislocation source more readily than the graphene. To verify this, we studied the metallic systems having defects in nickel crystal and the graphene is reinforced. Through these studies, we investigate the conditions in which the strengthening mechanisms overcome the weakening mechanisms, and improvement is observed in the mechanical properties, similar to some of the reported experimental works. Our results shed light on the deformation mechanisms in metal-graphene composites and can be used as a guide in designing and fabricating more efficient metal-matrix composites.

DISTRIBUTION A: Distribution approved for public release.

5.2 Introduction

Mechanical properties are highly affected by the behavior of dislocations in material systems. Lattice defects like twin boundaries, grain boundaries, and interfaces in nanolayered composites dictate the behavior of dislocations in a material system. In recent years [7, 9, 13, 74–76], graphene's 2D structure and excellent mechanical properties (Young's modulus $\simeq$ 1.0 terapascal, breaking strength $\simeq 42Nm^{-1}$)[1] have been utilized to fabricate layered metal graphene reinforced composites. The layered metal graphene composites have shown significant improvement in mechanical properties. The superior mechanical properties displayed are due to the graphene's ability to pin and annihilate dislocations that attempt to pass through the metal graphene interface [7, 9, 13, 20, 74–76]. Kim et al. [13] observed this dislocation impeding mechanism in-situ with TEM of nanopillars composed of mostly single grain or the double grained metal matrix. Our group has also shown that having graphene flakes with specific concentrations increases the strength of polycrystalline nickel, as a result of this same mechanism [20]. In the case of perfect crystal the metal graphene interface can also act as dislocation nucleating site during the mechanical loading [105]. The role of the dislocation impeding mechanism and dislocation nucleation at interface suggests that the interfacial properties like interface energy, adhesion strength and lattice geometry could have a determinate effect on the nanocomposites [26, 106, 107].

In the case of nickel graphene composites, experiments found that the preferred plane of nickel crystal in composites with graphene is (111) [26, 79, 80]. Based on the position of graphene on Ni(111) plane, the relative stability of six different stacking structures[2] has been studied using DFT [82, 86]. Although there are six different graphene stacking structures of the interface on the surface, due to two interfacial interactions on the inside of the crystal, there are only four unique structures when graphene is inside the nickel [26]. Bridgetop structure is the most stable on the Ni(111) surface, but our results show that when graphene is inside the nickel matrix, topfcc + topfcc structure is the most stable [26]. Given that the stability of the interfacial interaction varies with the stacking type, the effect of this variability on the nickel graphene's mechanical properties are yet to be studied.

In practice, fabrication techniques for both the graphene and composite limit the graphene in the composite to be particles with a finite size [9, 13, 20, 108, 109]. In polycrystalline nickel, graphene particles of finite sizes improves the mechanical properties [20] but such particles consistently underperform when compared with continuous layered graphene [13, 20]. One reason for this underperformance can be the inclusion of graphene edges that are similar to dislocation lines in geometry and can act as the dislocation nucleation site in the crystal [110]. Our ab-initio calculations have shown that the armchair edge of graphene is more stable and creates less distortion (compare to zigzag edge) inside the bulk nickel [26]. However, the effect of graphene edge during mechanical loading is still unexplored.

Measurement and observation of mechanisms that result from interface properties are challenging to be performed experimentally, but can be estimated with relative ease using atomistic simulations. Atomistic simulations also provide a way to isolate mechanisms to study in ways that would otherwise be impossible in the experiments. *Ab-initio* calculations provide the most accurate information at the atomistic scale but due to size limitation (or the number of atoms), studying the mechanical behavior or study of dislocation kinetics during the loading is not possible.

[2] In this work, the graphene stacking structure refers to the position of graphene relative to the nickel layers.

DISTRIBUTION A: Distribution approved for public release.

Molecular Dynamics, however, can simulate larger systems and has been used extensively in uncovering mechanisms associated with mechanical properties achieved by metal graphene composites [111–113].

Molecular dynamic simulations have shown that the pinning mechanism depends on the characteristics of the interface such as strong interfacial bonding energy, graphene's high bending stiffness, and a misalignment of slip planes across the interface [13, 20, 78, 88, 103, 114]. Atomistic simulations have been used to study the failure mechanisms, radiation-resistance and properties like stress intensity factor of cracks in the metal composites [7, 13, 70, 73–75, 78, 103, 115].

In this work, we employ molecular dynamics to determine the effect of different stacking structures of graphene and its edges on the mechanical properties. The dislocation nucleation and dislocation mobility have a determinate effect on mechanical properties. Many of the molecular dynamics simulation studies in this field utilize Lennard-Jones (LJ) potential or modified embedded-atom method (MEAM) potentials for Ni-C atom interaction [13, 20, 73, 77, 88]. For the nickel graphene interface, we have recently shown that the interaction depends on the structure of the graphene, and the LJ potential cannot capture this interaction [26]. MEAM potential parameters used for studying carbon nanotube reinforced nickel composites [116] and nanocrystalline nickel graphene composites [20] are used in this work. In summary, our results answer an unexplored question of "When and How the graphene sheets, as reinforcement, improves or weakens the mechanical properties of metals? ". This can be used as a unique guide in designing and fabricating more efficient metal-matrix composites.

5.3 Methods

A schematic of the graphene-metal composites used in this study are shown in Fig. 5.1. Both cubic and pillar single crystals of nickel with different sizes are considered in our studies. As it will be discussed in the following sections, we have considered both systems with no defects, and also some systems with a finite number of defects, randomly distributed in the geometry (see Fig. 5.1(b)). The Z-axis of the simulation box (the cylinder axis for the pillar) is perpendicular to the graphene and Ni(111) plane. Two sizes are considered for the cubes, in which the small cube has cell dimensions of 99.56 x 94.84 x 103.65 $Å^3$ and the larger one has cell dimensions of 251.39 x 250.044 x 249.97 $Å^3$. The nanopillar has a length of 201.2 Å with a diameter of 99.5 Å. For all systems the lattice directions where aligned with the axis as follows X-axis $[1\bar{1}0]$, Y-axis $[11\bar{2}]$, and Z-axis [111] (see Fig. 5.1 for reference).

DISTRIBUTION A: Distribution approved for public release.

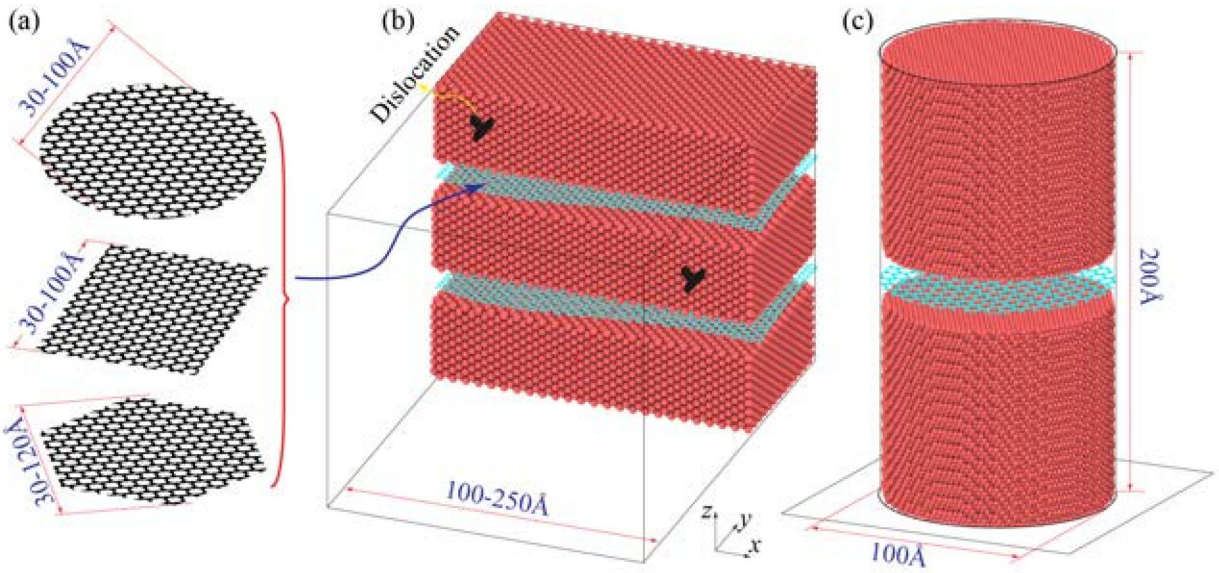

Figure 5.1: (a) Both graphene sheets, which cover all the matrix area, and also graphene particles or flakes with different shapes and sizes (which partially cover the matrix area) are considered in this work. (b, c) Both cubic systems and pillars are studied in this work. Besides defect-free single crystals, we also study the deformation mechanisms in systems with a random distributions of dislocations in the material.

Mono-layer graphene particles were used having dimensions ranging from 30×30 Å^2 to 120×120 Å^2, as shown in Fig. 5.1(a). Different arrangements have been considered for the graphene sheets or particles. In one case we consider the graphene which covers all the cross section of the matrix (which in practice is an infinite span in the cubic system with periodic boundary conditions). We refer this case as graphene sheets. In other cases, we consider graphene with different shapes as shown in Fig. 5.1(a) to partially covering the cross section of the matrix. In the following, we refer the graphene with edges as graphene flakes.

Both the graphene sheets and flakes can also be moved in plane, to obtain different interface stackings. In this work, we study the topfcc (topfcc + topfcc), bridgehcp (bridgehcp + bridgehcp), hcpfcc + topfcc, and hcpfcc + bridgetop interface stacking structures. See [26] for more details about the interface stacking. Various layer spacing for the monolayer graphene has been simulated to further explore the underlying mechanisms behind the interface structures' effects. In the small cube the average spacing for the 1, 2, 3, and 4 layers are 103.76, 55.85, 37.56, and 24.39 Å respectively. For the nanopillar the average spacing for the 1, 2, 3, and 7 layers are 201.2, 100, 67.07, and 30.48 Å respectively.

Molecular Dynamics (MD) simulations are carried out using time integration on Noose-Hoover style non-Hamiltonian equations of motion. These equations update the position and velocity of each atom during discrete time steps using canonical (NVT) and isothermal-isobaric (NPT) ensembles[66, 67]. Periodic boundary conditions in x, y, and z were given to the cubes to simulate an infinitely large bulk crystal. For the nanopillar, the periodic boundary condition is only applied along the z-axis, while fixed boundaries are used in x and y directions to have the surface of the cylinder exposed to the vacuum. A Modified Embedded Atom Method (MEAM) potential parameter used for studying carbon nanotube reinforced nickel composites [116] and nanocrystalline nickel graphene composites [20] has been used in this work. The Large-scale Atomic/Molecular Massively

DISTRIBUTION A: Distribution approved for public release.

Parallel Simulator (LAMMPS) is used to carry out all MD simulations in this work[54].

Energy minimization is done at the start of simulations to find the initial configuration of the composite or crystal. Minimization of total energy is done as a function of the Nth atom's coordinate. The position of atoms are iteratively adjusted until the energy change becomes less than 1e-10. Next, the system is equilibrated at a temperature of 300 K for 30 ps with the NPT ensemble using an oscillation dampening value of 0.2. Finally, the crystal is compressed by decreasing the cell length to 80-85% of its original length along the Ni[111] direction with NVT. The fast and slow strain rates used for this process are $10^{10}\ s^{-1}$ & $10^{9}\ s^{-1}$ respectively. The value of stress, along with the change in cell dimensions for strain, has been extracted to plot stress-strain graphs. The Open Visualization Tool (OVITO)[55] is used for visualization. The Dislocation Extraction Algorithm (DXA)[117], along with the centrosymmetry parameter, has been used to identify dislocations. In this work, the atoms with $centrosymmetry > 2$ are shown(in red), and corresponding dislocation lines calculated from DXA(in yellow) are superimposed in the images unless otherwise stated.

5.4 Results and Discussion

Initiation and propagation of dislocations play a prominent role in the deformation mechanisms at the atomistic scale, and consequently have a significant influence on the mechanical performance of nanocomposites [110, 118, 119]. In layered composites, interface plays the most significant role in determining the dislocation nucleation and kinetics [119]. As the first case to study, we consider a single crystalline cubic system with 1 to 4 layers of graphene sheets subjected to a compressive load. Initiation and propagation of dislocations in such a system without graphene is compared against systems with three layers of graphene with different configurations in figure 5.2. As shown in figure 5.2 (a) the yield strength of nickel crystal changes with the presence of the metal-graphene interface, dropping by almost 22 percent. The decrease in yield strength is due to a difference in dislocation nucleation mode, that occurs with even one layer of graphene. In the perfect crystal, dislocations are formed due to the homogeneous nucleation, while in the reinforced crystals, dislocations are formed due to the heterogeneous nucleation[110, 120–122]. Heterogeneous nucleation of dislocation requires a lower stress in comparison to that required for homogeneous nucleation [110, 123]. As shown in figure 5.3 and figure 5.2, dislocations nucleate at higher stress in graphene free crystal. The early dislocation nucleation in the reinforced crystal compared to perfect crystal is clearly seen in figure 5.2 (c)-(f) and figure 5.3. This phenomenon is the reason behind the observed reduction in strength in reinforced crystals [124]. These results are of significant importance since they imply that adding graphene can be a source of dislocations, and can significantly weaken the material's strength. A result that contradicts with the well-known idea that graphene can always improve the mechanical properties of metals, when it is used as a reinforcement. These results raises the necessity of performing a systematic study on the conditions in which graphene improves the mechanical properties versus the conditions for which graphene can activate the dislocation nucleation and weaken the strength.

DISTRIBUTION A: Distribution approved for public release.

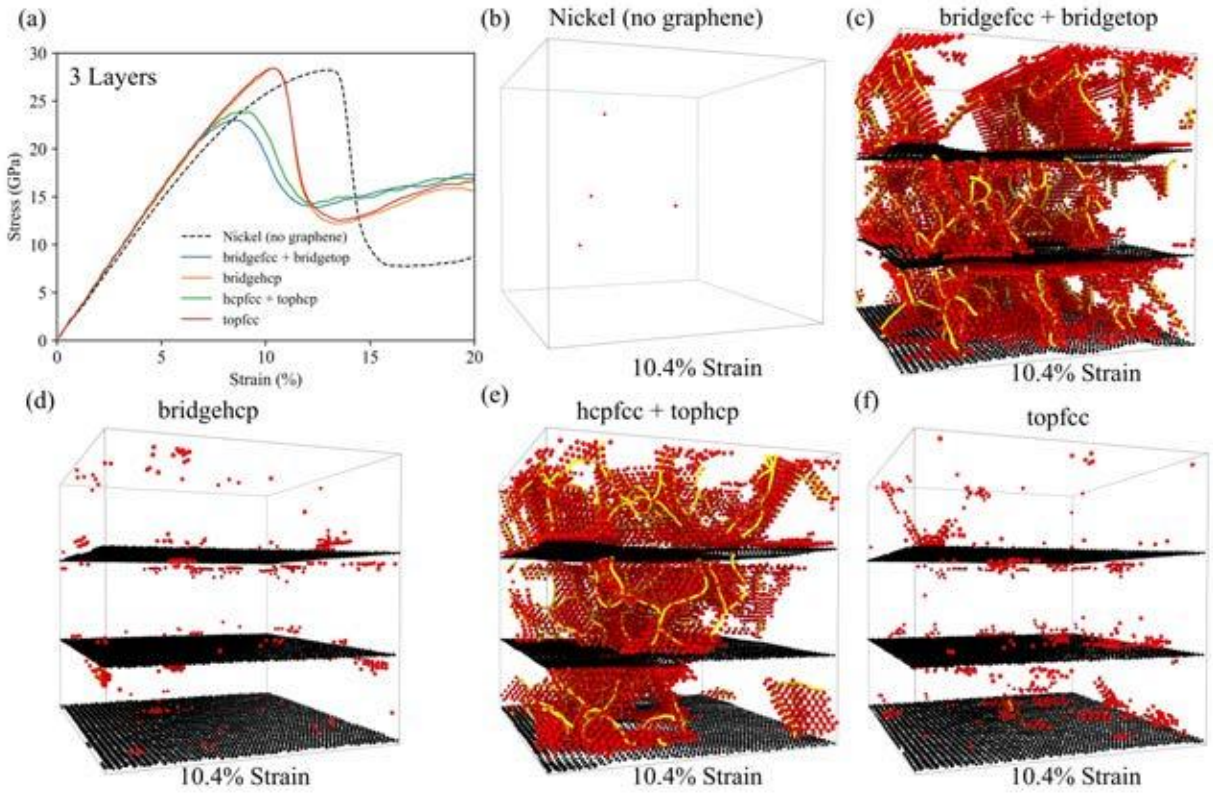

Figure 5.2: (a) Compares the compressive stress-strain curves of the crystal without graphene to the crystal with three layers of graphene in each of the four stacking structures. (b)-(f) Correspond with the state of dislocations at 10.4 % for nickel without graphene, bridgefcc + bridgetop, bridgehcp, hcpfcc + tophcp and topfcc, respectively. All the stacking structures have nucleated dislocation while the graphene free crystal shows no signs of dislocations. Note that that the topfcc and bridgehcp structures nucleate dislocation much later than the other structures, indicating that each stacking structure has a distinct role in the yielding of the composite crystal

As shown in figures 5.3 (a) and (c), yield strength of the reinforced crystal decreases, but flow stress of the reinforced crystal have increased in comparison to the perfect crystal. The behavior of dislocation density versus strain plot explains the improvement in the flow stress of the composites. As shown in Figures 5.3 (b) and (d), the dislocations form at lower strains for all the samples with graphene sheets, compared to the sample without graphene. This is in practice the reason behind observing a lower strength for the samples with added graphene sheets. However, at the post-yield regime, dislocation density is increasing monotonically with strain in graphene-free crystal, while in reinforced crystal, it decreases or remains constant. A closer look at this behavior can clarify the reason of having an improvement in the flow stress of samples with graphene sheets.

The flow stress region is defined by the continuous propagation, nucleation, and multiplication of dislocations to flow the material at a constant strain rate. The strain rate $\dot{\gamma}$ on the basis of dislocation theory is [125, 126]:

$$\dot{\gamma} = \rho b \bar{v} \tag{5.9}$$

DISTRIBUTION A: Distribution approved for public release.

where b and $\bar{v}$ are the magnitude of the Burgers vector and dislocation velocity, respectively. For constant strain rate we have:

$$\rho\bar{v} = C \tag{5.10}$$

where C is a constant depending on the strain rate. The dislocation velocity $\bar{v}$ is related to applied shear stress by following [120, 125]:

$$\bar{v} \propto \tau^m \tag{5.11}$$

which implies :

$$\rho\tau^m = K \tag{5.12}$$

where m is the dislocation velocity-stress exponent and K is a constant depending on the strain rate.

At the constant strain rate, according to the Eqs. 5.9, and 5.11 a decrease in dislocation density implies an increase in the required stress to move dislocations. Saying that, the decrease of dislocation densities as observed in Figures 5.3 (b) and (d) is the reason behind observing an improvement in the flow stress of samples with graphene layers as shown on Figures 5.3 (a) and (c).

DISTRIBUTION A: Distribution approved for public release.

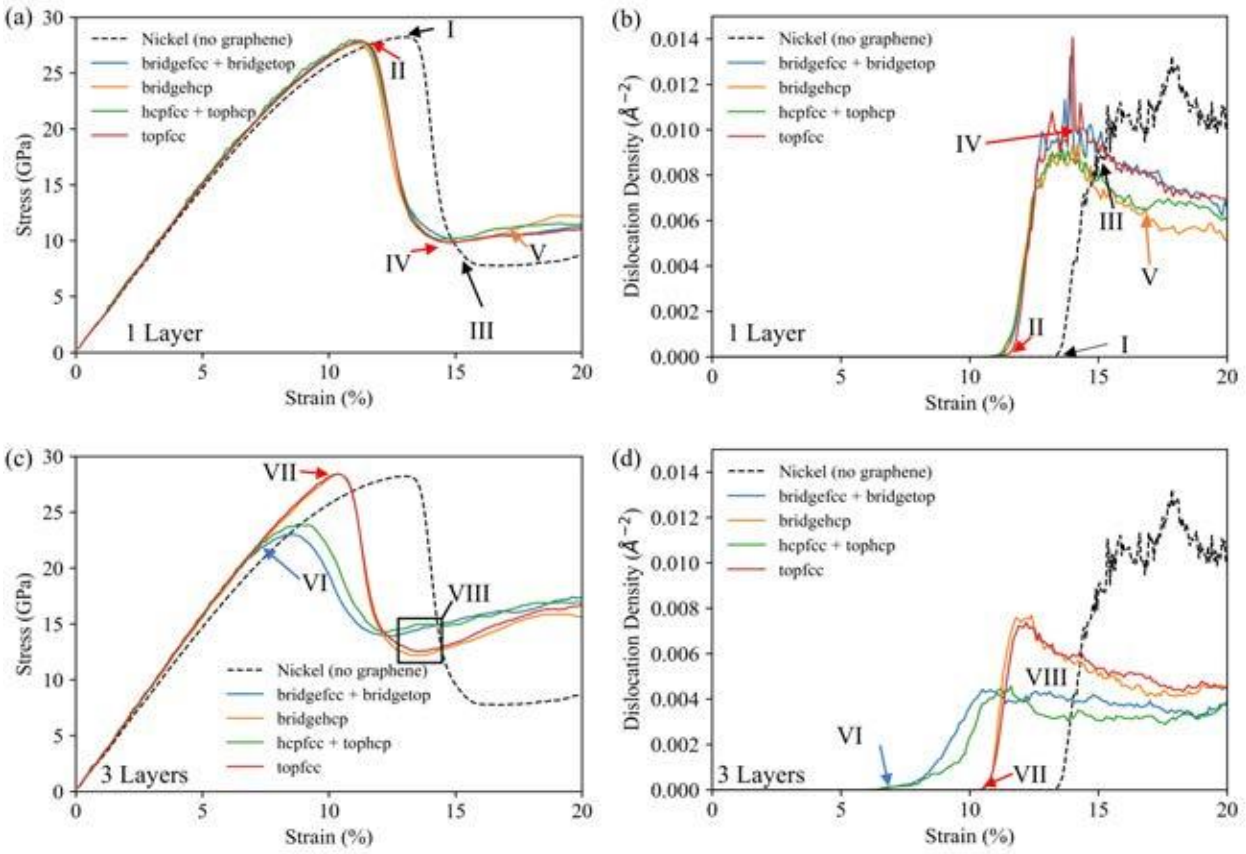

Figure 5.3: (a, b) are curves illustrating the evolution of stress and dislocation density, respectively, for the composite crystal with 1 layer of graphene compared to the crystal without graphene. (c, d) show similar curves but for the crystal with 3 layers of graphene. Point I is the stress and strain required to nucleate dislocations in graphene free crystal. Each stacking structure uniquely reduces the stress required for dislocation nucleation, as shown in points II(topfcc-1 Layer), VI(topfcc-3 Layers), VII(bridgefcc+bridgetop-3 Layers). The flow stress of the crystal is increased by all the stacking structures, as shown by Points III & IV. Region VIII highlights the difference in flow stress between the stacking structures due to lower dislocation density resulting in a delayed softening

The performance of crystals reinforced with different stacking configurations is also affected by the dislocation evolution near the interface. With 1 layer of graphene, dislocations have to travel nearly 100 Å before blocking by the interface can occur. While having additional layers of graphene increases the number of nucleation sites, it is also reducing the distance dislocations must travel to be blocked. These two opposing mechanisms also has to be studied to investigate if the graphene is improving or weakening the mechanical properties. With more layers, dislocations formed earlier with hcpfcc + tophcp and bridgefcc + bridgetop structures, as shown in Figures 5.2(c)-(d) and Figure 5.3(d). We see from Figures 5.3(c)-(d) that the nucleation requires higher stress for bridgehcp and topfcc structure. The reason topfcc and bridgehcp require higher stress is that topfcc and bridgehcp are the stable and metastable structures, respectively, of the four structures inside the nickel crystal. We have recently shown the stability of each configuration using DFT calculations [26]. The interfacial stability delays the dislocations allowing the crystals with topfcc (stable) and bridgehcp (meta-stable) to achieve higher strength. Points VI (bridgefcc + bridgetop) and VII (topfcc) in figure 5.3(c)-(d) show that the nucleation can occur at almost 20% higher stress

DISTRIBUTION A: Distribution approved for public release.

with the different stacking structures.

According to Equation 5.11, dislocation density in flow region is higher in the symmetric structures due to the higher stress at nucleation point[3]. According to Equation 5.9, higher dislocation density implies lower dislocation velocity in crystal reinforced with symmetric structures. After the nucleation point, the lower dislocation velocity requires lower flow stress, which explains the lower flow stress in composites with the symmetric structure in region VIII in Figure 5.3. In the flow stress region, dislocation density either decreases or plateaus with further plastic deformation, as shown in Figure 5.3(c). For the constant strain rate, decreasing or plateauing of dislocation density implies that the velocity of dislocation is increasing or keeps constant.

Having graphene sheets, which cover all the area of the sample, is unrealistic, particularly for larger samples. Graphene flakes are relatively easier to fabricate compared to the large sheets of graphene, and have also shown improvement when reinforced inside the nickel [20]. In the case of using flakes, in addition to the interface, graphene edges also distort the nickel matrix and can act as sources of dislocations. The two typical edges of graphene (zigzag and armchair as shown in the inset of Figure 5.4 (a)) are different. The armchair edge has a higher density of carbon atoms, which leads to the formation of the triple bond [91]. We have shown in our previous work [26] that due to the formation of the triple bond in armchair edge, the distortion caused by the armchair edge is less than the zigzag edge. Continuous graphene strips (as shown in figure 5.5) and the hexagonal flakes (as shown in figure 5.6) having only one kind of edge has been reinforced in the system to study the effect of both edges separately.

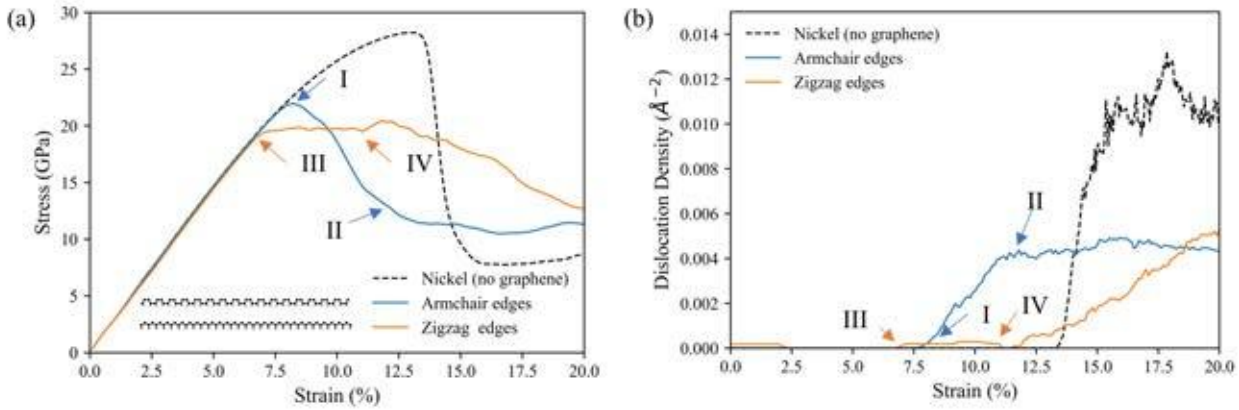

Figure 5.4: (a) Compressive stress-strain curve for the small cube geometry with either the zigzag or armchair edge exposed in the nickel crystal. (b) Corresponding Dislocation density-strain curves. Note that points I and III illustrate that the more stable edge, armchair, results in higher ultimate strength than the zigzag edge based on when dislocations nucleate. Points II and IV are states of dislocations as depicted in figure 5.5.

Due to its relative stability, graphene flake and strip with armchair edge have higher yield stress and ultimate strength compared to the zigzag edge. DFT calculations have showed that there is more distortion near 0 % strain in zigzag edge compare to armchair edge [26]. As shown in Figure 5.4 (b) and 5.6 (b), there is initial non-zero dislocation density in the case of zigzag edges. For the graphene strip with zigzag edge the dislocations are annihilated during the initial phase of loading. The second set of dislocations start at the zigzag edges at around 7 % of strain. As shown in Figure

[3]topfcc and bridgehcp structure together has been called symmetric structure while bridgefcc + bridgetop and hcpfcc + tophcp has been called unsymmetric structure in later part of this section.

DISTRIBUTION A: Distribution approved for public release.

5.4 (b) (near point IV), the second set of dislocations is absorbed by the nickel-graphene interface. Moving dislocations encounter graphene and cause bending in the graphene. Graphene bends in such a way that dislocation density becomes zero. The third set of dislocations starts again from the bended(or deformed) graphene, and this set continuously multiplies itself rather than moving. According to Eqs. (1)-(4), the multiplication increases the number of dislocation and decreases the dislocation velocity, which is directly proportional to the shear stress. Figures 5.4 (a) and (b) show that as the number of dislocations increases in the system, the required flow stress decreases.

The armchair edge at 0 % strain does not have any dislocations. As shown in Figures 5.4 (b) and 5.5 (b), the dislocations start from the armchair edge at the critical stress. With the increase in strain, the dislocation doesn't move like the second set of dislocations in zigzag edge; instead, it multiplies and increases the dislocation density. The dislocation density increases until the rate of multiplication, and the rate of annihilation becomes equal. The sharp increase in dislocation density decreases the flow stress of the crystal reinforced with the graphene having the armchair edge.The result shows that armchair edge may increase the yield strength more than the zigzag edge but may have the lower flow stress. In the system with defects the strength increase and flow stress behavior will depend on the relative position of defects, graphene flakes and its edges.

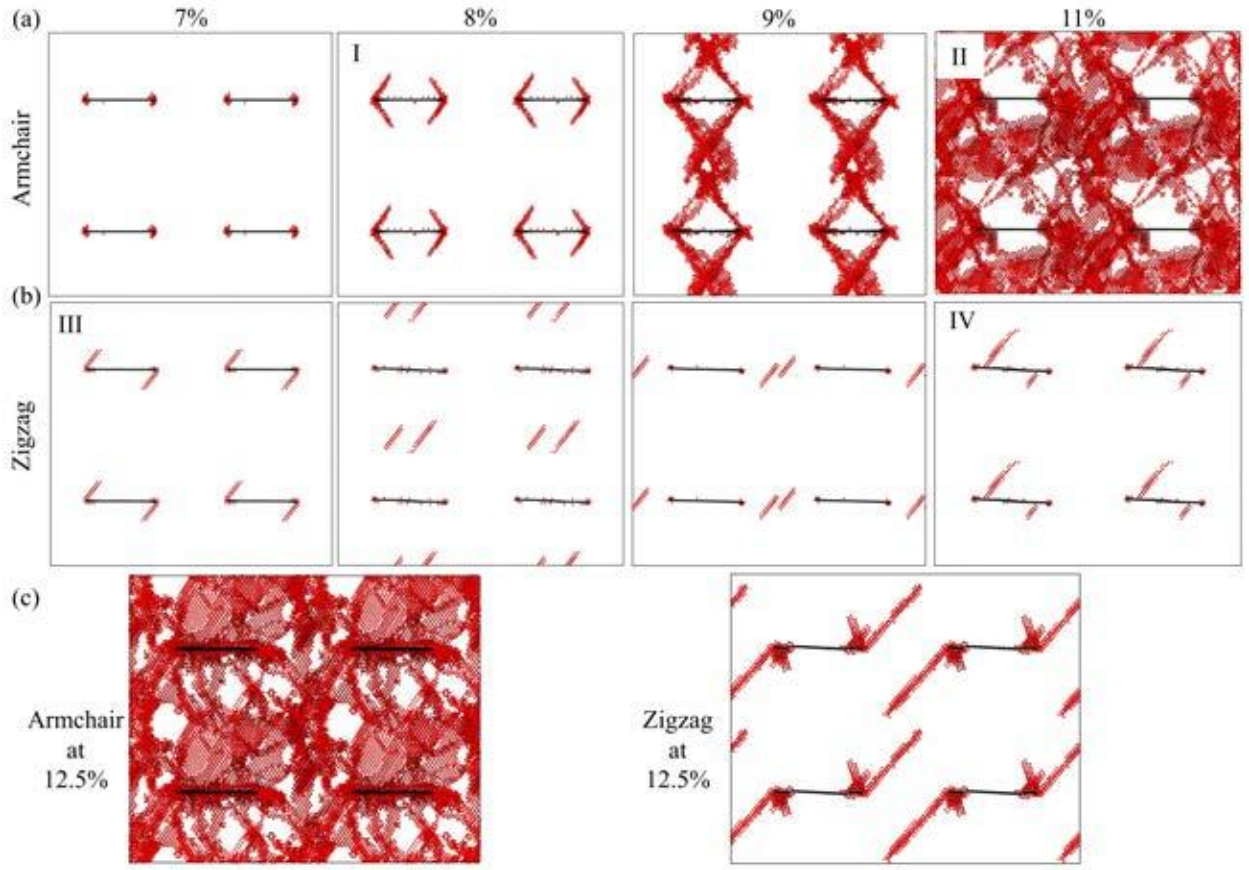

Figure 5.5: (a) Depicts the reinforced crystal with armchair edge graphene at stages of dislocation nucleation (point I), softening, and reaching flow stress (point II). (b) Reinforced crystal with zigzag edge graphene, at stages of dislocation nucleation(point III), hardening (point IV, where the dislocations are blocked by the interface), and softening. Note that points I-IV in (a, b) correspond to figure 5.4. (c) Shows the point at which the crystal with zigzag edges nucleate more dislocations while the armchair edges has saturated the volume with dislocations.

DISTRIBUTION A: Distribution approved for public release.

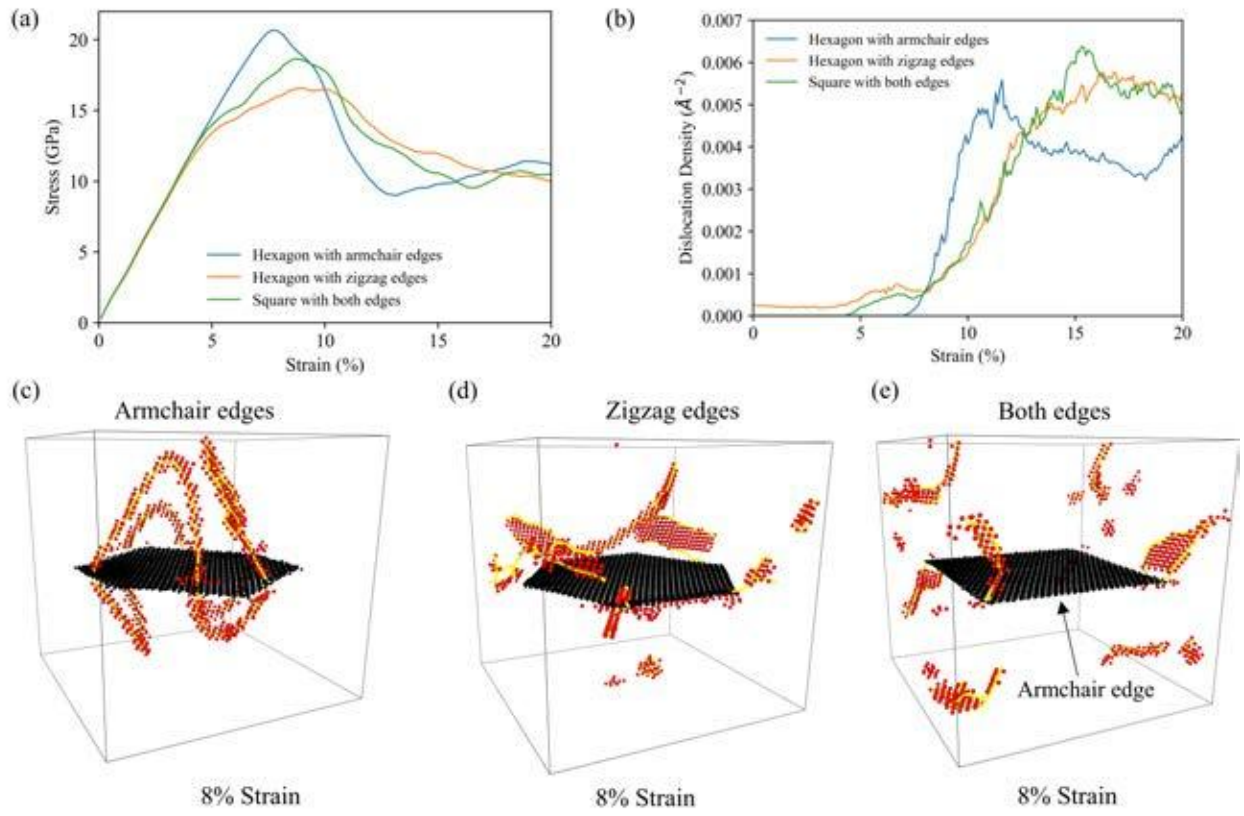

Figure 5.6: (a) Stress-strain curves for the small cube geometry comparing flakes with zigzag edge, armchair edge, or both edges in a 1 and 4 layer composite. Note that the armchair edges achieves the highest strength among the flakes (b) Corresponding dislocation density-strain curves. (c)-(e) State of dislocations at 10 % strain for the flakes with armchair, zigzag, and both edges. Notice how the dislocation morphology's are similar to 5.5 for the armchair and zigzag edges. This illustrates how the dislocation mechanisms are dictated by the zigzag edges in the flakes.

In all the cases studied so far in this work, the strength of the nickel has decreased due to the addition of graphene sheets or flakes in the system. This is contrary to previously reported experimental and computational studies [13, 20, 73, 77, 78, 114] which have shown improvement in the mechanical properties of layered nickel composites reinforced with graphene. The reason behind this contradiction is the presence of pre-existing dislocation nucleation sites which requires less stress to initiate dislocations in comparison to the dislocation nucleation at edge or interface in the system. In other words, our results show that adding graphene sheets or flakes to a defect free metallic crystal will always weaken the strength (although it can improve the flow stress), because by adding graphene we are adding dislocation nucleation site to a defect-free system. Although the added graphene has a potential to block the propagating dislocations, the effect of added dislocation nucleation site dominates the effect of dislocation blocking in this case. However, in reality having a defect-free crystal is rarely possible. Any of the previously reported works which have shown improvement in the strength after adding graphene are considering structures with pre-existing defects. [13, 20, 119]. In molecular dynamics studies, the defects have been present in the form of cracks [73, 78] or grain boundaries [20]. In some other MD simulations of defect-free systems, a large density of dislocations are originating from a nanoindenter head in the system [77, 114]. In

DISTRIBUTION A: Distribution approved for public release.

order to study the systems close to real metallic systems, we consider two cases. once, we introduced defects in the crystals and in the second case we will study a cylindrical system in which an inherent dislocation site in form of the free surface is present.

As the first case, to study how the composite's strength depends on defects, we added randomly located internal defects into the crystal. As shown in Figure 5.7(a), with these pre-existing defects in the nickel matrix, we found that the yield strength improves when adding graphene layers. This can be explained by tracking the dislocations density in the system, as shown in Figure 5.7(b). In defect-free systems adding graphene sheets or flakes was always initiating the dislocations at lower strains (see Figure 5.3(b, d) and Figure 5.4(b)). However, when the system has defects, as shown in 5.7(b), dislocations initiate and start propagating at same strain level in the systems with and without graphene. Tracking the density of dislocations clearly shows that graphene layers are efficiently impeding the dislocations. As shown in 5.7(c-e), graphene sheets are efficiently blocking the spread of dislocations which have mostly initiated form the vicinity of the pre-existing defects in the system.

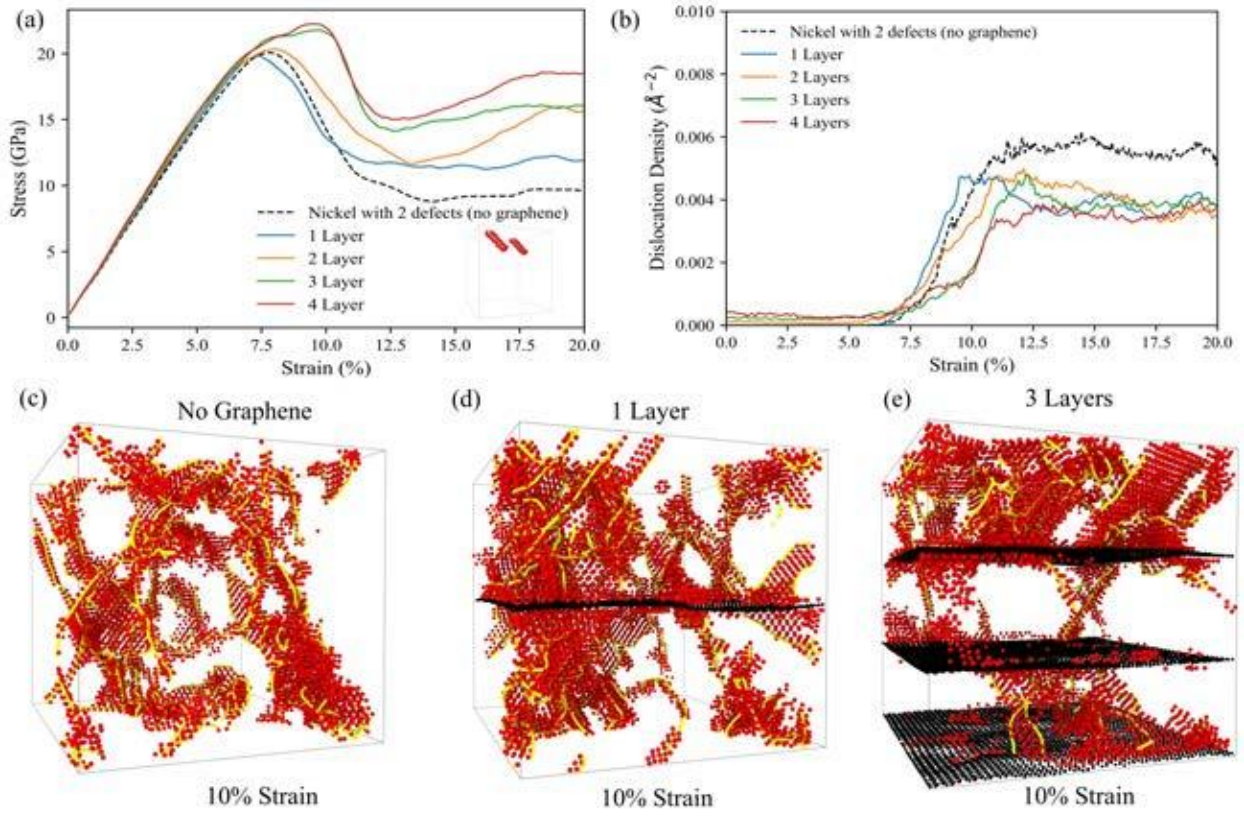

Figure 5.7: (a) Compressive stress-strain curve for the nickel crystal with two defects and nickel graphene composite (with the same arrangement of defects) with increasing number of graphene layers in topfcc structure, (b) Corresponding dislocation density vs. strain curves. (c)-(e) Dislocations at 10 % strain. Note that with the defects in the crystal, yielding occurs sooner than the base crystal or the crystal with graphene particles. This allows the graphene to increase the crystal's strength rather than reducing it (10.82% increase with 4 Layers).

It is worth noting that the observed switch in the effect of adding graphene shown here (from weakening to improving) was detected by only adding two small defects (which has been formed

DISTRIBUTION A: Distribution approved for public release.

by deleting around 0.23 % of total atoms) in the system. In practice, the crystal has a finite volume of defects, and adding more and more graphene will improve the mechanical properties. However, there is a turning point at which again a switch happens, and adding more graphene flakes will in practice add to the defects of the system, and weakening will be observed in the material. This is compatible with our recent experimental findings [20] we found an optimum value for the density of graphene particles after which adding more graphene was weakening the strength.

Other than internal defects, the free surface of a material can also be the source of dislocations. The free surface requires less stress to nucleate dislocations much like the metal graphene interface in the perfect crystal composites. A defect free cylindrical system, as shown in figure 5.8, having a free surface at cylindrical wall has been reinforced with graphene layers. In reinforced cylindrical systems, increase in flow stress has been observed due to the blocking of dislocations but there is no decrease in yield stress. In all the cases, as shown in figure 5.8 (b) and (c), the dislocations starts nucleating around the same strain. As there are no dislocations in the defect free cylindrical system, the yield stress is determined by the dislocation nucleation site which requires least stress. As graphene metal interface requires large stress for nucleating dislocations, the yield stress is determined by the free surface of cylinder. This is the reason that there is no decrease in the yield stress in reinforced defect free cylindrical system. As shown in figure 5.8 (a), little improvement with adding more graphene layer is observed. The reason behind this improvement is that the increasing the number of layers of graphene decreases the effective pinned length of cylinder which increases stress required for dislocation nucleation at the surface. As shown in figure 5.9, graphene improves the strength of system significantly when graphene is reinforced in the cylindrical system with defects. In the cylindrical system with defects, dislocations are present at 0% strain and are blocked by the graphene. The defects in the cylinder has been created by deleting 1.15 % of total nickel atoms. This concludes that ,in real metallic systems having dislocation nucleation sites in form of surfaces or having defects, graphene's ability to block dislocations will improve the strength of the reinforced system.

DISTRIBUTION A: Distribution approved for public release.

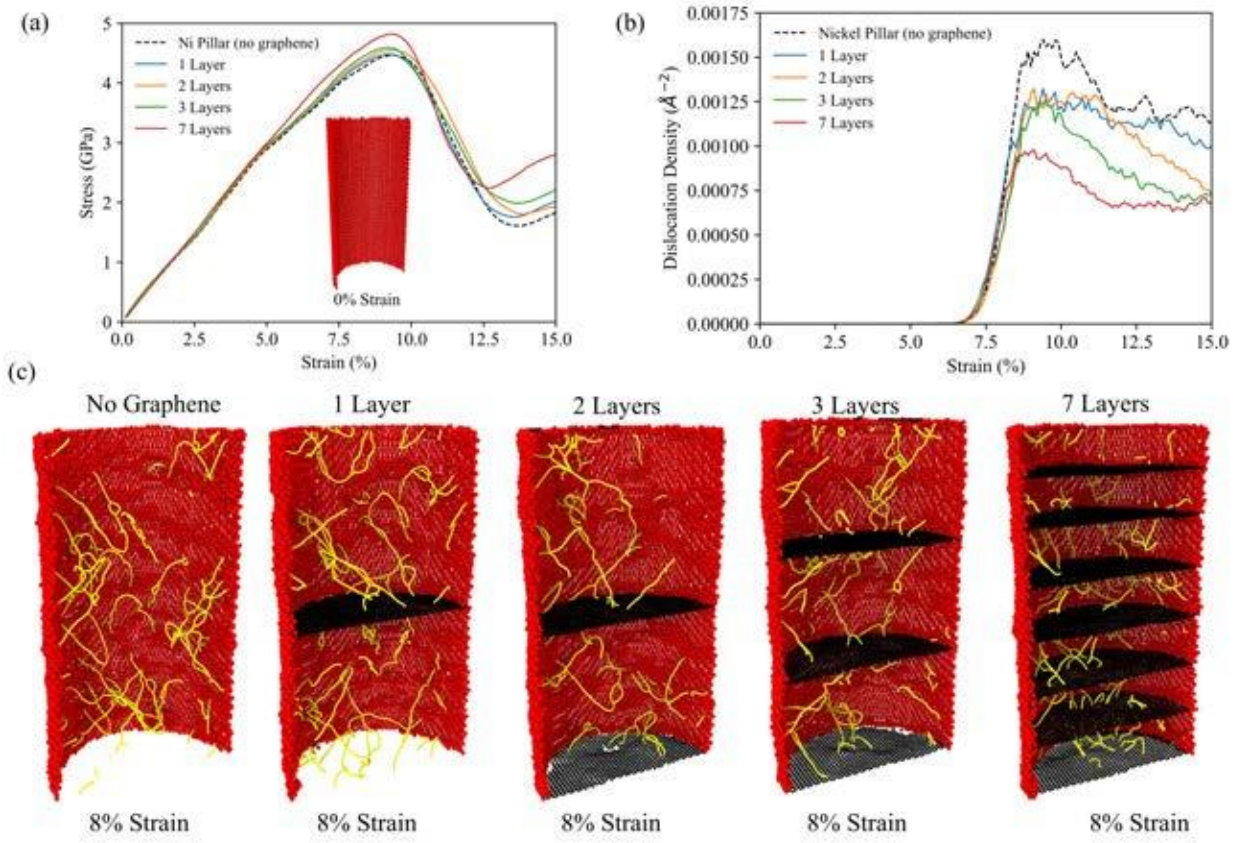

Figure 5.8: (a) Stress-strain curves for the nickel pillar and the nickel graphene composites with different number of graphene layers in topfcc structure. (b) Dislocation density vs. strain curve for the same configurations. (c)-(e) shows state of dislocations at 8 % strain. The dislocation density nucleates (from the free surface of cylinder) at similar strain in the nickel pillar and the composites which explains why there is no decrease in the strength of the composite.

DISTRIBUTION A: Distribution approved for public release.

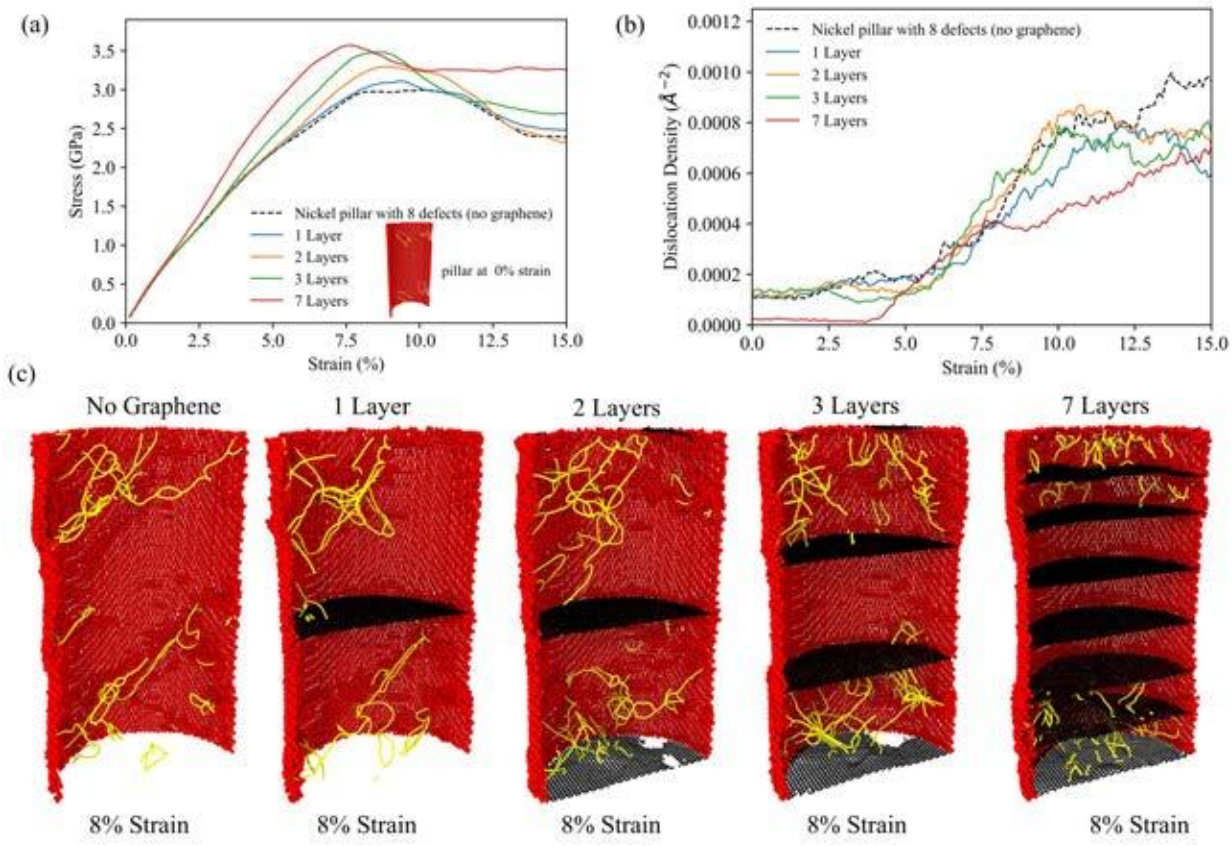

Figure 5.9: (a) Stress-strain curves for the nickel pillar with defects in the compression. Each curve represents the crystal having 8 defects with different number of graphene layers in the topfcc structure. (b) Dislocation density vs. strain curve for the same graphene-nickel configurations.(c)-(e) shows state of dislocations at 8% strain. The addition of defects causes dislocation density in the system at 0%. These dislocations travels in the system and multiplies significantly after the critical stress. The blocking of dislocation by the graphene plays a major role in this system and increases the strength of reinforced system in comparison to system without graphene.

DISTRIBUTION A: Distribution approved for public release.

5.5 Conclusion

Layered metal matrix composites using 2D material as reinforcement inside the 3D metal matrix are a new class of materials. Fundamental understanding of dislocation behavior is essential for designing new composites. In this work, using atomistic simulations, we studied the perfect crystal of nickel reinforced with graphene. The perfect crystal allows us to study the effect of metal graphene interface, and we found that the yield stress of graphene reinforced crystals decreases in comparison to perfect crystals, although the flow stress increases. We found that the topfcc and bridgehcp interface inside the nickel crystal leads to least decrease in yield stress which is also consistent with the DFT results that is the topfcc and bridgehcp are stable and metastable structures, respectively [26]. We also found that the difference in the graphene edge can change the behavior of reinforced crystal. Dislocation nucleates near the zigzag edges at low stress compare to armchair edges. Dislocation nucleation and kinetic explains the difference in mechanical behavior for different graphene structures. At the end, we showed that in the material with defects, the graphene improves the strength. We concluded that graphene improves the metal matrix when there are defects that require less stress for nucleating the dislocations. We hope the insights gain in this will be useful for designing metal matrix with other 2D materials like h-BN as well.

Decreasing dislocation density explains the increase in flow stress after dislocation nucleation in composites, but the reason dislocation density decreases in the reinforced crystal compare to perfect crystal remain unanswered. The difference in dislocation density might be related to the difference in energies of dislocations and electronic structures in a reinforced and perfect crystal. Understanding the interaction of different types of dislocations with graphene in the metal matrix (with defects) using the first principle will be reported in the future work by authors.

Acknowledgement

This material is based upon work supported by the Air Force Office of Scientific Research under award number FA9550-18-1-0169.

DISTRIBUTION A: Distribution approved for public release.

VI- Copper-Graphene Composites; Developing a Modified embedded-atom method interatomic potential and Investigating their Mechanical Properties

6.1 Overview

Unraveling the deformation mechanisms at the atomistic scale of metal matrix-graphene composites is a key step toward designing and fabricating these materials with exceptional mechanical properties. While these composites can be made by embedding graphene into multiple metallic matrices, it is shown that superior mechanical properties can be obtained by combining copper and graphene. In the past few years, molecular dynamics simulations have been used to investigate the fundamental deformation mechanisms at the nanoscale of Cu-graphene composites to facilitate designing these composites with improved mechanical properties. However, in all of the reported works, Lennard-Jones potential has been used for modeling the interaction between copper and carbon atoms. The complexities in the Cu-C interaction emerges the necessity of utilizing more accurate potentials. In this work, a 2NN MEAM (second nearest-neighbor modified embedded atomic method) potential for the copper and carbon atom interaction is developed. Since crystal structures like B1 or B2 are not experimentally available for the Cu-C system, first-principle calculations are used to determine the reference structure and its elastic constants in this work. It is shown that the B1 and B2 structure of Cu-C has positive formation energy, but B1 is dynamically stable. Accordingly, the B1 crystal structure is used as the reference structure for the Cu-C system to develop the interatomic potential. It is shown that the reported potential agrees reasonably well for phonon dispersion frequencies, stacking fault energies, and the atomic forces with the available experimental data and first-principle calculations. The developed potential is utilized to study the mechanical properties of copper-graphene composites subjected to uniaxial loading. Our results show that adding graphene to a defect-free Cu crystal weakens the metallic matrix's mechanical properties. However, when the graphene is embedded into a Cu matrix with some defects, e.g., in a polycrystalline Cu, it can significantly improve the mechanical properties.

DISTRIBUTION A: Distribution approved for public release.

6.2 Introduction

Good thermal and electrical conductivity makes copper one of the most useful metal in the world. The discovery of graphene in 2004 [2], has paved the way for the fabrication of many new 2D materials. These 2D materials have excellent mechanical properties for example, Graphene (Young's modulus $\simeq$ 1.0 TPa) [1], MoS_2 (Young's modulus $\simeq$ 0.270 TPa) [127] and hBN (Young's modulus $\simeq$ 0.865 TPa) [128]. The mechanical property and 2D structure makes them an ideal candidate for reinforcement in the metal matrix. In recent years, in multiple research works, 2D materials such as hexagonal Boron Nitride (hBN), Molybdenum Disulfide (MoS_2) and graphene have been used to design the mechanical, thermal and electrical properties of metal matrix [13, 21, 129, 130]. The applications of copper, for example, in integrated circuits and flexible electronics, usually requires high strength and conductivity. The addition of graphene improves both the properties [131, 132]. The addition of graphene in copper thin films has shown to increase fatigue resistance for flexible electronics [32]. The graphene's reinforcement has improved mechanical properties in both nanocomposites [13, 20] and bulk composites [130, 131]. Kim et al. [7] has reported that gain in mechanical properties due to multi-layer graphene is attributed to Orowan strengthening. It is shown by many researchers that layered graphene stops the propagation of dislocations inside the metal matrix, which is the primary reason for the improvement in mechanical properties [13, 20, 70]. The better understanding of these nanocomposites can pave the path to new applications. Due to the scale of interaction in these composites, only atomistic simulations can capture the interaction of graphene with metal-matrix.

Molecular dynamics is an efficient tool for understanding the underlying mechanisms of nanocomposites. The accuracy of molecular dynamic simulations strongly depends on the accuracy of the utilized inter-atomic potential in the simulations. There are several molecular dynamics studies of copper and carbon-based composites using either EAM or MEAM for Cu-Cu interaction and AIREBO for C-C interaction. However, in all these works [103, 111, 112, 115, 133–138], the Lennard-Jones (LJ) potential is used for Cu-C interaction. There are four sets of LJ parameters used in the past works, as shown in Table S1 of the supplementary document. As Lennard-Jones is a pair potential, the combination of the potentials ignores the higher order energy interaction involving copper and carbon atoms. This implies that there is a need of an interatomic potential which take accounts the multi-body interactions. For simulating copper-graphene composites, we need an interatomic potential that can simulate the metallic bond of copper and covalent bonds of graphene. One such potential is the modified embedded atomic method (MEAM), this potential has been used to simulate both metals and systems involving covalent bonds.

The first MEAM potential for copper was reported by Baskes, who developed the theory behind the MEAM potential [139]. The original MEAM potential only considered the first-nearest neighbor interaction. The inclusion of second-nearest neighbor interaction solved the shortcomings, such as structural instability and incorrect surface reconstructions for FCC elements. The first set of MEAM parameters based on second-nearest neighbor formulation was reported by Lee et al. in 2003 [140]. These parameters were optimized for the properties of copper only. A new set of MEAM potential was reported by Jelinek et al. [141]. This set was optimized for Cu and its alloys with Al, Si, Mg, and Fe. The parameters reported by Lee et al. [140] were modified by Asadi et al. [142] to solve the problems related to the two-phase solid-liquid coexistence. The parameters by Asadi et al. [142] was again modified by Etesami et al. [143] to solve the molecular dynamics problems near the melting point.

DISTRIBUTION A: Distribution approved for public release.

The first 2NN carbon MEAM potential is developed by Lee et al. [144]. This potential was used to develop Fe-C, Ti-C and Fe-Ti-C potentials [145, 146]. Another set of carbon potential was reported by Xiao et al. [147], which was also used to develop Ni-C potential. This potential cannot handle large tensile distortion in graphite and large tensile stress in the graphene [147]. The third set of carbon potential having similar parameters to [147] was used by Uddin et al. [116] to simulate Ni-CNT composites.

To the authors' best knowledge, all the reported MEAM potentials for the Cu-C are either optimized for copper or carbon. There is no reported set of MEAM potential parameters for the copper-carbon system. Here in this work, we report the MEAM potential parameters for the copper-carbon system. The reported 2NN MEAM potential parameters are obtained by fitting elastic constants of reference structure. For these parameters, comparison with available experimental data, first-principle calculations, and other atomic potential is also presented. In the end, the MEAM potential is also utilized to understand the deformation behavior of copper-graphene composite in the case of copper-single crystal and polycrystals.

6.3 Methods

1. 2NN MEAM potential

The MEAM potential [139] is an extension of embedded atom method (EAM) [58] which is based on Stott-Zaremba corollary to density functional theory (DFT). Stott-Zaremba corollary states that the energy of an impurity depends on the host material electron density without impurity. EAM uses this corollary by assuming each atom in a system as an impurity in the host consisting of all other atoms. EAM is modified by Baskes to include angular dependent terms in electron density function.

The total energy of a system is given by:

$$E_{tot} = \sum_i \left[F_i(\bar{\rho}_i) + \frac{1}{2} \sum_{i \neq j} S_{ij} \phi_{ij}(R_{ij}) \right] \tag{6.13}$$

where F_i, S_{ij} and $\phi_{ij}(R_{ij})$ are embedding energy as a function of background electron density $\bar{\rho}_i$, screening function and the pair interaction between atoms i and j separated by a distance R_{ij}. The embedding function is given as [148]:

$$F(\bar{\rho}) = AE_c(\bar{\rho}/\bar{\rho}^0) ln(\bar{\rho}/\bar{\rho}^0) \tag{6.14}$$

where A is an adjustable parameter, E_c is the sublimation energy, and $\bar{\rho}^0$ is the background electron density for a reference structures. The background electron density $\bar{\rho}_i$ is the combination of partial electron densities which has a spherically symmetric partial electron density $\rho_i^{(0)}$ and three angular contributions $\rho_i^{(1)}$, $\rho_i^{(2)}$, and $\rho_i^{(3)}$. The partial electron densities are the function of atomic configuration and atomic electron density. The atomic electron densities $\rho^{a(h)}$ $(h = 0 - 4)$ are given as:

$$\rho^{a(h)}(R) = \rho_0 exp[-\beta^{(h)}(R/r_e - 1)] \tag{6.15}$$

DISTRIBUTION A: Distribution approved for public release.

Table 6.1: Set of MEAM potential parameters for pure Cu and C. The reference structure of Cu and C are fcc and diamond, respectively. The value of screening parameters is C_{min} = 0.8 and C_{max} = 2.8 for both Cu and C. The units of cohesive Energy E_c, equilibrium nearest-neighbor distance r_e and Bulk modulus B are eV, Å and GPa

	E_c	r_e	B	A	$\beta^{(0)}$	$\beta^{(1)}$	$\beta^{(2)}$	$\beta^{(3)}$	$t^{(1)}$	$t^{(2)}$	$t^{(3)}$	d
Cu	3.54	2.5562	142.0	0.60	3.95	3.15	3.85	2.45	5.70	2.30	4.60	0.05
C	7.37	1.545	444.20	1.00	3.00	3.20	3.00	2.80	1.60	0.40	-5.4	-0.16

where the atomic electron density scaling factor ρ_0 and the decay length $\beta^{(h)}$ are adjustable parameters and r_e is the nearest-neighbor distance in the equilibrium reference structure.

The pair interaction term $\phi_{ij}(R_{ij})$ in Eq. (6.13) is computed using a reference structure. The value of $\phi_{ij}(R_{ij})$ is determined by subtracting the embedding function from the known value of the energy of an atom in reference structure. For total energy per atom, MEAM postulates the Rose universal equation of state [149]:

$$E^u(R) = -E_c(1 + a^* + da^{*3})e^{-a^*} \tag{6.16}$$

where d is an adjustable parameter,

$$a^* = \alpha(R/r_e - 1) \tag{6.17}$$

and

$$\alpha = \left(\frac{9B\Omega}{E_c}\right)^{(1/2)} \tag{6.18}$$

where r_e is the equilibrium nearest-neighbor distance, E_c is the cohesive energy, B is the bulk modulus, and Ω is the equilibrium atomic volume of the reference structure. The 2NN interactions are considered by adjusting the screening parameters (C_{min}, C_{max}) [56, 148]. More details about 2NN MEAM can be found in literature [56, 139, 148].

To describe the binary systems, a reference lattice consisting of both types of atoms is required. In conclusion, in 2NN MEAM, 14 independent parameters are required to describe a pure element, as shown in Table 6.1. For binary systems, 13 independent parameters (shown in Table 6.2) are required apart from the unary parameters.

2. DFT calculations for binary structures

Binary inter-metallic compounds where the first nearest neighbors are of different type of atom (B1 or B2 crystal structures) are used as a reference structure for many Binary compounds such as TiC [150], NiC [147], FeC [146] and NiTi [57]. The copper carbide has two known phases: dicopper acetylide (Cu_2C_2) and dicopper deacetylide (Cu_2C_4) [151, 152]. As B1 or B2 CuC structures has not been reported, experimentally, we used first principle calculations to determine the parameters related to universal equation of state for binary structure.

The DFT calculations were performed using Vienna *ab initio* simulation package (VASP) (Version 5.4.1) [93] with the use of projected augmented-wave pseudopotential parameters [94]. Energy cutoff of 500 eV and 3300 eV is used for plane wave basis and charge density grid,

DISTRIBUTION A: Distribution approved for public release.

Table 6.2: 2NN MEAM potential parameter sets for binary Cu-C systems. The reference structure of Cu-C is NaCl-type (B1) structure. The units of cohesive Energy E_c, equilibrium nearest-neighbor distance r_e and Bulk modulus B are eV, Å and GPa

Parameter	Value
$\Delta E_f = (0.5E_c^{Ni} + 0.5E_c^{Ti} - 0.5E_c^{B1})$	1.72
r_e	2.064
B	190.2
d	-0.13
ρ_0^B/ρ_0^A	6.80
$C_{min}(Cu, C, Cu)$	1.0
$C_{min}(C, Cu, C)$	1.25
$C_{min}(Cu, Cu, C)$	1.0
$C_{min}(C, C, Cu)$	1.35
$C_{max}(Cu, C, Cu)$	2.10
$C_{max}(C, Cu, C)$	2.35
$C_{max}(Cu, Cu, C)$	2.65
$C_{max}(C, C, Cu)$	2.40

respectively. It is known that local (spin) density approximation (LDA) and generalized gradient approximation (GGA) functional tends to overbind and underbind the systems, respectively [26, 86]. GGA gives a better prediction for both metal and graphene, but in the case of the hybrid system like the interaction between metal and graphene interface, the LDA is reported to give the results which are close to experiments [26, 90]. Hence, The local (spin) density approximation (LDA) approximation is used for exchange-correlation functional [92]. A k-point mesh of 15 × 15

×

15 is used for all B1 and B2 structure calculations.

The energy relaxation determined the lattice constants, and elastic constants were determined by the method of Page et al. [153] as implemented in VASP. The phonon dispersion data is obtained using the tool phonopy [154]. The phonon and elastic constant calculations are done with the supercell structure that has reached the total energy convergence of 0.2 meV with respect to k-point as shown in figure 6.10 of Appendix 6.6.

3. Copper-Graphene composite

The developed 2NN MEAM potential is used to compare the results of copper-graphene composite for single crystal and polycrystal copper. The large-scale atomic/molecular massively parallel (LAMMPS) [54] is used to perform all the molecular dynamics simulations. OVITO tool [55] is used to visualize the results. Two periodic three dimensional (3D) cells of copper are created, one having single crystal with lattice directions aligned X-axis [$1\bar{1}0$], Y-axis [$11\bar{2}$], and Z-axis [111] and the other containing 9 grains which are created using the Voronoi Tessellation algorithm. The size of single crystal and polycrystal simulation cells are 219.83 × 256.79 × 252.46 Å^3 and 249.46 × 248.12 × 250.0 Å^3, respectively. The grain size in the polycrystal simulation box is around 14.90

DISTRIBUTION A: Distribution approved for public release.

nm, and the above dimensions are chosen so that the graphene is also periodic in x and y directions.

The MD simulations are performed for four different cases of graphene in the simulation cell; (a) no graphene, (b) periodic graphene with no edge, (c) graphene particle with the edge in the direction of loading, and (d) graphene particle with the edge perpendicular to the direction of loading. In the polycrystal, the graphene is embedded in the system, and the overlapped copper atoms are deleted. In the single crystal, a gap is created between the copper layers to embed the graphene.

The systems are equilibrated at T = 300 K for 100 ps. After the equilibration, the simulation boxes are deformed in tension in the x-direction, which is in the plane of the graphene. For deciding the strain rate to represent the loading condition, we simulated three strain rates; 10^8, 10^9, and 10^{10} s^{-1}. The resulting stress-strain curves are shown in Figures 6.8 and 6.9 in the Appendix. The resultant stress-strain curves show that there is no significant behavior change between 10^8 s^{-1} and 10^9 s^{-1}. Hence, all the simulations in this work are performed using strain rate of 10^9 s^{-1}.

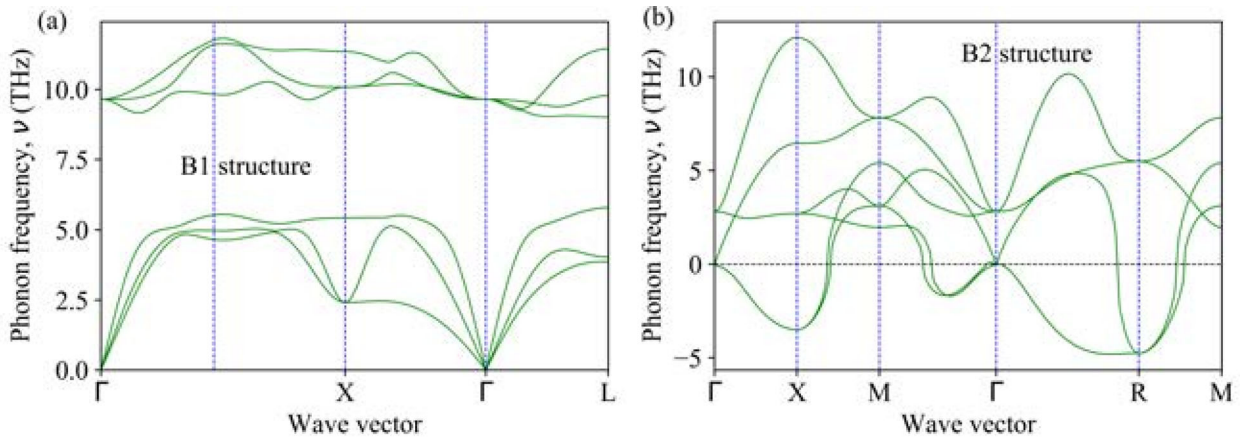

Figure 6.1: The phonon dispersion curves for CuC B1 and B2 crystal structures (a and b). The negative frequencies in dispersion curve of B2 CuC structure clearly indicates that B2 structure is dynamically unstable.

6.4 Results and Discussion

1. Determining the reference structure

In 2NN MEAM potential, the pair interaction part of the energy is calculated using reference structure. The reference structure plays an important role in determining the suitability of the potential. Generally, the experimentally available reference structures are used, for example, diamond for graphene and FCC for copper. However, in the case of copper-carbon, we found that none of the reference structures which are implemented in MEAM have been detected in the experiments. To overcome this issue, we used the first principle calculations to determine the properties of the reference structure. We found that the formation energy of both B1 and B2 structure of CuC are positive. The absence of imaginary frequencies in the B1 structure (as shown in Figure 6.1) confirms the dynamical stability. Due to dynamical stability, we have used the B1 structure instead of the B2 structure as the reference structure.

DISTRIBUTION A: Distribution approved for public release.

2. Accuracy of developed 2NN MEAM potential

The values of 2NN MEAM parameters obtained in this work are given in Tables 6.1 and 6.2. The comparison of elastic constants and lattice length with experimental or DFT values is shown in Table 6.3. The accuracy of elastic constant values of CuC B1 structure is sacrificed to make it stable at finite temperature. It should be noted that the elastic constant values are used in the optimization of the potential. In the following, we will compare the properties which have not been used in the optimization of potential.

Phonon dispersion relations provide information about the forces when atoms are slightly moved from their equilibrium position. This provides a good measure of the applicability of a potential. As shown in Figures 6.2 (a and b), the Cu and C potentials are able to reproduce all the features of phonon dispersion curves in the FCC structure of copper and in the diamond structure of carbon. In the case of carbon potential, the experimental phonon frequency values of the diamond structure are closer to the 2NN MEAM compared to AIREBO potential [155]. The 2NN MEAM potential is also able to reproduce the features of the graphene phonon dispersion curve, which indicates the suitability of the present potential to simulate the behavior of graphene. For B1 CuC structure, the potential is able to reproduce the acoustic and optic branches of phonons qualitatively. In comparison with DFT, the optical phonon dispersion branch of phonon obtained using the 2NN MEAM changes more quickly with the wave vector. The reason for having different phonon modes in B1 structure and 2NN MEAM is that the optimization of potential is done using elastic constants at 0 K, but the accuracy of elastic constants of B1 CuC is sacrificed to make the potential stable at finite temperature. This affects the accuracy of all other properties of B1 CuC at 0 K. Also, the 2NN MEAM potential depends on fitting the electron density function and how well it transfers to the other structures. We found during optimization that the carbon parameters working well for both diamond and B1 CuC cannot accurately reproduce graphene properties. As the focus of this work is copper-graphene composites, we decided to prioritize graphene properties over the B1 CuC structure.

DISTRIBUTION A: Distribution approved for public release.

Table 6.3: Comparison of the elastic constant values for the Carbon, Copper and CuC reference structures. The unit of all elastic constants (C_{11}, C_{12}, C_{44} and B) is GPa. The units of lattice length and energy of formation (E_c and ΔE_f) are Å and eV/atom, respectively.

Parameter	Experimental or DFT values	This work
Carbon (Diamond structure)		
Lattice length	3.567 [62]	3.567
C_{11}	1080.4 [63]	1091.9
C_{12}	127.0 [63]	120.4
C_{44}	576.6 [63]	653.0
B	444.8 [63]	444.2
E_c	-7.37	-7.37
Carbon (Graphene)		
Bond length	1.42	1.426
ΔE_c	-0.02^a	-0.26
Copper (FCC)		
Lattice length	3.62	3.615
C_{11}	176.2	188.4
C_{12}	124.9	118.9
C_{44}	81.8	72.2
B	142.0	142.0
E_c	-3.54	-3.54
CuC ($B1$ structure)		
Lattice length	4.128^b	4.128
ΔE_f	1.72^b	1.72
C_{11}	375.1^b	429.2
C_{12}	192.2^b	70.7
C_{44}	27.9^b	20.8
B	253.1^b	190.2

^{a} Graphite force field,^{b} DFT calculations

DISTRIBUTION A: Distribution approved for public release.

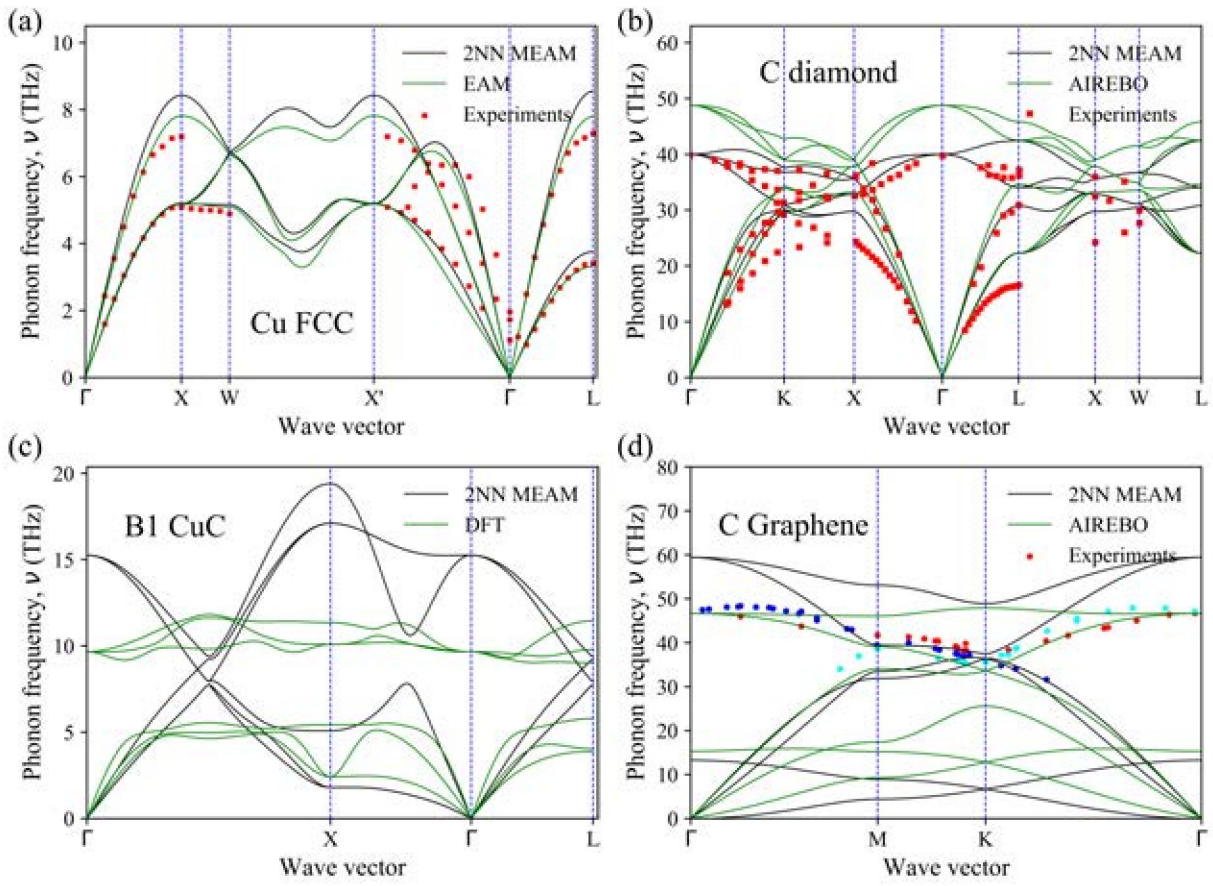

Figure 6.2: Comparison of the phonon dispersion curves for Cu FCC crystal structure using 2NN MEAM constructed in this work, EAM potential[156] and experiments [157] is shown in (a). (b) Shows the phonon dispersion curve for diamond structure. The phonon dispersion curve using the present 2NN MEAM is also compared with the phonon dispersion curves by the AIREBO potential [155] and experimental values [158]. The phonon dispersion curve for B1 CuC structure is compared with the first principle calculations in (c). (d) Shows the phonon dispersion curve for graphene. The phonon dispersion curve using the present 2NN MEAM is compared with the phonon dispersion curve by the AIREBO potential [155] and experimental values of graphite [159–161].

DISTRIBUTION A: Distribution approved for public release.

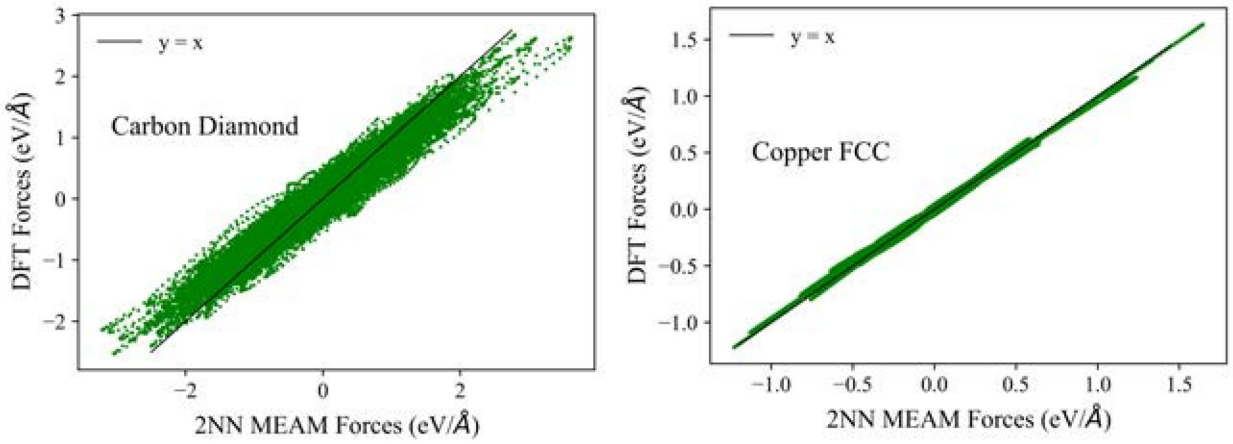

Figure 6.3: Force comparison in reference structure for Carbon and Copper are shown in (a) and (b), respectively. More than 150 configurations are used in both the cases. The line in the graphs represents the case where forces are equal. As the experimental lattice constants and bond length used for 2NN MEAM which are different from the DFT values, scaled coordinates have been used to make this comparison.

In Figure 6.4, the stacking fault energy of graphene and copper is compared with DFT and previously available atomic potential. For copper, as shown in Figure 6.4, the 2NN MEAM potential can reproduce the qualitative behavior of energy. For graphene, the optimized 2NN MEAM potential has all the features, but the difference in energy is large in the case of Glide stacking fault (passing through inclined bonds). The difference in energy indicates that care must be taken when using this potential for comparing the defect energies in graphene. Figure 6.3 compares the DFT forces for Diamond and copper FCC structure. The copper structure shows an excellent match between the forces. In the carbon diamond structure, the forces are close to matching and show the correct trend.

DISTRIBUTION A: Distribution approved for public release.

empty

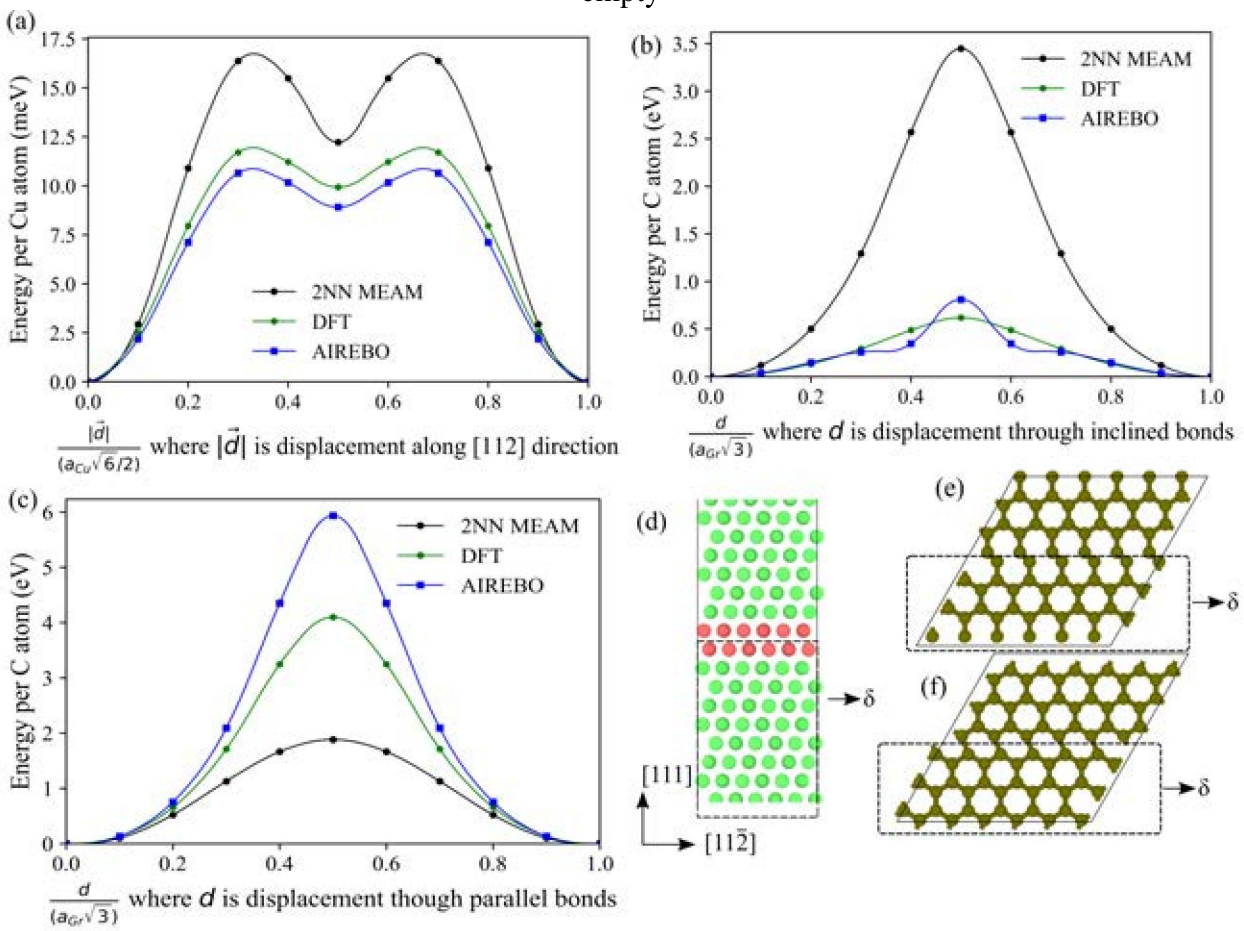

Figure 6.4: Comparison of general stacking fault energy curve for copper using 2NN MEAM, EAM potential[156] and DFT (a). (b and c) shows the energy curve comparison for Glide GSF: slip occurs across zigzag bonds and Shuffle GSF: slip occurs across parallel bonds. The energy curves of 2NN MEAM are compared with AIREBO [155] and DFT values. Schematic of displacement for Copper crystal is shown in (d). Red atoms represent the stacking fault due to the displacement. (e) and (f) show the slip across zigzag bond and parallel bond, respectively. a_{Cu} and a_{Gr} in above graphs represent lattice length for Copper crystal and graphene bond length, respectively.

The above comparison of phonon dispersion frequencies, energies, and forces with first-principle calculations shows that the reported potential is suitable for the atomistic simulations involving copper and carbon. We also found that the local structure of copper graphene composite by 2NN MEAM potential is more close to the first principle calculations as compared to Lennard-Jones potential used in previous studies (as shown in Table 6.5 and 6.6 in the Appendix).

3. Copper-Graphene composites

In this section, the new potential will be used to investigate the mechanical properties of Cu-graphene composites. The uniaxial tensile stress-strain curves for single crystal copper and its composite, with different arrangements of graphene in the Cu matrix, are shown in Figure 6.5 (a). The reinforcement of graphene in the loading plane increases Young's modulus, but reduces the yield strength of the copper single crystal. To investigate, we calculated the atomic shear strain near

DISTRIBUTION A: Distribution approved for public release.

the yield point for copper and composites. As shown in Figure 6.6 (a), in single crystal copper, various slip planes activate when the stress reaches the critical value, and there are no preferential nucleation points for the slip planes. When graphene is added in the perfect crystal, the interface between metal and graphene acts as a defect [15]. As shown in Figures 6.6 (b-d), the slip planes are originating from the interface or the edge of the graphene. Graphene edges can act as the dislocation lines and nucleation points for the slip planes. We also found that when the graphene edge is parallel to the loading direction, all the slip planes are in the same direction.

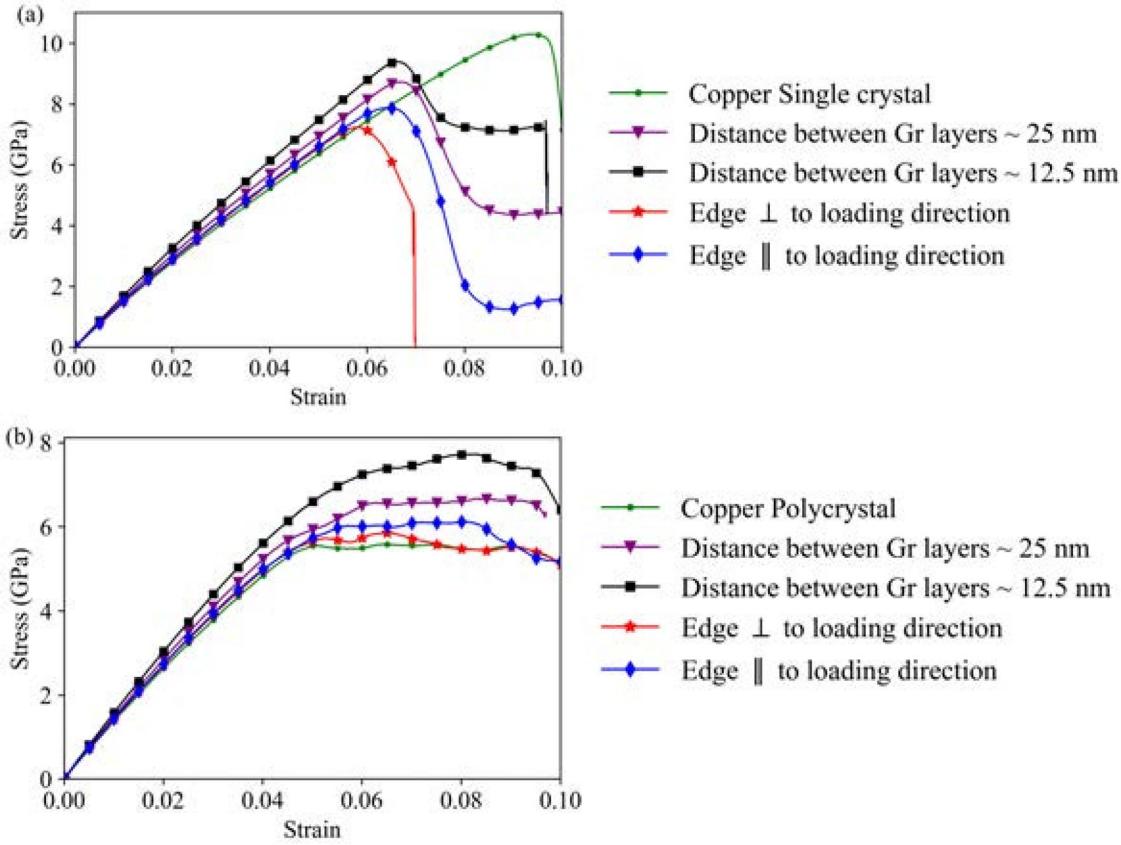

Figure 6.5: Tensile stress-strain curve for copper polycrystal and single crystal with and without graphene. The reinforcement of graphene improves the yield stress in the copper polycrystal, while the addition of graphene in the perfect crystal of copper weakens the metal matrix. The improvement in polycrystal increases with increasing the number of graphene layers. The improvement is more in the case of the full layer compared to the graphene with edges.

These results look to be in contrast with the experimental results that report improvement in the mechanical properties of metallic matrices by adding graphene. However, it should be noted that in those reported experiments, graphene is embedded into a metallic matrix with some pre-existing defects. In that case, graphene improves the mechanical properties by blocking dislocations, while in the case of having a perfect crystal, there are no pre-existing defects in the metallic matrix and the embedded graphene acts as a source for dislocations. To verify this, we ran a similar simulation with polycrystal copper, in which some defects exist at the grain boundaries. As shown in Figure 6.5 (b), the yield strength of polycrystalline copper increases with adding the graphene. The reason for this improvement is that the graphene particles are not the source of dislocations, but they block the propagation of dislocations that initiate at the grain boundaries, as shown in Figure 6.7.

DISTRIBUTION A: Distribution approved for public release.

In this case, the propagation of dislocations from the grain boundaries precedes the activation of slip planes at the vicinity of the Cu-graphene interface. By further loading the material, graphene acts as a barrier for the slip planes that propagate from the grain boundaries in the system. This mechanism increases the stress plateau in the stress-strain response. It is worth noting that a similar deformation mechanism (in which graphene impedes dislocations instead of acting as a dislocation source) will happen in a single crystal as well, with the condition that the single crystal contains some defects (see our recent work [15]). Graphene in a metal matrix composite can act as both a source or sink of dislocations, depending on the density of dislocations from other sources in the system. Consequently, embedding graphene into a metal matrix can potentially improve or weaken the mechanical properties. If the required critical strain for activating the slip systems around the metal matrix's defects is less than the metal-graphene interface, graphene will improve the strength of metal-matrix or vice-versa.

DISTRIBUTION A: Distribution approved for public release.

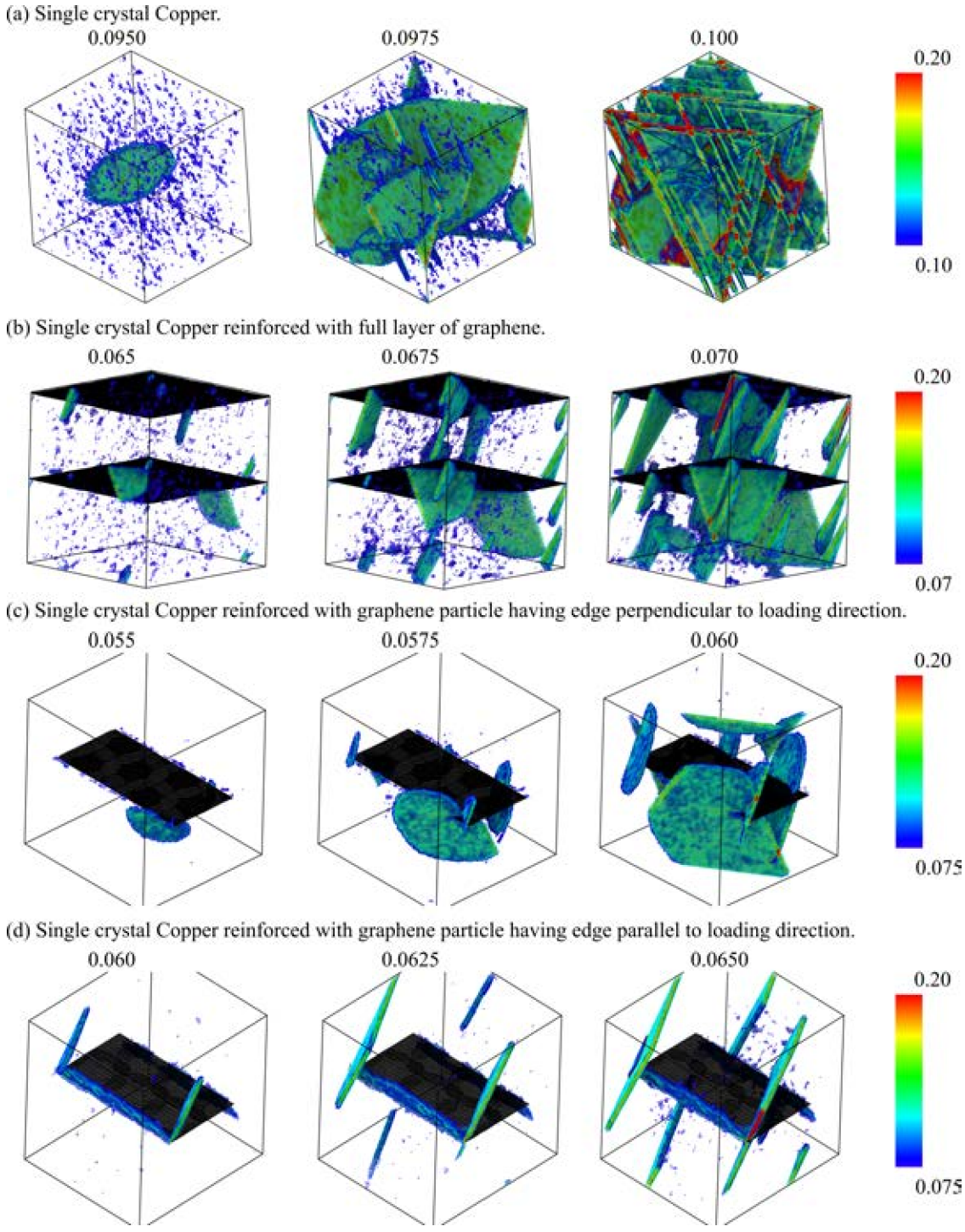

Figure 6.6: Slip planes of copper single crystal with and without reinforcement near the yielding point. The colour coding represents the local atomic shear strain. The copper atoms which have shear strains larger than the minimum value of colour mapping are shown. The slip planes originate homogeneously in the perfect crystal while in the crystal with reinforcement the slip planes originate from either the graphene-metal interface or the graphene edges. All the Carbon atoms are shown and are colored as black to show the interaction of slip planes. The supplementary video V1 shows the evolution of slip planes with strain in single crystal and composites.

DISTRIBUTION A: Distribution approved for public release.

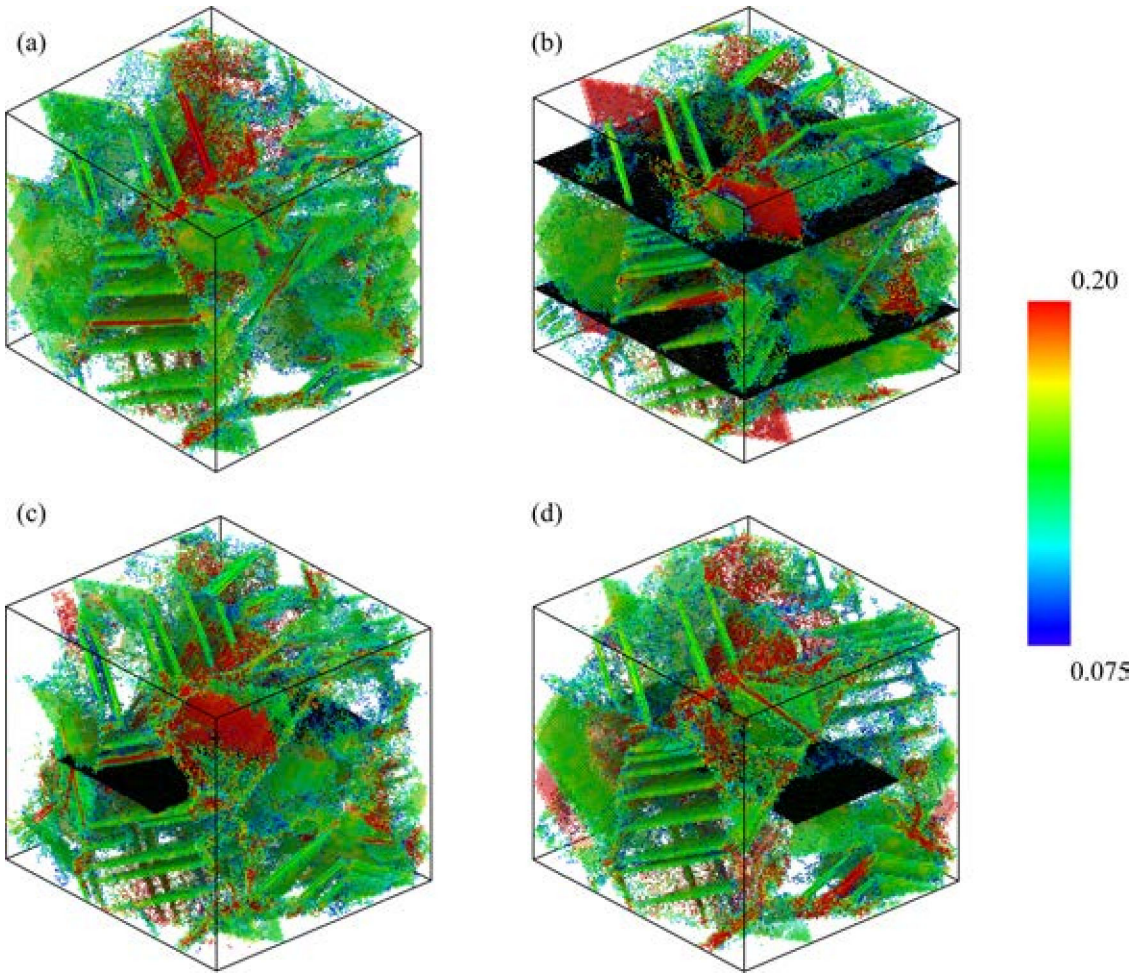

Figure 6.7: Slip planes in copper polycrystal and composite when uniaxial tensile strain is equal to 0.075. (a) Shows the snapshot for copper polycrystal. (b-d) Show the snapshots for copper polycrystal reinforced by a periodic layer of graphene, having a graphene edge perpendicular to loading direction and having a graphene edge parallel to the loading direction. The movement of slip planes is blocked by the copper-graphene interface. The copper atoms are coloured according to local shear strain. The copper atoms which have local atomic shear stains larger than 0.075 and coordination number of hexagonal closest packed (hcp) are shown. All the Carbon atoms are shown and are colored as black to show the interaction of slip planes. The supplementary video V2 shows the evolution of slip planes with strain in polycrystal and its composites.

6.5 Conclusion

In the previous few years, Various research groups have computationally investigated the mechanical properties of copper-graphene composites by Molecular dynamics simulations. However, all the Copper-Graphene composites' studies use Lennard-Jones potential to simulate the interaction between Copper and Carbon. These MD studies have used different sets of Lennard-Jones parameters (shown in Table 6.4 in Appendix). The Lennard-Jones potential is a 2-Body empirical potential, and it ignores the higher terms in the potential energy. In this work, a 2NN MEAM potential is developed for the interaction between copper and carbon atoms. In the process of developing the potential, ab-initio calculations are used for fitting the elastic constants of a B1 reference structure.

DISTRIBUTION A: Distribution approved for public release.

It is shown that the obtained 2NN MEAM potential can reasonably reproduce the phonon dispersion curves, stacking fault energies, and atomic forces. The obtained potential is used to study the mechanical properties of the copper-graphene composite. It is shown that adding graphene to a metallic matrix can both weaken or improve the mechanical properties, depending on the density of dislocations in the system. If there is no dislocation in the metallic matrix, graphene will act as a source of dislocations and will weaken the material. However, when there are other defects in the matrix, such as the grain boundaries in a polycrystalline matrix, graphene will impede the propagation of dislocation, which are initiated from the defects in the matrix, and will improve the mechanical properties. Copper and carbon are two ubiquitous atoms in engineering and nature. Understanding the interaction between these two atoms can lead to numerous discoveries in the field of materials science. Atomistic simulations are the precursor to many discoveries at the nanoscale, and the reported potential can facilitate uncovering the atomistic mechanisms involving copper and carbon atoms in metallic composite materials.

Acknowledgement

This material is based upon work supported by the Air Force Office of Scientific Research under award number FA9550-18-1-0169.

6.6 Appendix

1. Comparison of 2NN MEAM potential with Lennard-Jones potential used in previous studies.

There are four sets of Lennard Jones potential which have been used to simulate the interaction between copper and carbon atoms as shown in Table 6.4. To compare the effectiveness of developed 2NN MEAM potential we compare the energy and distance of copper layers for a small system with first principle calculations. We defined the initial structure using Cu(111) as z-direction of supercell and normal to graphene structure. The graphene was stretched to make a periodic system. The different structures of graphene inside the Copper (topfcc, bridgefcc + bridgetop,hcpfcc + tophcp, bridgehcp) are shown in figure 6.11. The structure or stacking names based on the graphene position over Cu(111) is the same as what has been used for Ni(111) in the past work [26]. In supercell, 48 layers of Copper in z-direction were considered, and graphene was inserted in between the Copper layers. To find the relaxed state for a particular graphene structure two steps were used. In the first step, the volume of the supercell has been relaxed and in the second step, the ions were allowed to move in the z-direction. The Brillouin zone was sampled with a $15 \times 15 \times 1$ grid within the Monkhorst-Pack scheme.

2. Comparison result

The comparison of energy and distance between Cu(111) layers when graphene is inserted is shown in Table S2 and Table S3. The topfcc is the most stable structure for stretched graphene inside the Cu(111) crystal. None of the Lennard-Jones parameters is able to predict the correct stable structure.

DISTRIBUTION A: Distribution approved for public release.

Table 6.4: Various Lennard-Jones parameters used for the Copper and Carbon interaction in the Literature.

	σ (Å^3)	ϵ (eV)	Works used
LJ1	3.0825	0.02578	[103, 111, 135, 162]
LJ2	3.225	0.019996	[112, 115, 133, 163]
LJ3	3.0023	0.0117	[134, 138]
LJ4	2.853	0.0328	[136]

Table 6.5: The following table compares the interaction energy of different configurations when graphene is inside Copper crystal having [111] plane perpendicular to the copper-graphene interface.

	LJ1	**LJ2**	**LJ3**	**LJ4**	**2NN MEAM**	**DFT**
topfcc	-0.366	-0.310	-0.154	-0.398	-0.348	-0.076
hcpfcc + tophcp	-0.382	-0.320	-0.162	-0.420	-0.137	-0.029
bridgehcp	-0.383	-0.328	-0.169	-0.445	-0.348	-0.017
bridgefcc + bridgetop	-0.374	-0.319	-0.163	-0.421	-0.348	-0.037

Table 6.6: The following table compares the interaction energy of different configurations when graphene is inside Copper crystal having [111] plane perpendicular to the copper-graphene interface.

	LJ1	**LJ2**	**LJ3**	**LJ4**	**2NN MEAM**	**DFT**
topfcc	6.04	6.28097	5.81809	5.63704	4.38765	4.74231
hcpfcc + tophcp	5.93647	6.17183	5.70357	5.50574	7.19094	4.99878
bridgehcp	6.14572	6.12954	5.60141	5.37604	4.38714	5.12191
bridgefcc + bridgetop	5.98065	6.18355	5.69939	5.49855	4.38765	4.95367

DISTRIBUTION A: Distribution approved for public release.

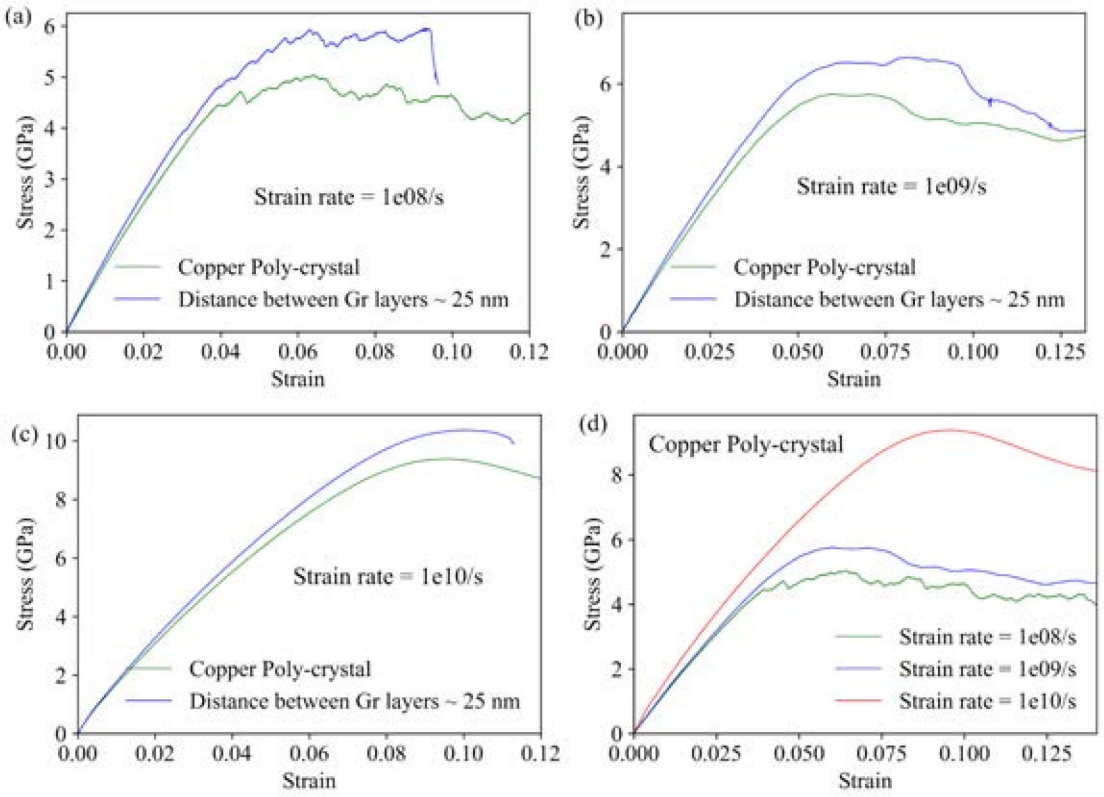

Figure 6.8: The comparison of stress-strain curves for different strain rates. The size of the simulation box is $249.46 \times 248.12 \times 250.0$ [3] and it contains 9 grains of Copper and a full sheet of graphene has been inserted in the x-y plane. All the structures have been equilibrated before applying the strain. The non-equilibrium MD (NEMD) has been used in the x-direction to apply uni-axial strain. Other directions have been controlled by using the isothermal-isobaric (NPT) ensemble. The above graphs clearly show that the strain rate has a significant effect on the stress-strain behavior of the composites. (d) show that the difference due to strain decreases with a decrease in strain rate. As there is not much difference in the stress-strain curve with strain rate 1e09/s and 1e08/s, we decided to use 1e09/s for poly-crystalline copper and its composite simulations.

Also, the 2NN MEAM potential is able to predict a closer value to DFT calculations when graphene is inserted inside the Cu(111) layers.

DISTRIBUTION A: Distribution approved for public release.

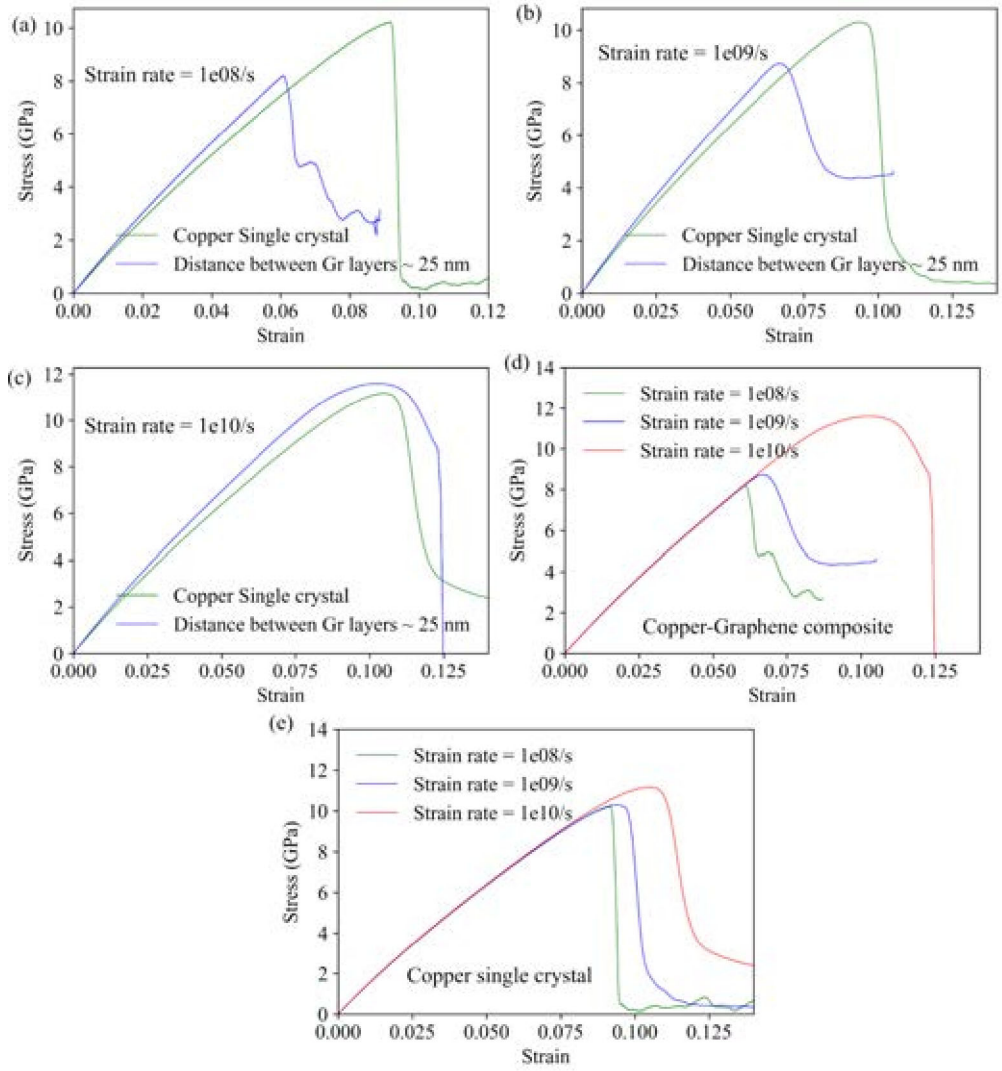

Figure 6.9: The comparison of the stress-strain curve of the copper single crystal with and without graphene for different strain rates. The size of the simulation box is 219.83 ×256.79 × 252.46 Å^3. The direction perpendicular to graphene is [111] plane of copper. All the structures have been equilibrated before applying the strain. The non-equilibrium MD (NEMD) has been used in the x-direction to apply uni-axial strain. Other directions have been controlled by using the Nose/Hoover pressure barostat. The temperature is controlled by using the Berendsen thermostat. The above graphs clearly show that the strain rate has a significant effect on the stress-strain behavior of the composites. In fact, for the slower rates graphene weakens the single-crystal metal matrix and for strain rate, ~1e10/s graphene shows an improvement. (d) and (e) show that the difference due to strain decreases with a decrease in strain rate. As there is not much difference in the stress-strain curve with strain rate 1e09/s and 1e08/s, we decided to use 1e09/s for single crystal copper and its composite simulations.

DISTRIBUTION A: Distribution approved for public release.

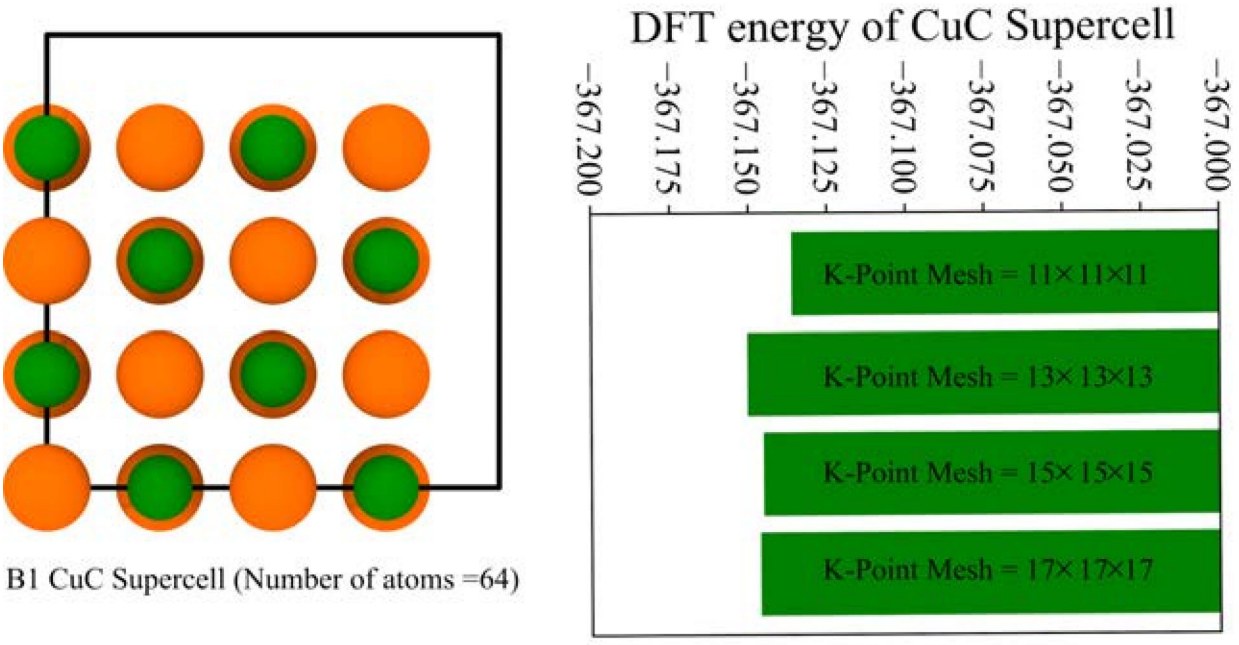

Figure 6.10: The figure shows the supercell for B1 CuC and energy convergence for K-Point mesh. The Brillouin zone was sampled with a $15 \times 15 \times 15$ grid as increasing the K-Point causes the energy difference of less than 0.01% (less than 2 meV).

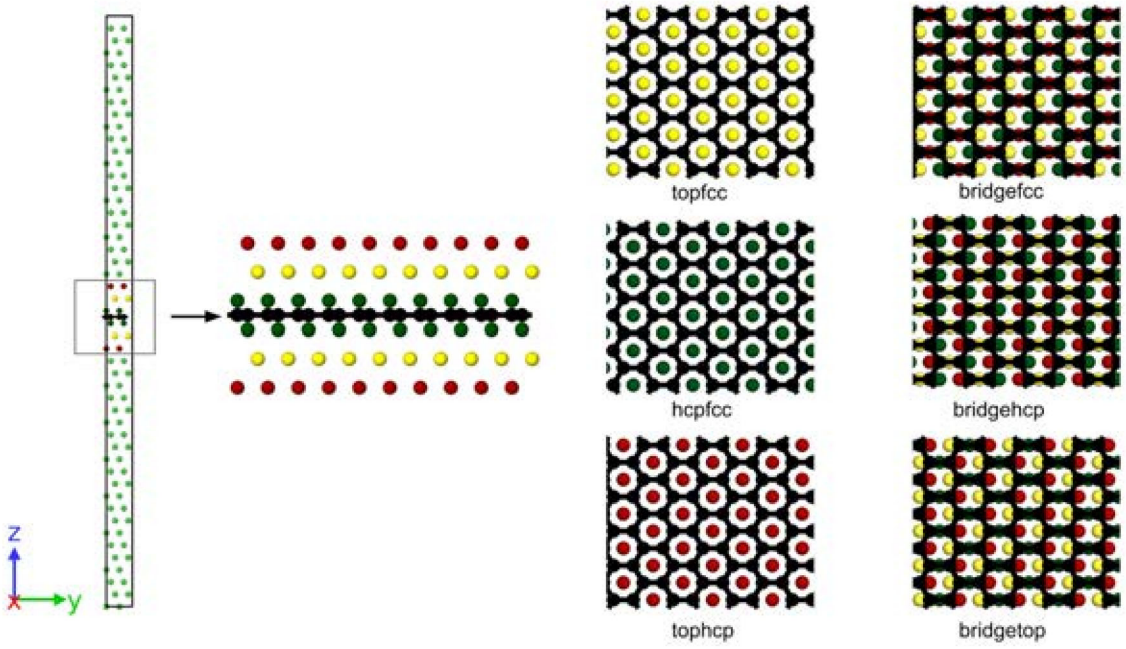

Figure 6.11: The figure shows the supercell for copper-graphene composite and the different interfacial structures used to compare the interfacial energy for 2NN MEAM and different sets of Lennard-Jones potential.

DISTRIBUTION A: Distribution approved for public release.

VII- Effect of polymer substrates on the properties of sputtered NiTi thin films

7.1 Overview

In this work, NiTi thin films are sputtered onto different substrates materials (polyimide foil, Si wafer, and Copper foil) with different deposition power, time, substrate temperature, and argon gas pressure. The sputter-deposited NiTi thin films on the polyimide foil substrates (Kapton, Upilex) and the Si substrates were analyzed to compare the characteristics of the thin films linked to the shape memory alloy properties of NiTi (composition, crystalline phases, and morphology). The polyimide substrates influence the Ni/Ti stoichiometry (up to -4.38 at.% Ni), morphology, and thickness (-417 nm to 132 nm) when compared to Si substrates. These effects are closely related to the difference in thermodynamic agreement of NiTi with the two substrates even when the films are deposited on both substrates simultaneously or with identical parameters. Additionally, the magnitude of effects caused by varying the power and pressure differ for each substrate type. Depositing NiTi over different Si-based substrates (i.e., Si(111), SiO, SiN) can also alter the film characteristics. However, those differences are often negligible, and the magnitudes are not as large as that observed when comparing the polyimide-grown and Si-grown films. The results indicate the need for direct characterization of films attached to polymer substrates due to differences in film characteristics that can alter the mechanical, optical, wetting, and shape memory alloy properties of NiTi thin films.

7.2 Introduction

NiTi-based shape memory alloys (SMAs) have received considerable interest as functional materials for many novel technologies owing to their outstanding biocompatibility, superelasticity, and shape memory effect [164–166]. In addition to investigations of the bulk material, advances in the miniaturization of technologies in the past two decades have encouraged integration of NiTi-based thin films in numerous devices including micro-actuators, micro-valves, micro-pumps, sensors, mirrors, and energy storage devices [167–173]. The large work output ($10\,\mathrm{J\,cm^{-3}}$) and elastic displacement (up to 10% strain) offered by the superelasticity and shape memory effect in NiTi thin films are particularly attractive as they exceed conventional micro-actuation mechanisms [172, 174, 175]. Well designed NiTi thin film actuators can also achieve frequency responses an order of magnitude higher than bulk counterparts due higher energy dissipation rates because of the larger surface area to volume ratio of the thin film [176]. While the biocompatability of NiTi is

DISTRIBUTION A: Distribution approved for public release.

linked to a TiO_2 surface layer that provides exceptional corrosion resistance and prevents leakage of Ni^+ ions into the body [166, 177]. The shape memory effect and superelasticy of NiTi are ascribed to the reversible martensitic phase transformation between the high-temperature Austenite phase (B2) and low-temperature Martensite phase (B19') [178]. The superelastic effect (SE) is caused by a stress-induced phase transformation between the two phases (B2↔B19'), while a thermally-induced transformation (B19'↔B2) causes the shape memory effect (SME) [164, 178]. The start and finish temperatures of each transformation along with the ambient temperature dictate which response will occur. This is due to the thermodynamic stability of each phase at those particular temperatures. At temperatures above martensite's thermodynamic stability, deformed NiTi recovers large stress and strains when unloaded (B2→B19'→B2). In comparison, heat is required to revert plastically deformed NiTi to its original shape below austenite's thermodynamic stability temperature (B19'→B2→B19'). Other than shape recovery, several material properties are altered during NiTi's phase transformation, including its crystal structure, elastic modulus, surface roughness, and electrical resistivity. The changes allow detection of the phase transformation and provide the basis for many of NiTi's proposed applications [169, 179–181].

Integration of NiTi-based thin films into many applications require the films to be released from the substrate. NiTi thin films are often deposited on rigid materials such as glass and Si-based wafers. A film adhered to a rigid substrate is sufficient for many applications, but deformable electronics (or Micro-Electromechanical Systems (MEMS) devices) require a flexible metal film and substrate combination [182, 183]. Glass and Si-based wafers are compatible with current microelectronic fabrication processes, however releasing the films from these substrates can be challenging. Numerous steps are required to release NiTi from the Si-based substrates that include dangerous chemicals such as the HF-based enchants for NiTi. In some cases, researchers have peeled thick NiTi films (thickness more than a few microns) from substrates, but this becomes non-trivial for the sub-micron films. With the continued miniaturization of devices sub-micron films will become more prevalent. A promising alternative is the direct deposition of NiTi on compliant polymer substrates [172, 184, 185]. Kapton and other polyimides are widely used as substrates for many notable micro/macro-electronic applications such as deformable electronics, micro-electromechanical systems (MEMS), and bimorph devices [27, 186]. Extensive work has been done to study and describe the behavior of such thin films on polymer substrates [25, 187, 188]. However, many unknowns remain in understanding how polymer substrates will influence the characteristics, behavior, and SMA properties of NiTi thin films, particularly in the sub-micron thickness regime.

DC/RF magnetron sputtering is the preferred technique for deposition of NiTi due to having better film quality, deposition rate, and film uniformity [174, 189]. While sputtering has these advantages in fabrication of the thin films, it also introduces challenges in controlling the films phase transforming ability. One being that sputtering NiTi from alloy targets yield films that have 2.0 at.% to 4.0 at.% Ti loss compared to the target due to the difference between the sputtering rates of Ni and Ti [174]. Precise control NiTi's composition is critical for controlling the martensitic phase transformation in the thin films [190, 191]. Every 0.1 at.% shift in the Ni content from the equiatomic ($Ni_{50}Ti_{50}$) stoichiometry can shift the start and finish temperatures of the phase transformations by up to 10 °C [165, 178, 192]. In many works, the loss is accounted for by placing extra Ti disks/flakes over the alloy target [193, 194] or by using Ti-rich targets [195–197]. Co-sputtering from either two elemental targets (Ni and Ti) or an alloy target ($Ni_{50}Ti_{50}$, Ti-rich, or Ni-rich) plus an elemental target allows fine adjustments over composition from process to process

DISTRIBUTION A: Distribution approved for public release.

[191, 197–201]. The crystalline nature of sputtered NiTi film is another challenge to the films transforming ability. The B2 or B19' phases are required for the martensitic phase transformation. However, thin films sputtered at room temperature are amorphous [178, 202]. Differential scanning calorimetry (DSC) shows that crystallization of the amorphous films occur at ~475 °C with an energy barrier of ~567.5 kJ mol^{-1} [199, 200, 203–206]. Research shows that one can often obtain crystallized films through a post-sputtering heat treatment near ~475 °C in a vacuum or inert gas environment. Apart from post-deposition heat treatment, films deposited on a heated substrate can also induce crystallization [172, 207–210]. The effects of heat treatment and substrate temperature on the microstructure of NiTi films on rigid substrates are well studied, but there are not many equivalent studies of that compare NiTi deposition on flexible polyimide substrates.

The thermal degradation of Kapton polyimide begins around ~400 °C with the outgassing of CO and CO_2 gases and is accompanied by shrinkage and loss of mechanical properties as temperatures increase further [211, 212]. This sensitivity to high temperatures makes it difficult to control the crystallization and transformation temperatures of NiTi films sputtered on polyimide substrates. In 1994, Hou et al. [213] demonstrated that the shape memory effect can be observed in NiTi thin films sputtered over polymer substrates for the first time with substrate heating of 400 °C. The 3 –7 µm thick NiTi films sputtered on 7.6 µm thick Polyimide (PI) were patterned into micro-actuators that recovered their undeformed shape when heated and cooled to liquid nitrogen temperatures [213]. Many other works have presented creative ways to overcome the crystallization barrier and control the phase transformation of NiTi deposited over polyimide substrates. Seguin et al. [207] showed that Ti-rich films crystallize more readily than Ni-rich films. Deposition parameters where first found for Ti-rich films with good shape memory properties sputtered on Si at a substrate temperature of 200 °C. Then the same deposition parameters were used to deposit NiTi films over polyimide foil substrates resulting in actuators capable of 2-way shape memory. Ishida et al [172, 208] successfully lowered the crystallization temperature of NiTi by optimizing a film alloyed with Cu. The parameters optimized on Si wafer were replicated on polyimide foil to create NiTiCu hairpin actuators with good actuation response. Kotnur et al [214] deposited NiTi thin films on spin-coated PI/Si, Kapton foil, and SiO_2/Si substrates at a substrate temperature of 450 °C. Each of the studied films were highly crystalline however the martensitic phase transformation only occurred in the films grown on the PI/Si and SiO_2/Si substrates. Residual stress during deposition caused the polyimide foils to lose contact with the substrate holder, leading to inadequate heat transfer, microcracking, and nonuniform film that suppressed the phase transformation. In a later work, Kotnur et al. [185] used a negatively RF-biased spin-coated PI/Si wafer as a substrate. The additional kinetic bombardment provided by the bias allowed in situ crystallization at a reduced substrate temperature of 350 °C. While work in improving film function and fabrication of free standing film has been presented, very few regarding polymer substrates have been presented [215]. These works have addressed other issues in the reliability of sputtered NiTi such as the effect of grain size [200, 216], surface oxidation and interface diffusion [217, 218], compositional uniformity [196], heat treatment [219, 220], and high cycle fatigue behavior [176]. The limited discussions of NiTi films deposited on polymer substrates in the literature indicate that much work remains to improve the technique. Nevertheless, the ability to sputter usable NiTi-based films on polymer substrates can broaden its application to many ares including wearable electronics and soft-bodied robotic actuators [171, 172, 183].

Recent works [173, 221] have highlighted current and past obstacles in the fabrication of NiTi thin-film devices. The influence of specific parameters on the characteristics and properties of NiTi

DISTRIBUTION A: Distribution approved for public release.

films are discussed exclusively in relation to Si, SiO_2, TiN, Si_3N_4, and polysilicon substrates. This work compares the composition, surface and cross-sectional morphology, crystalline nature, and shape memory effect of films sputtered on the polyimide foils to those sputtered on conventional Si and Cu substrates.

7.3 Methods

NiTi thin films are deposited using a DC/RF magnetron sputtering system (AJA, ATC Orion) equipped with in situ substrate heating and rotation. Two types of polyimide foils, Kapton 100HN and Upilex S, were chosen to study their influence on the films' characteristics. Upilex foils are less sensitive to higher temperatures compared to Kapton, making them more compatible with the thermal requirements for processing NiTi [211]. Si (100) wafers and Copper foils are also selected as substrates to compare their effect on the NiTi films to the polyimide foil substrates. Each film in this work is identified based on its processing group (R, H, A, T, P), substrate material (KP-Kapton, Si-Si(100), UP-Upilex S, Cu-Copper), and process set.

The films deposited with process R are sputtered from a single target at room temperature on Kapton and Si wafers. In process H, the films are also sputtered from a single target but at elevated substrate temperatures. Process A films are deposited under similar conditions as H but undergo post-deposition annealing without breaking the vacuum. Films processed with T are also deposited from a single target, but each film is deposited at a series of increasing substrate temperatures. Finally, process P films are co-sputtered from two targets using different power and pressure during each process run.

The processing parameters for each film deposited on Kapton and Si in group R are shown in Table 7.1 while those in group H are shown in Table 7.2. The Kapton and Si sputtered films from Tables 7.1 and 7.2 with the same process set are deposited together by attaching both substrates to the substrate holder. This arrangement allows us to study how NiTi films grown on Kapton differ from those sputtered onto Si. The films in Table 7.3 deposited on Cu foils are also sputtered at elevated substrate temperatures but have different parameters than the films in Table 7.2.

Table 7.1: Deposition parameters for sets of thin films sputtered from the $Ni_{43}Ti_{57}$ target at 100 W and 150 W power without substrate heating. The films in each set are deposited on the Kapton (R-KP*) and Si (R-Si*) substrates together.

Sample	Power (W)	Time (min)	Ar Pressure (mTorr)	Position (mm)	Ni (at.%)	Thickness (±10)(nm)
R-KP1	100	60	5	70	47.63	313
R-Si1					52.01	243
R-KP2		180			46.93	715
R-Si2					48.48	583
R-KP3	150	60	5	70	45.00	400
R-Si3					48.69	285
R-KP4		180			45.40	1000
R-Si4					47.35	877

Deposition parameters for the films deposited with process A are shown in Table S1 found in the supplementary document. Annealing is performed at 400 °C for 30 min without the flow of Ar

DISTRIBUTION A: Distribution approved for public release.

Table 7.2: Deposition parameters for three sets of thin films sputtered from a $Ni_{50}Ti_{50}$ target on Kapton and Si at elevated substrate temperature. The films on Kapton (H-KP*) and Si (H-Si*) in each set are deposited together.

Sample	Power (W)	Time (min)	Argon Pressure (mTorr)	Position (mm)	Substrate Temperature (°C)	Ni (at.%)	Indexed Phases	Film Thickness (± 10) (nm)
H-KP1	450	60	10	70	350	52.06	B2/R	832
H-Si1						53.08	-	865
H-KP2			2.7			48.32	B2	715
H-Si2						51.71	B2	1132
H-KP3	120	244	3	65	375	51.1	B2/R	385
H-Si3						52.57	-	1135

in the system. Group T and P contain films exclusively deposited on the Upilex foils. Table 7.4 shows parameters for films deposited on Upilex with temperatures ranging from 350 °C to 500 °C while all other parameters remain constant. Table 7.5 contains the films deposited on Upilex with all parameters held constant except the alternating of target power (80 W to 200 W) and argon pressure (3.5 mtorr to 8.0 mtorr).

Table 7.3: Films sputtered from $Ni_{50}Ti_{50}$ target on on Cu film with heated substrate.

Sample	Power (W)	Time (min)	Argon Pressure (mTorr)	Position (mm)	Substrate Temperature (°C)	Ni (at.%)	Indexed Phases	Film Thickness (± 10) (nm)
H-Cu1	450	300	3.5	70	430	51.02	-	5345
H-Cu2		290	3.5		450	49.74	B2	4100
H-Cu3		60	3		475	51.26	B2	1245

High purity (99.99% pure, ACI Alloys inc.) $Ni_{43}Ti_{57}$ or $Ni_{50}Ti_{50}$ targets are used for the single-target sputtering conditions, while a $Ni_{50}Ti_{50}$ and a Ti target are used for co-sputtering. Prior to sputtering, a base vacuum pressure of 1×10^{-7} mTorr is established, followed by back-filling the system with research-grade argon gas flowing at 10 cm^3 min^{-1}. The desired process pressure is then set and allowed to stabilize. A DC source supplies power to the alloy targets while the Ti target is supplied with a RF source. Each target is pre-sputtered for 10 min before deposition to remove any surface contamination. Unless otherwise noted, the polyimide substrates are cut into circles with mounting holes to secure them to the substrate holder. The holder is also rotated at a speed of 20 RPM to promote thermal and deposition uniformity and a soaking time of 30 min is used to allow the substrate to reach thermal equilibrium.

Planar morphologies of the NiTi films are obtained by Scanning Electron Microscopy (SEM, LEO (Zeiss) 1550) and Transmission Electron Microscopy (TEM, JEOL JEM 2100). The SEM samples are coated with 2 nm film of Platinum using a sputter-coater (Leica) to reduce charging effects. Cracking of the Platinum film is observed in a few micrographs. TEM samples are prepared from the Si substrates by back-polishing of the wafers up to 1200 grit SiC paper and 1 µm diamond suspension followed by ion milling to achieve the required electron transparency. Cross-sections are prepared with the dual-beam SEM/Focused Ion Beam (FIB, FEI Helios 600 NanoLab) to determine cross-sectional morphology and film thickness. Before sectioning, the film's surface is

DISTRIBUTION A: Distribution approved for public release.

Table 7.4: Deposition parameters for series of films sputtered on Upilex at elevated temperatures from $Ni_{50}Ti_{50}$ target.

Sample	Power (W)	Time (min)	Argon Pressure (mTorr)	Position (mm)	Substrate Temperature (°C)	Ni (at.%)	Indexed phases	Grain size ((nm)
T-UP1					350	49.71	-	48
T-UP2					400	50.61	B2	80
T-UP3	400	30	3.5	70	425	50.26	B2	90
T-UP4					450	50.28	B2	122
T-UP5					500	52.76	-	12.7

coated with a 500 nm thick layer of Platinum to protect against excessive ion beam damage. Each film's composition is obtained via Energy Disperse X-ray Spectroscopy (EDS) inside an SEM (FEI Quanta 600 FEG). The phases in the films are determined using X-ray diffraction (XRD, PANalytical X'pert Pro) with Cu-Kα(λ = 1.540 56 Å) X-rays. All films are characterized while attached to their respective substrates, and the indexed phases are provided in Tables 7.2- S2. Films on Kapton foils with the martensite R-phase are cut into a double-beam cantilever actuators to investigate their actuation properties [208, 213].

Table 7.5: Sputtering parameters for films co-sputtered on Upilex from the $Ni_{50}Ti_{50}$ and Ti targets. Power to the $Ni_{50}Ti_{50}$ was maintained at 200 W while varying Ti target power and argon pressure as shown.

Sample	Ti power (W)	Time (min)	Argon Pressure (mTorr)	Position (mm)	Substrate Temperature (°C)	Ni (at.%)	Indexed phases	Grain size ((nm)
P-UP1	200	30	8	70	400	49.40	B2	
P-UP2	80					58.10	B2	
P-UP3	200		3.5			47.50	R-phase	
P-UP4	80					54.80	B2	

7.4 Results and Discussion

1. Composition and thickness of films sputtered at room temperature

The unique sputtering conditions, composition, and thickness of the NiTi films deposited on Kapton and Si substrates at room temperature are shown in Fig. 7.1. The films with the same process number on the different substrates are deposited together by attaching both substrates to the substrate holder. In all films, the Ni atomic percentage is distinctly higher than the target's Ni content (43 at.%) as illustrated by the dashed blue line in Fig. 7.1. This difference is due to a difference in vapor pressure, the atomic mass difference of Ni and Ti atoms, and the higher sputtering rate of Ni atoms [190, 198]. The average deviation from the Ni content of the films from that of the target is 4.68 at.% Ni which agrees with values reported in the literature [197, 198, 222]. Fig. 7.1 (a,c) also show that the Ni content of the films sputtered on Kapton is distinctly lower than that of the films sputtered on Si.

DISTRIBUTION A: Distribution approved for public release.

The films on Kapton had lower Ni even with an increase the sputtering time from R-KP1 to R-KP2 (−4.38 at.% to −1.55 at.% Ni) or increase in target power from R-KP1 to R-KP3 (−4.38 at.% to −3.69 at.% Ni). Interestingly the thickness of the films obtain on kapton and silicon were also different with the films on kapton being 70 nm to 132 nm thicker for the 100 W depositing and 70 nm to 123 nm) for the 150 W as shown by Fig. 7.1 (c, d).

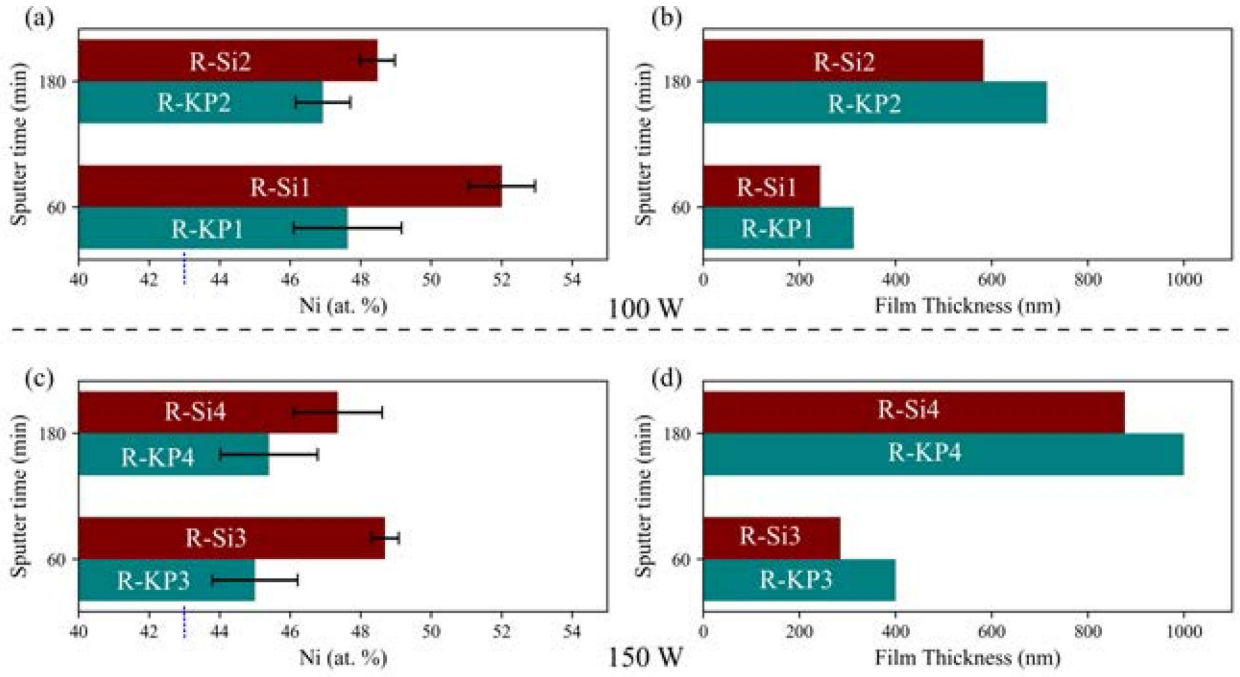

Figure 7.1: Composition and thickness measurements of samples deposited on Kapton and Si using the $Ni_{43}Ti_{57}$ target. Differences in the composition due to different substrate, sputtering time, and power are shown in (a) and (c), while the differences in thickness are shown in (b) and (d). The results illustrate that in addition to the compositional and thickness changes expected in NiTi films sputtered at different power and time, marked differences can be obtain when sputtering on Kapton compared to Si substrates.

This can be explained by differences in the films' growth mode due to the dissimilarity between the interface energies, sticking coefficient, and mobility (energy) of the adparticle on the two substrates. During room temperature deposition, the arriving atoms of Ni and Ti quench on the substrate surface to form islands [205, 215, 223]. Film nucleation sites precede the formation of islands and the number of nucleation sites depends on the energetic favorability of upcoming adparticles interacting with already formed nucleation sites or the substrate surface [33, 224]. The surface energy dependence implies that the substrate's surface plays a vital role in determining the morphology and growth mode of the films. While the difference in the composition and morphology between Si-based substrates can be negligible [199, 225] the balance of these three phenomena is far different between the polyimide and Si-based substrates than between Si-based substrates [214, 226]. Nucleation and an increased growth of NiTi crystallinity increases diffusion of the deposited atoms, which leads to a more dense microstructure. Therefore the density of nucleation site's plays a vital role in determining the the density of the final film. These effects will be discussed further in later section for the case of substrate heating. The observed decrease in the distribution of Ni and Ti atoms in the film with increased sputtering time is likely due to depletion of Ni on the surface of the target as the deposition process continues.

DISTRIBUTION A: Distribution approved for public release.

Ex situ crystallization of films with different characteristics

The samples deposited on Si were subsequently heat-treated for 30 minutes at 400 °C and their microstructural images are shown in Figure 7.2. All films prior to heat treatment had a diffuse ring pattern characteristic an amorphous matrix containing several nanocrystallites [209]. The amorphous films require heat treatment to become crystalline due to low adparticle mobility during deposition. The samples Si1A and Si2A are less than 600 nm thick. Wang et al. [204] have reported that below 600 nm, the grain growth rate decreases rapidly, clarifying the difference in the degree of crystallization in the Si3A from Si1A and Si2A. The crystallization dependence on thickness further reinforces the importance of substrate effects on film characteristics by influencing growth mechanics. Since the superelasticity and shape memory properties are closely linked to the composition and morphology of NiTi thin films. The results suggest that using films deposited on other substrates to characterize the thin films on polyimide substrates can lead to incorrect characterization and efforts should be made to conduct all characterization directly from PI-deposited films for accuracy.

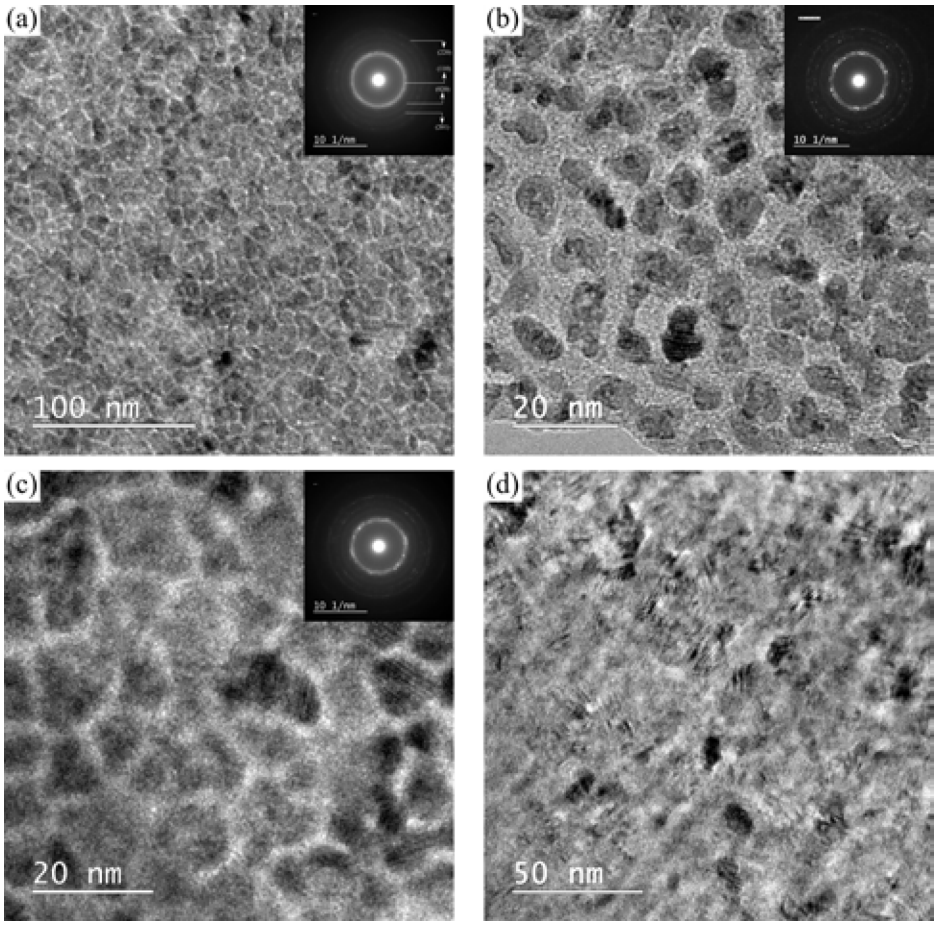

Figure 7.2: TEM images of the samples R-Si1, R-Si2, R-Si3, and R-Si4 after the heat treatment are shown in (a), (b), (c), and (d), respectivly. Insets show the diffraction pattern. As shown, the grains are nanoscaled with comparably thick amorphous matrix.

DISTRIBUTION A: Distribution approved for public release.

2. Morphology and crystalline nature of films deposited with substrate heating

Substrate materials' influence on energetics of film growth

The specific characteristics obtained in NiTi thin films deposited over Kapton and Si at elevated temperatures are shown in Fig 7.3 along with their parameters. Unlike the films in Section 1. these samples are deposited with a substrate temperature above room temperature to promote in-situ crystallization. The decrease in argon pressure in H-KP1 to H-KP2 and H-Si1 to H-Si2 lowers the Ni atomic percentage of the films. The change in Ni atomic percentage of film due to change in Argon pressure can be attributed to two factors: (a) The number of atoms getting knocked out from the target by the argon gas decreases with decrease in Argon pressure, but (b) The percentage of total atoms knocked out from the target reaching the substrate increases due fewer scattering events with gas. Higher argon gas pressures increase the probability of inelastic collisions between the argon atoms and the sputtered atoms traveling to the substrate. Thus, fewer Ti atoms reach the substrate due to their higher mass, increasing the atomic percentage of Ni in the film.

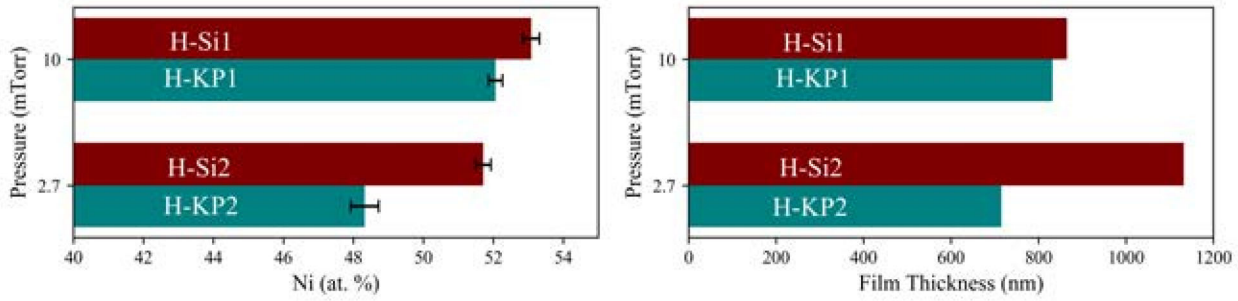

Figure 7.3: Composition and thickness of films deposited on Kapton and Si using the $Ni_{50}Ti_{50}$ target with a substrate temperature of 350 °C. Differences in the composition due to different substrate materials and pressure are shown in (a), while the differences in thickness are shown in (b). The results illustrate that in addition to the compositional and thickness changes expected in NiTi films sputtered at different power and time, marked differences can be obtain when sputtering on Kapton compared to Si substrates.

The deposition rate per unit power decreases with a decrease in power in samples KP2 (450 W), KP9 (330 W), and KP3 (120 W). The calculated values show a clear drop with the decrease in power ~0.0265 nm W^{-1} min^{-1}, ~0.0194 nm W^{-1} min^{-1}, and ~0.0131 nm W^{-1} min^{-1}.

The Ni content of films deposited in the case of Kapton is lower than the films deposited over the silicon wafer. The trend follows that of the films deposited from the $Ni_{43}Ti_{57}$ target in Section 1.. The trend in thickness is reversed in the samples deposited with in-situ heating. The thickness of the samples deposited over the Si wafer is larger in the in-situ heating case. A possible explanation for this is a change in the sticking coefficients and thus the growth mode of the film because of temperature.

Film H-Si2 is thicker than H-Si1, though the only difference between the processing parameters in these two samples is the argon gas pressure. The argon gas pressure in the chamber is responsible for knocking out the Ni and Ti atoms from the target, but it can also collide with the atoms before they reach the substrate. Increasing the Argon pressure increases the number of collisions and decreases the number of atoms reaching the substrate surface. The initial nuclei, growth shadowing, and mobility over the growing film surface play a major role in the final morphology of the films.

DISTRIBUTION A: Distribution approved for public release.

Jurusik defined the process as a superposition of adatom flux to the nuclei comprising of the The vapour flux onto the substrate is denoted and the adatom flux migrating over the substrate surface [227, 228]. these two process enlarge the nuclei with S2 then later by S2 involving incident atoms from S1 flux. the competition between S1 and S2 is dominated by S2 in the initial stages of growth however S1 will later dominate as the substrate is covered. Shadowing also takes over creating branched complex islands or only smaller islands. When the islands coalesces the flux S2 over the substrate surface is eliminated, and the films grow in thickness as the result of the incident flux S1 and the structure initiated in the earlier stage (i. e., large branched or smaller compact islands). The final growth structure gives rise to cauliflower-like or columnar structures. It was concluded that prerequisites for columnar growth were a limited surface mobility and an normal flux to substrate.

Si1 is amorphous nanoglass while sample Si2 is fully crystalline. Suggesting that the significantly lower argon pressure of Si2, compared to Si1, had a marked impact on the film's growth mode. The lower argon pressure also decreased Ni content. The width of the (110) B2 peak suggest that Si3 consists of partially amorphous and crystalline regions.

All three samples deposited over Kapton are crystalline, while only one sample deposited over the Si wafer is crystalline. The energy change of atoms reaching the substrate has changed the composition and has also affected the crystallinity of the film. The Si film deposited at 10 mTorr Ar pressure is amorphous and consists of nanoglass as shown in Figures 7.4. The film deposited at 2.7 mTorr is crystalline. A decrease in power has increased the Ni content in the H-Si3 sample for similar Argon pressure. The H-Si3 sample is also amorphous but has a more prominent glassy grain than the H-Si1 sample. The reason for this could be that due to a long time of sputtering in the H-Si3 sample, the amorphous grain boundaries have merged into each other [33]. The growth mode of H-KP1 and H-KP2 seem to be similar due to the presence of densely packed fibrous grains, as shown in Figure 7.4. The structure zone models proposed by Thornton or Anders suggest that the films lie in the transition zone[33, 229, 230]. The resultant structures in the transition zone are governed by the substrate temperature more than the argon pressure. Since H-KP1 and H-KP2 were deposited at the same temperature the structures are similar. However, the lower argon pressure of H-KP2 has increased the grain/cluster size as particles reaching the substrate surface have higher energy [33, 230]. Films H-KP1, H-KP2, and H-KP3 are fully crystalline, while sample KP9 is amorphous, as shown in Figure 7.4. Film KP9 is sputtered using less power than H-KP1 and H-KP2, implying that the atoms reaching the surface have lower energy in KP9. The deposition time of H-KP3 is four times longer than KP9 which likely contributed to it being crystalline.

The deposition of film has been carried out for substrate temperatures between the 350 °C and 400 °C that makes T_s/T_m ratio between 0.27 and 0.30. This implies that the microstructure of the film lies in transition zone (zone T) as defined by Thornton and Anders [229, 230]. The microstructure of the samples (densely packed fibrous grains or mounds) in Figs. 7.4, S1, and S2 confirm the insufficient adatom migration which caused nanocrystalline NiTi films [191, 201, 231].

DISTRIBUTION A: Distribution approved for public release.

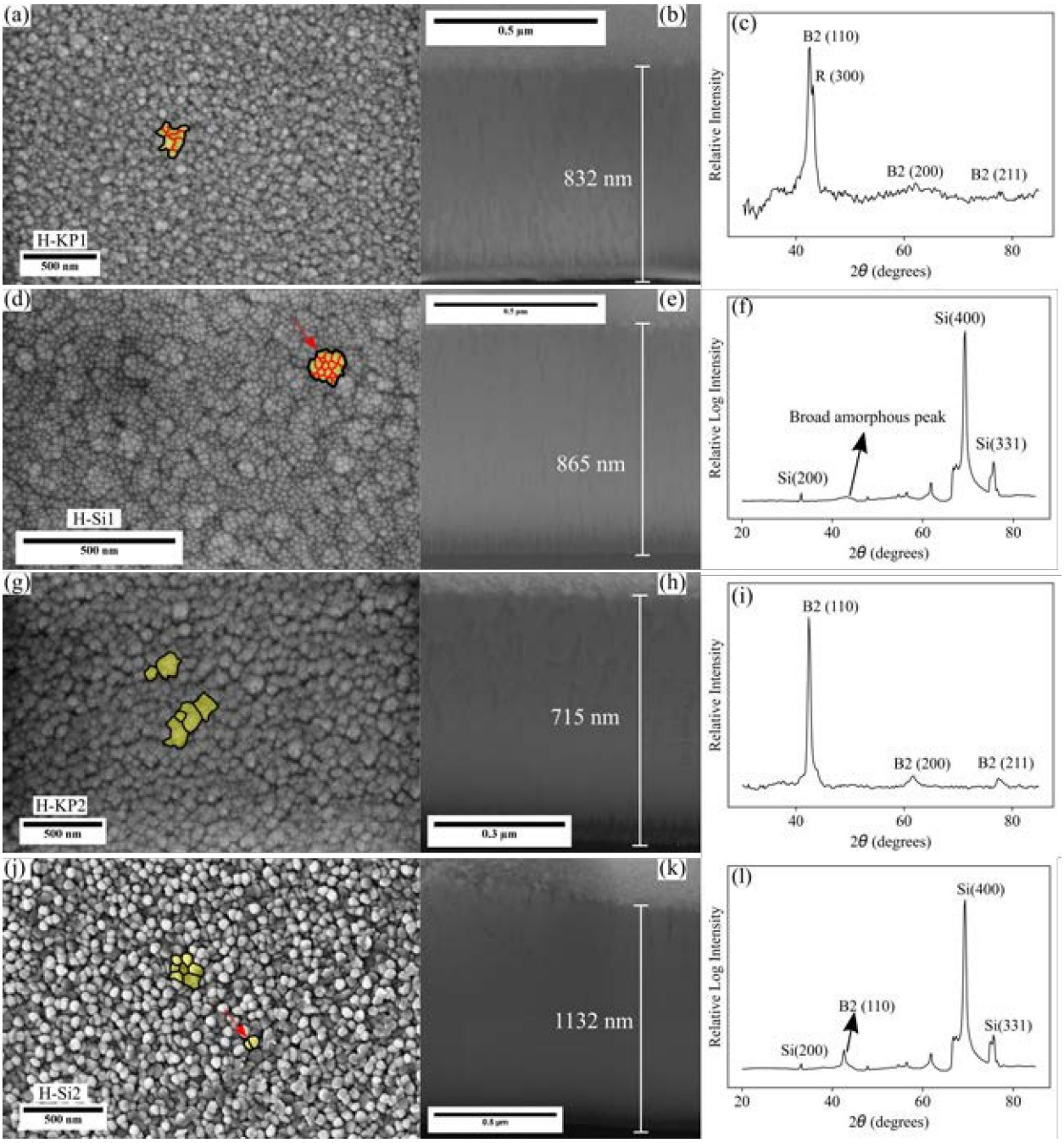

Figure 7.4: Surface and cross-sectional micrographs of films deposited on Kapton and Si with their corresponding x-ray diffraction patterns. H-KP1 (a)-(c) and H-Si1 (d)-(f) are deposited at 10 mtorr, while H-KP2 (g)-(i) and H-Si2 (j)-(l) are deposited at 2.7 mtorr. Both films on kapton contain B2 phase while only H-Si2 is crystalline. H-KP1 also contains the R-phase. The red boundaries show nanoclusteres in (a) and (d) that coalesces in the films at lower pressure to form the larger clusters of (g) and (d) in black (shown by red arrows).

DISTRIBUTION A: Distribution approved for public release.

Figure S2 compares the morphology and XRD scans of films KP5 and KP6. Film KP5 has a very sharp B2 peak, while sample KP6 consist of nanocrystallites. All deposition conditions of both samples are identical other than the sputtering time of KP5 being 25 min longer than film KP6. The increase in deposition time with in-situ heating provides more energy to the samples allowing the adatoms to assemble in a structured way; the same response was observed with KP3 from Figure 7.4 [33, 230]. It is reported that at thicknesses below 600 nm, the crystalline growth rate decreases, and there is an increase in the activation energy for crystallization, implying that crystallization needs higher temperatures to initiate [204, 219].

Coarsening of morphology with high substrate temperature

In terms of the structure zone models [33, 229, 230], the growth of H-Cu1 and H-Cu2 samples are in the transition zone (H-Cu1 has amorphous grains), while in H-Cu3, the growth is in Zone II. The NiTi film formed is either crystalline or amorphous, depending on the temperature. The increased temperature increases the probability of diffusion for incoming atoms. In Boltzmann statistic model the probability of diffusion is proportional to $\exp^{[-(E_a+n_nE_n)/kT]}$ where E_a is the activation energy for diffusion, E_n is the bonding energy with the nearest neighbor, n_n is the number of nearest neighbors, and k is the Boltzmann constant [232, 233]. The atoms diffuse in the thin films till $(E_a + n_nE_n)$ become large compare to kT and diffusion probability becomes small. For high temperatures, the atom needs a site where the bonding energy with neighbor atoms is high, leading to the formation of crystalline films.

DISTRIBUTION A: Distribution approved for public release.

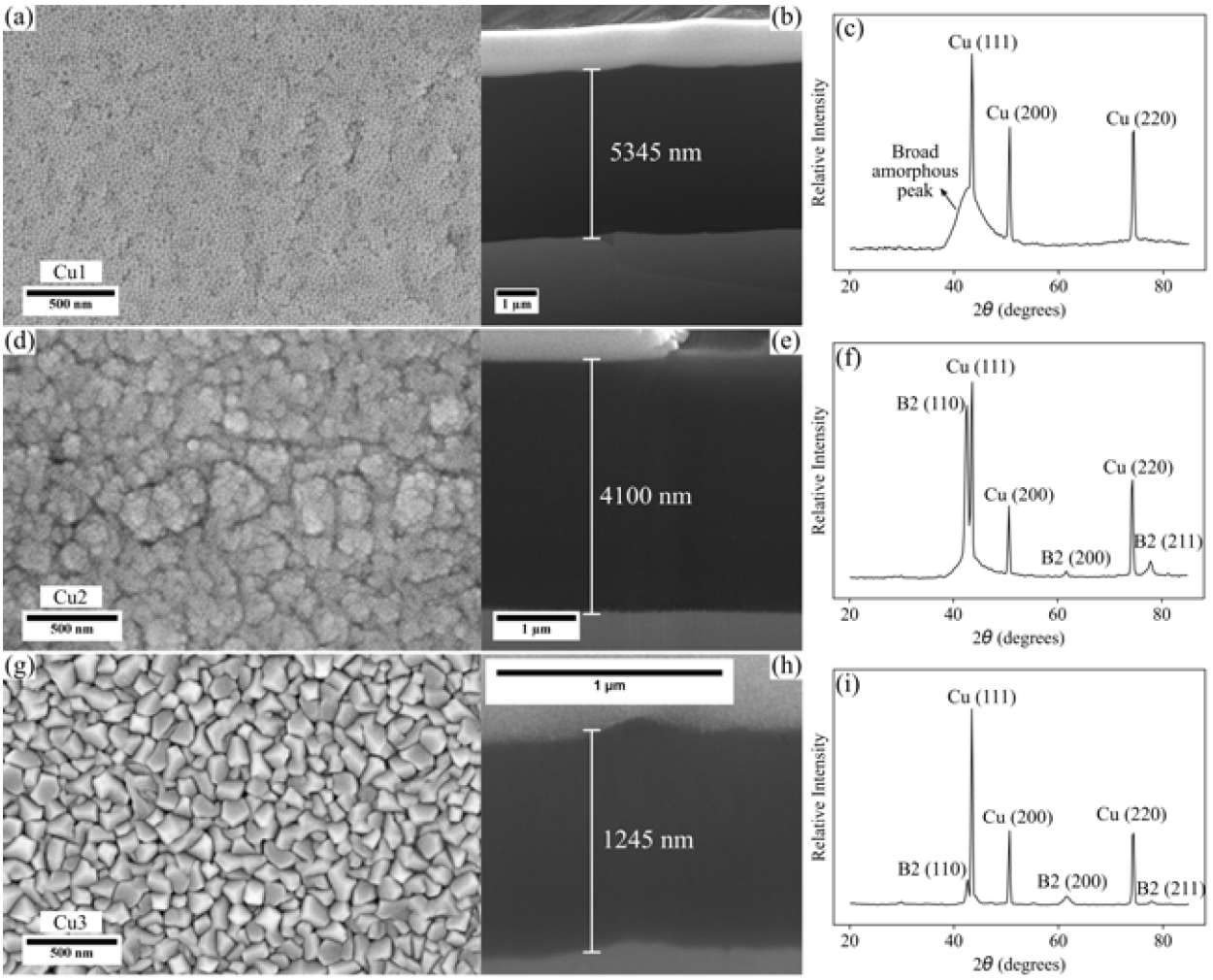

Figure 7.5: Surface micrographs, cross-sectional micrographs, and x-ray diffraction patterns of films deposited with a power setting of 450 W. Images (a)-(c) are from sample Cu1 (51.02 at.% Ni), (d)-(f) are from Cu2 (49.74 at.% Ni), and (g)-(i) is from Cu3 (51.26 at.% Ni). The argon pressure was maintained at 3.5 mTorr, 3.5 mTorr, and 3 mTorr with substrate temperatures of 430 °C, 450 °C, and 475 °C for H-Cu1, H-Cu2, and H-Cu3, respectively. Sample H-Cu1 is amorphous, and samples H-Cu2 and H-Cu3 are crystalline with larger cluster sizes. NiTi peaks are small in H-Cu3 compared to H-Cu2 because of the thickness of the NiTi layer. Both the increase in temperature and the lowering of Ar pressure from H-Cu1 to H-Cu2 promotes crystallization during sputtering. However, the reduction in temperature and time of H-Cu3 suggest that Ar pressure has a stronger effect on the growth mode. [H-Cu1 300min 3.5mtorr 430C 17.82 nm/min, H-Cu2 290min 3.5mtorr 450C 14.14 nm/min, H-Cu3 60min 3mtorr 475C 20.75 nm/min]

DISTRIBUTION A: Distribution approved for public release.

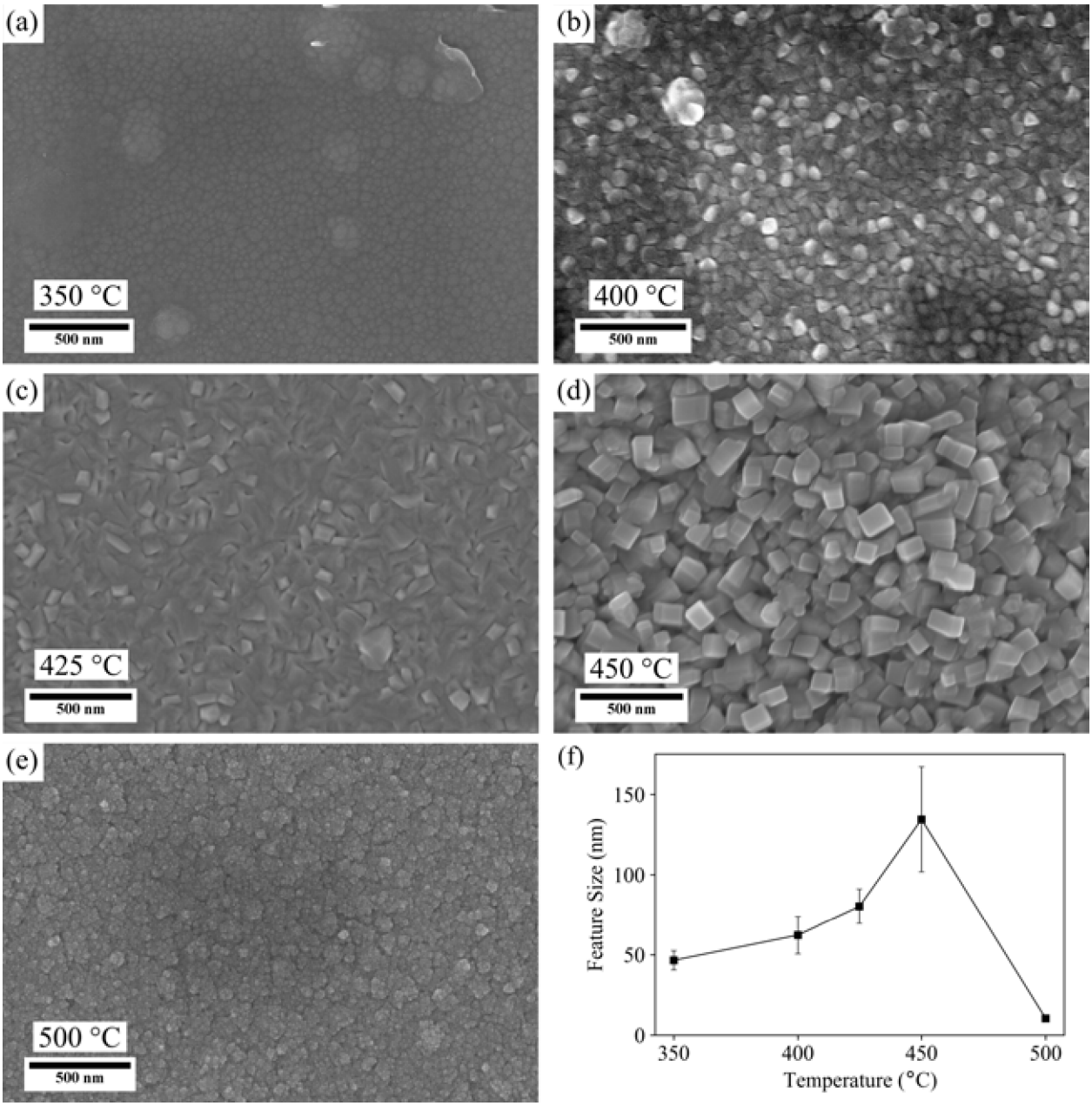

Figure 7.6: Surface micrographs of films deposited with 450 W power and an argon pressure of 3 mTorr on Upilex. Films T-UP1 (a), T-UP2 (b), T-UP3 (c), T-UP4 (d), and T-UP5 (e) were deposited with substrate temperatures of 350 °C, 400 °C, 425 °C, 450 °C, and 500 °C, respectively. The temperature influences the surface morphology of the films. Sputtering over Upilex allows use of higher temperatures for in situ crystallization, however at 500 °C the Upilex degrades and the film debonded from the substrate resulting in an amorphous structure.

DISTRIBUTION A: Distribution approved for public release.

The effects of substrate temperature on the microstructure and crystalline nature of the films is clearly shown in the three films deposited on copper of Fig. S3. As the power used in sputtering is the same, the difference in the deposition rate is due to the difference in substrate temperature. The sample sputtered at 430 °C is amorphous. The deposition rate has decreased with an increase in temperature from sample Cu1 ~ 17.82 nm min^{-1} to sample Cu2 ~ 14.14 nm min^{-1}. It should be noted that both H-Cu1 (T_s/T_m ~ 0.33) and H-Cu2 (T_s/T_m ~ 0.35) are near the end of Zone T of Thornton model and that's why they have fibrous grain (or mound) structure [33, 229, 230]. The deposition rate has increased in the case of H-Cu3 ~ 20.75 nm min^{-1}. The reason for this is the change in the growth mode of H-Cu3 (T_s/T_m ~ 0.37). The growth in the H-Cu3 sample lies in Zone II of the Thornton model, which can also be determined by looking at the surface morphology. Sample Cu3 is rougher. The reason for roughness is that the crystals, due to elevated mobility of surface atoms that migrate to crystallographic sites that minimizes energy, thus creating a faceted geometry. Later since the surface energy is less for particular surfaces in the Crystal (surfaces of Wulff shape), combined with the shadowing effect have made the surface rough [33]. this effect is opposite of that observed by mohri et al [215] due to our films crystallizing in situ while theirs were annealed ex situ. Sample Cu1 is amorphous, and samples Cu2 and Cu3 are crystalline with larger cluster sizes. NiTi peaks are small in Cu3 compared to Cu2 because of the thickness of the NiTi layer. Both the increase in temperature and the lowering of Ar pressure from H-Cu1 to H-Cu2 promotes crystallization during sputtering. However, the reduction in temperature and time of H-Cu3 suggest that Ar pressure has a stronger effect on the growth mode.[Cu1 300min 10mtorr 430C 17.82nm/min, H-Cu2 290min 3.5mtorr 450C 14.14nm/min, Cu3 60min 3mtorr 370C 20.75nm/min]

Pan et al [216] suggest that there is a dependence on thickness and grain size with R-phase of NiTi that allows it to be stable at room temperature. Also the residual stress caused R-phase detection at room temperature. 300 MPa 1000 nm from 1300 MPa at 200 nm.

In agreement with the literature, the results have shown that the parameters determining the energy (or velocity) of atoms reaching the substrate are power and argon pressure. The power controls the atoms' energy when knocked out from the sputtering target, while the argon pressure determines the number of inelastic collisions before condensing on the substrate. By changing these two parameters, we can get Ni-rich films (e.g., samples H-KP1 and H-KP3) or Ti-rich films (e.g., sample H-KP2 and KP13) from the equiatomic target[190]. Simply increasing the temperature and power does not result a fully crystalline film. Even with a substrate temperature of 430 °C Cu1, as shown in Figure S2, is not fully crystallized.

3. Relationship of thermomechanical history of NiTi and its actuation

It is worth noting that the phase was detected in the films through XRD were B2 even though the composition obtained from EDS predicted the B19' phase. From a metallurgical perspective, the composition of the solid solution needs to be taken into higher consideration since it is the only portion of the alloy that undergoes the phase transformation. However, heat treatment and residual stress can cause a secondary phase that will alter the stress and temperature requirements for the phase transformation. Therefore, this is expected due to the thermomechanical history of NiTi being more important than the overall composition of the material. It has been reported recently that grain size plays a critical role in the phase transformation of NiTi. The nanograins of the thin film are likely to stabilize the B2 phase, and more investigation is required to describe the relationship

DISTRIBUTION A: Distribution approved for public release.

entirely. Change in radius of the film/kapton actuator is used with the equation below was used to determine change in strain in the film in its two positions.

$$\varepsilon = \frac{h}{2r} \times 100\% \tag{7.19}$$

$$D_{recovery} = \frac{d_{rest} + d_{actuated}}{2D_{rest}} \tag{7.20}$$

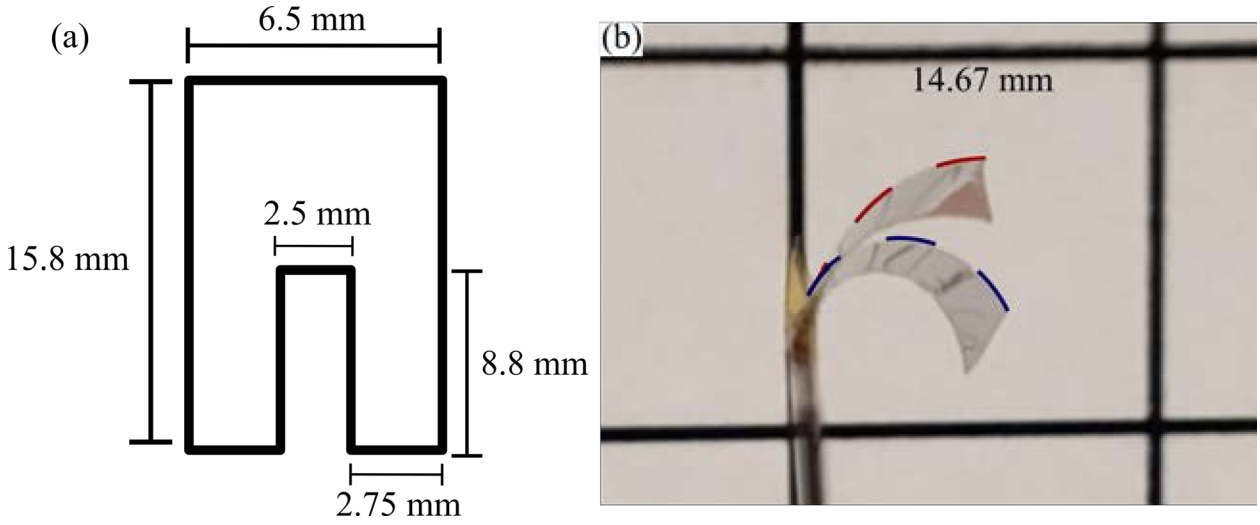

Figure 7.7: Simple double-beam cantilever actuators fashioned from the binary NiTi thin films sputtered on Kapton foil. The geometry of the actuator is shown in (a) and a demonstration of the actuation is shown in (b). The at rest state is outlined in blue ($r \approx 5$ mm 0.0083%) while the state after applying 5V to the legs of the hairpin is shown in red ($r \approx 7.5$ mm 0.0055%). The actuator shows two-way shape memory effect due to additional residual strain generated from thermal expansion coefficient mismatch. The two-way shape memory effect shows good cyclical response and has a stroke of ~6.30 mm. Only our films containing the martensite R-phase are capable of the shape memory affect. KP1 (200W 3.5mtorr) $D_{recovery} = 1.25$

7.5 Conclusion

In recent years, considerable progress has been made in utilizing the unique properties of NiTi-based shape memory alloys for numerous innovative devices in a wide range of applications. For many of the devices that operate at the microscale, NiTi should be fabricated as a thin film. The design of microstructural features and surface/interface properties is crucial for the development of a thin films for any particular application. The processes (like atomic migration, nucleation, etc.) during deposition at the substrate surface determine the microstructure and interface properties between NiTi film and substrate that dictate device performance. These processes can differ greatly with polymer substrates compared to rigid substrates. Hence, understanding the differences and similarities of the NiTi thin films deposited on polymer and rigid substrates is important to the development of reliable devices. In this work, by performing a parameter study, we show the interconnection between the processing parameters (including sputtering power, sputtering time, substrate temperature, the substrate to target distance, and argon pressure) and the properties of

DISTRIBUTION A: Distribution approved for public release.

sputter-deposited NiTi thin films on three different substrates (Silicon wafer, Copper, and Kapton). The results show that NiTi thin films will have remarkably different properties on different substrates even by selecting common sputtering parameters. In some past works, the film sputtered on Si wafers has been used to characterize the films on polyimide surfaces. So, our results here indicate that this can lead to a significant error in parameter selection for films sputtered on polyimide. Our results also investigate how the film's crystallinity can be improved by in-situ heating, increasing power, or decreasing the working argon pressure in the chamber. The dependence of the film composition on the sputtering parameters is also studied. It is shown how the Ni-rich or Ti-rich films can be deposited by adjusting the distance between target and substrate, power, and Argon pressure. This work will be invaluable in selecting sputtering parameters to obtain the crystalline film of NiTi with specific properties for various applications.

This work will be valuable to future scientists aiming to deposit novel NiTi-based structures on polymer substrates.The shape memory and superelastic effect of NiTi thin films combined with the polymer substrates can be utilized in devices, such as actuators in micro-electro-mechanical systems (MEMS).Thus, further investigation is required before widespread adoption of NiTi-based thin films in high cycle actuation applications. Several recent works have made significant progress toward this end.

Acknowledgement

This material is based upon work supported by the Air Force Office of Scientific Research under award number FA9550-18-1-0169.

7.6 Appendix

DISTRIBUTION A: Distribution approved for public release.

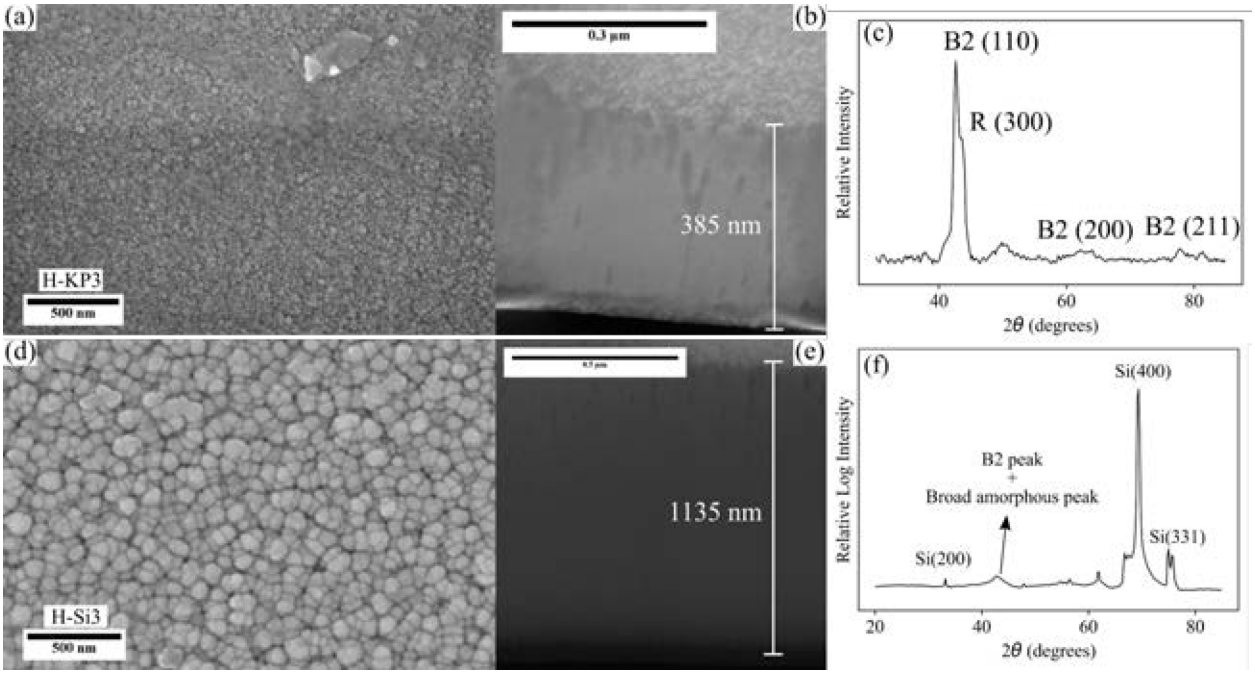

Figure 7.8: Surface micrographs, cross-sectional micrographs, and x-ray diffraction patterns from films sputtered on Kapton and Si at 370 °C with 120 W. H-KP3 51.1 at.% Ni is shown in (a)-(c) and H-Si3 52.57 at.% Ni) (d)-(f). The width of the (110) B2 peak suggests that H-Si3 consists of partially amorphous and crystalline regions. decreasing the argon pressure and increasing the sputtering power increases the crystalline of thin films.

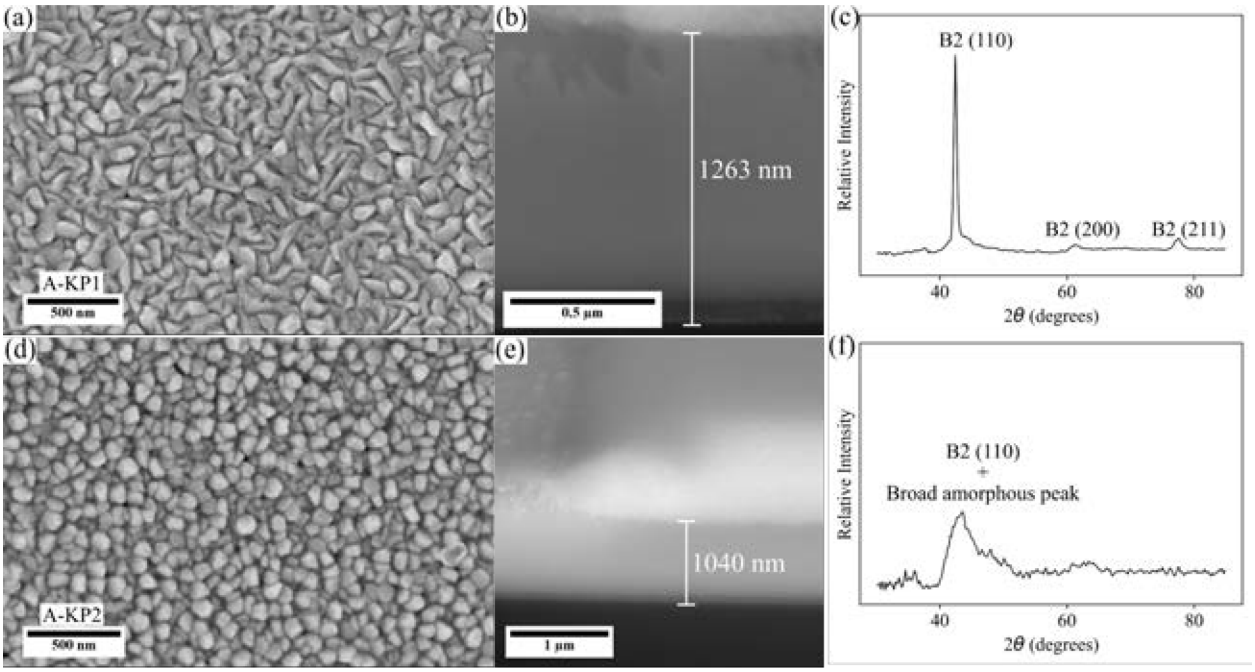

Figure 7.9: Surface micrographs, cross-sectional micrographs, and x-ray diffraction patterns of films deposited with 450 W power at a substrate temperature of 380 °C and argon pressure of 3 mTorr. Images (a)-(c) are from A-KP1 (49.25 at.% Ni) which was sputtered for 85 min, while (d)-(f) are from A-KP2 (49.04 at.% Ni) sputtered for 60 min. Although the samples were deposited with identical conditions, the higher deposition time of H-KP1 contributes to it being crystalline while H-KP2 remained amorphous. [KP5 17.33nm/min, KP6 14.86nm/min]

DISTRIBUTION A: Distribution approved for public release.

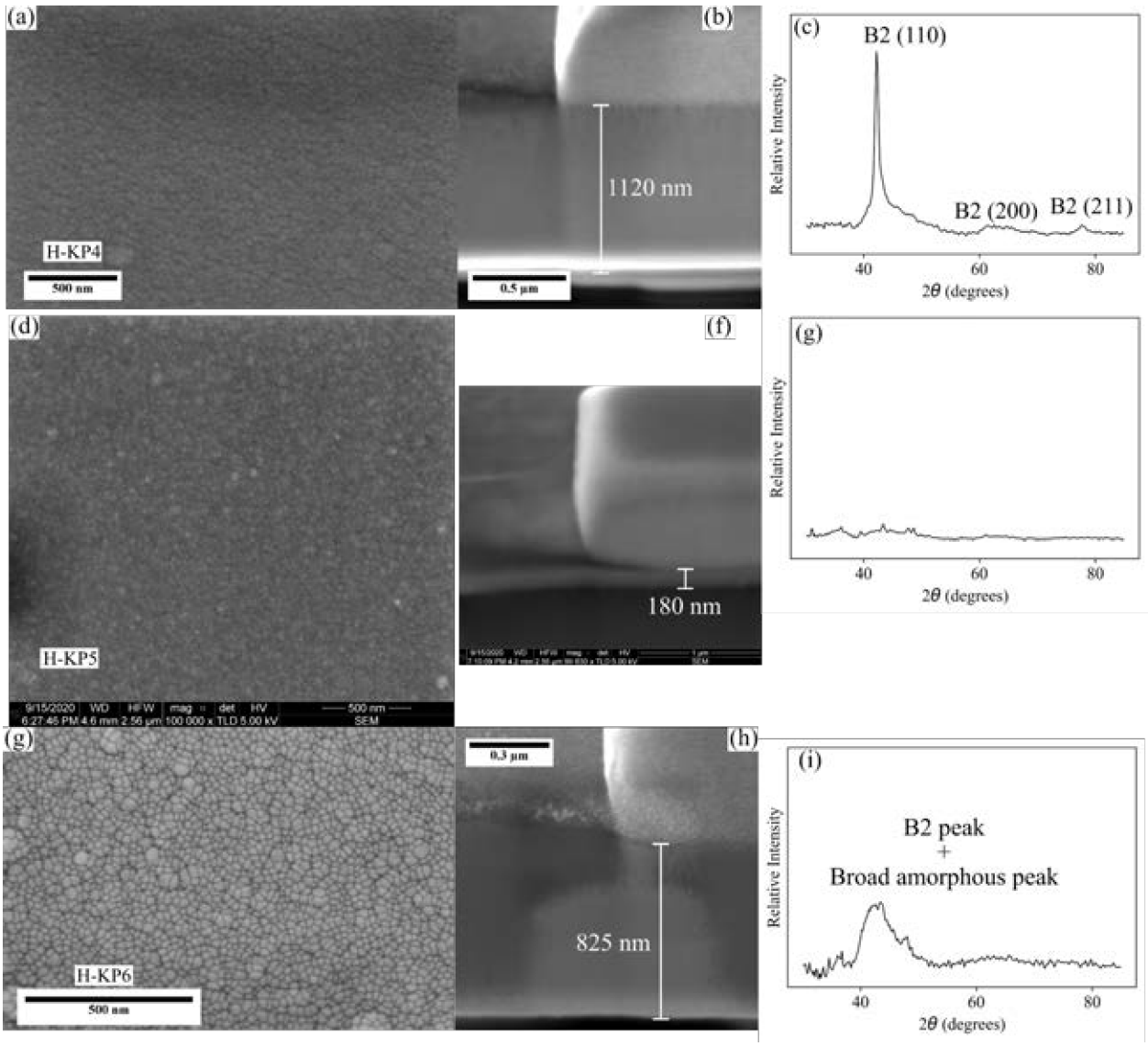

Figure 7.10: Comparison of samples H-KP4, H-KP5, and H-KP6

DISTRIBUTION A: Distribution approved for public release.

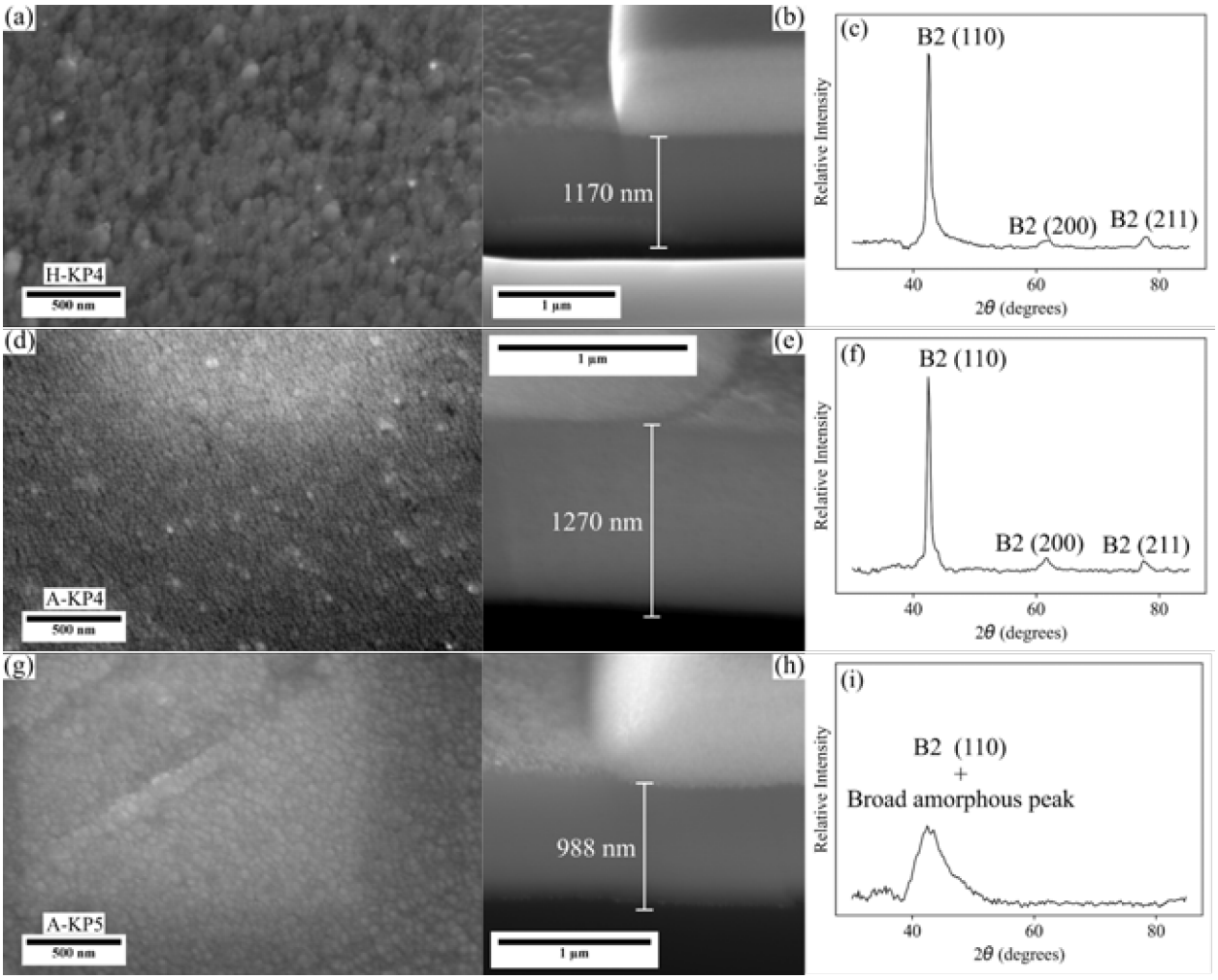

Figure 7.11: Surface and cross-sectional micrographs for select samples deposited on Kapton at 380 celsius and their corresponding x-ray diffraction patterns. Images (a)-(c), (d)-(f), and (g)-(i) are from sample H-KP4 (49.39 at.% Ni), A-KP4 (49.31 at.% Ni), and A-KP5 (47.92 at.% Ni), respectively. Sample KP13 is not fully crystalline when compared to H-KP4 and A-KP4. The increase in power (50 W) has made sample A-KP5 far from the NiTi equiatomic composition.

DISTRIBUTION A: Distribution approved for public release.

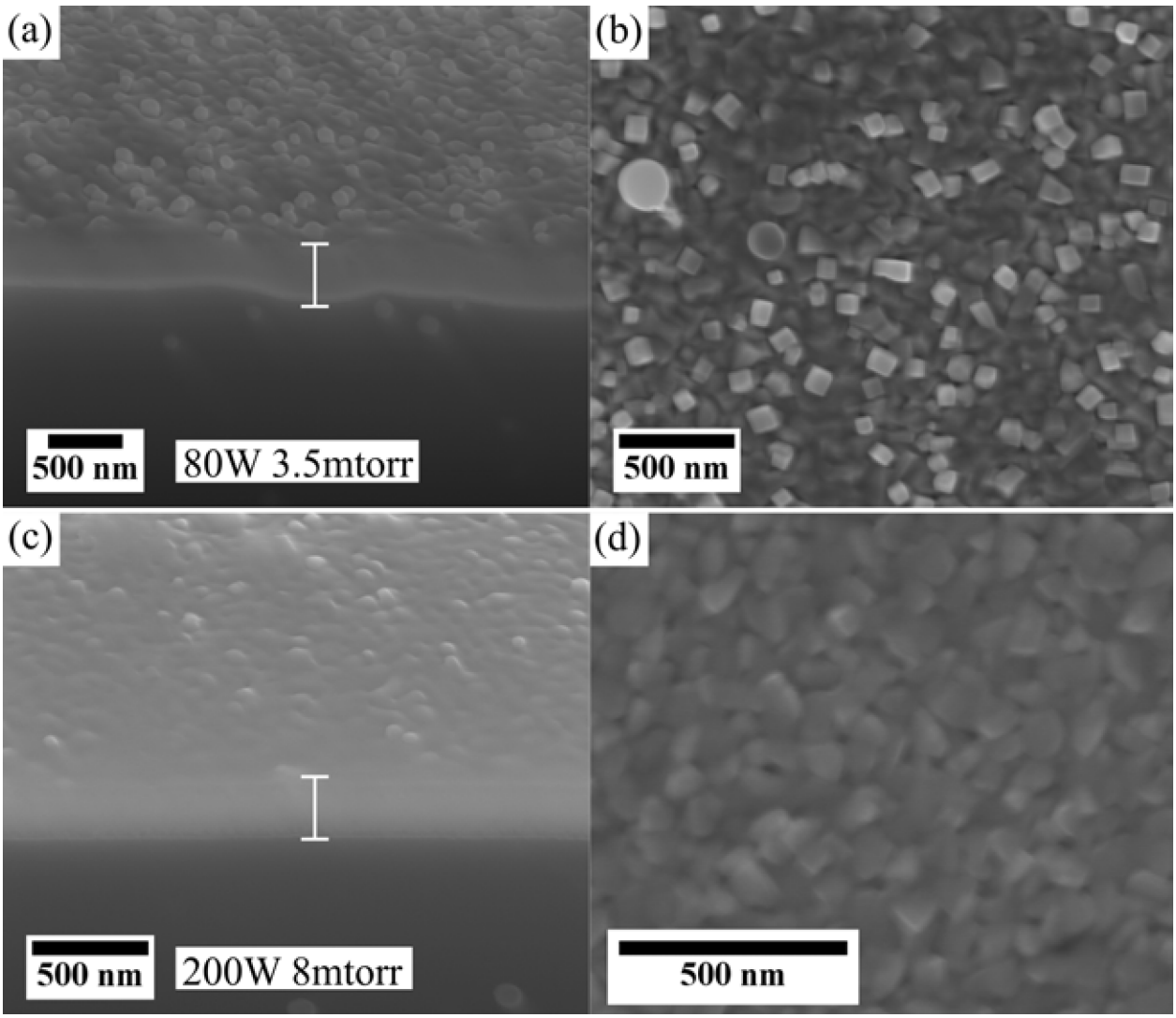

Figure 7.12: The cross-section and top surface of sample deposited on Upilex using two set of parameters.

DISTRIBUTION A: Distribution approved for public release.

VIII- Metallic Glass-Graphene Composites (MGGCs) with High Strength and Ductility

8.1 Abstract

While metallic glasses exhibit exceptionally high strength, their relatively low ductility, accompanied by catastrophic failure caused by the formation of shear bands, is the major obstacle to using these materials in practical applications. Despite discovering some methodologies for improving the near-zero ductility of metallic glasses, overcoming this deficiency is still the most active field of research in designing and fabricating bulk metallic glasses. This work utilizes computational studies at the atomistic scale to demonstrate that adding graphene to metallic glasses is a superior method to improve their ductility. Our results show that the graphene layers in metallic glass-graphene composites (MGGCs) will enhance the ductility by activation of three deformation mechanisms, including (*i*) confining the space for shear band formation, (*ii*) retarding the propagation of embryonic shear bands, and (*iii*) increasing the resistance of the metallic glass matrix against shearing during the nucleation and propagation of shear bands.

8.2 Introduction

8.3 Computational Investigation of Deformation Mechanisms at the Atomistic Scale of Metallic Glass-Graphene Composites (MGGCs)

The Discovery of metallic glasses, also known as amorphous metals, in 1960 promised a revolution in metals. The absence of slip systems and the dislocation-free deformation mechanisms at the atomistic scale of metallic glasses, because of their disordered structure, gives them a unique potential to have high yield strength, high fracture toughness, good corrosion resistance, and large elastic limit [234, 235]. However, despite these superior attributes, the use of metallic glasses is limited because of their near-zero ductility [236]. The lack of ductility is caused by the severe localization of plastic flow in these alloys, known as shear bands (SBs). shear bands are a type of material instability. They are initiated in the metallic glass regions where intrinsic resistance is low due to the local arrangement of atoms in the material [237, 238]. A catastrophic failure follows the formation of these highly localized SBs in the material. The mechanisms causing a delay in the formation of shear bands increase the ductility of metallic glasses.

DISTRIBUTION A: Distribution approved for public release.

The ductility of metallic glasses can be efficiently improved by inhibiting the formation, stopping the propagation, or delocalizing the growth of shear bands [234, 239]. Over the past few years, multiple attempts have been reported to introduce structural heterogeneities or utilize the size reduction in metallic glasses, which can affect the shear bands formation and propagation to improve the ductility. The structural heterogeneity can be introduced by adding nano precipitates [240], crystalline nanolayers [234] or structural boundaries, as in nanoglass [241]. The formation of crystalline phase (such as dendrites [242–247] or in form of nanolayers [234, 248–250]) inside the amorphous phase have also been shown to increase the ductility of metallic glasses. In some successful attempts, the ductility of Ti-Zr based bulk metallic glass (BMG) exceeded 10% [247], and ductility of La-based BMG was increased to 6-7% [245] due to reinforcement of crystalline dendrites. By investigating the fracture surfaces in Cu/amorphous CuNb multilayer, Fan et al. [234] have shown that adding crystalline phase can lead to ductile fracture of amorphous materials. Similar improvement and suppression of localized shear bands have been reported for Cu50Zr50/Cu, and Cu54Zr46/ Cu multilayers composites [249, 250]. These improvements have resulted from either unavailability of the critical size needed for shear band formation or increased resistance to shear bands propagation due to structural heterogeneities.

Graphene has emerged as a promising reinforcement material for crystalline metals in recent years [13, 20]. It is well established that the dislocation impeding by the graphene is the leading cause of improvement in mechanical properties of metal-graphene composites [13, 15, 16]. There are very few studies investigating the reinforcement of graphene in metallic glasses. In an experimental investigation, Park et al. [24] have shown that reinforcement of graphene in Cu50Zr50 metallic glasses increases the ultimate tensile strength and increases the fracture strain from $3.69\% \pm 0.04\%$ to $5.39\% \pm 0.32\%$. This increase was attributed to the enhanced plastic flow on sub-100 nm layers (thickness of metallic glass layer was 60 nm). Rezaei et al. [239] have studied the effect of graphene interface in the nanolaminates using atomistic simulations and have found that proper dispersion of graphene can increase ductility by 100 % and toughness by 150 %. In more recent work, Xie et al. [251] have utilized molecular dynamics simulations to study the effect of metallic glass layer thickness on the mechanical properties of metallic glass-graphene nanoplatelet composites. Their results show that increasing the fraction of graphene nanoplatelets in the composite enhances tensile strength and the fracture strain.

While the results in these few works have shown the prominent potential of graphene to improve the ductility of metallic glasses, the fundamental deformation mechanisms behind this phenomenon are still highly unknown. In this paper, we unravel these mechanisms at the atomistic scale by molecular dynamics simulations. Our results show that embedding graphene will improve the ductility of metallic glasses with three mechanisms, as schematically shown in Figure 8.1. As it will be shown, these mechanisms will also contribute to boosting the strength, besides improving the ductility. It is worth noting that it is not accurate to consider the ductility in the Molecular Dynamics (MD) simulations of metallic glasses as the full failure or the end of the stress-strain curves. Instead, it is much more accurate to quantify the ductility by tracking the formation and propagation of shear bands. In experiments, when the shear bands form, the material is at a very high risk of experiencing a catastrophic failure. However, in the MD calculations, the simulated system is defect-free, and the loading is applied as a continuous strain-controlled deformation of the box which contains the material. With these assumptions, unlike the response in experiments, a catastrophic failure will not happen in the MD simulations. For the same reasons, it has been proposed that the critical condition in metallic glasses corresponds to embryonic shear band (ESB)

DISTRIBUTION A: Distribution approved for public release.

propagation, not its nucleation [235]. To resolve this inconsistency, we will consider the formation of shear bands, which is accompanied with a negative slope in the stress-strain curve, and the stress required for the propagation of shear bands (known as τ_{glue} [235]) as the gauge of ductility. The quasi-steady-state glue traction, τ_{glue} is explained in more details in section 2. and 3..

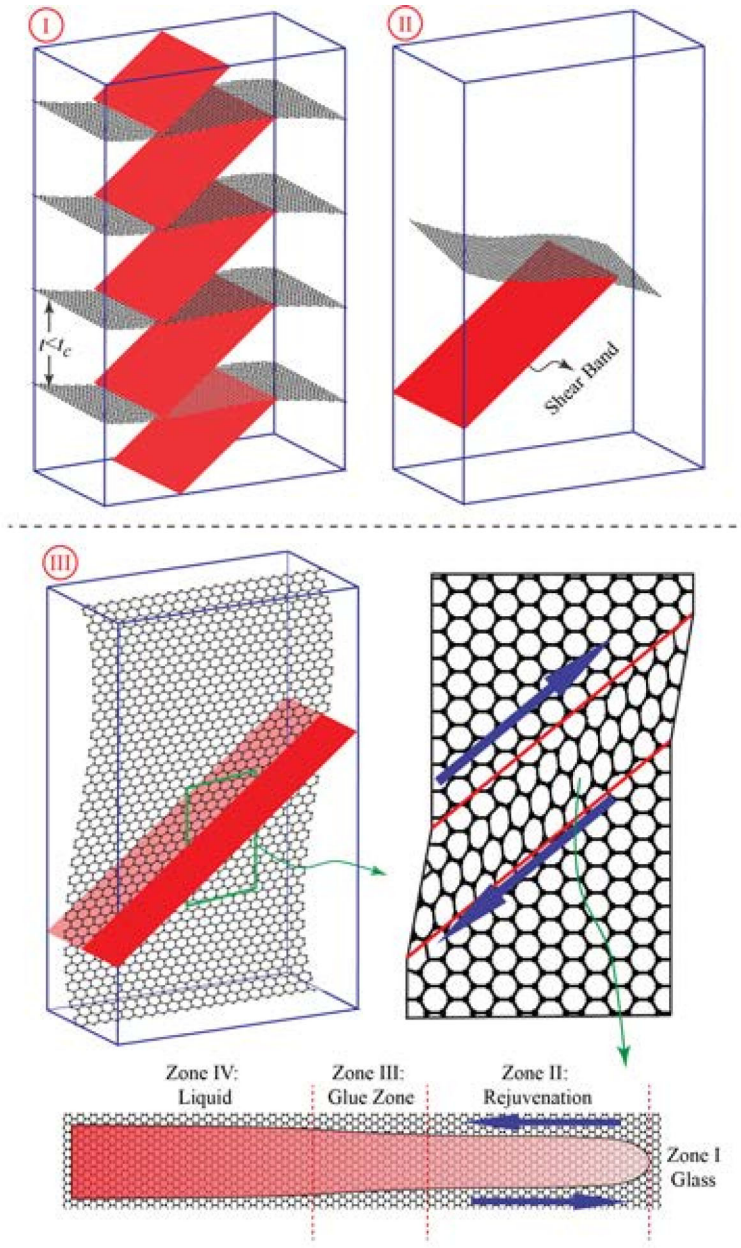

Figure 8.1: (I-III) Three methods by which the embedded graphene can improve the strength and ductility in metallic glasses. The bottom panel shows the deformation mechanisms around each shear band (see text for details).

In mechanism I, the total thickness is fragmented by the graphene sheets into partitions with smaller thicknesses compared to the sample thickness. Experiments and computational works have shown that the shear bands will not form if the available thickness of a metallic glass layer is less than a critical value t_c (usually between 10 to 50 nm) [235, 252–255]. It is worth noting that some

DISTRIBUTION A: Distribution approved for public release.

experimental works have been reported on using this property to improve the ductility of metallic glasses in the past few years. For this purpose, multilayer structures have been fabricated, made of alternating crystalline and glass layers, in which the thickness of the glass layer is less than this critical value [234, 253, 256–261]. Although adding crystalline layers in between the glassy layers improves the ductility to some extent, a portion of the strength is inevitably compromised because (*i*) the strength of the crystalline layers is much lower than that of the glass layers, (*ii*) the interfaces between the amorphous and crystalline layers act as a very active source of defects and dislocations in the crystalline layer [234, 255, 257, 258]. On the other side, dislocations in the crystalline layer pileup at the crystalline-amorphous interfaces, and the stress concentration at the tip of these pileups triggers shear bands in the amorphous layers [262]. In this paper, we will show that making a lamellar structure with glassy layers separated with graphene sheets (see Figure 8.1-I) will cause the system to be ductile without compromising its strength. In this case, the total thickness is fragmented into partitions with thicknesses smaller than the critical length. However, in contrast with adding crystalline layers into the metallic glass, a weak interface is not added to the structure, and there will be no dislocation pileup in graphene's case. Also, the single-atomic layer of graphene will not make any defect in the matrix material.

As discussed above, when the stress in metallic glasses reaches a threshold value, multiple embryonic shear bands nucleate in the material [263–266]. At this stage, the material is still not failed. Catastrophic failure happens when these discrete shear band embryos join each other and start propagating as continuous shear bands [235]. In the following sections, we will show that the graphene flakes will retard the propagation of these continuous shear bands (This is Mechanism II, as schematically shown in Figure 8.1-II). In this case, shear bands are confined and cannot propagate as extended defects in the whole material. With this mechanism, deformation becomes significantly more homogeneous, which improves the global ductility of the material. Our results show that there is also a third mechanism that improves both ductility and strength (Mechanism III, in Figure 8.1). The formation of shear bands can be simplified by considering a shear band as a plane with a finite thickness, such as the red plane shown in Figure 8.1-III. This shear band nucleates and propagates when the shear stress in the metallic glass reaches a critical value, which can start and continue sliding a slab of the material in the left side of that plane against the other slab on the right side [235, 267–269]. Our results show that when the graphene sheets or flakes are in the shear plane, resistance to sliding the slabs will remarkably increase because the shear stress needs to overcome the shear strength of the graphene to form and propagate the shear bands (schematically shown in Figure 8.1-III). All these three mechanisms are investigated, and the deformation mechanisms at the atomistic scale and their interaction with the mechanical properties are studied in this paper.

DISTRIBUTION A: Distribution approved for public release.

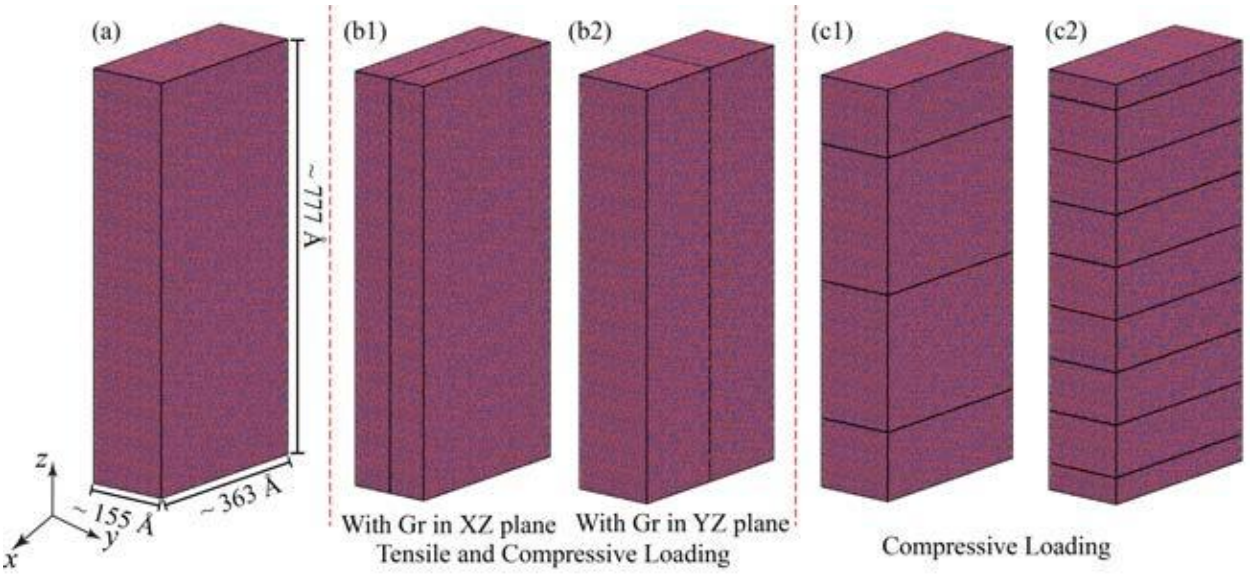

Figure 8.2: The metallic glass slab and its composites are used to study graphene's impact on mechanical properties of the material. (a) Shows the reference slab, (b1) and (b2) show the slab for tensile and compressive loading in which the graphene is in the plane of loading, (c1) and (c2) show the slab for compressive loading in which the graphene is perpendicular to the loading direction.

8.4 Methods

In this work, we consider two metallic glass-graphene composite systems in the form of a slab and a cube. A schematic of the slab is shown in Figure 8.2(a), and the cubic system is shown in the Appendix 8.7 (Figure 8.9). Embedded atom method (EAM) potential developed by Mendelev et al. [270] is used to simulate the interaction between Cu-Cu, Zr-Zr, and Cu-Zr atoms. The amorphous alloy structure generated by EAM potential using the cooling rate of 0.49 K/s has been shown to have a reasonable agreement with x-ray diffraction data [270] and has predicted the elastic constant values close to experimental values [271]. We generated the amorphous structure using four cooling rates: 0.005, 0.01, 0.1, and 1 K/ps. The cooling rate does not affect the radial distribution function but has an effect on the local structure (Voronoi Polyhedron), as shown in Figure 8.10 in the Appendix 8.7. The difference in local structure (Voronoi Polyhedron) becomes less with a decrease in cooling rate. We choose 0.01 K/ps as our cooling rate as the difference in local structure for 0.005 K/ps, and 0.01 K/ps is less than 3%. There is not much difference in density for the samples produced by these four cooling rates. The densities for 0.005, 0.01, 0.1 and 1 K/ps cooling rates are 7.59, 7.57, 7.56 and 7.55 g/cm3, respectively.

To make the geometry, in the first step, eight thousand atoms of composition $Cu_{64}Zr_{36}$ are quenched from the melt with a cooling rate of 0.01 K/ps to form a metallic glass state. The specimens for mechanical testing are generated by the multiplication of this quenched metallic glass. Three-dimensional (3D) periodic cells of metallic glass are created with two different sizes, 249.5×251.5×249.5 $Å^3$ (called cube) and 363×157×777 $Å^3$ (called slab). The dimensions of simulation boxes are chosen so that the graphene does not have to be stretched or compressed to fit the simulation box. After inserting the graphene, metallic glass atoms in the vicinity (having a distance less than 1.4 Å from carbon atoms) of graphene are removed from the simulation cell. The

DISTRIBUTION A: Distribution approved for public release.

cube cell is reinforced with one and five graphene sheets and is subject to shear and tensile loads (See Figure S1). The tensile loading is applied to both cube and slab to show that the conclusions obtained from simulations in this work do not depend on the shape and size of the simulation box. Two different kinds of reinforcements are used for the slab cell. The compressive and tensile loading is applied in the cases in which graphene is reinforced in the loading planes parallel to the larger and smaller surfaces as shown in Figures 8.2(b1) and (b2). The compressive loading is applied when graphene is reinforced perpendicular to the loading direction with different densities, which is made by having a different number of graphene layers as shown in Figures 8.2(c1) and (c2).

Before loading, the systems are both equilibrated at 50 K and zero stress using the isothermal-isobaric ensemble for 200 ps. After equilibration, cubic cells are deformed by shear and tensile strains, and slab cells are deformed by compression and tensile strains. The stress components were allowed to relax in directions other than the applied strain using the isenthalpic ensemble, and the Berendsen thermostat controls the temperature. The strain rates for uniaxial and shear loading are 10^8/s and 2×10^8/s, respectively. The shear band is the dominant mode of plasticity in metallic glass, and its formation in molecular dynamics simulation is necessary to have the same deformation mechanism as experiments. For deciding the strain rate to represent the loading, we simulated the metallic glass slab with graphene in YZ and XZ plane with four tensile strain rates: 10^7/s, 10^8/s, 10^9/s, and 10^{10}/s. The resulting stress-strain curves are shown in Figure 8.11 in the Appendix 8.7. The formation of shear bands requires a change in local structure. The shear bands do not form in case of strain rates: 10^9/s and 10^{10}/s as sufficient time is not available for local structure changes, as shown in Figure 8.12 in the Appendix 8.7. The resultant stress-strain curves show that the results converge for 10^7/s and 10^8/s, and shear bands form for 10^8/s. Hence, in this work, we used the strain rate of order 10^8/s for all the simulations. The Airebo potential is used for the Carbon atoms [155]. The Lennard-Jones potential models the interaction between Cu-C and Zr-C. The parameters used are $\sigma_{Cu-C} = 2.84863$, $\epsilon_{Cu-C} = 0.03844$, $\sigma_{Zr-C} = 3.1659$ and $\epsilon_{Zr-C} = 0.04580$ [272]. The Large-scale Atomic/Molecular Massively Parallel Simulator (LAMMPS) [54] is used to carry out all the MD simulations in this work. The shear bands are visualized using the atomic shear strain as implemented in OVITO [55]. In the following Figures, the metallic glass atoms with the atomic shear strain less than 0.18 are hidden to see the highly sheared regions in the shear bands.

The general stacking fault energy of metallic glass is calculated using the cubic simulation box as discussed in section 3. The box is divided into two halves, and the upper half slides over the lower half by the distance δ. The boundary condition to the plane that divides the box into two halves is non-periodic, and atoms are allowed to relax in directions other than displacement direction, δ.

8.5 Results and Discussion

In this section, the three deformation mechanisms, at the atomistic scale, by which graphene improves the ductility of metallic glasses are investigated (see Figure 8.1).

1. Fragmentation of the thickness

As discussed earlier, the formation of shear bands in metallic glasses depends upon the availability of a critical thickness in the material. The critical thickness for the formation of shear bands in metallic glasses ($\tilde{1}$0-50 nm) is remarkably smaller than the conventional polycrystalline alloys ($\tilde{1}$0-

DISTRIBUTION A: Distribution approved for public release.

500 μm). This difference is mainly because the shear bands in metallic glasses do not form by an adiabatic shear, but are created by dilatancy effects (expansion of volume) [238, 273]. A simple model based on the force lines explains the necessity of having a critical thickness by equating the cluster of atoms to hard particles in granular materials [273, 274]. When the material is under stress, the force lines pass through these particles (clusters of atoms) and change their direction. If the force line passes through a sufficient number of particles, it can rotate by 180°. The change in the force line's direction causes expansion in volume regions through which the force line passes [274]. The expansion decreases the strength of the local volumetric region compared to the surroundings. The decrease in strength concentrates the strain rates in the regions where the strength has decreased and causes the formation of shear bands.

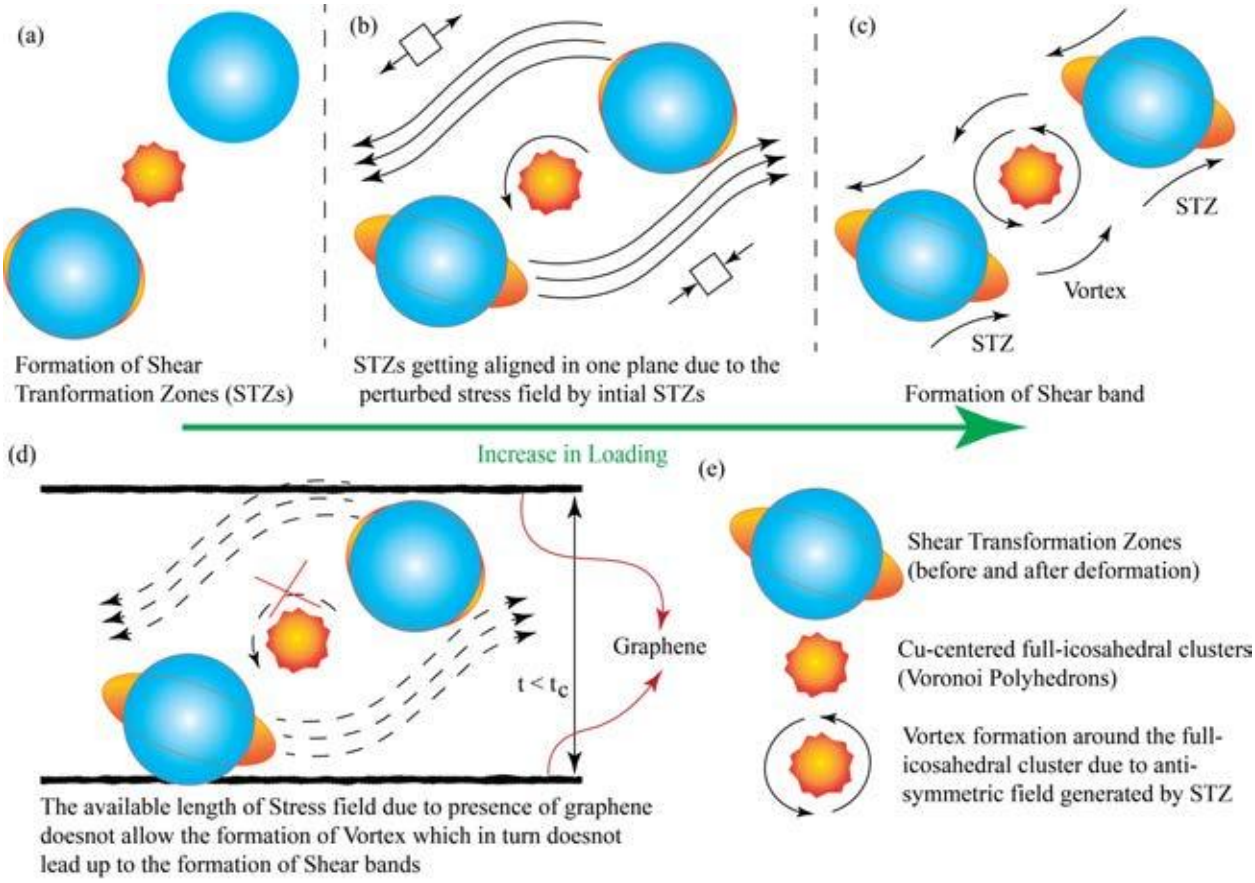

Figure 8.3: The "STZ-Vortex" mechanism required for the formation of shear bands is shown in (a), (b) and (c) panels. As shown in (d) presence of graphene layers with a small inter-layer distance ($t < t_c$) changes the stress field and does not allow the formation of vortexes. The change in the stress field prevents Shear Transformation Zones (STZs) to get aligned in one plane and stops the formation of shear bands. The local angle of rotation as shown in Figure 8.4 confirms the change the in local rotation due to the unavailability of critical length.

DISTRIBUTION A: Distribution approved for public release.

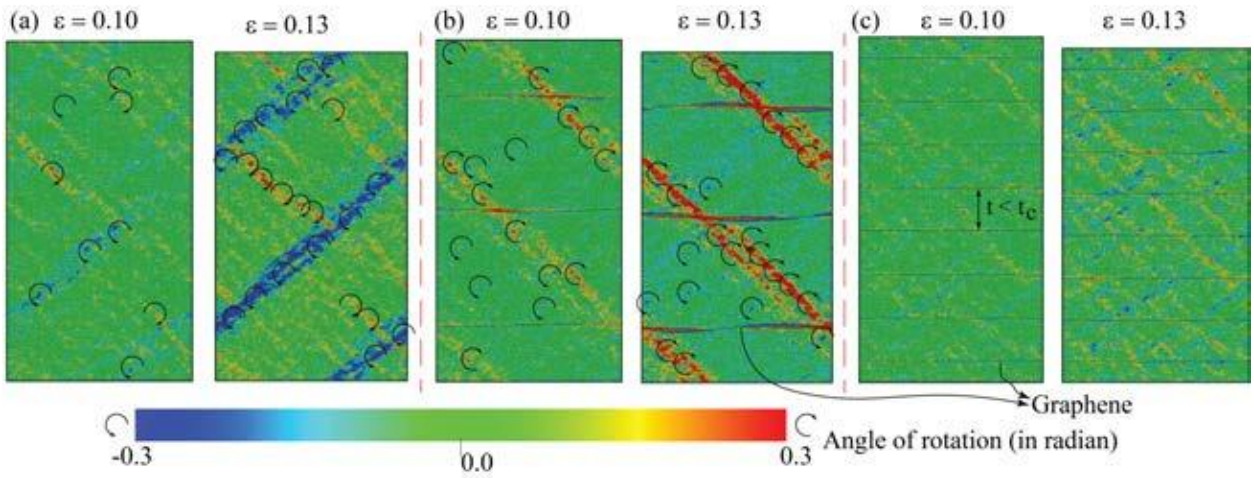

Figure 8.4: The local rotation angle for slabs compressed with and without graphene in the plane perpendicular to loading. In (a) and (b), where these is no graphene or the distance between the layers is more than the critical value, the atoms have local rotation to form shear bands through the "STZ-vortex" mechanism. However, in (c) with the distance between the layers being less than the critical value, the vortexes are not formed due to the change in the stress field by the presence of graphene. The procedure to calculate the local rotation is given in section 1 in the supplementary documents.

In metallic glasses, with applying stress the small cluster of atoms experience an increase in local free volume and a subsequent increase in local shear strain [275]. These highly localized and sheared regions are known as Shear Transformation Zones (STZs). The percolation of STZs in the viable plane of maximum shear stress leads to the formation of shear bands [276]. This procedure is schematically shown in Figure 8.3 (a)-(c). The STZ generates a local perturbed stress field which causes a formation of strong rotation field (due to presence of favored motifs of atoms) near the STZ. The stress field perturbation and generation of strong rotation field (called 'vortex') triggers the activation of neighboring STZ as shown in Figure 8.3 (c). This leads to the percolation and assembly of STZs, ultimately leading to the formation of a shear band. As shown in Figure 8.3 (d), the presence of graphene layers with small inter-layer distance (due to $t < t_c$) changes the stress field and does not allow the formation of rotation field which stops the triggering of neighboring STZ and that inhibits the formation of shear bands.

Figure 8.5 (a-c) shows the effect of decreasing available thickness in metallic glasses by graphene reinforcement. In these Figures, atoms are colored according to the atomic shear strain, and atoms with less than 0.18 shear strain are deleted to show the shear bands clearly. Figure 8.5 (a1, a2, and a3) shows three snapshots of the system with no graphene at compressive strains equal to 0.0, 0.10, and 0.20, respectively. The same set of snapshots are shown in Figures 8.5 (b1-b3) and 8.5 (c1-c3) for systems in which graphene layers are embedded with inter-layer distances of 26.0 nm and 9.90 nm, respectively. The stress-strain curve (shown in 8.5 (d)) show that the presence of graphene has increased the stress and strain required for the formation of shear bands. As explained in Introduction section, the ductility of metallic glasses in MD simulations has to be quantified by tracking the formation and propagation of shear bands. The increase in required yield strain, decrease in negative slope in stress-strain, and increase in the stress (τ_{glue}, explained in section 2. and 3.) required for propagation of shear band indicate the increase in ductility in composite system compared to metallic glass.

DISTRIBUTION A: Distribution approved for public release.

The shear band forms in the case where the interlayer distance between graphene layers is 26.0 nm ($t > t_c$), but not when the thickness is more fragmented, and the interlayer distance between graphene layers is 9.90 nm, which is smaller than the critical value (shown in Figure 8.5 (b1-b3) and (c1-c3)). As described in Figure 8.3, there is no formation of vortexes (shown in Figure 8.4) due to the change in the stress field caused by the unavailability of critical length. The inhibition of local rotation stops STZs from percolating and assembling to form the shear band. As shown in Figure 8.5(d), adding graphene and inhibiting the shear band formation intercepts the sudden drop in the stress-strain response, prevents catastrophic failure, and improves the material's ductility.

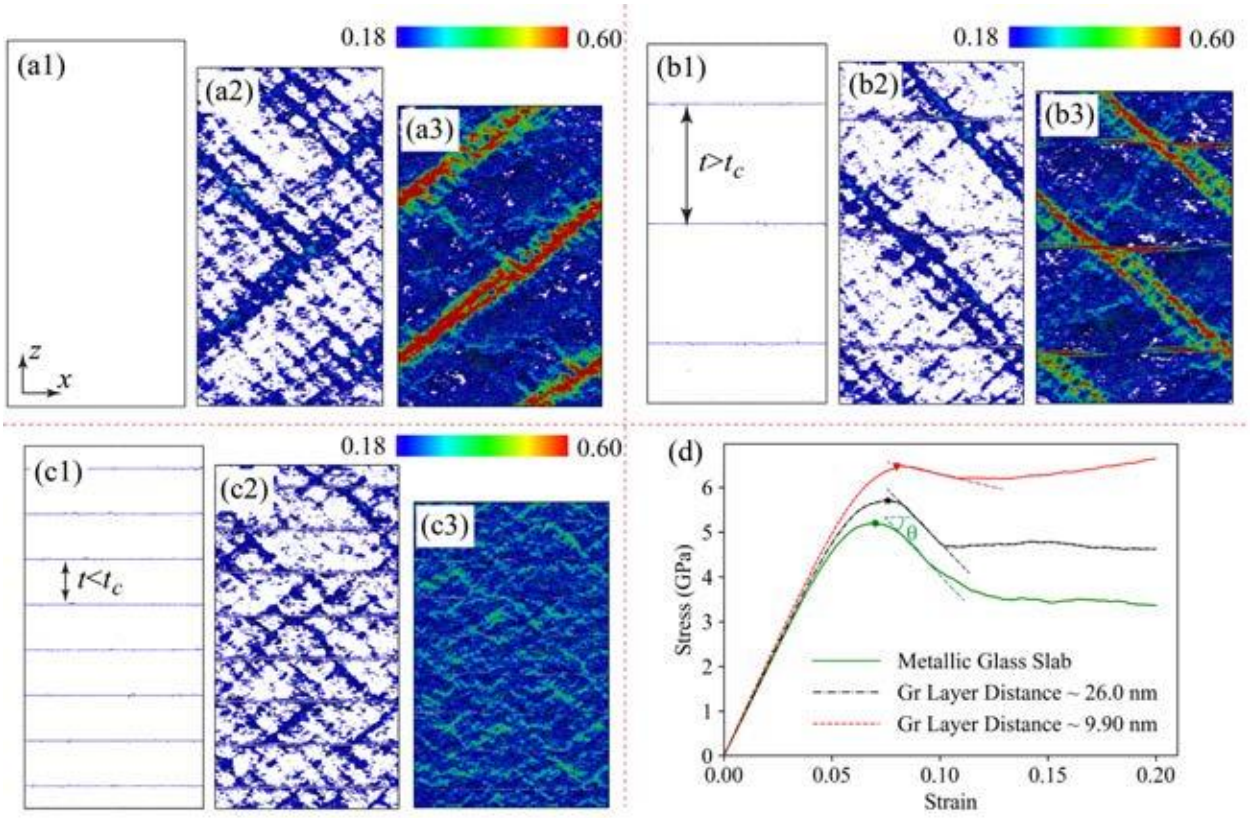

Figure 8.5: The effect of graphene reinforcement on the initiation and propagation of shear bands when the graphene is perpendicular to the loading direction. Material is subjected to compressive loading and in each of the panels (a) to (c), 1, 2 and 3 represent 0.0, 0.10, and 0.20 compressive strain, respectively. Atoms are colored according to atomic shear strain, and atoms (Cu and Zr) with less than 0.18 shear strain are deleted to see higher strain atoms. (a) shows the metallic glass, (b) and (c) show the metallic glass with graphene reinforcement perpendicular to loading direction with inter-layer distances of 26.0 nm and 9.90 nm. The shear blobs shown in (a2) and (b2) combine to form shear bands. The flow of shear bands is resisted by the graphene in (b2), which led to the improvement shown in the stress-strain curve (d). The formation of shear bands from shear blobs needs a critical amount of thickness for the metallic glass, which is not available in (c). Hence, there is no formation of shear bands in (c3). The increase in yield point strain (shown by markers), decrease in negative slope and increase in stress required to propagate shear band (τ_{glue}) in stress-strain curve (d) indicate increase in ductility due to reinforcement of graphene.

DISTRIBUTION A: Distribution approved for public release.

2. Retarding the propagation of shear bands

The free volume (v_f), defined as the fraction of the metallic glass having a lower atomic coordination number and lower density than the surroundings, plays an essential role in forming shear bands. At the start of loading, v_f is very small, and the material has only a few sites where the free volume is more than the rest of the matrix. The dilation caused by elastic deformation causes some specific sites to have less intrinsic resistance. The lower resistance causes these sites, or blobs, to have higher shear strain rate ($\dot{\gamma}_b$) than the remaining matrix's shear strain rate ($\dot{\gamma}_m$). The number and volume of these sites increase with the increase in strain, and these sites add up to form a continuous shear band [238].

After the shear band formation, the strain is localized in very thin bands and causes inhomogeneous flow [237]. The shear band's macroscopic flow is a net result of individual atomic jumps [237]. The individual atomic jump is a function of free volume in the nearest neighbor and the surrounding stress. The presence of graphene hinders the atomic jump (across the graphene) by changing nearest neighbors and increasing the required stress needed for the flow of shear bands, as shown in Figure 8.13 and 8.14 (a) in the Appendix 8.7. To better study the effect of graphene on the propagation of shear bands, we need to look at the strain rate in a representative volume of the material. The metallic glasses volume has two fractions, shear bands covering a fraction f and the remaining matrix covering (1-f) fraction of the volume. For a region shearing at a strain rate $\dot{\gamma}_o$, the strain contribution of band and matrix region will be [238]:

$$f\dot{\gamma}_b + (1 - f)\dot{\gamma}_m = \dot{\gamma}_o, \tag{8.21}$$

where $\dot{\gamma}_b$ and $\dot{\gamma}_m$ are the shear strain rates in the shear band and the matrix, respectively.

The presence of graphene stops the propagation of the shear band by blocking the atoms from passing across the graphene. The propagation of shear bands stopped by graphene increases the resistance and decreases the shear strain rate ($\dot{\gamma}_b$) inside the shear bands. To better understand this effect, we need to look at the deformation mechanisms in the shear band at the atomistic scale. More details of these deformation mechanisms during the initiation and propagation of a shear band are studied in Section 3.3, and here we look at one of the three zones. As schematically shown in Figure 8.1), the shear band consists of multiple regions, among which the shear-alienated glass area is called the glue zone (Zone III in Figure 8.1).

DISTRIBUTION A: Distribution approved for public release.

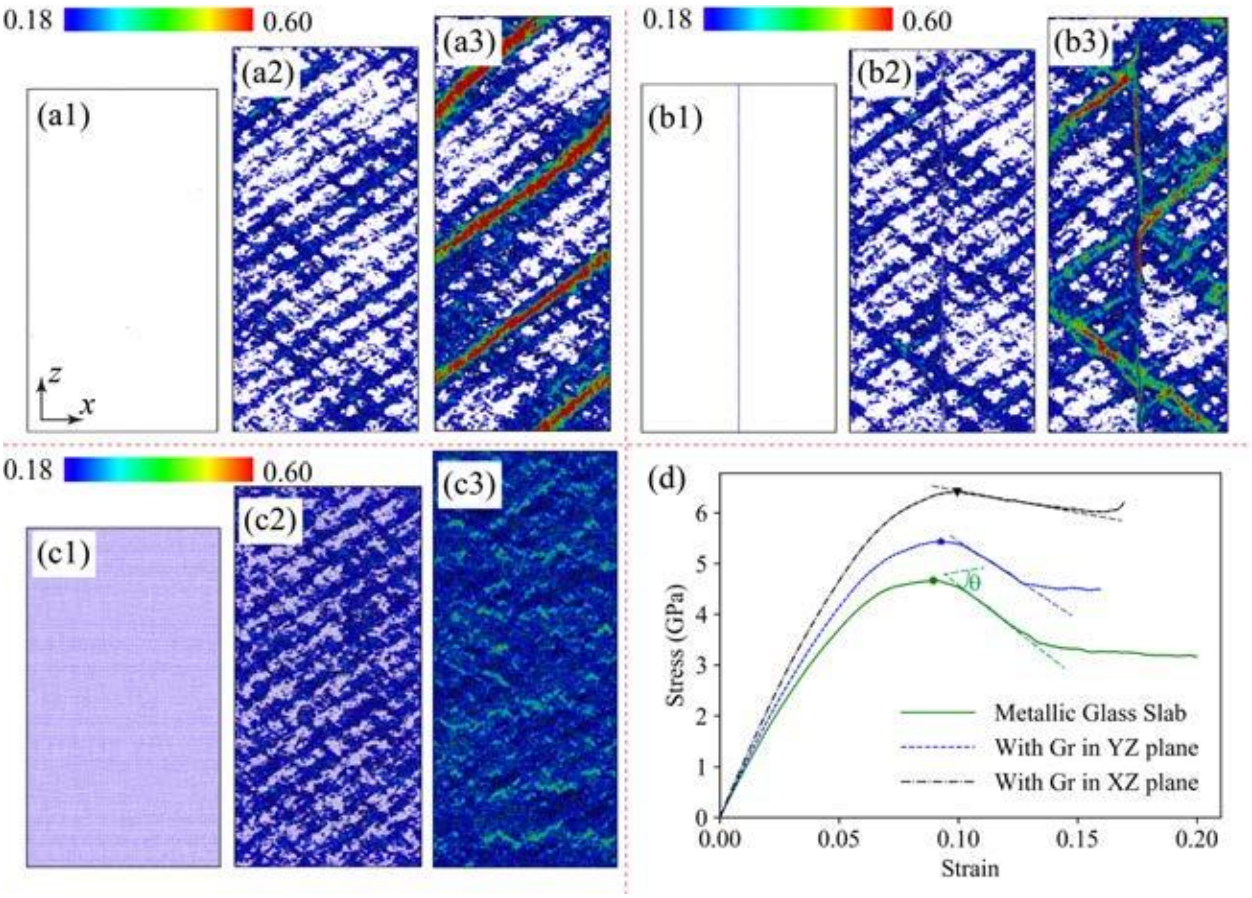

Figure 8.6: The effect of graphene reinforcement on shear band formation when the graphene is in the plane of loading. Material is subjected to tensile loading and in each of the panels (a) to (c), 1, 2 and 3 represent 0.0, 0.11, and 0.15 strain, respectively. The shear blobs are formed in (a2), (b2), and (c2). In (a3) and (b3), shear blobs combine to form shear bands. The formation of shear bands needs shear flow in the loading plane. As shown, the shear band does not form (or shear does not get localized) in (c3) due to strain compatibility as it will require shearing of graphene in localized regions. The stress-strain response of all the three systems is compared in (d). It is clearly shown that the graphene is improving the ductility, and strength. It also vanishes the sharp drop in the stress-strain curve, which shown the graphene is preventing the catastrophic failure due to formation of shear bands. For better visualization of location and orientation of graphene layer see method Figure 8.2. The increase in yield point strain, decrease in negative slope and increase in stress required to propagate shear band in stress-strain curve (d) indicate increase in ductility due to reinforcement of graphene.

DISTRIBUTION A: Distribution approved for public release.

The activation of local shear transformation zones during loading creates some embryonic shear bands (ESBs). These regions propagate in a quasi-steady-state manner and mature into a hot, bonafide shear crack [235]. Propagation of ESBs requires that $\tau_\infty > \tau_{glue}$ is satisfied for a minimum incubation length scale, where τ_∞ is the far-field shear stress and τ_{glue} is the resistance against shear band propagation in Zone III (conceptually equivalent to the drag of a stacking fault behind a Shockley partial dislocation) [235]. In the molecular dynamics simulations, τ_{glue} is the shear traction needed for constant shear strain after the material is alienated and sheared (i.e., after 0.08-0.10 shear strain). The hindrance caused by the graphene to the inhomogeneous flow of the shear bands, as shown in Figures 8.5 (b) and 8.6 (b), increases the required τ_{glue}.

The yield point of metallic glasses is related to τ_{glue} [235], and mechanism II causes an improvement in the yield strength and τ_{glue} when graphene is embedded into the metallic glasses and is perpendicular to the shear band plane. A system similar to what was studied in the previous section is modeled under tensile and compressive loading to investigate this effect better. Atoms with shear strains larger than 0.18 are shown for a system with no graphene at different tensile strains of 0.0, 0.11, and 0.15 in Figure 8.6 (a1-a3). The same snapshots are shown in Figure 8.6 (b1-b3) for a system with one graphene layer in the loading plane and parallel to the smaller surface of the slab, and in Figure 8.6 (c1-c3) when the graphene is parallel to the larger surface. The stress-strain curves for all three systems are shown in Figure 8.6 (d). The improvement by retarding the propagation of shear bands is obviously seen in stress-strain curve Figure 8.6(d). It is worth noting that the end of stress-strain curve does not correspond to the final failure of material. In Figures 5 and 6, the curves end at the maximum applies strain which is 20%. As shown in two cases of Figure 6, the stress-strain curve ends at a lower strain, and that happened because of numerical convergency issues. The increase in yield strain, decrease in negative slope and increase in glue indicate that the reinforcement of graphene in loading plane has increased the ductility of metallic glasses. It is worth noting that mechanism II was also activated in the case shown in Figure 8.5(d). The delay in the formation of the shear band, as shown in Figure 8.6(c), follows a different mechanism that will be studied in the next section. When compressive loading is applied to the System as shown in Figure 8.6, the wrinkling of graphene starts and causes a drop in strength of the composite, as shown in Figure 8.15 in Appendix 8.7. In compression, when graphene is in the plane of loading, graphene improves the mechanical properties of composite until the system reaches the strain, which causes wrinkling in graphene. After wrinkling, the graphene does not affect the strain and stress needed for the formation of shear bands.

3. Improving the shear strength in shear bands

The material in the metallic glasses can be divided into four zones during the deformation (see a schematic in the bottom panel of Figure 8.1) which are; the well-aged glass, rejuvenation region, alienated glass (glue zone), and liquid zone [235]. The far-field shear stress required in each zone for constant strain rate decreases in the sequence that the zones are mentioned. In this section, we will investigate how the shear stress is affected by the graphene in MGGCs.

The well-aged glass (Zone I) is quenched glass in which metallic atoms have been given sufficient time to find local minimum potential energy. Metallic glass deforms elastically in Zone I. If the graphene is in the loading plane in Zone I (see Mechanism III and the bottom panel in Figure 8.1), graphene will also deform elastically, increasing the required stress for deforming the material in this zone. Zone II represents the rejuvenation zone, in which glass is in a higher energy

DISTRIBUTION A: Distribution approved for public release.

state due to large deformations. The rejuvenation stress (τ_r) controls the nucleation of embryonic shear bands [235]. Similar to crystalline materials, the generalized stacking fault energy (GSFE), $\gamma(\delta)$ can be defined for a well-aged glass by separating the metallic glass cube in two halves and sliding the upper half against the lower half, as shown in Figure 8.7. For this purpose, cubic systems with and without graphene are created, as shown in Figures 8.7 (a) and (c). Both these systems are divided into two halves (Figure 8.7(b)), and the top half is moved against the lower one with a displacement δ as shown in Figure 8.7(d). The change in energy and it's derivative with respect to δ are calculated and shown in Figure 8.7 (e) and (f), respectively. The rejuvenation stress, τ_r, can be calculated using the derivative of generalized stacking fault energy (GSFE) which is the average energy increase per area: $\gamma(\delta) = \Delta E(\delta)/S_0$. The change in GSFE and its derivative in the metallic glass system with and without graphene are compared in Figure 8.7.

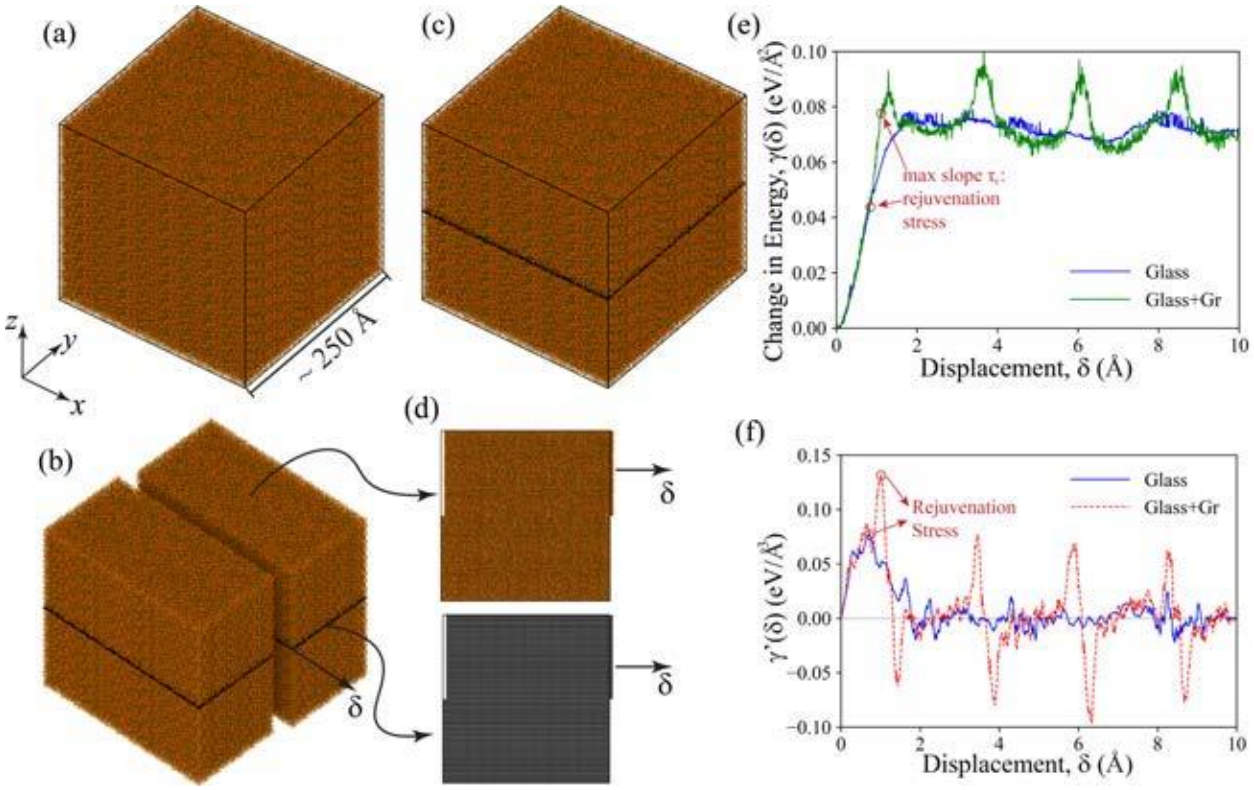

Figure 8.7: The general stacking fault energy for metallic glass systems with and without graphene is calculated. (a) and (c) show the glass cube system used for calculations. Two blocks of metallic glass with and without graphene are moved on each other as shown in (b) and (d). (e) Shows the change in energy due to the movement of the blocks. (f) Shows the derivative of the change in energy with respect to δ (equivalent to shear stress). Rejuvenation stress, τ_r (or athermal nucleation strength) is shown in (e) and (f). The introduction of graphene has increased the rejuvenation stress and amplitude of energy's derivative for the composite system. This increase in rejuvenation stress explains the increase in required yield stress for composites compare to metallic glass.

The derivative of energy ($\gamma'(\delta)$) is the resistance traction against the localized shearing. As shown in 8.7(f), while in the metallic glass, this resistance drops quickly during loading. In the material with graphene, the resistance is observed even at large displacements, which is due to the force needed for breaking and forming the bonds in graphene. The $\max_\delta \gamma'(\delta)$ represents the athermal nucleation strength or rejuvenation stress, τ_r [235]. Figures 8.7 (e) and (f) show that the

DISTRIBUTION A: Distribution approved for public release.

rejuvenation stress is increased in the material by adding graphene, which explains the higher yield stress required for forming shear bands in molecular dynamic simulations. With more sliding of the upper half (increasing δ), the variation in energy decreases. Energy roughly oscillates (distance between either maximum or minimum of energy remain similar) around mean atomic spacing of metallic glass (= $(\Omega/N)^{1/3} \sim 2.52$ Å where Ω is Volume and N is the number of atoms). The amplitude of oscillation is equivalent to the resistance needed to overcome the energy barrier of stacking fault energy. As shown, the presence of graphene (0.42 wt. %) increases the required resistance (amplitude in $(\gamma'(\delta))$) by three times compared to metallic glass, which explains the increasing difficulty of shear band flow when graphene needs to be sheared for the flow.

As discussed in section 2., a shear stress $\tau_\infty > \tau_{glue}$ is needed for the propagation of ESBs in Zone III. The presence of graphene in the plane of shear not only increases the τ_{glue}, it also homogenizes the strain distribution in the material, opposed to the strain locality in the shear bands, which causes the catastrophic failure and low ductility. By comparing panels (a) and (b) in Figure 8.8, it is shown that while the strain distributions in the pristine metallic glass (Figure 8.8(a)) is highly localized in the shear bands, the graphene deformation in the MGGC (as shown in Figure 8.8(d)) remarkably homogenizes the strain distribution in the material (Figure 8.8(b)). This strain homogenization delays the formation of shear bands, improves the strength, and also increases the ductility, as shown in Figure 8.8(c). As shown in this Figure, increasing the density of graphene by decreasing the distance between the layers significantly magnifies the improvement of mechanical properties (see Figure S8 for the same study on a larger cubic system). A similar study is also performed for the case that the material is subjected to a tensile loading (see Figure S9). In that case, a similar improvement is observed with the same deformation mechanisms at the atomistic scale. Under tensile loading, multiple shear bands start forming. However, one of them dominates with the increase in loading. Comparing the strain distribution in metallic glass and two systems with different densities of graphene (Figure S9 (a-d)) clearly shows the effect of graphene on homogenization of the strain distribution and consequent improvement in both the strength and ductility in tensile loading, as shown in Figure S9(e). The shear strain distribution in the graphene near the shear bands is shown in Figure S9(f).

DISTRIBUTION A: Distribution approved for public release.

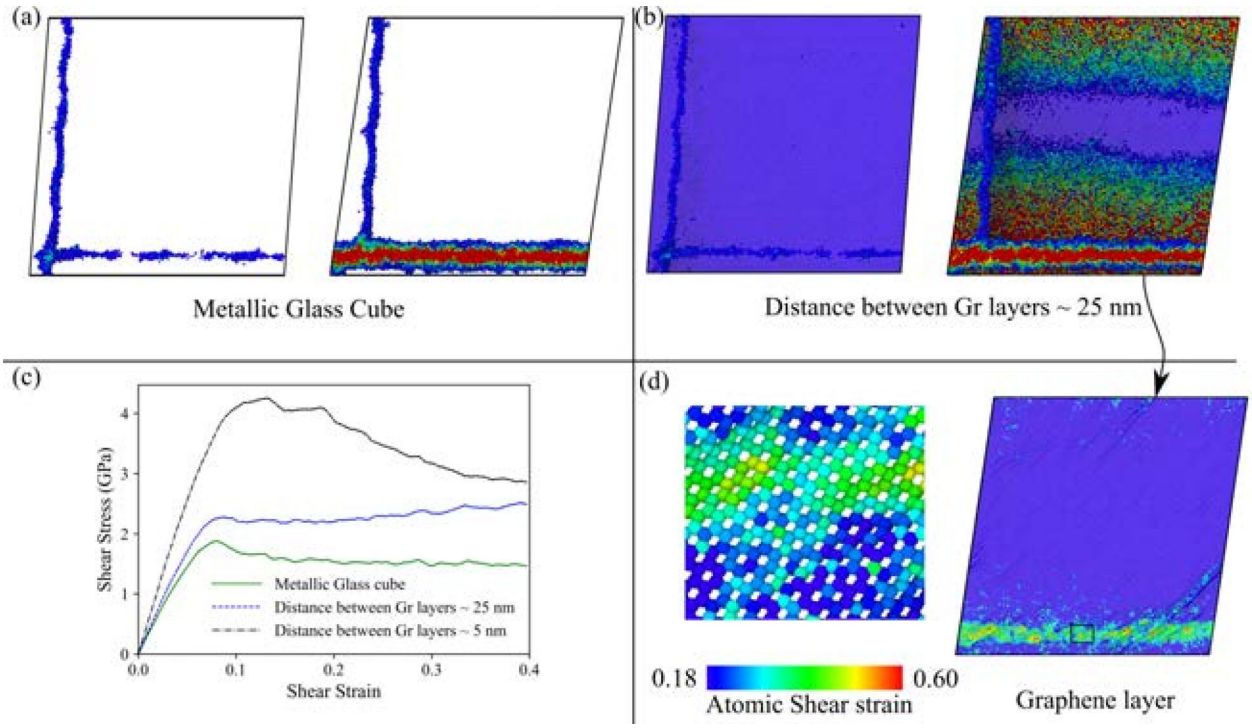

Figure 8.8: The effect of graphene reinforcement on the formation of shear bands during shear loading. The graphene reinforcement increases the required stress to shear the metallic glass. The atoms are color-coded according to the atomic shear strain. The Cu and Zr atoms having an atomic shear strain value less than 0.18 are deleted to see high shear areas. (a) And (b) show the snapshot (at 0.0744 and 0.1488 shear strains) for glass cube without and with one graphene layer. (c) Shows the shear stress-strain curve. Due to strain compatibility, graphene deforms near the shear band and also increases the shear homogenization in the system. (d) Shows the sheared graphene (see text for more details).

Mechanisms II and III both increase the overall shear stress required for the flow of shear bands. In mechanism II, graphene blocks propagation of the shear band, while graphene does not have any in-plane shearing in high sheared regions, as shown in Figure 8.14 (a1)-(a3) in Appendix 8.7. In mechanism III, the shear band travels in the graphene plane and causes in-plane shearing in graphene, as shown in Figure S6 (b1)-(b3). The in-plane shearing of graphene increases the homogeneity of shear strain inside the matrix, and delocalizes the severe localization of shear strain which creates shear bands.

The effect of graphene on the formation of shear bands can also be studied by tracking the change in local atomic structures using Voronoi polyhedrons (VPs) in the system [277, 278]. The formation of a shear band is determined by whether it is energetically favorable to deform the local structure or form a shear band. The local structure of the material does not change much after forming the dominant shear band, as most of the strain is concentrated in the narrow volume of that shear band. We studied the relative composition of the three most available Voronoi Polyhedron in all the systems that have been investigated in this paper, as shown in Figure 8.18 in Appendix 8.7. There are three parts in these graphs; (i) Elastic deformation (Zone I), (ii) formation of shear bands (Zone II), and (iii) deformation after the formation of dominant shear bands (Zone III). The local structure changes less in (i) and (iii) compare to (ii). In the cases (like tensile slab reinforced with Graphene in XZ plane) where there is no formation of the shear band due to the presence

DISTRIBUTION A: Distribution approved for public release.

Table 8.1: Summary of all the simulations in this work. Graphene increases the modulus, yield stress and yield strain in all the cases.

Case	Modulus (GPa)	Yield stress (GPa)	Yield strain (%)
Metallic Glass cube shear	34.33	1.88	7.98
Distance between Gr layers ~ 25 nm	38.93	2.28	8.85
Distance between Gr layers ~ 5 nm	55.67	4.25	13.13
Metallic Glass cube tensile	97.98	4.805	8.87
Distance between Gr layers ~ 25 nm	107.92	5.90	9.46
Distance between Gr layers ~ 5 nm*	149.07	11.49	17.29
Metallic Glass slab compression	97.32	5.20	7.01
Gr layer Distance ~ 26.0 nm	99.44	5.71	7.58
Gr layer Distance ~ 9.90 nm	103.60	6.64	8.25
Metallic Glass slab tensile	95.93	4.67	8.94
With Gr in YZ Plane	102.34	5.44	9.26
With Gr in XZ plane	112.65	6.41	9.95

* No yield point in the system. Data for Breaking point is shown.

of graphene, the (iii) part (or Zone III) does not exist, and the local structure keeps deforming as shown in Figure 8.18 in Appendix 8.7. The presence of graphene makes shear band formation energetically unfavorable compared to the deformation of local atomic structures and strong local rotation fields.

A summary of the calculated improvements in the mechanical properties of metallic glasses by adding graphene to their nanostructure for multiple geometries and loading conditions is given in Table 8.1. The results show that in all the cases, regardless of the orientation of the graphene or the loading condition, reinforcement of graphene layers has improved the strength and ductility of metallic glasses by the above-described mechanisms.

8.6 Conclusions

In this work, the mechanisms by which graphene interacts and enhances the mechanical properties of metallic glasses are explored. Our results show that while the introduced Metallic Glass-Graphene Composites (MGGCs) maintain the exceptionally high strength of metallic glasses, the embedded graphene in the nanostructure improves their ductility, prevents the catastrophic failure due to the sudden formation of shear bands, and even improved the strength of the material compared to metallic glasses. It is shown that these improvements are caused by a network of multiple mechanisms at the atomistic scale, including blocking the propagation of shear bands, resisting the dominant shear band formation, increasing strain rate homogeneity due to planar strength, and not allowing the material to have the critical length (that is needed for shear band formation). Our results also confirm that activation of these mechanisms can happen concurrently, and the improvement is observed regardless of the orientation of graphene and the loading condition in the metallic glasses. Experimental verification of these results will be addressed in a future communication by the authors.

DISTRIBUTION A: Distribution approved for public release.

Acknowledgement

This material is based upon work supported by the Air Force Office of Scientific Research under award number FA9550-18-1-0169.

8.7 Appendix

The Appendix 8.7 show the geometry and deformation mechanisms in the cubic system, the mechanisms by which graphene hinders the atomic jump across the graphene, and the relative composition of three most occurring Voronoi polyhedrons in various systems during the loading.

1. Calculation of local angle of rotation and Stress tensor eigenvalues for atoms:

OVITO [55] is used to calculate the von Mises shear strain and local rotation angle. OVITO calculates the atomic deformation gradient **F** using the displacement vectors. The Polar decomposition of **F** yields the local rotation tensor **R** and a stretch tensor **U**. The local Rotation tensor **R** is encoded as quaternions (R_x, R_y, R_z, R_w) in OVITO.

$$\mathbf{R} = R_w + R_x\mathbf{i} + R_y\mathbf{j} + R_z\mathbf{k}$$

The angle of rotation can be calculated as $\theta = 2arccos(R_w)$. In addition to the value, we calculated the sign of angle using the sign of R_y, where Y is the direction perpendicular to the Vortex (SB). We calculated the eigenvalues for the atomic stress tensor for each atom. We plotted the average eigenvalues of the stress tensor in the X-Z plane shown in figure 8.12. The values are averaged along the Y-direction. The values are also averaged in Z-direction and X-direction by dividing them into 200 and 100 bins.

DISTRIBUTION A: Distribution approved for public release.

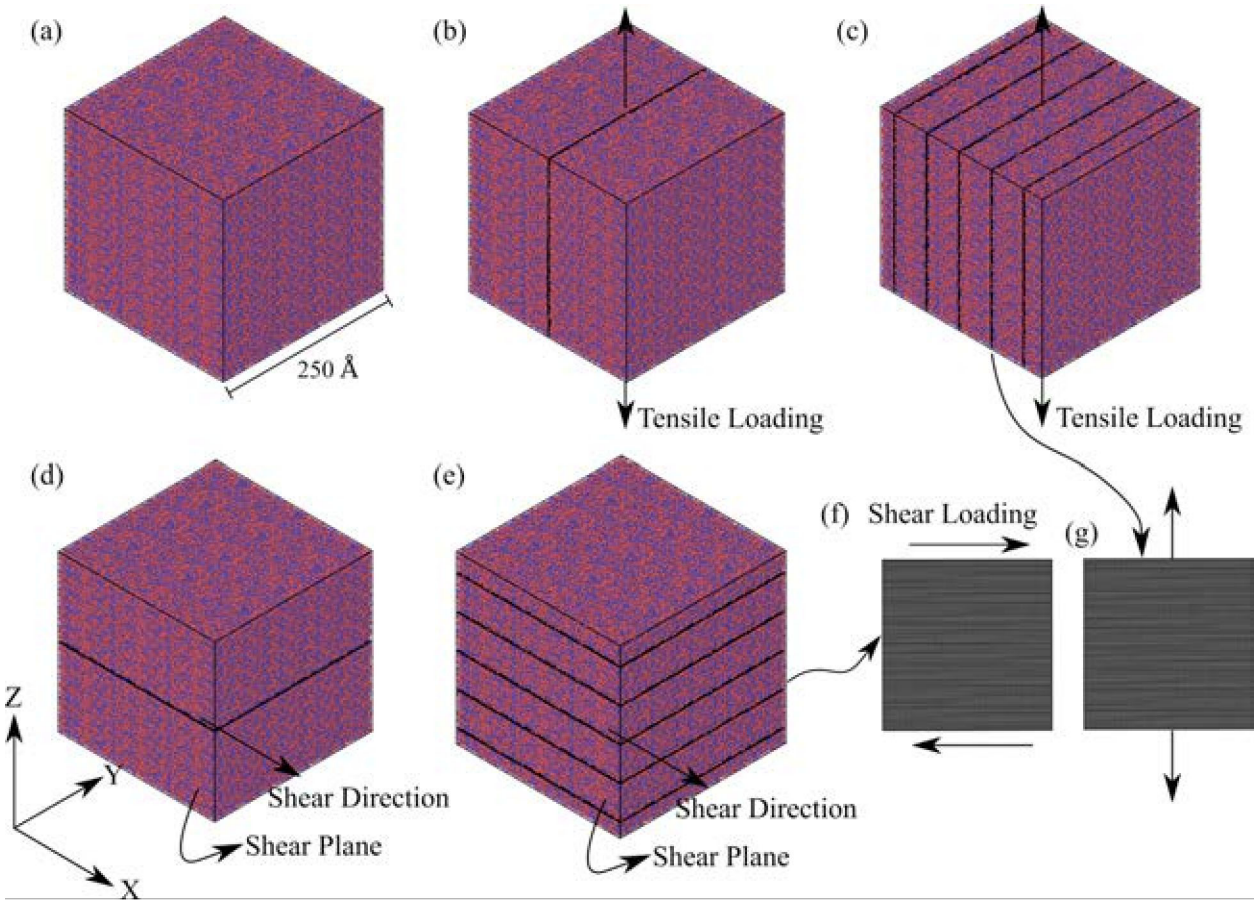

Figure 8.9: Glass-Graphene composite is studied using the bulk metallic glass cube with and without Graphene reinforcement. Two different types of loading, tensile and shear loading, are explored. (a) Shows the metallic glass cube, (b) and (c) show the systems used for tensile loading, (d) and (e) show the system used for shear loading. The bulk metallic glass cube shown in (a) is loaded both ways to compare the effect of graphene. (f) and (g) Show the loading in composites with respect to graphene layers.

DISTRIBUTION A: Distribution approved for public release.

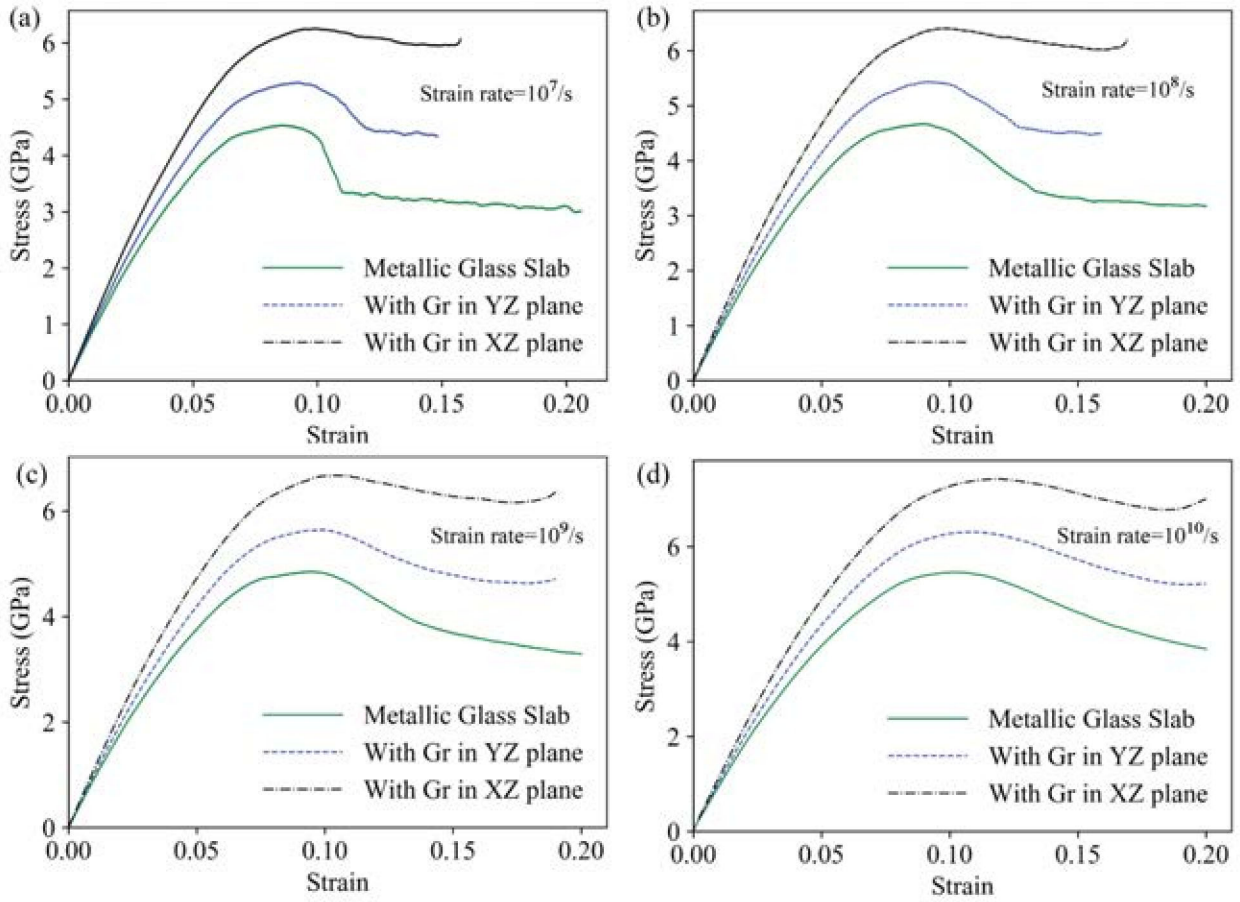

Figure 8.10: The comparison of stress-strain curves for different strain rates. The above graphs clearly show that the strain rate has a significant effect on stress-strain behavior. As there is not much difference in the stress-strain curve with strain rate 10e07/s and 10e08/s, we decided to use 10e08 for the simulations.

DISTRIBUTION A: Distribution approved for public release.

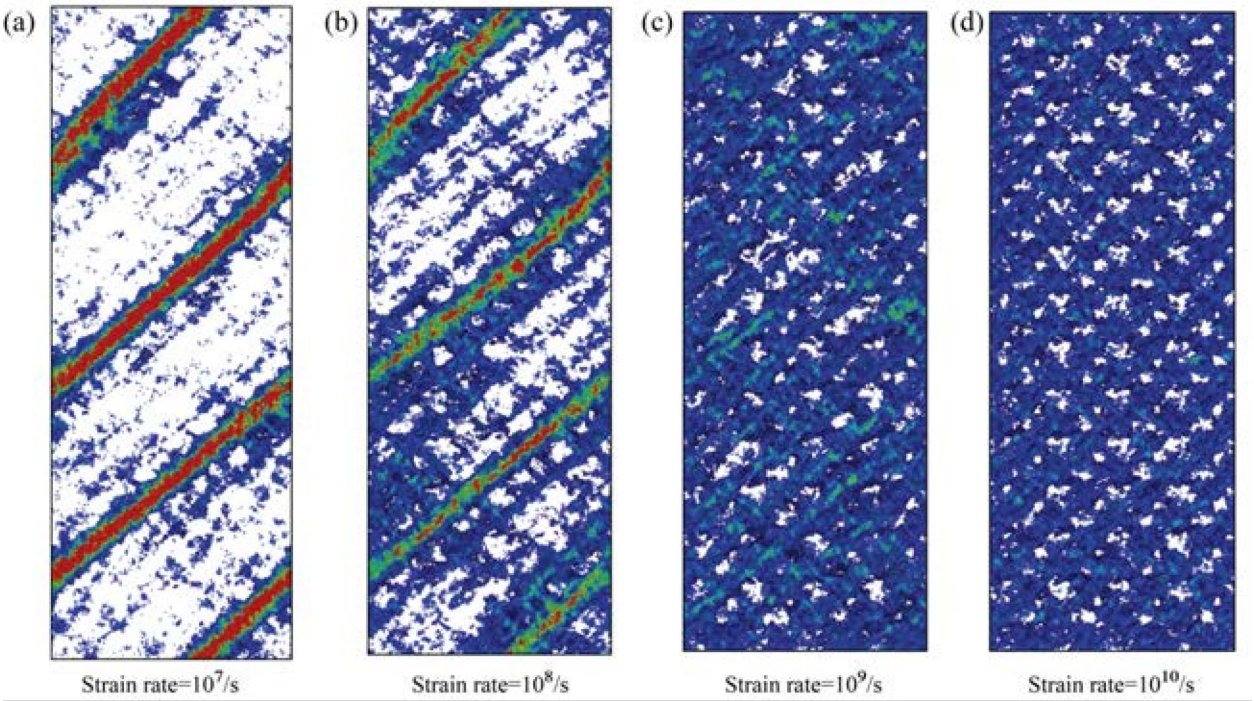

Figure 8.11: The figure shows the atomic shear strain for the glass slab at 15% tensile strain. The atoms with an atomic shear strain less than 0.18 are deleted to show the high sheared regions. As shown by the snapshots the shear bands only form in strain rates 10e07/s and 10e08/s. Hence we decided to use 10e08/s for the simulations.

DISTRIBUTION A: Distribution approved for public release.

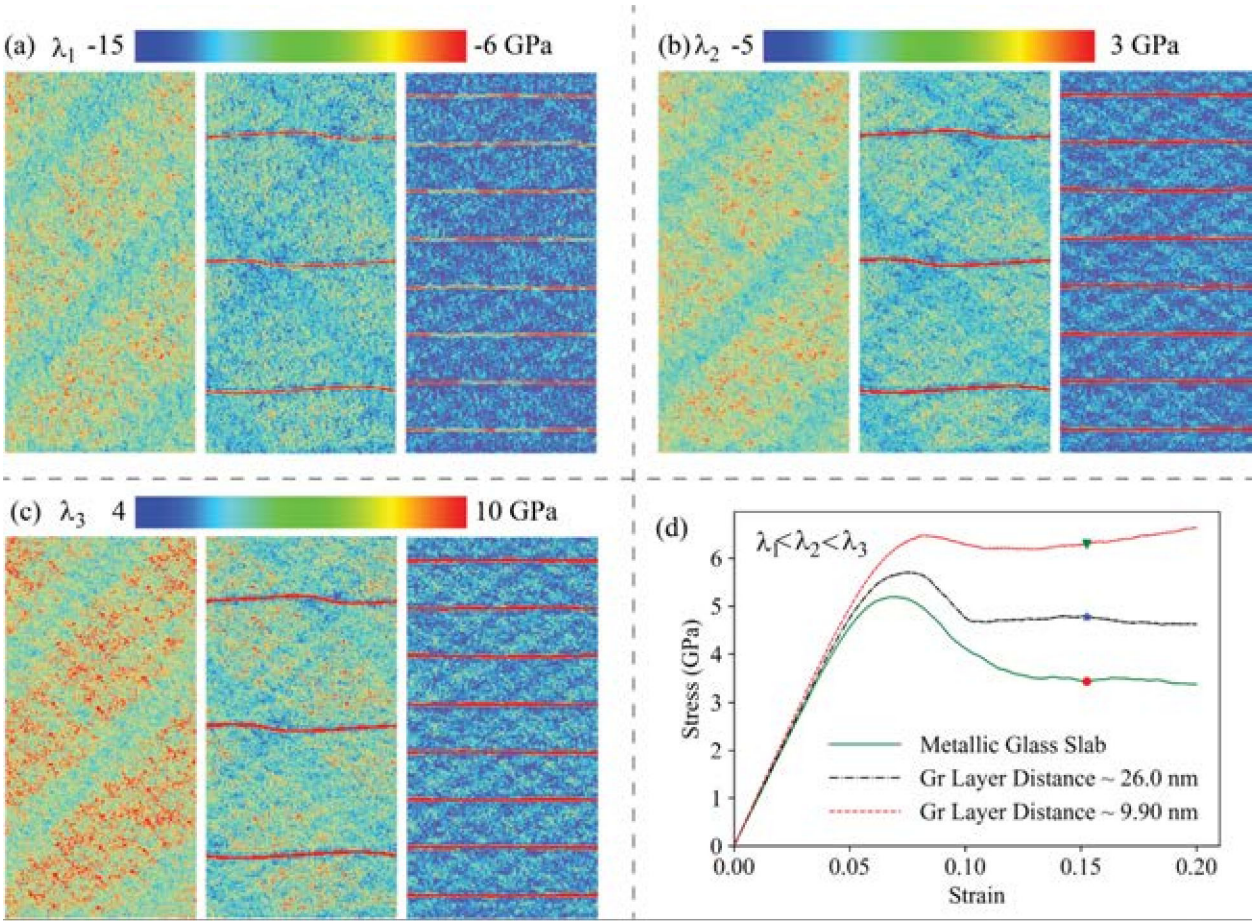

Figure 8.12: The figure shows the eigenvalues of atomic stress in the case where the slab is compressed with Graphene in the plane perpendicular to the loading direction. The stress field has changed due to the presence of graphene (unavailability of critical length). There is no formation of a vortex (shown in figure 5 of the paper) due to the change and which causes non-formation of Shear bands in the case when the distance between the graphene layer is less than a critical length. (d) shows the stress-strain curve and the point where the snapshot of stress eigenvalues are shown.

DISTRIBUTION A: Distribution approved for public release.

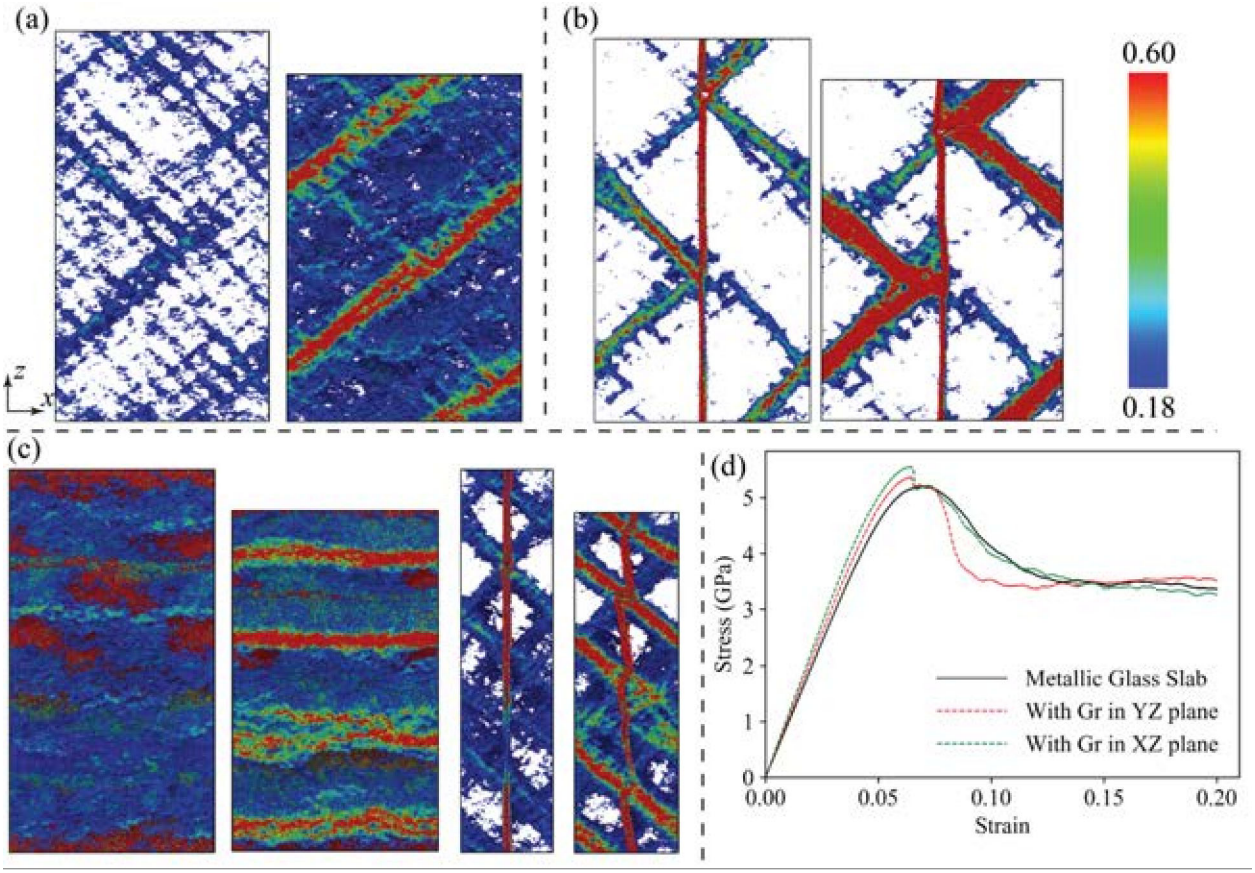

Figure 8.13: The figure shows the response of metallic glass and the composites with having graphene plane in the loading direction. For better visualization of location and orientation of graphene layer, see method figure 2. The first drop in the stress-strain curve is due to the wrinkling of the graphene. Due to graphene's 2d structure, the graphene cannot improve the mechanical properties of metallic glass after wrinkling. (a), (b), and (c) show the snapshot of atomic shear strain (at 0.10 and 0.20 strain) for metallic glass and composite. The shear bands are formed in the plane perpendicular to the graphene. (d) shows the stress-strain curve.

DISTRIBUTION A: Distribution approved for public release.

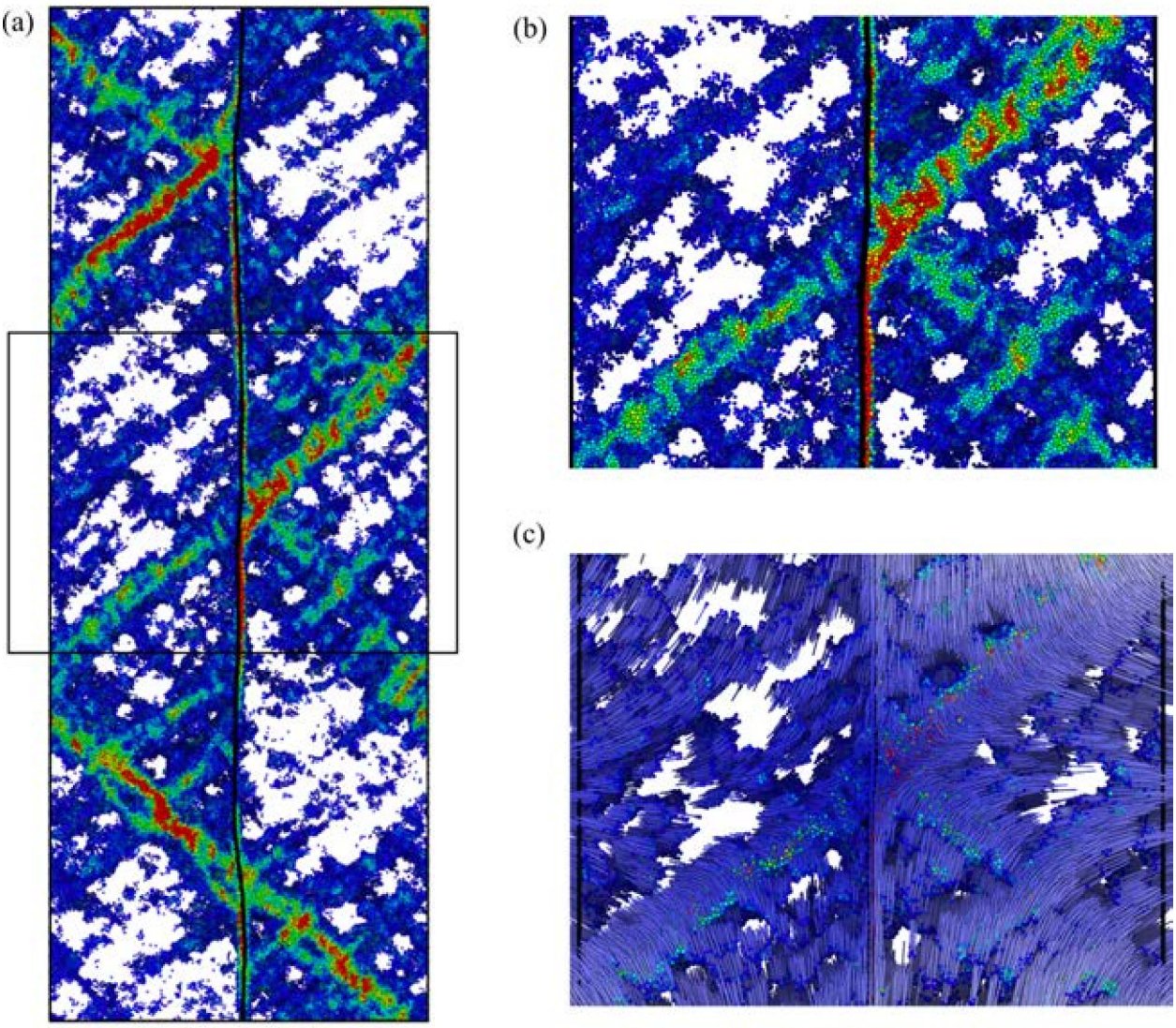

Figure 8.14: Shear band getting stopped by the graphene. (a) Shows atoms with a shear strain less than 0.18, (b) and (c) show the close-up of atoms with and without displacement near the graphene. The graphene does not allow the atoms in shear bands to jump across and the displacements of atoms near the graphene are parallel to the graphene surface.

DISTRIBUTION A: Distribution approved for public release.

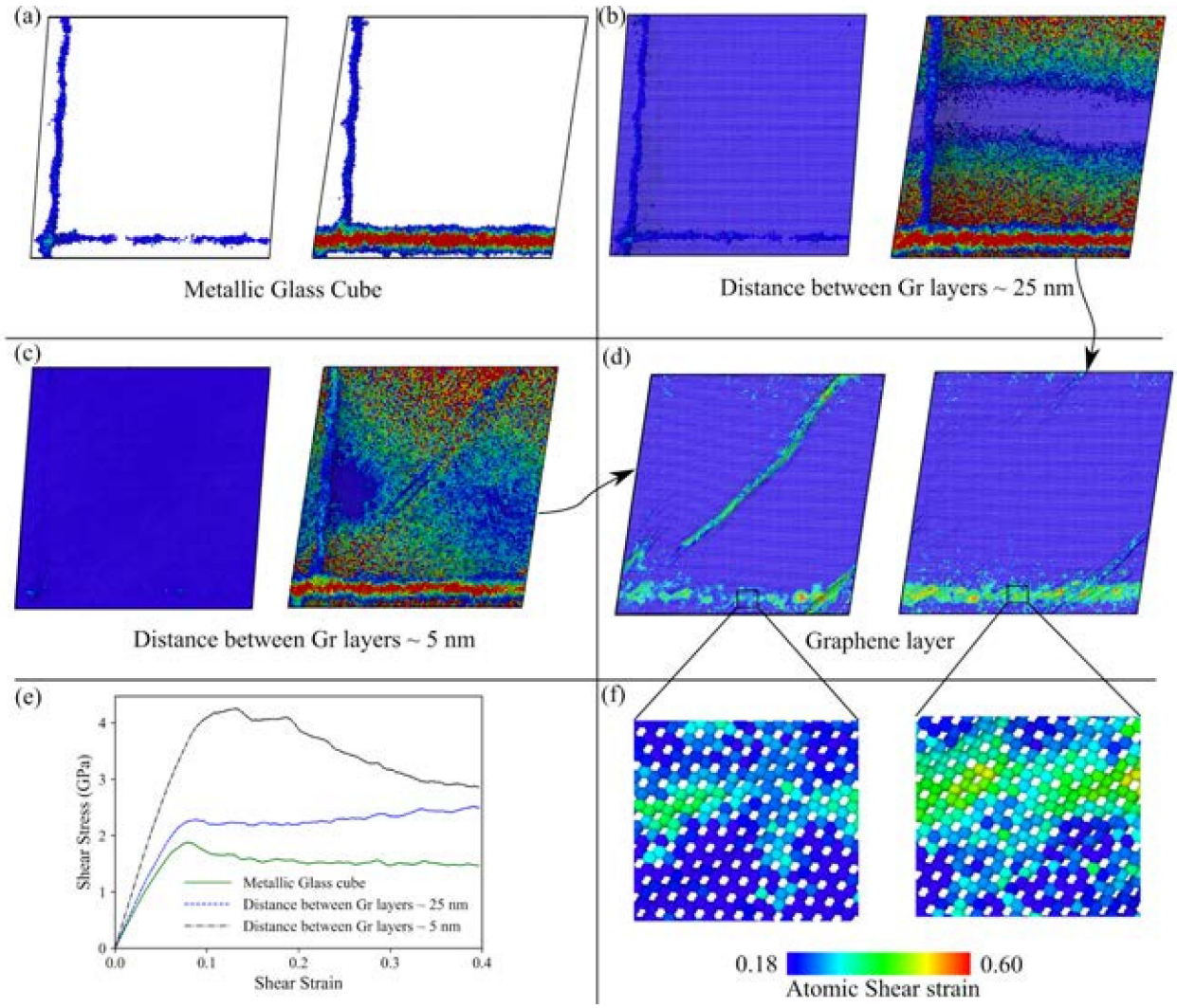

Figure 8.15: The effect of graphene reinforcement during shear loading. The graphene reinforcement increases the required stress to shear the metallic glass. The atoms are color-coded according to the atomic shear strain. The Cu and Zr atoms having an atomic shear strain value less than 0.18 are deleted to see high shear areas. (a), (b) and (c) Show the snapshots (at 0.0744 and 0.1488 shear strains) for glass cube, with one graphene layer and five graphene layers, respectively. (d) Shows the graphene layer during the deformation. (e) Show the shear stress-strain curve. Due to strain compatibility, graphene deforms near the shear band and increases the shear homogenization in the system. (f) Shows the sheared graphene

DISTRIBUTION A: Distribution approved for public release.

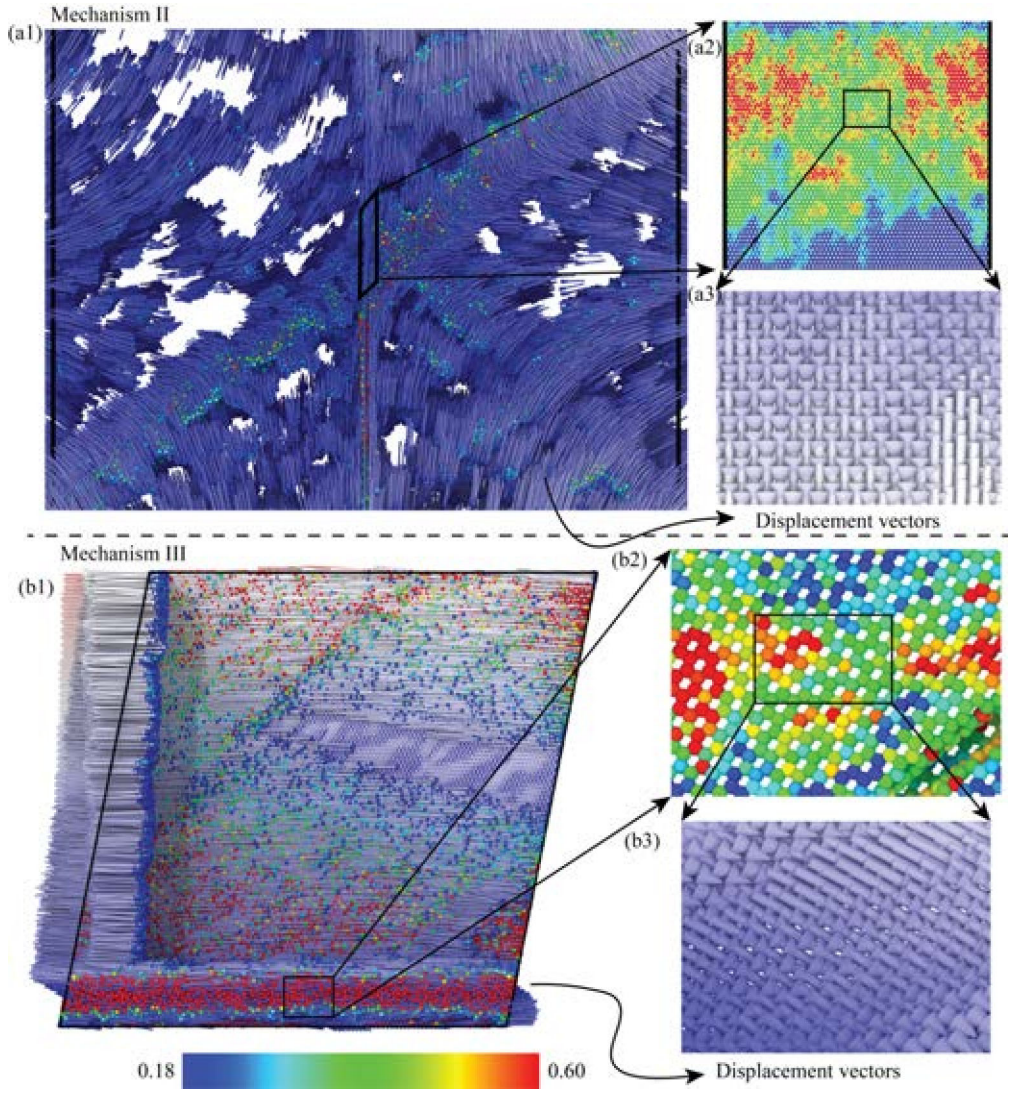

Figure 8.16: The figure shows the difference between mechanisms II and III. In both mechanisms, the required shear stress to propagate the shear band increases. In mechanism II, the shear band cannot travel through the graphene, but graphene does not have any in-plane shearing in high sheared regions. In mechanism III, the shear band travels through graphene and causes in-plane shearing in graphene. The in-plane shearing of graphene causes shearing in the volume regions (close to graphene-metallic glass interface) in the parts where Shear bands have not formed. (a1) shows the blocking of the shear band by graphene, (a2) shows the shear strain in the graphene region, which is interacted with the shear band, (a3) shows the displacement of graphene in high sheared regions which indicates that there is no in-plane shearing. (b1) shows the shearing of graphene with metallic glass, (b2) and (b3) illustrate the sheared graphene and displacement vectors of graphene in high sheared regions. The displacement vectors show that there is an in-plane shear in the case of mechanism III.

DISTRIBUTION A: Distribution approved for public release.

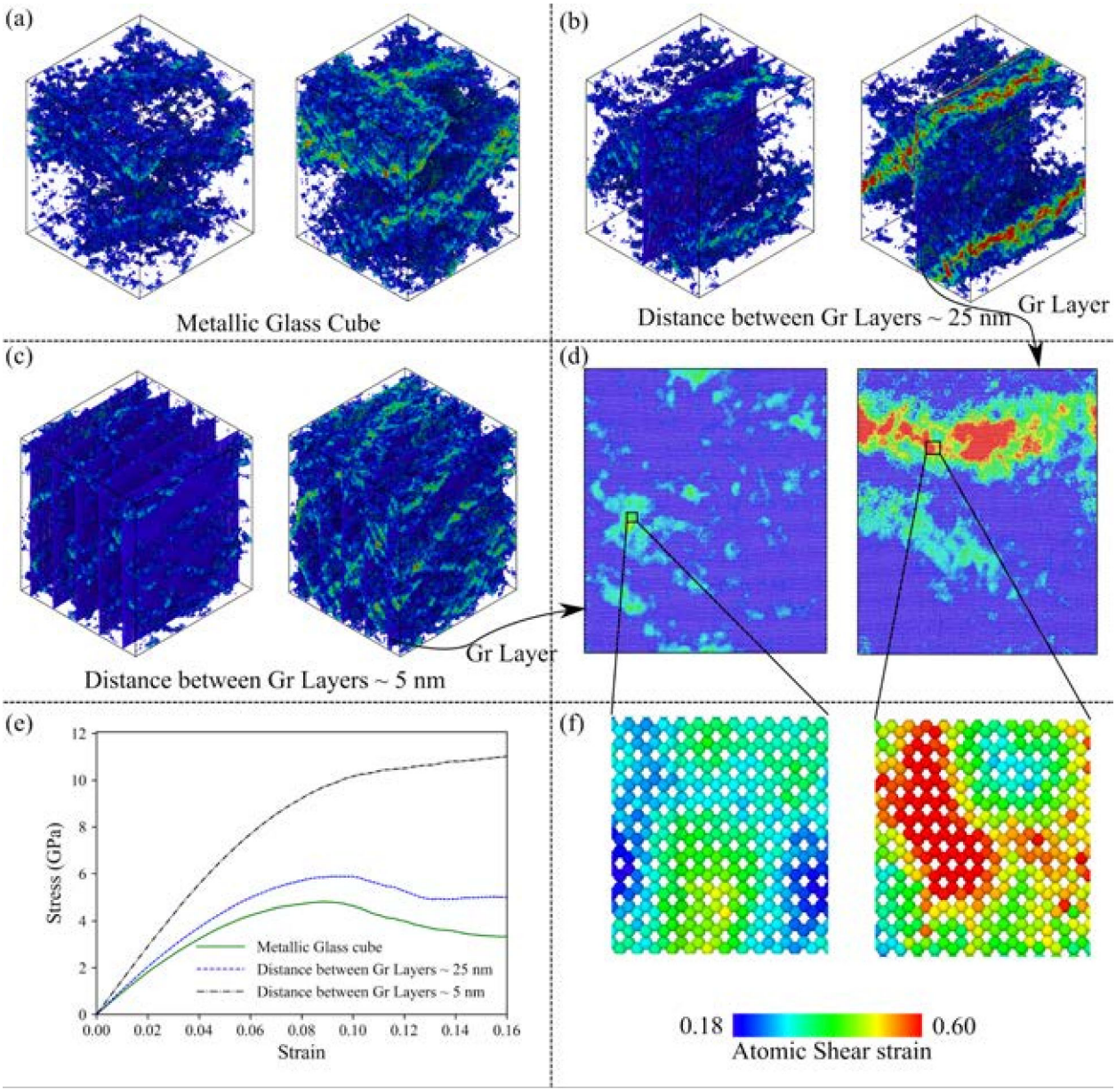

Figure 8.17: The effect of graphene reinforcement during tensile loading of MG cube and its composite. The graphene reinforcement increases the required stress to form shear bands. The atoms are color-coded according to the atomic shear strain. The Cu and Zr atoms having an atomic shear strain value less than 0.18 are deleted to see high shear areas. (a), (b) and (c) Show the snapshot at 0.12 and 0.16 tensile strain for glass cube, with one graphene layer and five graphene layers, respectively. (d) Shows the graphene layer during the deformation. (e) Shows the tensile stress-strain curve. (f) Shows the graphene near the shear bands.

DISTRIBUTION A: Distribution approved for public release.

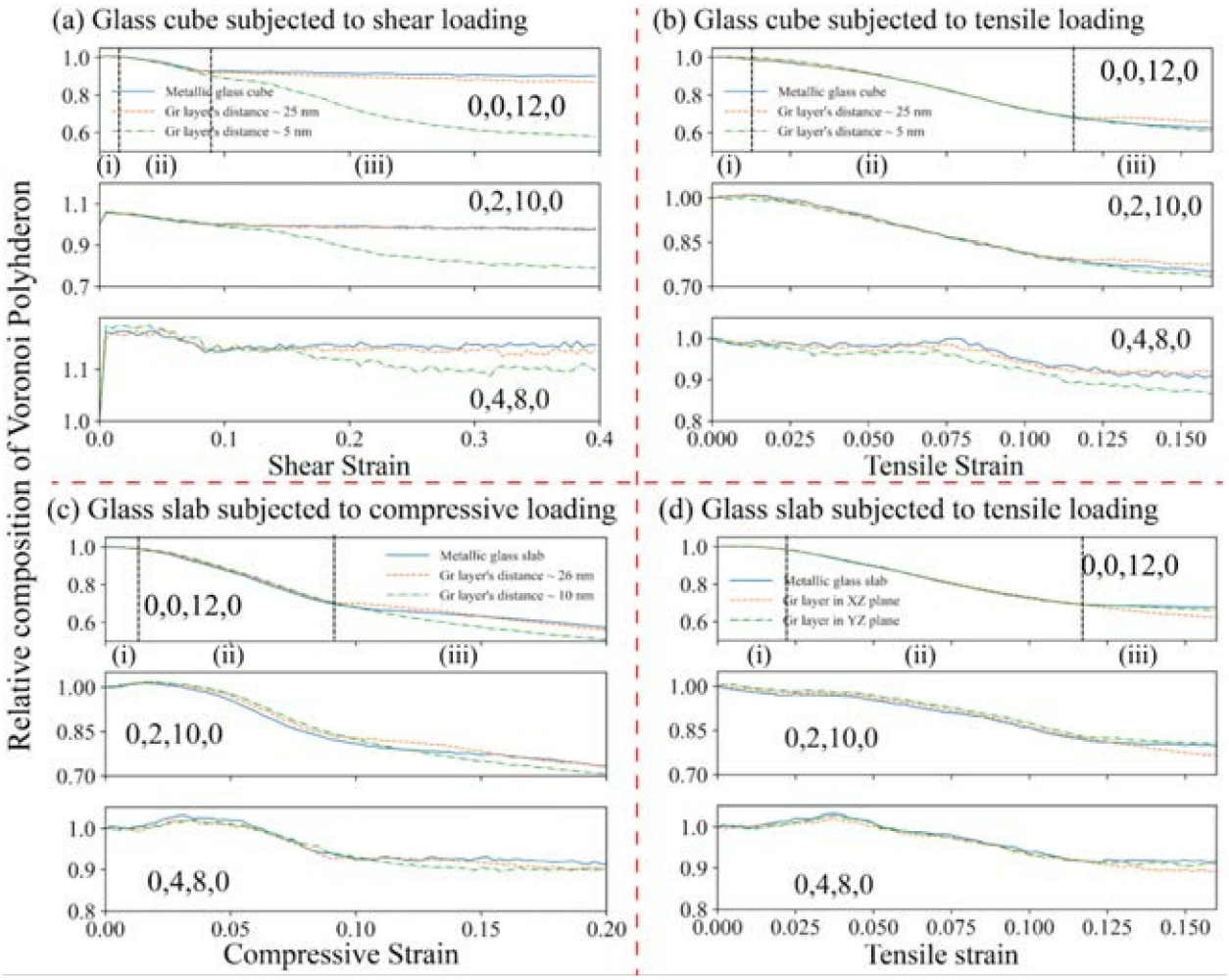

Figure 8.18: The relative composition of the three most occurring Voronoi polyhedrons (VPs) in the various systems during the loading is shown. After forming the dominant shear band, the strain rate in regions other than the shear band decreases, which decreases the deformation of local structures (VPs). This change can be seen in (a) where the shear band starts around 0.08 in the Glass cube and no formation of shear band in the cube which is reinforced with five graphene sheets. In (b) case, reinforcement of graphene makes a dominant shear band, which decreases the change in the number of VP in the case where the distance between graphene layers is 25 nm. In (c) (and (d)) case, the shear band does not form when the distance between Gr layers is 10 nm (Gr layer in XZ plane in (d) case). As shown, the local deformation continues and which contributes to the change in the number of VPs.

DISTRIBUTION A: Distribution approved for public release.

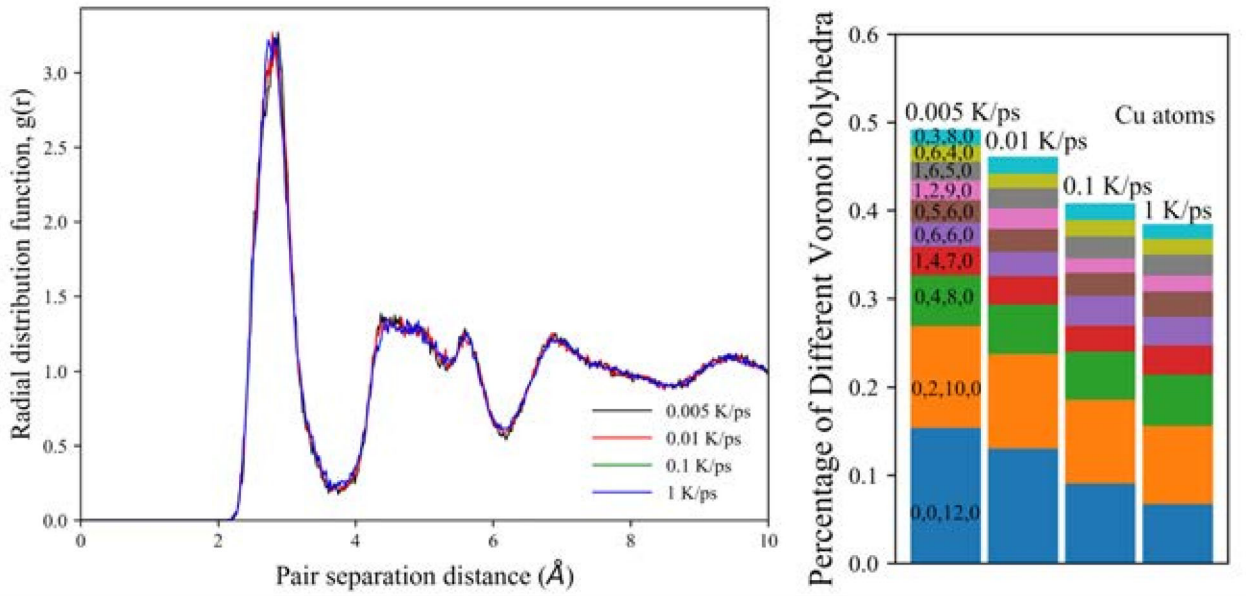

Figure 8.19: The figure shows the effect of different cooling rates (0.005, 0.01, 0.1 and 1 K/ps) on radial distribution function and effect on the first 10 Voronoi polyhedra for Cu atoms. The cooling rate does not affect the radial distribution function but has a significant effect on Voronoi polyhedra. The difference becomes less with a decrease in cooling rate. We choose 0.01 K/ps as our cooling rate as the difference in local structure for 0.005 K/ps and 0.01 K/ps is less than 3%. There is not much difference in density for the samples produced by these 4 cooling rates. The densities for 0.005, 0.01, 0.1 and 1 K/ps cooling rates are 7.59, 7.57, 7.56 and 7.55 g/cm3, respectively.

DISTRIBUTION A: Distribution approved for public release.

IX- Ni-graphene composites by electrochemical deposition

As abovementioned, the mechanical properties of metals can be improved with the addition of graphene. Electrochemical deposition is an attractive candidate for the fabrication of these composites due to it being more facile, faster, and more scalable. In the case of electrochemical deposition, there are also several strategies one can take to fabricate both pure metal-graphene and alloy metal-graphene composites. In this study, we present select strategies for obtaining Ni-graphene composites and NiTi-graphene composites.

A Ni^{+} ion-based electrolyte solution, as shown in Figure 9.1a, was used as the source of Ni atoms for the metal. The chemical composition of the electrolyte and the experimental conditions are listed in Table 9.1. As shown in Figure 9.1, the graphene and Ti powders can then be selectively added to the bath. The bath is stirred for ~30 min before the deposition to ensure the mixture becomes homogeneous. This promotes the uniform introduction of Ti and graphene particles into composite while the matrix is growing. A major advantage of this method is that with fine control of parameters the film growth can be changed according to the need.

Table 9.1: The chemical composition of the electrolyte and the experimental conditions

Chemical/Parameter	Values
$NiSO_4$	250 g/L
$NiCl_2$	40 g/L
Graphene Powder	2.5 g/L
Ti Powder (45 μm)	10 g/L
Sodium dodecyl sulfate (SDS)	0.6 g/L
Boric acid	13 g/L
Current density	~1 A/dm^2
pH	~3.6 - 4.5
Temperature	Room temperature
Stirring	300 rpm

DISTRIBUTION A: Distribution approved for public release.

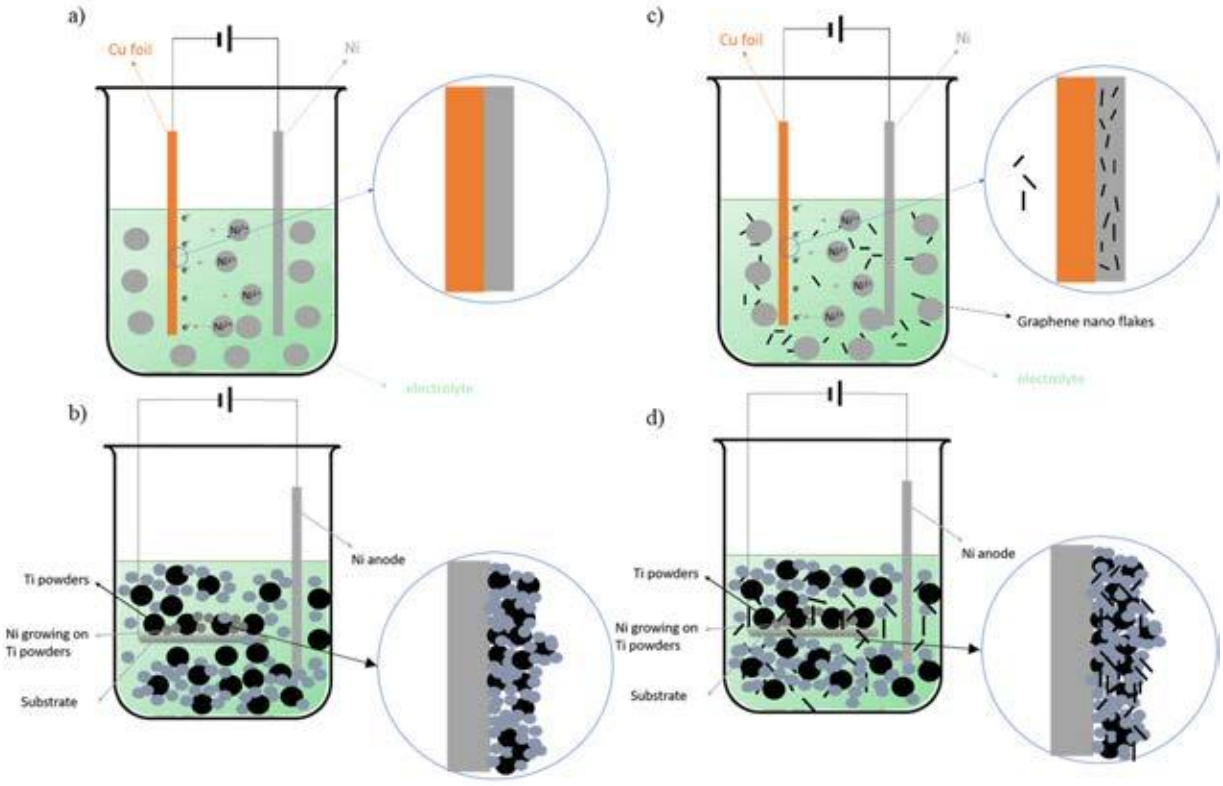

Figure 9.1: (a, b) are schematic representations of the electrodeposition process for both the Ni and Ni≡Ti metal, respectively. (c, d) show the same baths with the addition of graphene particles. In all cases, a nickel slab is used as the anode to replenish the bath with Ni_2^+ ions while the substrate is interchangeable. During NiTi deposition Ni ions first surround the Ti particles, then gravity assists in settling the mixture onto the substrate. For both graphene and Ti powders mixing is required to ensure a homogeneous mixture is obtained.

9.1 Nickel-graphene Composites

1. Dispersed graphene fabrication

The typical growing progress of the Nickel-graphene composite with the first strategy was illustrated in Figure 9.2. As shown in Figure 9.2a, the loose graphene particles were firstly attached onto the Ni surface. This may be due to the low weight of graphene and static charge. The fast stirring can ensure the graphene particles suspended in the electrolyte solution, which can further help the graphene adhesion. Then the subsequently grown Ni phase could bury the graphene particles inside, by which the graphene particles can be introduced into the metal matrix. Figure 9.2b and Figure 9.2c present the graphene particles were partially and fully buried by Ni phase, respectively. Figure 9.2d and 9.2e are the EDS mapping of the Ni and C in Figure 9.2b, demonstrating that the graphene particles were surrounded by the Ni phase.

DISTRIBUTION A: Distribution approved for public release.

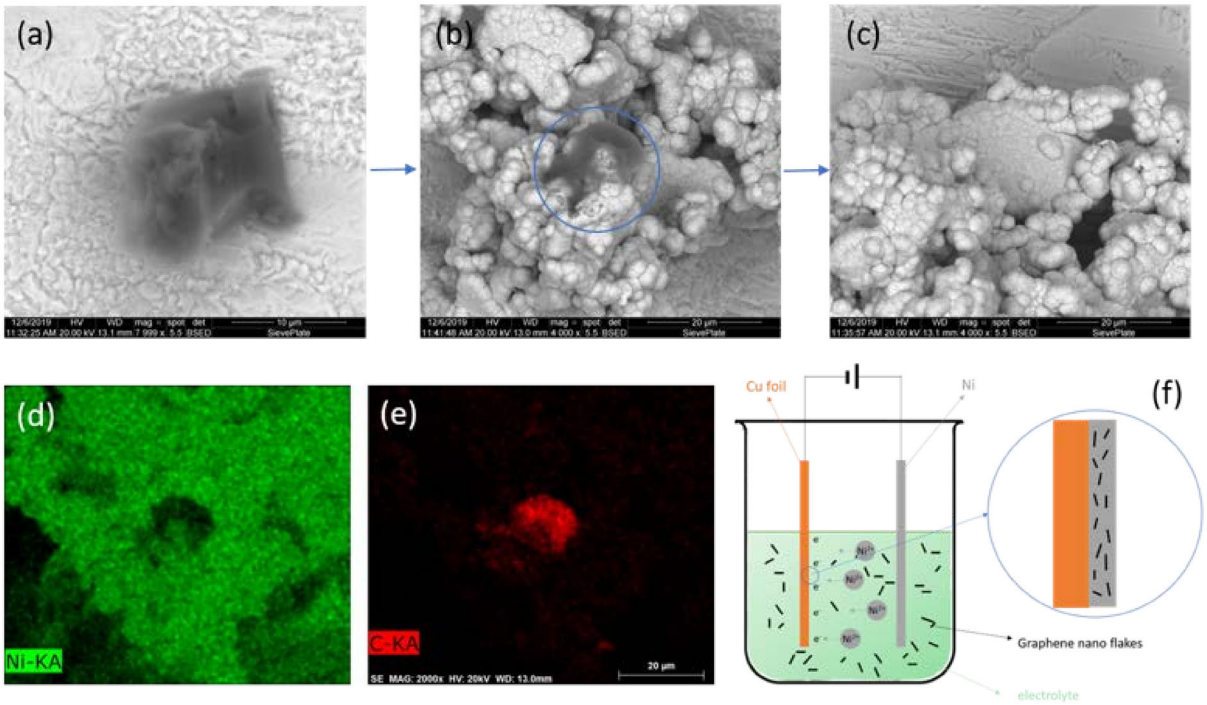

Figure 9.2: (a) Graphene particles adhered on the Ni surface. (b) The graphene particle (blue circle) was partially buried by the growing Ni phase. (c) The graphene particle was fully buried by the Ni phase. The corresponding EDS mapping of Ni (d) and C (e) in (b). (f) The setup for the electrochemical deposition process

2. Layered graphene

The second strategy was that a continuous layer of graphene was first fabricated, then a layer of metal was grown on the graphene layer. With this method, a ply containing a continuous layer of graphene and continuous layer of Ni can be obtained. After this process, these layered structures can be stacked and sintered to produce a final multilayered Ni-graphene composite. Figure 9.3 displays the typical process to fabricate the laminated Ni-graphene composite. The upper box and lower box denote the ply fabrication and composite fabrication, respectively.

Nonetheless, on the one hand, it is cumbersome to obtain a layer of continuous carbon phase with traditional methods. For example, one of the mainstream methods to fabricate continuous carbon is Chemical Vapor Deposition (CVD), which not only requires costly equipment, but also needs very long processing time. On the other hand, although several outstanding pioneering previous studies have developed facile methods to fabricate continuous carbon layer (e.g. graphene, graphene oxide, graphene-like polymer), however, the direct applications are quite limited, to the best of our knowledge. In this study, we propose a novel facile method to fabricate macrolevel laminated Ni-graphene composites, using continuous graphene layers and electrochemical deposition. The advantages of this method include: it is much easier and cheaper than CVD method, the continuous layers of graphene may have larger property improvement than uniformly distributed graphene, and it has large potential to scale up to industrial level.

Ply fabrication. Firstly, a strip (1 in x 3 in) of silicone rubber was synthesized (Ecoflex ®, part A & B mixing ratio 1:1) after degassing and curing at 50 degrees Celsius in a regular petri dish. Then the silicone rubber was adhered on a glass slide with its self-surface-adhesion. Subsequently,

DISTRIBUTION A: Distribution approved for public release.

the silicone rubber and glass slide was dipped into the pre-prepared graphene DI water suspension (xgsciences® C-300, 5 mg/mL), and sonicated for 30 min. After thoroughly drying, a continuous layer of graphene was firmly adhered on the silicone rubber, which was then used as the cathode for electrochemical deposition for 12 h. The current density is 1 mA/cm2. The low current density can help reduce the defects (e.g. cracks, holes) generated during deposition, because of low growing rate. Consequently, a ply containing a layer of continuous graphene and continuous Ni can be obtained, followed by carefully peeling off the silicone rubber stripe. Loose graphene particles on the ply can be removed by bath sonication in ethanol.

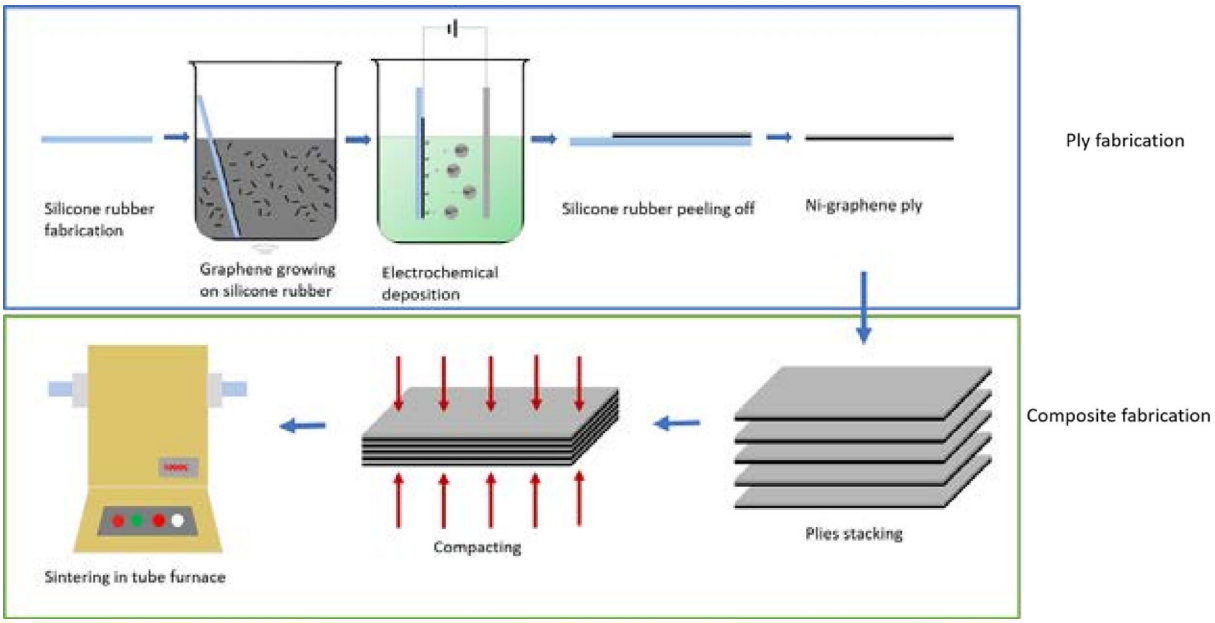

Figure 9.3: The schematic for the ply and composite fabrication for the continuous laminated Ni-graphene composite

Composite fabrication. A typical laminated composite contains five plies. A binder was used for better ply adhesion and sintering. The binder solution was prepared with 0.1 g binder (Acryloid B-72, Talas®) fully dissolving into 10 mL acetone. Then the solution was uniformly applied onto the ply surface with a pipette, and the plies were stacked on top of each other. A little pressure was applied on the stacked plies, and the plies can be adhered together when the acetone was fully evaporated (2 h). Subsequently, the stacked plies were sintered in a tube furnace at 1080 oC for 1 h with flowing N2. A dead weight (1 lb) was placed on the stacked plies during sintering.

DISTRIBUTION A: Distribution approved for public release.

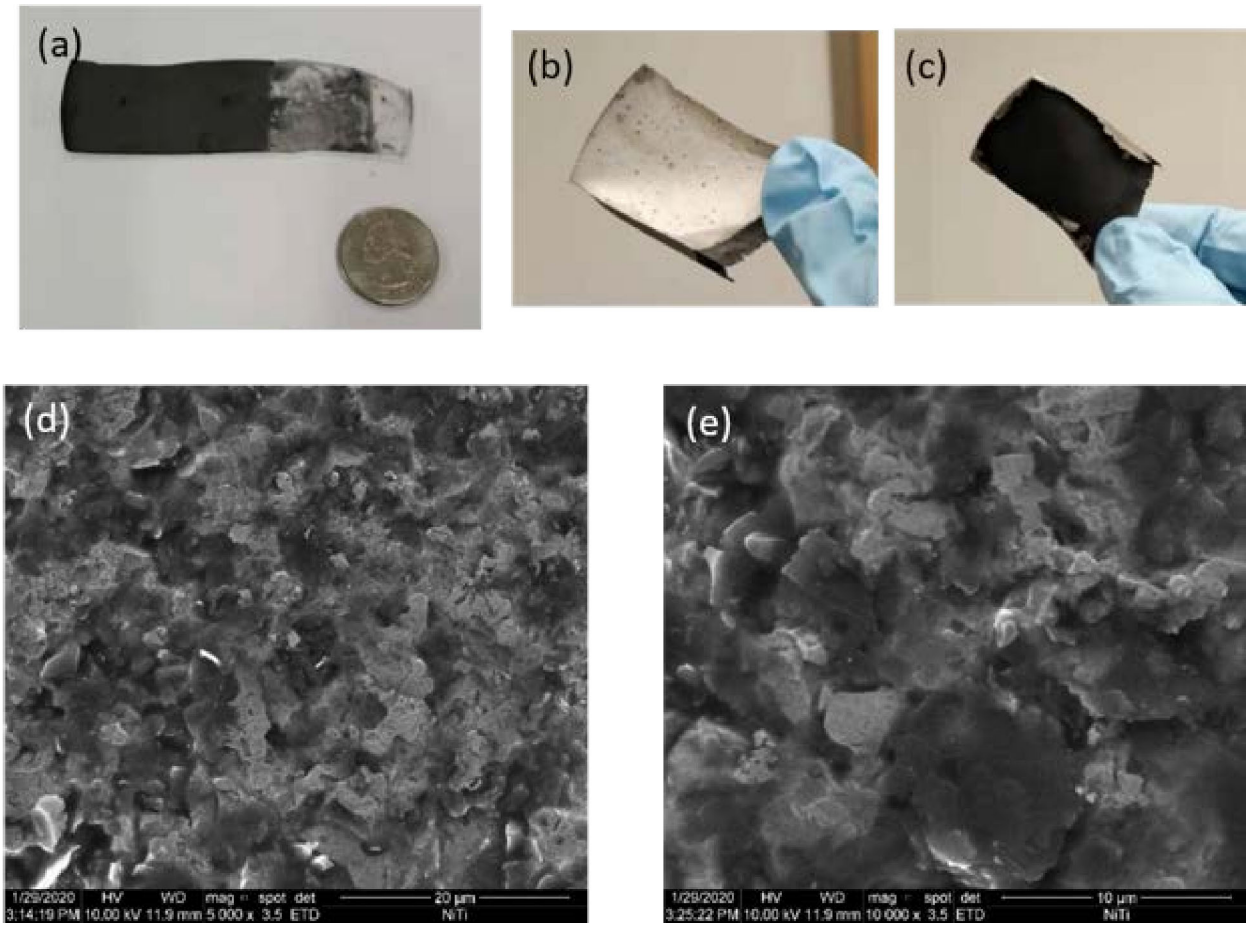

Figure 9.4: (a) The graphene (dark area) grown on the silicone rubber (transparent area). The digital and SEM images of the Ni side (b, d), and the graphene side (c, e) of one macrolevel freestanding Ni-graphene ply

Figure 9.4 (a) displays the silicone rubber with uniformly grown graphene. The graphene self-assembled on the silicone rubber with bath sonication applied. The mechanism may be two-folds. On the one hand, both the silicone rubber and graphene are hydrophobic, hereby, the adhesion of graphene and silicone rubber surface can reduce the total surface energy of the system. On the other hand, the silicone rubber surface is sticky, which can lead to better physical adhesion once the graphene contacted it. Figure 9.4 (b) and 9.4 (c) exhibit the Ni side and graphene side of the macrolevel freestanding ply after deposition, respectively. It can be seen that a uniform graphene layer can come off with the grown Ni phase. The Ni shows very few defects, such as holes or cracks. Figure 9.4 (d) and (e) are the SEM images of the Ni and graphene side of the ply, respectively. As shown in these figures, immediately after deposition, the grain size is no larger than 10 microns.

DISTRIBUTION A: Distribution approved for public release.

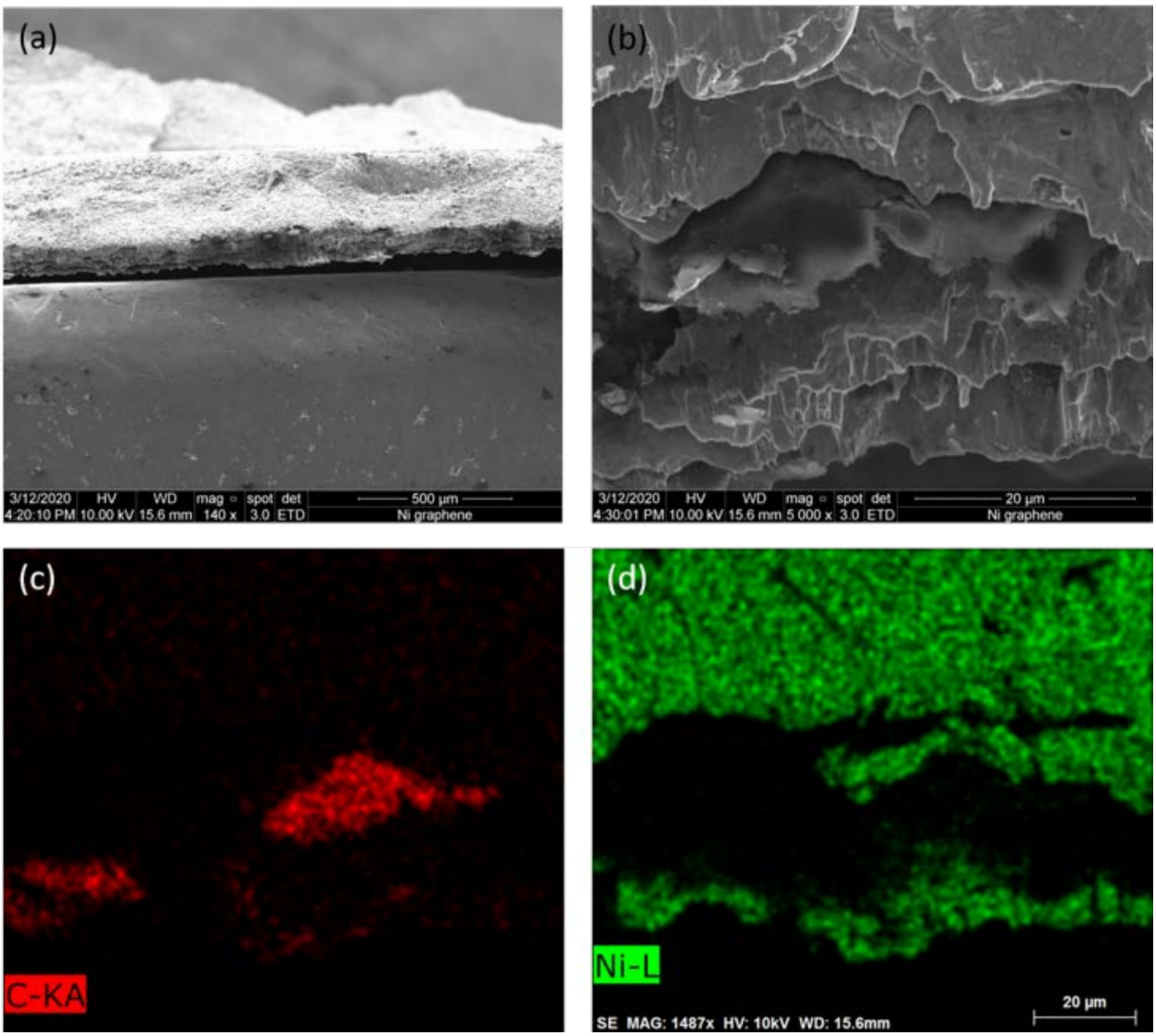

Figure 9.5: The SEM images of the laminated Ni-graphene composites, (a) low mag, and (b) high mag. The green arrow in (a) denotes the viewing angle of (b). The corresponding EDS mapping of C (c) and Ni (d) in (b)

Figure 9.5 (a) and (b) show the crossection of the laminated composite after the sintering. Notably, to better observe the step structures, the viewing direction of Figure 9.5b is a little inclined with the side, instead of perpendicular with the side (denoted in Figure 4a with a green arrow). The steps demonstrate the Ni layer and graphene layers stacking on each other alternatively, illustrating that laminated structure was successfully obtained. Nonetheless, it was also noted that the bonding among layers was not strong enough. The possible reason for that is the sintering temperature was not high enough. Figure 9.5 (c) and (d) are the EDS mapping of carbon and Ni for Figure 9.5 (b).

DISTRIBUTION A: Distribution approved for public release.

9.2 NiTi-graphene Composites

As shown Figure 9.1 (b) and (d), two preliminary baths where made for the NiTi-Graphene composites using the experimental conditions in Table 9.1. The reference bath with only the Ti powder was labeled as bath A while the one with both the Ti and graphene powder was labeled as bath B.

Figure 9.6 shows the embedding of Ti powders in the Ni matrix. The coverage of Ti particles inside the Ni matrix is not uniform. This may be due to the irregular shape of the Ti particles as well as the large range of particle sizes in the powder. The elemental map also suggests a higher density of graphene powders should be used in the bath to improve increase the weight percentage.

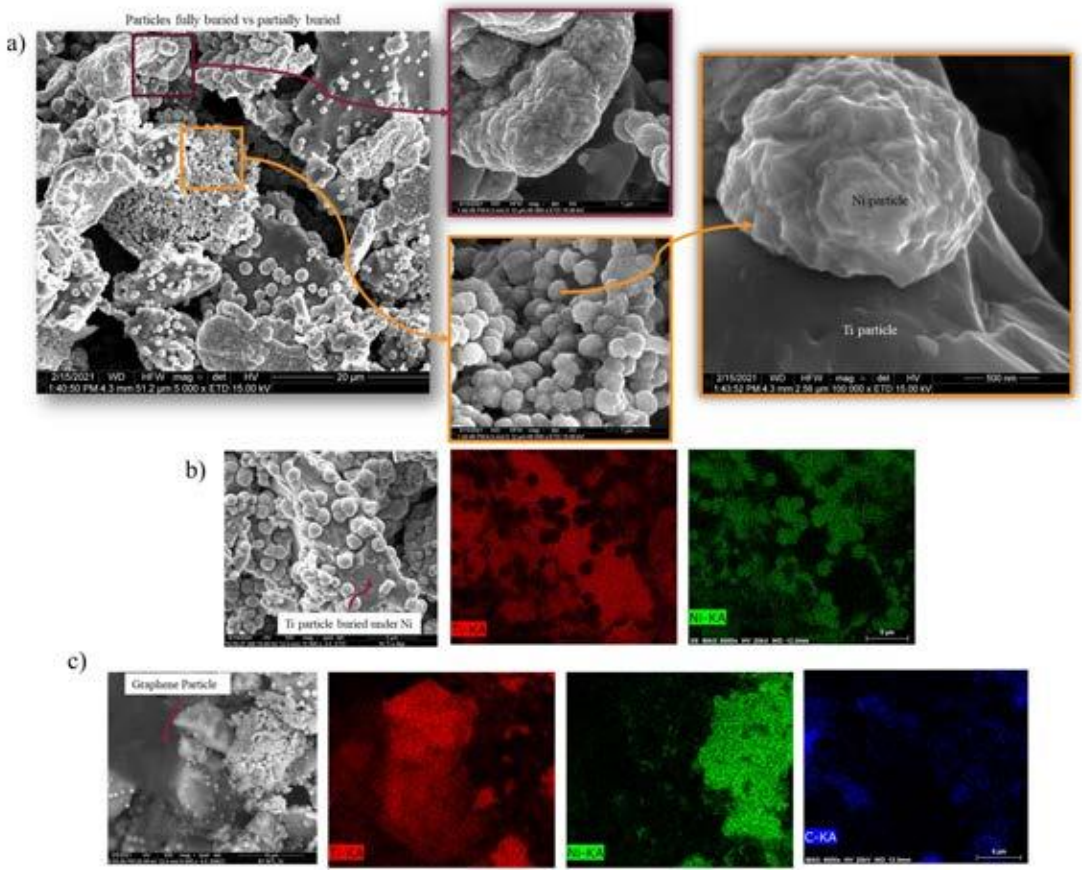

Figure 9.6: a) Secondary electron image showing the distribution of particles in the film as represented in Figure 9.1 a & d. (b, c) show the elemental map of the film separating Titanium (red), Nickel (green), and Carbon (blue). This shows that in some areas Ni_2^+ ions did not fully cover the Ti particles.

Samples A1-A3 and B1 were deposited using the additional parameters in Table 9.2. Following the deposition, a sintering heat treatment was done to burn out the inorganic compounds used in the bath and crystallize the films. Temperatures of 400 C° and 1100 C° were used. Figure 9.7 shows 3 samples in the as-deposited vs the heat-treated conditions. After heat-treatment of B1, we see that Ni+Ti did not completely diffuse into NiTi leading to a rather in-homogeneous material. In the backscattered electron images (BSE) the bright white contrast represents Ni-rich material, the darkest contrast represent carbon, and Ti-rich components are shown in between. We also find that

DISTRIBUTION A: Distribution approved for public release.

the conditions of A3 result in a more dense and uniform sample.

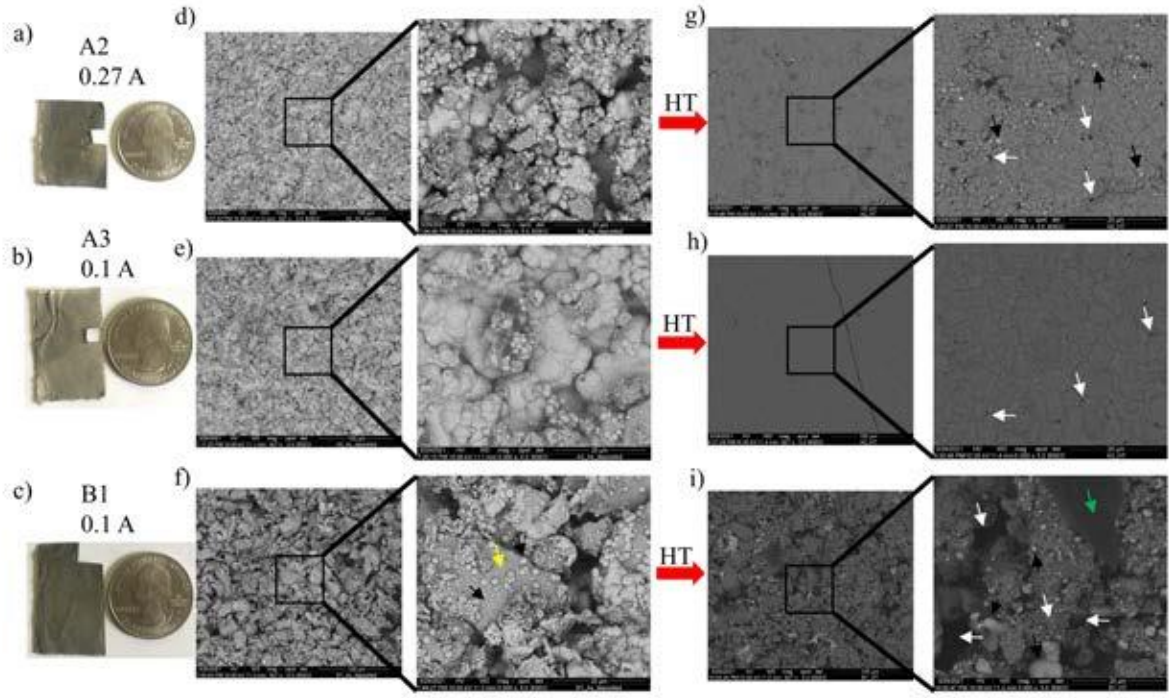

Figure 9.7: (a - c) show select samples deposited with bath A and B using different currents. (d - f) Are all backscattered electron images of the as-deposited A2, A3, and B1 films, respectively. (g - i) Are samples A2, A3, and B1, respectively, after sintering at 400 C° for 30 min then heat-treatment at 1100 C° for 60 min. The black arrows highlight areas of nickel-rich composition while the white arrows showing porosity. The green arrow points to a graphene particle while the yellow arrow shows partially buried Ti particles.

From the cross-section in Figure 9.8 we find that graphene flakes becomes completely embed inside the Ni matrix rather than land directly on Ti particles. The current densities used to lie at the upper and lower limits that we would require, meaning some intermediate current will give us a more uniform content of Ni+Ti in the film.

DISTRIBUTION A: Distribution approved for public release.

Table 9.2: The following parameters where kept constant between the two baths for the Ni+Ti samples while the current of $0.27A$ or $0.1A$ was used.

Parameter	Values
Area	26 mm x 20 mm
Bath Temperature	50 C°
Time	180 min

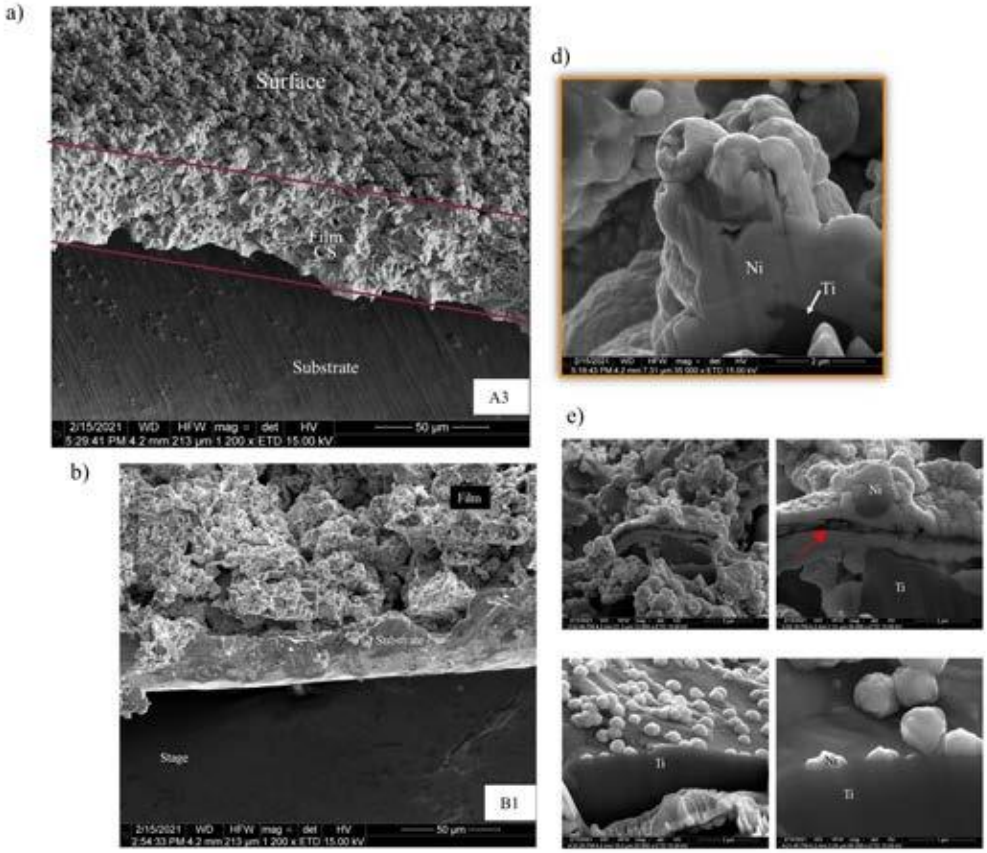

Figure 9.8: (a, b) show cross-section view of samples A3 and B1, respectively. (d, e) are sectioned particles deposited in the film. A relatively dense film was obtained from A3 compared to B1. This view also suggests that A3 is substantially Ni-rich while large areas of B1 may be Ti-rich. The red arrow shows a graphene particle embed inside a Ni matrix.

DISTRIBUTION A: Distribution approved for public release.

Bibliography

[1] C. Lee, X. Wei, J. W. Kysar, and J. Hone, "Measurement of the Elastic Properties and Intrinsic Strength of Monolayer Graphene," *Science*, vol. 321, pp. 385–388, July 2008.

[2] K. S. Novoselov, A. K. Geim, S. V. Morozov, D. Jiang, Y. Zhang, S. V. Dubonos, I. V. Grigorieva, and A. A. Firsov, "Electric Field Effect in Atomically Thin Carbon Films," *Science*, vol. 306, pp. 666–669, Oct. 2004. Publisher: American Association for the Advancement of Science Section: Report.

[3] H. Yue, L. Yao, X. Gao, S. Zhang, E. Guo, H. Zhang, X. Lin, and B. Wang, "Effect of ball-milling and graphene contents on the mechanical properties and fracture mechanisms of graphene nanosheets reinforced copper matrix composites," *Journal of Alloys and Compounds*, vol. 691, pp. 755–762, Jan. 2017.

[4] C. Ayyappadas, A. Muthuchamy, A. Raja Annamalai, and D. K. Agrawal, "An investigation on the effect of sintering mode on various properties of copper-graphene metal matrix composite," *Advanced Powder Technology*, vol. 28, pp. 1760–1768, July 2017.

[5] N. Khobragade, K. Sikdar, B. Kumar, S. Bera, and D. Roy, "Mechanical and electrical properties of copper-graphene nanocomposite fabricated by high pressure torsion," *Journal of Alloys and Compounds*, vol. 776, pp. 123–132, Mar. 2019.

[6] Y. Chen, X. Zhang, E. Liu, C. He, Y. Han, Q. Li, P. Nash, and N. Zhao, "Fabrication of three-dimensional graphene/Cu composite by in-situ CVD and its strengthening mechanism," *Journal of Alloys and Compounds*, vol. 688, pp. 69–76, Dec. 2016.

[7] W. J. Kim, T. J. Lee, and S. H. Han, "Multi-layer graphene/copper composites: Preparation using high-ratio differential speed rolling, microstructure and mechanical properties," *Carbon*, vol. 69, pp. 55–65, Apr. 2014.

[8] J. Dutkiewicz, P. Ozga, W. Maziarz, J. Pstruś, B. Kania, P. Bobrowski, and J. Stolarska, "Microstructure and properties of bulk copper matrix composites strengthened with various kinds of graphene nanoplatelets," *Materials Science and Engineering: A*, vol. 628, pp. 124–134, Mar. 2015.

[9] M. Cao, D.-B. Xiong, Z. Tan, G. Ji, B. Amin-Ahmadi, Q. Guo, G. Fan, C. Guo, Z. Li, and D. Zhang, "Aligning graphene in bulk copper: Nacre-inspired nanolaminated architecture coupled with in-situ processing for enhanced mechanical properties and high electrical conductivity," *Carbon*, vol. 117, pp. 65–74, June 2017.

DISTRIBUTION A: Distribution approved for public release.

[10] Y. J. Mai, M. P. Zhou, H. J. Ling, F. X. Chen, W. Q. Lian, and X. H. Jie, "Surfactant-free electrodeposition of reduced graphene oxide/copper composite coatings with enhanced wear resistance," *Applied Surface Science*, vol. 433, pp. 232–239, Mar. 2018.

[11] A. Kamboj, Y. Raghupathy, M. Y. Rekha, and C. Srivastava, "Morphology, Texture and Corrosion Behavior of Nanocrystalline Copper–Graphene Composite Coatings," *JOM*, vol. 69, pp. 1149–1154, July 2017.

[12] H. S. Maharana, P. K. Rai, and A. Basu, "Surface-mechanical and electrical properties of pulse electrodeposited Cu–graphene oxide composite coating for electrical contacts," *Journal of Materials Science*, vol. 52, pp. 1089–1105, Jan. 2017.

[13] Y. Kim, J. Lee, M. S. Yeom, J. W. Shin, H. Kim, Y. Cui, J. W. Kysar, J. Hone, Y. Jung, S. Jeon, and S. M. Han, "Strengthening effect of single-atomic-layer graphene in metal–graphene nanolayered composites," *Nature Communications*, vol. 4, p. 2114, July 2013.

[14] F. Shuang, Z. Dai, and K. E. Aifantis, "Strengthening in Metal/Graphene Composites: Capturing the Transition from Interface to Precipitate Hardening," *ACS Applied Materials & Interfaces*, vol. 13, pp. 26610–26620, June 2021. Publisher: American Chemical Society.

[15] J. Charleston, A. Agrawal, and R. Mirzaeifar, "Effect of interface configuration on the mechanical properties and dislocation mechanisms in metal graphene composites," *Computational Materials Science*, vol. 178, p. 109621, June 2020.

[16] A. Agrawal and R. Mirzaeifar, "Copper-graphene composites; developing the MEAM potential and investigating their mechanical properties," *Computational Materials Science*, vol. 188, p. 110204, Feb. 2021.

[17] B. Hwang, W. Kim, J. Kim, S. Lee, S. Lim, S. Kim, S. H. Oh, S. Ryu, and S. M. Han, "Role of Graphene in Reducing Fatigue Damage in Cu/Gr Nanolayered Composite," *Nano Letters*, vol. 17, pp. 4740–4745, Aug. 2017. Publisher: American Chemical Society.

[18] S. Feng, Q. Guo, Z. Li, G. Fan, Z. Li, D.-B. Xiong, Y. Su, Z. Tan, J. Zhang, and D. Zhang, "Strengthening and toughening mechanisms in graphene-Al nanolaminated composite micro-pillars," *Acta Materialia*, vol. 125, pp. 98–108, Feb. 2017.

[19] X. Fu, Z. Li, Q. Guo, G. Fan, Z. Li, D.-B. Xiong, Z. Tan, Y. Su, S. Osovski, and D. Zhang, "Orientation-Dependent Tensile Behavior of Nanolaminated Graphene-Al Composites: An In Situ Study," *Metallurgical and Materials Transactions A*, vol. 49, pp. 5229–5234, Nov. 2018.

[20] F. Yazdandoost, A. Yari Boroujeni, and R. Mirzaeifar, "Nanocrystalline nickel-graphene nanoplatelets composite: Superior mechanical properties and mechanics of properties enhancement at the atomistic level," *Physical Review Materials*, vol. 1, p. 076001, Dec. 2017.

[21] Z. Li, L. Zhao, Q. Guo, Z. Li, G. Fan, C. Guo, and D. Zhang, "Enhanced dislocation obstruction in nanolaminated graphene/Cu composite as revealed by stress relaxation experiments," *Scripta Materialia*, vol. 131, pp. 67–71, Apr. 2017.

DISTRIBUTION A: Distribution approved for public release.

[22] L. Zhao, Q. Guo, Z. Li, D.-B. Xiong, S. Osovski, Y. Su, and D. Zhang, "Strengthening and deformation mechanisms in nanolaminated graphene-Al composite micro-pillars affected by graphene in-plane sizes," *International Journal of Plasticity*, vol. 116, pp. 265–279, May 2019.

[23] Y. Kim, J. Baek, S. Kim, S. Kim, S. Ryu, S. Jeon, and S. M. Han, "Radiation Resistant Vanadium-Graphene Nanolayered Composite," *Scientific Reports*, vol. 6, p. 24785, Apr. 2016. Number: 1 Publisher: Nature Publishing Group.

[24] S.-Y. Park, E.-J. Gwak, M. Huang, R. S. Ruoff, and J.-Y. Kim, "Nanolaminate of metallic glass and graphene with enhanced elastic modulus, strength, and ductility in tension," *Scripta Materialia*, vol. 139, pp. 63–66, Oct. 2017.

[25] N. Lu, Z. Suo, and J. J. Vlassak, "The effect of film thickness on the failure strain of polymer-supported metal films," *Acta Materialia*, vol. 58, pp. 1679–1687, Mar. 2010.

[26] A. Agrawal and R. Mirzaeifar, "Graphene-Nickel interaction in layered metal-matrix composites," *Surface Science*, vol. 688, pp. 1–6, Oct. 2019.

[27] F. Zeng, F. Lv, R. Zong, S. Wen, X. Zhu, and F. Pan, "Tensile properties of Cr inserted amorphous Co85Zr9Nb6 films deposited on polymer substrate," *Journal of Alloys and Compounds*, vol. 477, pp. 239–242, May 2009.

[28] D. Y. W. Yu and F. Spaepen, "The yield strength of thin copper films on Kapton," *Journal of Applied Physics*, vol. 95, pp. 2991–2997, Mar. 2004.

[29] F. Macionczyk and W. Brückner, "Tensile testing of AlCu thin films on polyimide foils," *Journal of Applied Physics*, vol. 86, pp. 4922–4929, Nov. 1999.

[30] Y.-S. Kang and P. S. Ho, "Thickness dependent mechanical behavior of submicron aluminum films," *Journal of Electronic Materials*, vol. 26, pp. 805–813, July 1997.

[31] Y.-J. Yang, B. Zhang, H.-Y. Wan, K. Liu, and G.-P. Zhang, "Bilayer graphene-covered Cu flexible electrode with excellent mechanical reliability and electrical performance," *Journal of Materials Research*, vol. 34, pp. 3645–3653, Nov. 2019.

[32] Y.-J. Yang, B. Zhang, H.-Y. Wan, and G.-P. Zhang, "Role of Cu/graphene interface in suppressing fatigue damage of submicron Cu films for flexible electronics," *Materials Science and Engineering: A*, vol. 792, p. 139786, Aug. 2020.

[33] S. Mahieu, P. Ghekiere, D. Depla, and R. De Gryse, "Biaxial alignment in sputter deposited thin films," *Thin Solid Films*, vol. 515, pp. 1229–1249, Dec. 2006.

[34] V. M. Marx, F. Toth, A. Wiesinger, J. Berger, C. Kirchlechner, M. J. Cordill, F. D. Fischer, F. G. Rammerstorfer, and G. Dehm, "The influence of a brittle Cr interlayer on the deformation behavior of thin Cu films on flexible substrates: Experiment and model," *Acta Materialia*, vol. 89, pp. 278–289, May 2015.

DISTRIBUTION A: Distribution approved for public release.

[35] C. Xie and W. Tong, "Cracking and decohesion of a thin Al2O3 film on a ductile Al–5%Mg substrate," *Acta Materialia*, vol. 53, pp. 477–485, Jan. 2005.

[36] J. Hutchinson and Z. Suo, "Mixed Mode Cracking in Layered Materials," in *Advances in Applied Mechanics*, vol. 29, pp. 63–191, Elsevier, 1991.

[37] J. L. Beuth, "Cracking of thin bonded films in residual tension," *International Journal of Solids and Structures*, vol. 29, pp. 1657–1675, Jan. 1992.

[38] F. Macionczyk, W. Brückner, and G. Reiss, "Stress-Strain Curves by Tensile Testing of Thin Metallic Films On Thin Polyimide Foils: Al, AlCu, CuNi(Mn)," *MRS Online Proceedings Library (OPL)*, vol. 505, 1997. Publisher: Cambridge University Press.

[39] T. Li, Z. Y. Huang, Z. C. Xi, S. P. Lacour, S. Wagner, and Z. Suo, "Delocalizing strain in a thin metal film on a polymer substrate," *Mechanics of Materials*, vol. 37, pp. 261–273, Feb. 2005.

[40] M. Yanaka, Y. Tsukahara, N. Nakaso, and M. Yanaka, "Cracking phenomena of brittle films in nanostructure composites analysed by a modified shear lag model with residual strain," *Journal of Materials Science*, vol. 33, pp. 2111–2119, Apr. 1998.

[41] P. A. Gruber, J. Böhm, F. Onuseit, A. Wanner, R. Spolenak, and E. Arzt, "Size effects on yield strength and strain hardening for ultra-thin Cu films with and without passivation: A study by synchrotron and bulge test techniques," *Acta Materialia*, vol. 56, pp. 2318–2335, June 2008.

[42] M. J. Cordill, A. Taylor, J. Schalko, and G. Dehm, "Fracture and Delamination of Chromium Thin Films on Polymer Substrates," *Metallurgical and Materials Transactions A*, vol. 41, pp. 870–875, Apr. 2010.

[43] H. Ming-Yuan and J. W. Hutchinson, "Crack deflection at an interface between dissimilar elastic materials," *International Journal of Solids and Structures*, vol. 25, pp. 1053–1067, Jan. 1989.

[44] H. M. Ledbetter and E. R. Naimon, "Elastic Properties of Metals and Alloys. II. Copper," *Journal of Physical and Chemical Reference Data*, vol. 3, pp. 897–935, Oct. 1974. Publisher: American Institute of Physics.

[45] A. Politano and G. Chiarello, "Probing the Young's modulus and Poisson's ratio in graphene/metal interfaces and graphite: a comparative study," *Nano Research*, vol. 8, pp. 1847–1856, June 2015.

[46] X. Liu, T. H. Metcalf, J. T. Robinson, B. H. Houston, and F. Scarpa, "Shear Modulus of Monolayer Graphene Prepared by Chemical Vapor Deposition," *Nano Letters*, vol. 12, pp. 1013–1017, Feb. 2012. Publisher: American Chemical Society.

[47] P. Zhang, L. Ma, F. Fan, Z. Zeng, C. Peng, P. E. Loya, Z. Liu, Y. Gong, J. Zhang, X. Zhang, P. M. Ajayan, T. Zhu, and J. Lou, "Fracture toughness of graphene," *Nature Communications*, vol. 5, p. 3782, Apr. 2014. Number: 1 Publisher: Nature Publishing Group.

DISTRIBUTION A: Distribution approved for public release.

[48] J. Li, Y. Yang, G. Feng, X. Luo, Q. Sun, and N. Jin, "Adhesion and fracture toughness at -Ti(0001)/TiC(111): A first-principles investigation," *Applied Surface Science*, vol. 286, pp. 240–248, Dec. 2013.

[49] K. Chen and M. Bielawski, "Interfacial fracture toughness of transition metal nitrides," *Surface and Coatings Technology*, vol. 203, pp. 598–601, Dec. 2008.

[50] T. Yoon, W. C. Shin, T. Y. Kim, J. H. Mun, T.-S. Kim, and B. J. Cho, "Direct Measurement of Adhesion Energy of Monolayer Graphene As-Grown on Copper and Its Application to Renewable Transfer Process," *Nano Letters*, vol. 12, pp. 1448–1452, Mar. 2012. Publisher: American Chemical Society.

[51] Z. Li, Q. Guo, Z. Li, G. Fan, D.-B. Xiong, Y. Su, J. Zhang, and D. Zhang, "Enhanced Mechanical Properties of Graphene (Reduced Graphene Oxide)/Aluminum Composites with a Bioinspired Nanolaminated Structure," *Nano Letters*, vol. 15, pp. 8077–8083, Dec. 2015.

[52] D.-B. Xiong, M. Cao, Q. Guo, Z. Tan, G. Fan, Z. Li, and D. Zhang, "Graphene-and-Copper Artificial Nacre Fabricated by a Preform Impregnation Process: Bioinspired Strategy for Strengthening-Toughening of Metal Matrix Composite," *ACS Nano*, vol. 9, pp. 6934–6943, July 2015. Publisher: American Chemical Society.

[53] A. F. Bower, *Applied Mechanics of Solids*. CRC Press, Oct. 2009. Google-Books-ID: 1_sCzMNZMEsC.

[54] S. Plimpton, "Fast Parallel Algorithms for Short-Range Molecular Dynamics," *Journal of Computational Physics*, vol. 117, pp. 1–19, Mar. 1995.

[55] A. Stukowski, "Visualization and analysis of atomistic simulation data with OVITO–the Open Visualization Tool," *Modelling and Simulation in Materials Science and Engineering*, vol. 18, p. 015012, Jan. 2010.

[56] B.-J. Lee and M. I. Baskes, "Second nearest-neighbor modified embedded-atom-method potential," *Physical Review B*, vol. 62, pp. 8564–8567, Oct. 2000.

[57] W.-S. Ko, B. Grabowski, and J. Neugebauer, "Development and application of a Ni-Ti interatomic potential with high predictive accuracy of the martensitic phase transition," *Physical Review B*, vol. 92, p. 134107, Oct. 2015.

[58] M. S. Daw and M. I. Baskes, "Semiempirical, Quantum Mechanical Calculation of Hydrogen Embrittlement in Metals," *Physical Review Letters*, vol. 50, pp. 1285–1288, Apr. 1983.

[59] M. S. Daw and M. I. Baskes, "Embedded-atom method: Derivation and application to impurities, surfaces, and other defects in metals," *Physical Review B*, vol. 29, pp. 6443–6453, June 1984.

[60] M. I. Baskes, "Application of the Embedded-Atom Method to Covalent Materials: A Semiempirical Potential for Silicon," *Physical Review Letters*, vol. 59, pp. 2666–2669, Dec. 1987.

DISTRIBUTION A: Distribution approved for public release.

[61] M. I. Baskes, J. S. Nelson, and A. F. Wright, "Semiempirical modified embedded-atom potentials for silicon and germanium," *Physical Review B*, vol. 40, pp. 6085–6100, Sept. 1989.

[62] T. Yamanaka, S. Morimoto, and H. Kanda, "Influence of the isotope ratio on the lattice constant of diamond," *Physical Review B*, vol. 49, pp. 9341–9343, Apr. 1994.

[63] R. Vogelgesang, A. K. Ramdas, S. Rodriguez, M. Grimsditch, and T. R. Anthony, "Brillouin and Raman scattering in natural and isotopically controlled diamond," *Physical Review B*, vol. 54, pp. 3989–3999, Aug. 1996.

[64] J. Kelling, P. Zahn, J. Schuster, and S. Gemming, "Elastic and piezoresistive properties of nickel carbides from first principles," *Physical Review B*, vol. 95, Jan. 2017.

[65] J. S. Gibson, J. Uddin, T. R. Cundari, N. K. Bodiford, and A. K. Wilson, "First-principle study of structure and stability of nickel carbides," *Journal of Physics: Condensed Matter*, vol. 22, no. 44, p. 445503, 2010.

[66] W. G. Hoover, "Canonical dynamics: Equilibrium phase-space distributions," *Physical Review A*, vol. 31, pp. 1695–1697, Mar. 1985.

[67] W. G. Hoover, "Constant-pressure equations of motion," *Physical Review A*, vol. 34, pp. 2499–2500, Sept. 1986.

[68] W.-S. Ko, S. B. Maisel, B. Grabowski, J. B. Jeon, and J. Neugebauer, "Atomic scale processes of phase transformations in nanocrystalline NiTi shape-memory alloys," *Acta Materialia*, vol. 123, pp. 90–101, Jan. 2017.

[69] Y. Xiao, P. Zeng, and L. Lei, "Grain size effect on mechanical performance of nanostructured superelastic NiTi alloy," *Materials Research Express*, vol. 4, p. 035702, Mar. 2017. Publisher: IOP Publishing.

[70] L. Wang, J. Jin, J. Cao, P. Yang, and Q. Peng, "Interaction of Edge Dislocations with Graphene Nanosheets in Graphene/Fe Composites," *Crystals*, vol. 8, p. 160, Apr. 2018.

[71] S. F. Bartolucci, J. Paras, M. A. Rafiee, J. Rafiee, S. Lee, D. Kapoor, and N. Koratkar, "Graphene–aluminum nanocomposites," *Materials Science and Engineering: A*, vol. 528, pp. 7933–7937, Oct. 2011.

[72] A. F. Fonseca, T. Liang, D. Zhang, K. Choudhary, S. R. Phillpot, and S. B. Sinnott, "Titanium-Carbide Formation at Defective Curved Graphene-Titanium Interfaces," *MRS Advances*, vol. 3, no. 8-9, pp. 457–462, 2018.

[73] S. E. Muller, R. R. Santhapuram, and A. K. Nair, "Failure mechanisms in pre-cracked Ni-graphene nanocomposites," *Computational Materials Science*, vol. 152, pp. 341–350, Sept. 2018.

[74] L. Zhao, Q. Guo, Z. Li, G. Fan, Z. Li, D.-B. Xiong, Y. Su, Z. Tan, C. Guo, and D. Zhang, "Grain boundary-assisted deformation in graphene–Al nanolaminated composite micro-pillars," *Materials Research Letters*, vol. 6, pp. 41–48, Jan. 2018.

DISTRIBUTION A: Distribution approved for public release.

[75] S. E. Shin, H. J. Choi, J. H. Shin, and D. H. Bae, "Strengthening behavior of few-layered graphene/aluminum composites," *Carbon*, vol. 82, pp. 143–151, Feb. 2015.

[76] Z. Hu, F. Chen, D. Lin, Q. Nian, P. Parandoush, X. Zhu, Z. Shao, and G. J. Cheng, "Laser additive manufacturing bulk graphene–copper nanocomposites," *Nanotechnology*, vol. 28, p. 445705, Oct. 2017.

[77] Y. Yan, S. Zhou, and S. Liu, "Atomistic simulation on nanomechanical response of indented graphene/nickel system," *Computational Materials Science*, vol. 130, pp. 16–20, Apr. 2017.

[78] S. E. Muller and A. K. Nair, "Dislocation Nucleation in Nickel-Graphene Nanocomposites Under Mode I Loading," *JOM*, vol. 68, pp. 1909–1914, July 2016.

[79] Z. Ren, N. Meng, K. Shehzad, Y. Xu, S. Qu, B. Yu, and J. K. Luo, "Mechanical properties of nickel-graphene composites synthesized by electrochemical deposition," *Nanotechnology*, vol. 26, no. 6, p. 065706, 2015.

[80] D. Kuang, L. Xu, L. Liu, W. Hu, and Y. Wu, "Graphene–nickel composites," *Applied Surface Science*, vol. 273, pp. 484–490, May 2013.

[81] A. F. Fonseca, T. Liang, D. Zhang, K. Choudhary, S. R. Phillpot, and S. B. Sinnott, "Graphene–Titanium Interfaces from Molecular Dynamics Simulations," *ACS Applied Materials & Interfaces*, vol. 9, pp. 33288–33297, Sept. 2017.

[82] M. Fuentes-Cabrera, M. I. Baskes, A. V. Melechko, and M. L. Simpson, "Bridge structure for the graphene/Ni(111) system: A first principles study," *Physical Review B*, vol. 77, p. 035405, Jan. 2008.

[83] A. Dahal and M. Batzill, "Graphene–nickel interfaces: a review," *Nanoscale*, vol. 6, pp. 2548–2562, Feb. 2014.

[84] Y. Gamo, A. Nagashima, M. Wakabayashi, M. Terai, and C. Oshima, "Atomic structure of monolayer graphite formed on Ni(111)," *Surface Science*, vol. 374, pp. 61–64, Mar. 1997.

[85] W. Zhao, S. M. Kozlov, O. Höfert, K. Gotterbarm, M. P. A. Lorenz, F. Viñes, C. Papp, A. Görling, and H.-P. Steinrück, "Graphene on Ni(111): Coexistence of Different Surface Structures," *The Journal of Physical Chemistry Letters*, vol. 2, pp. 759–764, Apr. 2011.

[86] Z. Xu and M. J. Buehler, "Interface structure and mechanics between graphene and metal substrates: a first-principles study," *Journal of Physics: Condensed Matter*, vol. 22, no. 48, p. 485301, 2010.

[87] X. Zhang, J. Zhou, H. Song, X. Chen, Y. V. Fedoseeva, A. V. Okotrub, and L. G. Bulusheva, ""Butterfly Effect" in CuO/Graphene Composite Nanosheets: A Small Interfacial Adjustment Triggers Big Changes in Electronic Structure and Li-Ion Storage Performance," *ACS Applied Materials & Interfaces*, vol. 6, pp. 17236–17244, Oct. 2014.

[88] S.-W. Chang, A. K. Nair, and M. J. Buehler, "Nanoindentation study of size effects in nickel–graphene nanocomposites," *Philosophical Magazine Letters*, vol. 93, pp. 196–203, Apr. 2013.

DISTRIBUTION A: Distribution approved for public release.

[89] C. K. Gan and D. J. Srolovitz, "First-principles study of graphene edge properties and flake shapes," *Physical Review B*, vol. 81, Mar. 2010.

[90] M. Vanin, J. J. Mortensen, A. K. Kelkkanen, J. M. Garcia-Lastra, K. S. Thygesen, and K. W. Jacobsen, "Graphene on metals: A van der Waals density functional study," *Physical Review B*, vol. 81, p. 081408, Feb. 2010.

[91] Y. Liu, A. Dobrinsky, and B. I. Yakobson, "Graphene Edge from Armchair to Zigzag: The Origins of Nanotube Chirality?," *Physical Review Letters*, vol. 105, p. 235502, Dec. 2010.

[92] R. O. Jones and O. Gunnarsson, "The density functional formalism, its applications and prospects," *Reviews of Modern Physics*, vol. 61, pp. 689–746, July 1989.

[93] G. Kresse and J. Furthmüller, "Efficiency of ab-initio total energy calculations for metals and semiconductors using a plane-wave basis set," *Computational Materials Science*, vol. 6, pp. 15–50, July 1996.

[94] P. E. Blöchl, "Projector augmented-wave method," *Physical Review B*, vol. 50, pp. 17953–17979, Dec. 1994.

[95] H. J. Monkhorst and J. D. Pack, "Special points for Brillouin-zone integrations," *Physical Review B*, vol. 13, pp. 5188–5192, June 1976.

[96] X. Sun, S. Entani, Y. Yamauchi, A. Pratt, and M. Kurahashi, "Spin polarization study of graphene on the Ni(111) surface by density functional theory calculations with a semiempirical long-range dispersion correction," *Journal of Applied Physics*, vol. 114, p. 143713, Oct. 2013.

[97] A. A. Taleb and D. Farías, "Phonon dynamics of graphene on metals," *Journal of Physics: Condensed Matter*, vol. 28, p. 103005, Feb. 2016.

[98] G. Anagnostopoulos, C. Androulidakis, E. N. Koukaras, G. Tsoukleri, I. Polyzos, J. Parthenios, K. Papagelis, and C. Galiotis, "Stress Transfer Mechanisms at the Submicron Level for Graphene/Polymer Systems," *ACS Applied Materials & Interfaces*, vol. 7, pp. 4216–4223, Feb. 2015.

[99] S. M. Kozlov, F. Viñes, and A. Görling, "Bonding Mechanisms of Graphene on Metal Surfaces," *The Journal of Physical Chemistry C*, vol. 116, pp. 7360–7366, Apr. 2012.

[100] P. Nicolini, E. Guàrdia, and M. Masia, "Shortcomings of the standard Lennard–Jones dispersion term in water models, studied with force matching," *The Journal of Chemical Physics*, vol. 139, p. 184111, Nov. 2013.

[101] K. Lu, L. Lu, and S. Suresh, "Strengthening Materials by Engineering Coherent Internal Boundaries at the Nanoscale," *Science*, vol. 324, pp. 349–352, Apr. 2009.

[102] X. L. Wu, Y. T. Zhu, Y. G. Wei, and Q. Wei, "Strong Strain Hardening in Nanocrystalline Nickel," *Physical Review Letters*, vol. 103, p. 205504, Nov. 2009.

DISTRIBUTION A: Distribution approved for public release.

[103] S. Weng, H. Ning, T. Fu, N. Hu, Y. Zhao, C. Huang, and X. Peng, "Molecular dynamics study of strengthening mechanism of nanolaminated graphene/Cu composites under compression," *Scientific Reports*, vol. 8, p. 3089, Feb. 2018. Number: 1 Publisher: Nature Publishing Group.

[104] V. I. Artyukhov, Y. Hao, R. S. Ruoff, and B. I. Yakobson, "Breaking of Symmetry in Graphene Growth on Metal Substrates," *Physical Review Letters*, vol. 114, p. 115502, Mar. 2015.

[105] W. Peng and K. Sun, "Effects of Cu/graphene interface on the mechanical properties of multilayer Cu/graphene composites," *Mechanics of Materials*, p. 103270, Dec. 2019.

[106] Y. Zhang and S. Sanvito, "Interface engineering of graphene nanosheet reinforced ${\mathrm{ZrB}}_{2}$ composites by tuning surface contacts," *Physical Review Materials*, vol. 3, p. 073604, July 2019.

[107] C. Kalcher, T. Brink, J. Rohrer, A. Stukowski, and K. Albe, "Elastostatic loading of metallic glass-crystal nanocomposites: Relationship of creep rate and interface energy," *Physical Review Materials*, vol. 3, p. 093605, Sept. 2019.

[108] X. Li, W. Cai, J. An, S. Kim, J. Nah, D. Yang, R. Piner, A. Velamakanni, I. Jung, E. Tutuc, S. K. Banerjee, L. Colombo, and R. S. Ruoff, "Large-Area Synthesis of High-Quality and Uniform Graphene Films on Copper Foils," *Science*, vol. 324, no. 5932, pp. 1312–1314, 2009.

[109] K. S. Kim, Y. Zhao, H. Jang, S. Y. Lee, J. M. Kim, K. S. Kim, J.-H. Ahn, P. Kim, J.-Y. Choi, and B. H. Hong, "Large-scale pattern growth of graphene films for stretchable transparent electrodes," *Nature*, vol. 457, pp. 706–710, Feb. 2009.

[110] D. Hull and D. J. Bacon, *Introduction to dislocations*. Amsterdam: Elsevier/Butterworth-Heinemann, 5. ed ed., 2011.

[111] K. Duan, F. Zhu, K. Tang, L. He, Y. Chen, and S. Liu, "Effects of chirality and number of graphene layers on the mechanical properties of graphene-embedded copper nanocomposites," *Computational Materials Science*, vol. 117, pp. 294–299, May 2016.

[112] Y. He, F. Huang, H. Li, Y. Sui, F. Wei, Q. Meng, W. Yang, and J. Qi, "Tensile mechanical properties of nano-layered copper/graphene composite," *Physica E: Low-dimensional Systems and Nanostructures*, vol. 87, pp. 233–236, Mar. 2017.

[113] R. Rezaei, "Tensile mechanical characteristics and deformation mechanism of metal-graphene nanolayered composites," *Computational Materials Science*, vol. 151, pp. 181–188, Aug. 2018.

[114] V. H. Vardanyan and H. M. Urbassek, "Dislocation interactions during nanoindentation of nickel-graphene nanocomposites," *Computational Materials Science*, vol. 170, p. 109158, Dec. 2019.

[115] H. Huang, X. Tang, F. Chen, J. Liu, H. Li, and D. Chen, "Graphene damage effects on radiation-resistance and configuration of copper–graphene nanocomposite under irradiation: A molecular dynamics study," *Scientific Reports*, vol. 6, p. 39391, Dec. 2016. Number: 1 Publisher: Nature Publishing Group.

DISTRIBUTION A: Distribution approved for public release.

[116] J. Uddin, M. I. Baskes, S. G. Srinivasan, T. R. Cundari, and A. K. Wilson, "Modified embedded atom method study of the mechanical properties of carbon nanotube reinforced nickel composites," *Physical Review B*, vol. 81, p. 104103, Mar. 2010.

[117] A. Stukowski, V. V. Bulatov, and A. Arsenlis, "Automated identification and indexing of dislocations in crystal interfaces," *Modelling and Simulation in Materials Science and Engineering*, vol. 20, p. 085007, Oct. 2012.

[118] D. Chachamovitz and D. Mordehai, "The Stress-Dependent Activation Parameters for Dislocation Nucleation in Molybdenum Nanoparticles," *Scientific Reports*, vol. 8, pp. 1–10, Mar. 2018.

[119] J. Wang, Q. Zhou, S. Shao, and A. Misra, "Strength and plasticity of nanolaminated materials," *Materials Research Letters*, vol. 5, pp. 1–19, Jan. 2017.

[120] J. J. Gilman and W. G. Johnston, "Dislocations in Lithium Fluoride Crystals," in *Solid State Physics* (F. Seitz and D. Turnbull, eds.), vol. 13, pp. 147–222, Academic Press, Jan. 1962.

[121] J. Frenkel, "Zur Theorie der Elastizittsgrenze und der Festigkeit kristallinischer Krper," *Zeitschrift fr Physik*, vol. 37, pp. 572–609, July 1926.

[122] E. Orowan, "Fracture and strength of solids," *Reports on Progress in Physics*, vol. 12, pp. 185–232, Jan. 1949.

[123] Y.-L. Liu, Y. Zhang, H.-B. Zhou, G.-H. Lu, and M. Kohyama, "Theoretical strength and charge redistribution of fcc Ni in tension and shear," *Journal of Physics: Condensed Matter*, vol. 20, p. 335216, Aug. 2008.

[124] P. Schall, M. Feuerbacher, M. Bartsch, U. Messerschmidt, and K. Urban, "Dislocation density evolution upon plastic deformation of Al-Pd-Mn single quasicrystals," *Philosophical Magazine Letters*, vol. 79, pp. 785–796, Oct. 1999.

[125] L. Zhang, N. Sekido, and T. Ohmura, "Real time correlation between flow stress and dislocation density in steel during deformation," *Materials Science and Engineering: A*, vol. 611, pp. 188–193, Aug. 2014.

[126] M. Zaiser, "Scale invariance in plastic flow of crystalline solids," *Advances in Physics*, vol. 55, pp. 185–245, Jan. 2006.

[127] D. Akinwande, N. Petrone, and J. Hone, "Two-dimensional flexible nanoelectronics," *Nature Communications*, vol. 5, p. 5678, Dec. 2014. Number: 1 Publisher: Nature Publishing Group.

[128] A. Falin, Q. Cai, E. J. G. Santos, D. Scullion, D. Qian, R. Zhang, Z. Yang, S. Huang, K. Watanabe, T. Taniguchi, M. R. Barnett, Y. Chen, R. S. Ruoff, and L. H. Li, "Mechanical properties of atomically thin boron nitride and the role of interlayer interactions," *Nature Communications*, vol. 8, p. 15815, June 2017. Number: 1 Publisher: Nature Publishing Group.

DISTRIBUTION A: Distribution approved for public release.

[129] J. Wozniak, M. Kostecki, T. Cygan, M. Buczek, and A. Olszyna, "Self-lubricating aluminium matrix composites reinforced with 2D crystals," *Composites Part B: Engineering*, vol. 111, pp. 1–9, Feb. 2017.

[130] K. Chu and C. Jia, "Enhanced strength in bulk graphene–copper composites," *physica status solidi (a)*, vol. 211, no. 1, pp. 184–190, 2014. _eprint: https://onlinelibrary.wiley.com/doi/pdf/10.1002/pssa.201330051.

[131] R. Jiang, X. Zhou, Q. Fang, and Z. Liu, "Copper–graphene bulk composites with homogeneous graphene dispersion and enhanced mechanical properties," *Materials Science and Engineering: A*, vol. 654, pp. 124–130, Jan. 2016.

[132] K. Chu, X.-h. Wang, F. Wang, Y.-b. Li, D.-j. Huang, H. Liu, W.-l. Ma, F.-x. Liu, and H. Zhang, "Largely enhanced thermal conductivity of graphene/copper composites with highly aligned graphene network," *Carbon*, vol. 127, pp. 102–112, Feb. 2018.

[133] S. Bashirvand and A. Montazeri, "New aspects on the metal reinforcement by carbon nanofillers: A molecular dynamics study," *Materials & Design*, vol. 91, pp. 306–313, Feb. 2016.

[134] H. Huang, X. Tang, F. Chen, Y. Yang, J. Liu, H. Li, and D. Chen, "Radiation damage resistance and interface stability of copper–graphene nanolayered composite," *Journal of Nuclear Materials*, vol. 460, pp. 16–22, May 2015.

[135] X. J. Long, B. Li, L. Wang, J. Y. Huang, J. Zhu, and S. N. Luo, "Shock response of Cu/graphene nanolayered composites," *Carbon*, vol. 103, pp. 457–463, July 2016.

[136] H. Shang and W. Wang, "Shock responses of graphene reinforced composites via molecular dynamics simulations," *Journal of Physics: Conference Series*, vol. 500, p. 112059, May 2014. Publisher: IOP Publishing.

[137] Y. Zhao, X. Peng, T. Fu, X. Zhu, N. Hu, and C. Yan, "Strengthening mechanisms of graphene coated copper under nanoindentation," *Computational Materials Science*, vol. 144, pp. 42–49, Mar. 2018.

[138] Y. Yan, Y. Lei, and S. Liu, "Tensile responses of carbon nanotubes-reinforced copper nanocomposites: Molecular dynamics simulation," *Computational Materials Science*, vol. 151, pp. 273–277, Aug. 2018.

[139] M. I. Baskes, "Modified embedded-atom potentials for cubic materials and impurities," *Physical Review B*, vol. 46, pp. 2727–2742, Aug. 1992. Publisher: American Physical Society.

[140] B.-J. Lee, J.-H. Shim, and M. I. Baskes, "Semiempirical atomic potentials for the fcc metals Cu, Ag, Au, Ni, Pd, Pt, Al, and Pb based on first and second nearest-neighbor modified embedded atom method," *Physical Review B*, vol. 68, Oct. 2003.

DISTRIBUTION A: Distribution approved for public release.

[141] B. Jelinek, S. Groh, M. F. Horstemeyer, J. Houze, S. G. Kim, G. J. Wagner, A. Moitra, and M. I. Baskes, "Modified embedded atom method potential for Al, Si, Mg, Cu, and Fe alloys," *Physical Review B*, vol. 85, June 2012.

[142] E. Asadi, M. Asle Zaeem, S. Nouranian, and M. I. Baskes, "Two-phase solid–liquid coexistence of Ni, Cu, and Al by molecular dynamics simulations using the modified embedded-atom method," *Acta Materialia*, vol. 86, pp. 169–181, Mar. 2015.

[143] S. A. Etesami and E. Asadi, "Molecular dynamics for near melting temperatures simulations of metals using modified embedded-atom method," *Journal of Physics and Chemistry of Solids*, vol. 112, pp. 61–72, Jan. 2018.

[144] B.-J. Lee and J. W. Lee, "A modified embedded atom method interatomic potential for carbon," *Calphad*, vol. 29, pp. 7–16, Mar. 2005.

[145] B.-J. Lee, "A modified embedded-atom method interatomic potential for the Fe–C system," *Acta Materialia*, vol. 54, pp. 701–711, Feb. 2006.

[146] H.-K. Kim, W.-S. Jung, and B.-J. Lee, "Modified embedded-atom method interatomic potentials for the Fe–Ti–C and Fe–Ti–N ternary systems," *Acta Materialia*, vol. 57, pp. 3140–3147, June 2009.

[147] W. Xiao, M. I. Baskes, and K. Cho, "MEAM study of carbon atom interaction with Ni nano particle," *Surface Science*, vol. 603, pp. 1985–1998, July 2009.

[148] B.-J. Lee, M. Baskes, H. Kim, and Y. Koo Cho, "Second nearest-neighbor modified embedded atom method potentials for bcc transition metals," *Physical Review B*, vol. 64, p. 184102, Oct. 2001.

[149] J. H. Rose, J. R. Smith, F. Guinea, and J. Ferrante, "Universal features of the equation of state of metals," *Physical Review B*, vol. 29, pp. 2963–2969, Mar. 1984.

[150] Y.-M. Kim and B.-J. Lee, "A modified embedded-atom method interatomic potential for the Cu–Zr system," *Journal of Materials Research*, vol. 23, pp. 1095–1104, Apr. 2008. Publisher: Cambridge University Press.

[151] F. Cataldo, "Structural relationships between dicopper diacetylide (Cu-CC-CC-Cu) and dicopper acetylide (Cu-CC-Cu)," *European Journal of Solid State and Inorganic Chemistry*, vol. 35, pp. 281–291, Mar. 1998.

[152] B. Balamurugan, B. R. Mehta, and S. M. Shivaprasad, ""Nanoparticle route" for the synthesis of a stable and stoichiometric Cu2C2 phase—a semiconductor material," *Applied Physics Letters*, vol. 82, pp. 115–117, Dec. 2002. Publisher: American Institute of Physics.

[153] Y. Le Page and P. Saxe, "Symmetry-general least-squares extraction of elastic data for strained materials from ab initio calculations of stress," *Physical Review B*, vol. 65, p. 104104, Feb. 2002. Publisher: American Physical Society.

DISTRIBUTION A: Distribution approved for public release.

[154] A. Togo and I. Tanaka, "First principles phonon calculations in materials science," *Scripta Materialia*, vol. 108, pp. 1–5, Nov. 2015.

[155] S. J. Stuart, A. B. Tutein, and J. A. Harrison, "A reactive potential for hydrocarbons with intermolecular interactions," *The Journal of Chemical Physics*, vol. 112, pp. 6472–6486, Mar. 2000. Publisher: American Institute of Physics.

[156] Y. Mishin, M. J. Mehl, D. A. Papaconstantopoulos, A. F. Voter, and J. D. Kress, "Structural stability and lattice defects in copper: Ab initio, tight-binding, and embedded-atom calculations," *Physical Review B*, vol. 63, p. 224106, May 2001. Publisher: American Physical Society.

[157] R. M. Nicklow, G. Gilat, H. G. Smith, L. J. Raubenheimer, and M. K. Wilkinson, "Phonon Frequencies in Copper at 49 and 298\ifmmode^\circ\else\textdegree\fi{}K," *Physical Review*, vol. 164, pp. 922–928, Dec. 1967. Publisher: American Physical Society.

[158] J. L. Warren, J. L. Yarnell, G. Dolling, and R. A. Cowley, "Lattice Dynamics of Diamond," *Physical Review*, vol. 158, pp. 805–808, June 1967.

[159] R. Nicklow, N. Wakabayashi, and H. G. Smith, "Lattice Dynamics of Pyrolytic Graphite," *Physical Review B*, vol. 5, pp. 4951–4962, June 1972. Publisher: American Physical Society.

[160] C. Oshima, T. Aizawa, R. Souda, Y. Ishizawa, and Y. Sumiyoshi, "Surface phonon dispersion curves of graphite (0001) over the entire energy region," *Solid State Communications*, vol. 65, pp. 1601–1604, Mar. 1988.

[161] S. Siebentritt, R. Pues, K.-H. Rieder, and A. M. Shikin, "Surface phonon dispersion in graphite and in a lanthanum graphite intercalation compound," *Physical Review B*, vol. 55, pp. 7927–7934, Mar. 1997.

[162] A. T. Pham, M. Barisik, and B. Kim, "Interfacial thermal resistance between the graphene-coated copper and liquid water," *International Journal of Heat and Mass Transfer*, vol. 97, pp. 422–431, June 2016.

[163] C. Zhang, C. Lu, L. Pei, J. Li, R. Wang, and K. Tieu, "The negative Poisson's ratio and strengthening mechanism of nanolayered graphene/Cu composites," *Carbon*, vol. 143, pp. 125–137, Mar. 2019.

[164] S. Miyazaki, S. Kimura, F. Takei, T. Miura, K. Otsuka, and Y. Suzuki, "Shape memory effect and pseudoelasticity in a TiNi single crystal," *Scripta Metallurgica*, vol. 17, pp. 1057–1062, Sept. 1983.

[165] K. Otsuka and C. M. Wayman, *Shape Memory Materials*. Cambridge University Press, Oct. 1999. Google-Books-ID: DvItE9XUlN8C.

[166] M. Es-Souni, M. Es-Souni, and H. Fischer-Brandies, "Assessing the biocompatibility of NiTi shape memory alloys used for medical applications," *Analytical and Bioanalytical Chemistry*, vol. 381, pp. 557–567, Feb. 2005.

DISTRIBUTION A: Distribution approved for public release.

[167] A. Ishida, M. Sato, and S. Miyazaki, "Mechanical properties of Ti–Ni shape memory thin films formed by sputtering," *Materials Science and Engineering: A*, vol. 273-275, pp. 754–757, Dec. 1999.

[168] W. Huang, "On the selection of shape memory alloys for actuators," *Materials & Design*, vol. 23, pp. 11–19, Feb. 2002.

[169] J. J. Gill, D. T. Chang, L. A. Momoda, and G. P. Carman, "Manufacturing issues of thin film NiTi microwrapper," *Sensors and Actuators A: Physical*, vol. 93, pp. 148–156, Sept. 2001.

[170] Y. Q. Fu, J. K. Luo, W. M. Huang, A. J. Flewitt, and W. I. Milne, "Thin film shape memory alloys for optical sensing applications," *Journal of Physics: Conference Series*, vol. 76, p. 012032, July 2007.

[171] J. Subbian, S. Raikwar, N. K. Sindam, M. T. Madhav, and P. I. Anand, "Design and Development of NiTi Shape Memory Alloy Belt for Waste Heat Energy Recovery System," *Journal of Materials Engineering and Performance*, Aug. 2021.

[172] A. Ishida, "Ti–Ni–Cu/polyimide composite-film actuator and simulation tool," *Sensors and Actuators A: Physical*, vol. 222, pp. 228–236, Feb. 2015.

[173] A. Behera, D. K. Rajak, R. Kolahchi, M.-L. Scutaru, and C. I. Pruncu, "Current global scenario of Sputter deposited NiTi smart systems," *Journal of Materials Research and Technology*, vol. 9, pp. 14582–14598, Nov. 2020.

[174] S. Miyazaki, Y. Q. Fu, and W. M. Huang, *Thin Film Shape Memory Alloys: Fundamentals and Device Applications*. Cambridge University Press, 2009.

[175] S. Jayachandran, K. Akash, S. S. Mani Prabu, M. Manikandan, M. Muralidharan, A. Brolin, and I. A. Palani, "Investigations on performance viability of NiTi, NiTiCu, CuAlNi and CuAlNiMn shape memory alloy/Kapton composite thin film for actuator application," *Composites Part B: Engineering*, vol. 176, p. 107182, Nov. 2019.

[176] C. R. Knick, D. J. Sharar, A. A. Wilson, G. L. Smith, C. J. Morris, and H. A. Bruck, "High frequency, low power, electrically actuated shape memory alloy MEMS bimorph thermal actuators," *Journal of Micromechanics and Microengineering*, vol. 29, p. 075005, May 2019. Publisher: IOP Publishing.

[177] K. Loger, A. Engel, J. Haupt, Q. Li, R. Lima de Miranda, E. Quandt, G. Lutter, and C. Selhuber-Unkel, "Cell adhesion on NiTi thin film sputter-deposited meshes," *Materials Science and Engineering: C*, vol. 59, pp. 611–616, Feb. 2016.

[178] K. Otsuka and X. Ren, "Physical metallurgy of Ti–Ni-based shape memory alloys," *Progress in Materials Science*, vol. 50, pp. 511–678, July 2005.

[179] T. W. Duerig, K. N. Melton, D. Stöckel, and C. M. Wayman, *Engineering Aspects of Shape Memory Alloys*. Butterworth-Heinemann, Jan. 1990. Google-Books-ID: y7QgBQAAQBAJ.

DISTRIBUTION A: Distribution approved for public release.

[180] Y. Fu, H. Du, W. Huang, S. Zhang, and M. Hu, "TiNi-based thin films in MEMS applications: a review," *Sensors and Actuators A: Physical*, vol. 112, pp. 395–408, May 2004.

[181] K. Gangwar, S. Jayachandran, A. Sahu, A. Singh, and I. A. Palani, "Influence of pre-strain on attributes of Ni-rich NiTi/ Kapton polyimide bimorph for flexible mirrors," *Sensors and Actuators A: Physical*, vol. 341, p. 113607, July 2022.

[182] P. Kreiml, M. Rausch, V. L. Terziyska, H. Köstenbauer, J. Winkler, C. Mitterer, and M. J. Cordill, "Improved electro-mechanical reliability of flexible systems with alloyed Mo-Ta adhesion layers," *Thin Solid Films*, vol. 720, p. 138533, Feb. 2021.

[183] M. Cordill, A. Kleinbichler, B. Völker, P. Kraker, D. Economy, D. Többens, C. Kirchlechner, and M. Kennedy, "In-situ observations of the fracture and adhesion of Cu/Nb multilayers on polyimide substrates," *Materials Science and Engineering: A*, vol. 735, pp. 456–462, Sept. 2018.

[184] A. Ishida and M. Sato, "Development of Polyimide/SMA Thin-Film Actuator," *Materials Science Forum*, vol. 654-656, pp. 2075–2078, June 2010.

[185] V. G. Kotnur, F. D. Tichelaar, W. T. Fu, J. T. M. De Hosson, and G. C. A. M. Janssen, "Shape memory NiTi thin films deposited on polyimide at low temperature," *Surface and Coatings Technology*, vol. 258, pp. 1145–1151, Nov. 2014.

[186] Y. Xiang, T. Li, Z. Suo, and J. J. Vlassak, "High ductility of a metal film adherent on a polymer substrate," *Applied Physics Letters*, vol. 87, p. 161910, Oct. 2005. Publisher: American Institute of Physics.

[187] M. J. Cordill, D. F. Bahr, N. R. Moody, and W. W. Gerberich, "Adhesion measurements using telephone cord buckles," *Materials Science and Engineering: A*, vol. 443, pp. 150–155, Jan. 2007.

[188] N. Lu, X. Wang, Z. Suo, and J. Vlassak, "Metal films on polymer substrates stretched beyond 50%," *Applied Physics Letters*, vol. 91, p. 221909, Nov. 2007.

[189] B. Winzek, S. Schmitz, H. Rumpf, T. Sterzl, R. Hassdorf, S. Thienhaus, J. Feydt, M. Moske, and E. Quandt, "Recent developments in shape memory thin film technology," *Materials Science and Engineering: A*, vol. 378, pp. 40–46, July 2004.

[190] K. K. Ho and G. P. Carman, "Sputter deposition of NiTi thin ®lm shape memory alloy using a heated target," *Thin Solid Films*, p. 12, 2000.

[191] B. G. Priyadarshini, S. Aich, and M. Chakraborty, "Nano-crystalline NiTi alloy thin films fabricated using magnetron co-sputtering from elemental targets: Effect of substrate conditions," *Thin Solid Films*, vol. 616, pp. 733–745, Oct. 2016.

[192] J. Frenzel, E. P. George, A. Dlouhy, C. Somsen, M. F. X. Wagner, and G. Eggeler, "Influence of Ni on martensitic phase transformations in NiTi shape memory alloys," *Acta Materialia*, vol. 58, pp. 3444–3458, May 2010.

DISTRIBUTION A: Distribution approved for public release.

[193] S. Miyazaki and A. Ishida, "Martensitic transformation and shape memory behavior in sputter-deposited TiNi-base thin films," *Materials Science and Engineering: A*, vol. 273-275, pp. 106–133, Dec. 1999.

[194] A. Gyobu, Y. Kawamura, H. Horikawa, and T. Saburi, "Martensitic Transformations in Sputter-Deposited Shape Memory Ti–Ni Films," *Materials Transactions, JIM*, vol. 37, no. 4, pp. 697–702, 1996.

[195] E. Quandt, C. Halene, H. Holleck, K. Feit, M. Kohl, P. Schlomacher, A. Skokan, and K. D. Skrobanck, "Sputter deposition of TiNi, TiNiPd and TiPd films displaying the two-way shape-memory effect," *Sensors and Actuators A: Physical*, vol. 53, pp. 434–439, May 1996.

[196] M. Kabla, H. Seiner, M. Musilova, M. Landa, and D. Shilo, "The relationships between sputter deposition conditions, grain size, and phase transformation temperatures in NiTi thin films," *Acta Materialia*, vol. 70, pp. 79–91, May 2014.

[197] W. Tillmann and S. Momeni, "Comparison of NiTi thin films sputtered from separate elemental targets and Ti-rich alloy targets," *Journal of Materials Processing Technology*, vol. 220, pp. 184–190, June 2015.

[198] C.-L. Shih, B.-K. Lai, H. Kahn, S. Phillips, and A. Heuer, "A robust co-sputtering fabrication procedure for TiNi shape memory alloys for MEMS," *Journal of Microelectromechanical Systems*, vol. 10, no. 1, pp. 69–79, 2001.

[199] H.-J. Lee and A. G. Ramirez, "Crystallization and phase transformations in amorphous NiTi thin films for microelectromechanical systems," *Applied Physics Letters*, vol. 85, pp. 1146–1148, Aug. 2004.

[200] J. Bae, H. Lee, D. Seo, S. Yun, J. Yang, S. Huh, H. Jeong, and J. Noh, "Grain Size and Phase Transformation Behavior of TiNi Shape-Memory-Alloy Thin Film under Different Deposition Conditions," *Materials*, vol. 13, p. 3229, Jan. 2020. Number: 14 Publisher: Multidisciplinary Digital Publishing Institute.

[201] H. Hou, R. F. Hamilton, M. W. Horn, and Y. Jin, "NiTi thin films prepared by biased target ion beam deposition co-sputtering from elemental Ni and Ti targets," *Thin Solid Films*, vol. 570, pp. 1–6, Nov. 2014.

[202] A. Ishida, A. Takei, and S. Miyazaki, "Shape memory thin film of TiNi formed by sputtering," *Thin Solid Films*, vol. 228, pp. 210–214, May 1993.

[203] H.-J. Lee, H. Ni, D. T. Wu, and A. G. Ramirez, "A Microstructural Map of Crystallized NiTi Thin Film Derived from <I>In Situ</I> TEM Methods," *MATERIALS TRANSACTIONS*, vol. 47, no. 3, pp. 527–531, 2006.

[204] X. Wang, M. Rein, and J. J. Vlassak, "Crystallization kinetics of amorphous equiatomic NiTi thin films: Effect of film thickness," *Journal of Applied Physics*, vol. 103, p. 023501, Jan. 2008.

DISTRIBUTION A: Distribution approved for public release.

[205] X. Huang and A. G. Ramirez, "Structural relaxation and crystallization of NiTi thin film metallic glasses," *Applied Physics Letters*, vol. 95, p. 121911, Sept. 2009.

[206] H. Hou, R. F. Hamilton, and M. W. Horn, "Crystallization and microstructure evolution of nanoscale NiTi thin films prepared by biased target ion beam deposition," *Journal of Vacuum Science & Technology B*, vol. 34, p. 010601, Nov. 2015. Publisher: American Vacuum Society.

[207] J. L. Seguin, M. Bendahan, A. Isalgue, V. Esteve-Cano, H. Carchano, and V. Torra, "Low temperature crystallised Ti-rich NiTi shape memory alloy films for microactuators," *Sensors and Actuators A: Physical*, vol. 74, pp. 65–69, Apr. 1999.

[208] A. Ishida and M. Sato, "Ti–Ni–Cu shape-memory alloy thin film formed on polyimide substrate," *Thin Solid Films*, vol. 516, pp. 7836–7839, Sept. 2008.

[209] W. Tillmann and S. Momeni, "In-situ annealing of NiTi thin films at different temperatures," *Sensors and Actuators A: Physical*, vol. 221, pp. 9–14, Jan. 2015.

[210] H. Cicek, I. Efeoglu, Y. Totik, K. V. Ezirmik, and E. Arslan, "A low temperature in-situ crystalline TiNi shape memory thin film deposited by magnetron sputtering," *Surface and Coatings Technology*, vol. 284, pp. 90–93, Dec. 2015.

[211] S. Heltzel and C. O. A. Semprimoschnig, "A Detailed Study on the Thermal Endurance of Kapton HN®i and Upilex S®," *High Performance Polymers*, vol. 16, pp. 235–248, June 2004. Publisher: SAGE Publications Ltd STM.

[212] K. Battes, C. Day, and V. Hauer, "Outgassing behavior of different high-temperature resistant polymers," *Journal of Vacuum Science & Technology A*, vol. 36, p. 021602, Dec. 2017.

[213] L. Hou, T. J. Pence, and D. S. Grummon, "Structure and Thermal Stability in Titanium-Nickel Thin Films Sputtered at Elevated-Temperature on Inorganic and Polymeric Substrates," *MRS Proceedings*, vol. 360, Jan. 1994.

[214] V. G. Kotnur, F. D. Tichelaar, and G. C. A. M. Janssen, "Sputter deposited Ni–Ti thin films on polyimide substrate," *Surface and Coatings Technology*, vol. 222, pp. 44–47, May 2013.

[215] M. Mohri and M. Nili-Ahmadabadi, "On the nano-glass formation of the Ni–Ti thin films and related micro-structure and mechanical properties by controlling sputtering conditions," *Materials Research Express*, vol. 6, p. 076421, Apr. 2019.

[216] G. Pan, Z. Cao, M. Wei, J. Shi, L. Xu, and X. Meng, "Thickness and grain size dependence of B2–R martensitic transformation behaviors in nanoscale TiNi films," *Materials Letters*, vol. 130, pp. 285–288, Sept. 2014.

[217] Y. Q. Fu, S. Zhang, M. J. Wu, W. M. Huang, H. J. Du, J. K. Luo, A. J. Flewitt, and W. I. Milne, "On the lower thickness boundary of sputtered TiNi films for shape memory application," *Thin Solid Films*, vol. 515, pp. 80–86, Sept. 2006.

DISTRIBUTION A: Distribution approved for public release.

[218] Y. Fu, H. Du, and S. Zhang, "Adhesion and interfacial structure of magnetron sputtered TiNi films on Si/SiO2 substrate," *Thin Solid Films*, vol. 444, pp. 85–90, Nov. 2003.

[219] H. Hou, R. F. Hamilton, and M. W. Horn, "Structure and interfacial analysis of nanoscale TiNi thin film prepared by biased target ion beam deposition," *Journal of Vacuum Science & Technology A*, vol. 33, p. 040601, May 2015. Publisher: American Vacuum Society.

[220] G. P. Badhirappan, "Understanding structure–property relation in nano-crystalline Ni–Ti shape memory alloy thin film micro-actuator," *ISSS Journal of Micro and Smart Systems*, vol. 8, pp. 1–11, June 2019.

[221] B. C. G. Marupalli, A. Behera, and S. Aich, "A Critical Review on Nickel–Titanium Thin-Film Shape Memory Alloy Fabricated by Magnetron Sputtering and Influence of Process Parameters," *Transactions of the Indian Institute of Metals*, vol. 74, pp. 2521–2540, Oct. 2021.

[222] M. Ohring, *The Materials Science of Thin Films*. Academic Press, 2 ed., Oct. 2001.

[223] M. R. Chellali, S. H. Nandam, S. Li, M. H. Fawey, E. Moreno-Pineda, L. Velasco, T. Boll, L. Pastewka, R. Kruk, P. Gumbsch, and H. Hahn, "Amorphous nickel nanophases inducing ferromagnetism in equiatomic NiTi alloy," *Acta Materialia*, vol. 161, pp. 47–53, Dec. 2018.

[224] L. B. Freund and S. Suresh, *Thin Film Materials: Stress, Defect Formation and Surface Evolution*. Cambridge University Press, Dec. 2008. Google-Books-ID: qPssHAAACAAJ.

[225] X. Huang, G. J. Ackland, and K. M. Rabe, "Crystal structures and shape-memory behaviour of NiTi," *Nature Materials*, vol. 2, pp. 307–311, May 2003.

[226] X. Huang and Y. Liu, "Surface morphology of sputtered NiTi-based shape memory alloy thin films," *Surface and Coatings Technology*, vol. 190, pp. 400–405, Jan. 2005.

[227] R. D. Gould, S. Kasap, and A. K. Ray, "Thin Films," in *Springer Handbook of Electronic and Photonic Materials* (S. Kasap and P. Capper, eds.), Springer Handbooks, pp. 1–1, Cham: Springer International Publishing, 2017.

[228] J. Jurusik, "Transmission electron microscopy investigation of the post-nucleation growth structure of amorphous cadmium arsenide thin films," *Thin Solid Films*, vol. 214, pp. 117–122, 1992.

[229] J. A. Thornton, "Influence of substrate temperature and deposition rate on structure of thick sputtered Cu coatings," *Journal of Vacuum Science and Technology*, vol. 12, pp. 830–835, July 1975. Publisher: American Vacuum Society.

[230] A. Anders, "A structure zone diagram including plasma-based deposition and ion etching," *Thin Solid Films*, vol. 518, pp. 4087–4090, May 2010.

[231] H. Hou, R. F. Hamilton, and M. W. Horn, "Crystallization of nanoscale NiTi alloy thin films using rapid thermal annealing," *Journal of Vacuum Science & Technology B, Nanotechnology and Microelectronics: Materials, Processing, Measurement, and Phenomena*, vol. 34, p. 06KK01, Nov. 2016.

DISTRIBUTION A: Distribution approved for public release.

[232] T. Karabacak, Y.-P. Zhao, G.-C. Wang, and T.-M. Lu, "Growth front roughening in silicon nitride films by plasma-enhanced chemical vapor deposition," *Physical Review B*, vol. 66, Aug. 2002.

[233] M. Pelliccione and T.-M. Lu, *Evolution of Thin Film Morphology: Modeling and Simulations*. Springer Series in Materials Science, New York: Springer-Verlag, 2008.

[234] Z. Fan, J. Li, Y. Yang, J. Wang, Q. Li, S. Xue, H. Wang, J. Lou, and X. Zhang, ""Ductile" Fracture of Metallic Glass Nanolaminates," *Advanced Materials Interfaces*, vol. 4, no. 21, p. 1700510, 2017. _eprint: https://onlinelibrary.wiley.com/doi/pdf/10.1002/admi.201700510.

[235] F. Shimizu, S. Ogata, and J. Li, "Yield point of metallic glass," *Acta Materialia*, vol. 54, pp. 4293–4298, Sept. 2006.

[236] M. F. Ashby and A. L. Greer, "Metallic glasses as structural materials," *Scripta Materialia*, vol. 54, pp. 321–326, Feb. 2006.

[237] F. Spaepen, "A microscopic mechanism for steady state inhomogeneous flow in metallic glasses," *Acta Metallurgica*, vol. 25, pp. 407–415, Apr. 1977.

[238] A. Argon, "Plastic deformation in metallic glasses," *Acta Metallurgica*, vol. 27, pp. 47–58, Jan. 1979.

[239] R. Rezaei, C. Deng, M. Shariati, and H. Tavakoli-Anbaran, "The ductility and toughness improvement in metallic glass through the dual effects of graphene interface," *Journal of Materials Research; Warrendale*, vol. 32, pp. 392–403, Jan. 2017. Num Pages: 12 Place: Warrendale, United Kingdom, Warrendale Publisher: Cambridge University Press.

[240] T. Brink, M. Peterlechner, H. Rösner, K. Albe, and G. Wilde, "Influence of Crystalline Nanoprecipitates on Shear-Band Propagation in Cu-Zr-Based Metallic Glasses," *Physical Review Applied*, vol. 5, p. 054005, May 2016. Publisher: American Physical Society.

[241] K. Albe, Y. Ritter, and D. Şopu, "Enhancing the plasticity of metallic glasses: Shear band formation, nanocomposites and nanoglasses investigated by molecular dynamics simulations," *Mechanics of Materials*, vol. 67, pp. 94–103, Dec. 2013.

[242] D. J. Ha, C. P. Kim, and S. Lee, "Tensile deformation behavior of two Ti-based amorphous matrix composites containing ductile dendrites," *Materials Science and Engineering: A*, vol. 552, pp. 404–409, Aug. 2012.

[243] T. Zhang, H. Y. Ye, J. Y. Shi, H. J. Yang, and J. W. Qiao, "Dendrite size dependence of tensile plasticity of in situ Ti-based metallic glass matrix composites," *Journal of Alloys and Compounds*, vol. 583, pp. 593–597, Jan. 2014.

[244] L. Zhang, H. Zhang, W. Li, T. Gemming, P. Wang, M. Bönisch, D. Şopu, J. Eckert, and S. Pauly, "-type Ti-based bulk metallic glass composites with tailored structural metastability," *Journal of Alloys and Compounds*, vol. 708, pp. 972–981, June 2017.

DISTRIBUTION A: Distribution approved for public release.

[245] M. L. Lee, Y. Li, and C. A. Schuh, "Effect of a controlled volume fraction of dendritic phases on tensile and compressive ductility in La-based metallic glass matrix composites," *Acta Materialia*, vol. 52, pp. 4121–4131, Aug. 2004.

[246] B. Zhang, D. Q. Zhao, M. X. Pan, W. H. Wang, and A. L. Greer, "Amorphous Metallic Plastic," *Physical Review Letters*, vol. 94, p. 205502, May 2005. Publisher: American Physical Society.

[247] D. C. Hofmann, J.-Y. Suh, A. Wiest, G. Duan, M.-L. Lind, M. D. Demetriou, and W. L. Johnson, "Designing metallic glass matrix composites with high toughness and tensile ductility," *Nature*, vol. 451, pp. 1085–1089, Feb. 2008. Number: 7182 Publisher: Nature Publishing Group.

[248] Y. Wu, Y. Xiao, G. Chen, C. T. Liu, and Z. Lu, "Bulk Metallic Glass Composites with Transformation-Mediated Work-Hardening and Ductility," *Advanced Materials*, vol. 22, no. 25, pp. 2770–2773, 2010. _eprint: https://onlinelibrary.wiley.com/doi/pdf/10.1002/adma.201000482.

[249] J.-Y. Kim, D. Jang, and J. R. Greer, "Nanolaminates Utilizing Size-Dependent Homogeneous Plasticity of Metallic Glasses," *Advanced Functional Materials*, vol. 21, no. 23, pp. 4550–4554, 2011. _eprint: https://onlinelibrary.wiley.com/doi/pdf/10.1002/adfm.201101164.

[250] W. Guo, E. Jägle, J. Yao, V. Maier, S. Korte-Kerzel, J. M. Schneider, and D. Raabe, "Intrinsic and extrinsic size effects in the deformation of amorphous CuZr/nanocrystalline Cu nanolaminates," *Acta Materialia*, vol. 80, pp. 94–106, Nov. 2014.

[251] Z. Xie, W.-R. Jian, Z. Wang, X. Zhang, and X. Yao, "Layer thickness effects on the strengthening and toughening mechanisms in metallic glass-graphene nanolaminates," *Computational Materials Science*, vol. 177, p. 109536, May 2020.

[252] H. Guo, P. F. Yan, Y. B. Wang, J. Tan, Z. F. Zhang, M. L. Sui, and E. Ma, "Tensile ductility and necking of metallic glass," *Nature Materials*, vol. 6, pp. 735–739, Oct. 2007. Number: 10 Publisher: Nature Publishing Group.

[253] S. Kuan, H. Chou, M. Liu, X. Du, and J. Huang, "Micromechanical response for the amorphous/amorphous nanolaminates," *Intermetallics*, vol. 18, pp. 2453–2457, Dec. 2010.

[254] J. J. Lewandowski and A. L. Greer, "Temperature rise at shear bands in metallic glasses," *Nature Materials*, vol. 5, pp. 15–18, Jan. 2006. Number: 1 Publisher: Nature Publishing Group.

[255] M. Liu, C. Lee, Y. Lai, and J. Huang, "Microscale deformation behavior of amorphous/nanocrystalline multilayered pillars," *Thin Solid Films*, vol. 518, pp. 7295–7299, Oct. 2010.

[256] A. Donohue, F. Spaepen, R. G. Hoagland, and A. Misra, "Suppression of the shear band instability during plastic flow of nanometer-scale confined metallic glasses," *Applied Physics Letters*, vol. 91, p. 241905, Dec. 2007. Publisher: American Institute of Physics.

DISTRIBUTION A: Distribution approved for public release.

[257] Z. Fan, S. Xue, J. Wang, K. Y. Yu, H. Wang, and X. Zhang, "Unusual size dependent strengthening mechanisms of Cu/amorphous CuNb multilayers," *Acta Materialia*, vol. 120, pp. 327–336, Nov. 2016.

[258] T. G. Nieh, T. W. Barbee, and J. Wadsworth, "Tensile properties of a free-standing Cu/Zr nanolaminate (or compositionally-modulated thin film)," *Scripta Materialia*, vol. 41, pp. 929–935, Oct. 1999.

[259] H. J. Pei, C. J. Lee, X. H. Du, Y. C. Chang, and J. C. Huang, "Tension behavior of metallic glass coating on Cu foil," *Materials Science and Engineering: A*, vol. 528, pp. 7317–7322, Sept. 2011.

[260] P. Sharma, K. Yubuta, H. Kimura, and A. Inoue, "Brittle metallic glass deforms plastically at room temperature in glassy multilayers," *Physical Review B*, vol. 80, p. 024106, July 2009. Publisher: American Physical Society.

[261] Y. Wang, J. Li, A. V. Hamza, and T. W. Barbee, "Ductile crystalline–amorphous nanolaminates," *Proceedings of the National Academy of Sciences*, vol. 104, pp. 11155–11160, July 2007. Publisher: National Academy of Sciences Section: Physical Sciences.

[262] H. T. Tran, H. Mraied, S. Izadi, A. A. Volinsky, and W. Cai, "Optimizing ductility and fracture of amorphous metal thin films on polyimide using multilayers," *International Journal of Fracture*, vol. 204, pp. 129–142, Apr. 2017.

[263] A. L. Greer, Y. Q. Cheng, and E. Ma, "Shear bands in metallic glasses," *Materials Science and Engineering: R: Reports*, vol. 74, pp. 71–132, Apr. 2013.

[264] Y. Li, Y. Wei, K. Zhang, Y. Zhang, Y. Wang, W. Tang, and B. Wei, "Rejuvenation, embryonic shear bands and improved tensile plasticity of metallic glasses by nanosecond laser shock wave," *Journal of Non-Crystalline Solids*, vol. 513, pp. 76–83, June 2019.

[265] C. A. Schuh, T. C. Hufnagel, and U. Ramamurty, "Mechanical behavior of amorphous alloys," *Acta Materialia*, vol. 55, pp. 4067–4109, July 2007.

[266] J. E. Velasco, A. Concustell, E. Pineda, and D. Crespo, "Plastic deformation induced anisotropy in metallic glasses: A molecular dynamics study," *Journal of Alloys and Compounds*, vol. 707, pp. 102–107, June 2017.

[267] J. R. Greer and J. T. M. De Hosson, "Plasticity in small-sized metallic systems: Intrinsic versus extrinsic size effect," *Progress in Materials Science*, vol. 56, pp. 654–724, Aug. 2011.

[268] C. E. Packard and C. A. Schuh, "Initiation of shear bands near a stress concentration in metallic glass," *Acta Materialia*, vol. 55, pp. 5348–5358, Sept. 2007.

[269] F. Shimizu, S. Ogata, and J. Li, "Theory of Shear Banding in Metallic Glasses and Molecular Dynamics Calculations," *MATERIALS TRANSACTIONS*, vol. 48, no. 11, pp. 2923–2927, 2007.

DISTRIBUTION A: Distribution approved for public release.

[270] M. I. Mendelev, D. J. Sordelet, and M. J. Kramer, "Using atomistic computer simulations to analyze x-ray diffraction data from metallic glasses," *Journal of Applied Physics*, vol. 102, p. 043501, Aug. 2007. Publisher: American Institute of Physics.

[271] M. I. Mendelev, D. K. Rehbein, R. T. Ott, M. J. Kramer, and D. J. Sordelet, "Computer simulation and experimental study of elastic properties of amorphous Cu-Zr alloys," *Journal of Applied Physics*, vol. 102, p. 093518, Nov. 2007. Publisher: American Institute of Physics.

[272] Z. Xie, W.-R. Jian, X. Tang, X. Zhang, and X. Yao, "Strengthening and toughening mechanisms of metallic glass nanocomposites via graphene nanoplatelets," *Journal of Non-Crystalline Solids*, vol. 546, p. 120284, Oct. 2020.

[273] Y. Zhang and A. L. Greer, "Thickness of shear bands in metallic glasses," *Applied Physics Letters*, vol. 89, p. 071907, Aug. 2006. Publisher: American Institute of Physics.

[274] B. Francois, F. Lacombe, and H. J. Herrmann, "Finite width of shear zones," *Physical Review E*, vol. 65, p. 031311, Mar. 2002. Publisher: American Physical Society.

[275] Y. Lu, M. Jiang, X. Lu, Z. Qin, Y. Huang, and J. Shen, "Dilatancy of Shear Transformations in a Colloidal Glass," *Physical Review Applied*, vol. 9, p. 014023, Jan. 2018.

[276] D. Şopu, A. Stukowski, M. Stoica, and S. Scudino, "Atomic-Level Processes of Shear Band Nucleation in Metallic Glasses," *Physical Review Letters*, vol. 119, p. 195503, Nov. 2017.

[277] Y. Bai and C. She, "Atomic structure evolution in metallic glasses under cyclic deformation," *Computational Materials Science*, vol. 169, p. 109094, Nov. 2019.

[278] S. Feng, L. Qi, L. Wang, S. Pan, M. Ma, X. Zhang, G. Li, and R. Liu, "Atomic structure of shear bands in Cu64Zr36 metallic glasses studied by molecular dynamics simulations," *Acta Materialia*, vol. 95, pp. 236–243, Aug. 2015.

DISTRIBUTION A: Distribution approved for public release.